HARVARD
Kenneth C. Griffin

GRADUATE SCHOOL
OF ARTS AND SCIENCES

THESIS ACCEPTANCE CERTIFICATE

The undersigned, appointed by the

Department of Physics

have examined a dissertation entitled

Motional Control of Polyatomic Molecules for Precision Measurement

presented by Alexander Frenett

candidate for the degree of Doctor of Philosophy and hereby certify that it is worthy of acceptance.

Signature _____

Typed name: Prof. John Doyle

Signature _____

Typed name: Prof. Susanne Yelin

Signature _____

Typed name: Prof. Matthew Reece

Date: August 12, 2024

Motional Control of Polyatomic Molecules for Precision Measurement

A DISSERTATION PRESENTED
BY
ALEXANDER FRENETT
TO
THE DEPARTMENT OF PHYSICS

IN PARTIAL FULFILLMENT OF THE REQUIREMENTS
FOR THE DEGREE OF
DOCTOR OF PHILOSOPHY
IN THE SUBJECT OF
PHYSICS

HARVARD UNIVERSITY
CAMBRIDGE, MASSACHUSETTS

AUGUST 2024

Thesis advisor: John M. Doyle Alexander Frenett

Motional Control of Polyatomic Molecules for Precision Measurement

Abstract

Extending AMO techniques of motional control to heavy polyatomic molecules opens new possibilities for precision measurements of fundamental physics. Though various laser-cooling and deceleration techniques have been applied to diatomic molecules throughout the last decade, their application to more complex molecules has heretofore been focused on light species, leaving generalizability to heavy species an open question. To investigate the high-mass frontier, we here study how to extend motional control to heavy-atom-containing polyatomic molecules. First, we discuss Zeeman-Sisyphus deceleration of YbOH, which can be used to decelerate species capable of scattering only 10s of photons. Then, we discuss radiative slowing and magneto-optical trapping of SrOH, techniques only extendable to species capable of scattering $\sim 10^4$ photons. The last work focuses on spectroscopy of nonlinear molecules to assess the viability of extending techniques of motional control to more complex species. We find a dependence of both rotational and vibrational control on symmetry group, and identify a next-generation candidate for laser cooling. We end with a overview tying these projects together, and assessing the future of motional control along mass and complexity axes, including brief suggestions of how complementary methods to those studied here can further expand into the frontiers of molecular control.

Contents

Listing of figures

To all the educators, both formal and informal, who have made this work possible.

Acknowledgments

First, I would like to thank my advisor John, without whom the opportunity to even attempt any of the work herein would be impossible. His ability to see the scientific opportunity in a project and to convince others of the same is unparalleled. I've learned a lot from him, both about the physics of our experiments and the effort required to navigate the social and organizational aspects of our work, a combination which is not often found.

If John's leadership was necessary support and organize our research, the next most important people were those who helped (and whom I helped) doing the actual research: the rest of the Doyle group. Every project in the group is necessarily a massively joint affair, and none of the work would have been possible without interest and dedication from every member of the experiments. In particular, the YbOH and SrOH teams contributed to all of the results herein, and made them what they were. Members of other experiments also provided useful input on both technical and theoretical ideas that helped us all advance further. All of these students and post-docs helped me learn more physics than any class, both through their assistance when I don't know something, and by trusting me to help them understand new concepts themselves when I did. Special thanks to Zack Lasner for his unwavering skepticism of my at-times mediocre understanding of physics. He constantly challenged me to hone my understanding of subtle concepts in an admirably supportive way.

A special thank you to the the staff in the lab and department that assisted me both personally and on an experimental level throughout my time here. In lab affairs, I appreciate the help and support of all the lab management of finances, reimburements, event organizing, etc. that worked with the group and CUA throughout my time, including but not limited to Erica Mantone, Adam Ackerman, Samantha Douklas, and Clare Ploucha. In the department, Jim in the electronics shop and Stan, Steve, Andy, and Alejandro in the machine shop helped us build much of our experimental components. In addition, the custodial staff was invaluable in their help upkeeping the lab and physics department physical environments. Thanks also to Lisa Cacciabaudo for her help organizationally, and also for maintaining all of our sanity and reminding us when we inevitably forget that one deadline we were definitely not supposed to forget.

Of course, making it through grad school would have been impossible for me without a network of friends and confidantes both in and out of the physics world. In lab, particularly to Abdullah, Annika, and Paige - thank you for making the day-to-day in lab fun, it made all the difference. Too many people in my cohort are deserving of appreciation to list here, but you all helped me make it through the program and have possibly too much fun at times while doing it (Quantum I final whiskey, anyone?).

Outside of lab, many thanks for the support and good times I had while playing with the Gambeta Futbol Club. It was great playing with you all. A huge thank you to Phi Ngyuen and Caroline Foscato at South End Soccer for giving me a chance to coach kids soccer for almost three years despite my busy schedule; it was a great to work with kids excited about soccer and to get a break from the physics department basements. Also from my time at SES, thank you to Matt Groppo. You taught me a lot about coaching and about life more broadly; you will be missed.

Last, but certainly not least, thank you to my family. To Mom and Dad - thank you for all the support, interest, and probably-not-frequent-enough calls throughout the last six years and all of the visits. To Ben and Marissa, thank you for the breaks from the chaos and the consistent family gossip. To my grandparents, both with us and passed on, thank you for all your love and belief throughout my entire educational journey; you all paved the path for me in many ways. To the rest of the family, including but not limited to aunts, uncles, cousins, second-cousins, third-cousins once-removed, etc.: thank you for all the love. I hope I didn't bore you all too much at family gatherings with talk of physics and mushrooms.

I know I am leaving people off who deserve to be on this list; there are so many of you all who have shaped my life throughout the program. To everyone who has been a part of my time here, thank you.

And to whom do we owe this magnificent inferno if not to you, to people like you? Tell me, Professor, when did all this madness begin? When did we cease to understand the world?

Benjamìn Labatut

1 Introduction

Advancement in scientific progress requires advancement in technology. This is the foundational principle behind the work presented here. In particular, our work aims to provide a route for improved measurements of fundamental physics using cold molecules as probes. Since it is difficult to improve the fundamental sensitivity of molecules to these phenomena, the advancements we pursue are related to control of the molecules of interest. Improved control will improve the measurement process it-

self, even with similar or even lower fundamental sensitivity than current-generation experiments.

We start here with discussion of the physics that we hope, one day, to measure. By understanding the target phenomena it is then possible to derive how new physics produces low-energy effects. These effects then motivate certain molecular species as candidates for measurements, including those used in ongoing experiments. Only after understanding the molecular structure necessary for the physics applications can we begin to examine how we can hope to exert motional control over some subset of the set of physically-relevant species.

We end the chapter with an outline of the remainder of the thesis, in which we present methods and results of molecular control for species that are indeed sensitive to some instances of new physics.

1.1 Fundamental Physics

1.1.1 The Standard Model

The Standard Model is the most accurate microscopic physical model of our universe. Some of the constituents are intimately familiar to atomic, molecular and optical (AMO) physicists through their omnipresence in the low-energy world, like electrons and photons. Others are rarely encountered in our day-to-day work, like strange quarks and W bosons. Nevertheless, these too affect the structure of atoms and molecules through their contributions to nuclear structure and dressing of nuclear - electronic interactions. Indeed, all constituents of the Standard Model are necessary to describe any interaction of fundamental particles; it is this complexity that gives the theory astounding precision. An outline of the basic structure of the theory is useful

to understanding how fundamental "particle physics" affects the systems we study in AMO.

The Standard Model is a quantum field theory (QFT) composed of a number of fields that permeate all of space. Fundamental matter like leptons and quarks are described as spin-1/2 fermionic quantum fields. Interactions between these fermions are represented by spin-1 "gauge bosons": photons mediate the electromagnetic interaction, W/Z bosons mediate the weak interaction, and gluons mediate the strong interaction. Lastly, a scalar bosonic field, the Higgs, enables a mechanism by which fundamental particles are able to acquire mass. The model itself is written as a Lagrangian that describes these fields and their interactions; time evolution of a system can be derived by solving the Lagrange equations of motion for initial conditions as with a classical mechanics Lagrangian.

Because the universe is mostly empty, most* of the fields are well-described as harmonic oscillators which spend most of the time in their ground state when analyzing typical physical phenomena. "Particles" (either massive or massless) and their interactions appear as excitations of these fields on the mostly-empty background of vacuum. The universe remains near the ground state when such excitations are sparse, which allows us to use perturbation theory to calculate higher-order contributions to physical processes.

An easy method of visualizing (and, ultimately, calculating) the various orders of contributions to a SM interaction are *Feynman diagrams*. In a Feynman diagram, particles' motions through spacetime are just shown by lines, with each SM field (or at least type of field) represented by a different line. Time usually moves left to right,

*Fields related to the strong interaction are the exception to this, though low-energy effective field theories of these components act as the other fundamental fields.

though occasionally up to down. The particle trajectories can only change when two or more particles directly interact, which occurs at a *vertex*. These vertices are not arbitrary, and can only exist between particles when a term linking two or more fields exists in the SM Lagrangian. Processes that are "actions at a distance" in nonrelativistic quantum mechanics are distilled into sets of point-like interactions. The particles that appear internally in a diagram are called "virtual particles." Virtual particles' kinematics are allowed to violate the mass-energy relation of their real counterparts. These particles hence do not really "exist," unless the collision occurs at high enough CM energy to produce the rest mass of the virtual particle from vacuum.

This diagrammatic formulation, in addition to making it easier to write down mathematically what is occurring as we will see, also makes it easier to see that processes are Lorentz invariant, as the following example demonstrates. Take the dominant contribution to the electromagnetic interaction between electrons: the electromagnetic field is shown as the exchange of a photon in Fig. 1.1. Changing the inertial reference frame makes the slopes of particles' trajectories change, but not the fundamental process, making it easier to interpret than having to compute the classical electromagnetic force in reference frames with different velocities. Working in the center of momentum (CM) frame for interaction processes ends up being the simplest approach most of the time.

A physical interaction does *not* correspond to a single Feynman diagram. Instead, the interaction is represented by the sum of *all diagrams* that exist between the interacting particles; each diagram represents a quantum mechanical amplitude for a route through which the process can go. The total "cross-section" for a collision between two particles is the absolute value squared of the sum of all possible amplitudes. These cross-sections are typically what is calculated in high-energy physics,

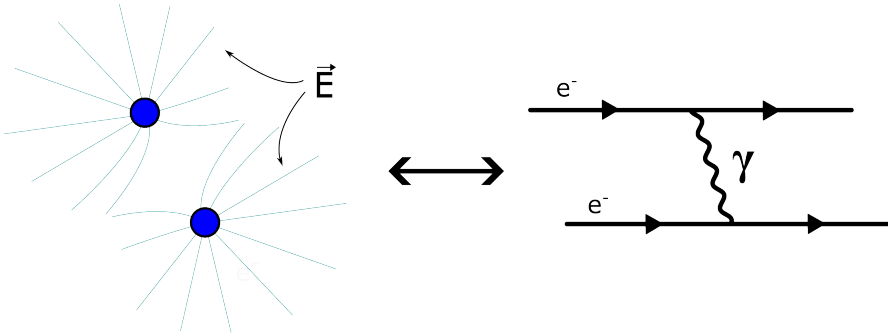

Figure 1.1: Comparison of a "traditional" electrostatic picture of electrons repelling each other to the tree-level Feynman diagram approximating the process. The slope of the photon representing the electric field indicates the finite time it takes for the interaction to travel between the two electrons, a property not easily seen on the left.

since high-energy experiments are often quite literally collisions of particles. Relevant AMO-type quantities can also be derived from these diagrams, though, as *all* SM interactions are essentially collisions between SM particles.

Luckily[†], not all diagrams contribute to the total cross section equally. Instead, they contribute relative to how many *loops* exist in the diagram, where a loop is a closed subsection of a Feynman diagram. These diagrams represent small additional effects to the overall process due to higher-order terms in a perturbation expansion. This expansion is visualized through these loop diagrams by interactions with other fields in the Lagrangian.

Diagrams with loops are suppressed by the coupling constants of the loop verticies compared to the loop-free "tree-level" diagrams. A factor of $\sim 1/m^2$ accompanies any virtual particle propagator, including those in loops, where m is the mass of the particle in the loop. For most SM processes, physical effects are dominated by the character of tree-level diagrams, with small perturbations added by 1-loop diagrams,

[†]Not "luckily" *per se*, but because the SM coupling constants are typically order 1 or smaller [1].

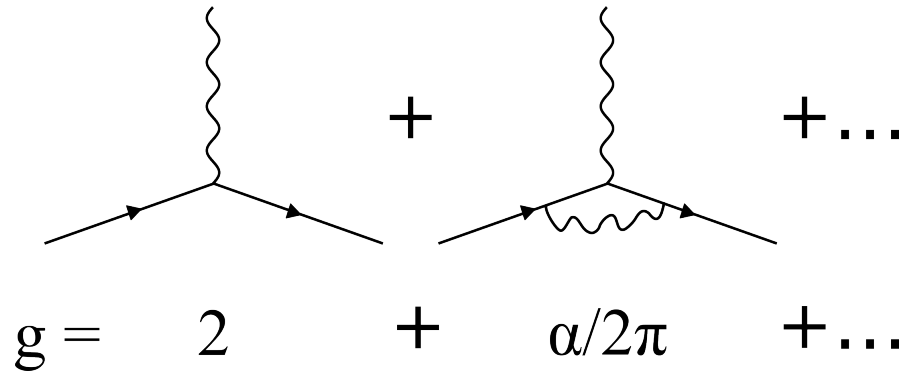

Figure 1.2: The two lowest order Feynman diagrams for the magnetic interaction of the electron and the corresponding values of the electronic g factor they produce.

still smaller added by 2-loop, etc. Note that treating these loops correctly requires a process called renormalization to get rid of divergences in the calculation, but this is beyond the scope of this review[1].

A simple example, and one that we will use below to understand *beyond* SM physics, of how Feynman diagrams easily illustrate perturbations to tree-level structure is the one-loop contribution to the magnetic interaction as illustrated in Fig. 1.2. This corresponds to the first nonzero contribution to $g-2$. The tree-level diagram of the interaction is just a vertex between an electron (or other charged particle) and a photon. Calculating the strength of the magnetic interaction, H_m, gives

$$H_m = g\vec{s}\cdot\vec{\mathcal{B}}, \tag{1.1}$$

where $\vec{s}$ in the spin of the particle, $\vec{\mathcal{B}}$ in the magnetic field vector, and the interaction strength is set by a g-factor of exactly 2. In other words, the tree-level diagram reproduces the Dirac equation result for the relativistic interaction between an electron and magnetic field.

However, we know experimentally that the g-factor is *not* exactly 2. There are no

other tree-level SM interactions between charged particles and photons (how could there be?), so one-loop diagrams are necessary to extend the precision of the predicted interaction strength. In quantum electrodynamics (QED) there is only one diagram with one loop, seen in Fig. 1.2. A virtual photon dresses the interaction, and adds a contribution to the overall process. Calculating the interaction strength from this diagram gives the famous $\alpha/2\pi$ addition to the g-factor, which brings the SM prediction to agreement with the measured value to 4 decimal places with a separate measurement of α [1]. Adding diagrams with more loops improves the agreement further; the current precision calculations calculate the contribution from all diagrams up to 5 loops[2], and agrees with the measured values to 10 decimal places [3]! Notably, loops at this level involve *all* SM phenomena, and thus measurements of the magnetic interaction of the electron serve as a probe of all SM physics. Of course, such a probe is not the most accurate way to test an arbitrary SM constituent, but agreement at this level between theory and experiment ensures that no large unexplained phenomena contribute to the interaction of electron and photon to the 5-loop level in the SM.

The point of this discussion is threefold: to outline what the SM *is*, to emphasize its accuracy, and to give a sense of how Feyman diagrams can model familiar low-energy physical quantities. Our goal is not to teach the reader how to do these numerical calculations (if you want, see Schwartz [1], Peskin and Schroeder [4]), but rather to provide an idea of how "particle physics" phenomena produce low-energy observable effects. Understanding how we move from a theory to these effects will make it easier to understand how *new* particles can affect the SM world.

1.1.2 Beyond the SM

As powerful as the SM is, it is at best incomplete. There are several large mysteries that it cannot explain microscopically. Despite these inefficiencies, it is also unclear how (i.e. at what energy or what length scale, with what interaction) the model breaks. Direct experimental evidence of a particle or interaction that produces an effect that *disagrees* with the SM is necessary to pinpoint how exactly a new, more encompassing theory fits around it. While some mysteries in the SM are not likely to be resolved in manners that produce low-energy observable effects, others can be generically explained by theories that produce signatures that are actually easier to measure in low-energy experiments than in current colliders. Two particular phenomena in the latter case motivate the experimental work in this thesis: (lack of) CP-violation in the SM and dark matter. We first explain what is meant by each of these, and why they describe universes incommensurate with the SM. Then, using the language of QFTs described above, we extrapolate how possible BSM models that explain these mysteries can produce specific low-energy effects we can hope to measure.

CP Violation

CP violation is the breaking of the combination symmetry of charge conjugation (C) (swaps particle $\leftrightarrow$ antiparticle) and parity (P). The relative absence of CP violation is conceptually at the center of a few specific mysteries in the SM.

The only CP violation in the SM occurs in the Cabibbo–Kobayashi–Maskawa (CKM) matrix, which describes the weak interactions of quarks [5, 6]. The amount of violation can be described by a complex phase which determines the relative strength of a CP-even and CP-odd part of the interaction. In the CKM matrix, the phase is

of order unity, indicating close-to-maximal CP violation [6]. Though it is perhaps odd that the symmetry is broken at all, there are actually two other possible terms in the SM which could, in principle also violate CP. The first is the Pontecorvo–Maki–Nakagawa–Sakata (PMNS) matrix, which is analogous to the CKM matrix but related to the weak interactions of neutrinos [6]. The CP violating phase is currently contested and may or may not indicate CP violation [6–8]. The second is the θ_{QCD} term in the QCD Lagrangian related to the strong interactions of quarks. This term naively appears when writing down the QCD Lagrangian [5, 6, 9]. However, the CP-violating phase in this term has been bounded to be smaller than 10^{-10} [10, 11], somewhat anomalous given the typically order-unity size of coupling coefficients in the rest of the SM. While this θ parameter is generically *allowed* to take any value, no other coupling constant in the SM is consistent with zero to measurement resolution, which raises questions of whether this term is "randomly" zero or zero because the model is an inaccurate representation of some other physics that can explain the smallness of the term. The odd size of this coefficient, especially in light of the nearly-maximal CKM matrix CP violation, is known as "the strong CP problem."

A reasonable question to ask is: so what? Perhaps there is just less CP-violation in the universe than is abstractly possible. (Un)fortunately, the small amount of CP violation that occurs is also a macroscopic issue. As is, the SM is fundamentally incompatible with many models of the formation of our universe [5]. In particular, the universe today is almost 100% matter, with essentially no anti-matter. Yet the laws of the SM are nearly symmetric between the two. Unless the initial ratio of matter to antimatter was fine-tuned to evolve into the distribution we see today, new laws of physics are necessary to be able to generate such asymmetry from a more generic distribution. In a seminal 1967 paper, Sakharov noted that laws violating C symme-

try alone (which do differentiate between matter and antimatter) are not sufficient to generate such violation, because formation of matter particles of one parity would be equalized by formation of antimatter particles of the opposite [12]. CP symmetry must *also* be sufficiently violated to generate an asymmetry between matter and antimatter formation [12]. Though there is some CP violation in the SM, it is insufficient to explain the degree of asymmetry we observe [13]. Thus the lack of CP violation in the model finds itself at the crux of both micro- and macro-scopic mysteries of the SM.

Various theoretical resolutions to one or both problems have been conceived within a field theory framework by introducing new quantum fields/particles that would not have previously been detected. A famous example turns the θ_{QCD} coupling coefficient from a number into a quantum field. The ultralight particles produced as excitations of this field are called *QCD axions* [14]. Such a field can have a non-perturbative non-zero expectation value in the early universe, which "turns on" the θ_{QCD} interaction and allows substantial CP-violation from the SM term. As the universe expands and cools, the field value can relax to near-zero at current day, masking any signature of the previously strong SM interaction. Plentiful other theoretical solutions involve adding massive CP violating particles, with small interactions to SM species that similarly allow the generation of baryon asymmetry during the early universe [5, 15]. The effects of such particles would also be nearly imperceptible today due to their large masses (recall the $1/m^2$ suppression), but would have been more active participants in physical processes at earlier times, when the temperature and density of the universe were substantially higher.

Dark Matter

A separate issue (at least nominally) with the SM is that it is unable to provide a microscopic description of the largest mass contribution to our universe, dark matter.

There is plentiful astrophysical evidence of dark matter [16]. Famously, the velocities of solar systems near the edge of galaxies are far too fast to be explained by regular kinematics if light-emitting matter (e.g stars) dominates the mass distribution [17]. Other analysis of collisions between two fast-moving galactic clusters, referred to as the Bullet Cluster, reveals a discrepancy between the cluster centers of mass (determined by gravitational lensing) and the center of the solar mass distribution. Lest these examples seem like they may be explained by contemporary misunderstandings of the universe, gravitational clustering of the ancient universe, as observed in cosmic microwave background fluctuations, are not explained by SM matter distributions alone, but seem to indicate large amounts of additional mass were present in the early universe as well.

Though some of these phenomena can be easily explained by modifying Newtonian gravity at large length scales, it is difficult to get any particular model to agree with all astrophysical observations [16]. A simpler solution is that there is *actually* a lot of mass in the universe. If such matter exists, it does not interact readily with light, giving rise to the term dark matter. For a while, it was conceivable that dark matter could be comprised of SM or SM-adjacent phenomena, like large amounts of neutrinos or primordial black holes [18]. SM neutrinos are now known to be incompatible with the observed kinetic energy of dark matter. Primordial black holes are now generally disfavored, though not entirely ruled out, by more stringent experimental bounds and better theoretical understanding of black hole formation.

Most current hypothetical solutions to the dark matter problem model it as a new particle in the quantum field theory paradigm. Such a particle would appear to mostly interact with the other SM particles through gravitation to match current observation. Akin to the above discussion of CP violation, though, there is theoretical motivation for other interactions to exist between SM and DM particles. In particular, the formation of dark matter from an earlier radiation-dominated universe likely necessitates some interaction with SM particles, though the identity of this interaction is capable of taking many forms [19].

While minimal BSM extensions just add new particles *ad hoc* that can explain the DM density, many others add particles capable of resolving multiple theoretical discrepancies of the SM at once. QCD axions are one such example, capable of resolving the strong-CP problem and possibly the matter/antimatter asymmetry. Dilatons are another example, which can signify the existence of other dimensions that are compactified to small scales, indicating evidence of certain string theories [16]. We will not look for effects of these particular models, though the fact that many dark matter candidates also can explain additional phenomena can make the motivation stronger.

1.2 Low-energy effects

To search for direct evidence of CP violation or dark matter, it is necessary to understand what effects possible solutions would create. Though alternatives have been considered, models of larger theories are typically still embedded in a quantum field theory framework. This embedding makes it possible to use the same Feynman diagrams as with SM processes to model how new particles change or add to interactions between SM particles.

1.2.1 EDMs

Many CP violating new particles are typically modelled as massive bosons. Such particles were historically favored because they naturally appeared in supersymmetric (SUSY) models which would contain bosonic counterparts to all SM fermionic particles (and vice versa). Though the simplest SUSY models have since been ruled out by experimental work (including of the type we will study), CP violating bosons generically exist in many other BSM models that are poorly bounded by measurement [15]. The existence of heavy unknown particles is separately well-motivated around current LHC mass sensitivity limits because electroweak symmetry breaking occurs around this scale [1]. Such a heavy new particle need not be CP violating, which continues to motivate high-energy experimental work. However, if a new particle is both of large mass and has CP-violating interactions with SM particles, CP-violating perturbative effects can arise in low-energy systems. This turns out to be true even if the CP-violating massive particle is much more massive than any conceivable collider could produce, and thus offers a unique probe of fundamental physics complementary to traditional high-energy experimental methods.

To understand the origin of these effects and why low-energy experiments provide such an advantage, it is useful to compare Feynman diagrams that include a hypothetical new particle, χ, that couples to the electron. As noted earlier, Fig. 1.3 shows the first-order correction to the electron g-factor. If the new particle that replaces the virtual photon in the diagram has some complex vertex interaction, the interaction that led to a modification of the magnetic dipole moment of the electron now also dresses the *electric* dipole moment (EDM), as seen in the same figure. The size of this dipole moment is found to be related to $\sin(\theta_{CP})/m_\chi^2$, where $\sin(\theta_{CP})$ is the imag-

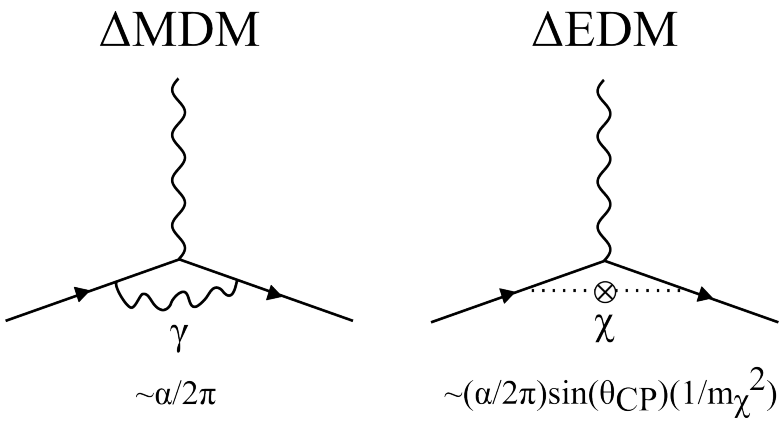

Figure 1.3: Comparison of 1-loop diagram contributions to the magnetic dipole moment (MDM) and electric dipole moment (EDM). The MDM diagram is explained in the text and in Fig. 1.2. The EDM diagram looks similar, but is modelled as arising from a massive particle χ in the loop which has an complex phase (designated by the cross on the line). These factors end up multiplying the result of the loop contribution from the MDM by $\sin(\theta_{CP})/m_\chi^2$.

inary (CP-violating) part of the coupling to the electron and m_χ is the mass of the new particle, via analogous computation to determining the $g-2$ modification [15]. Notably, the EDM size depends predominantly on these two parameters and SM values; it is not a many-dimensional parameter space. If the new particle does not directly couple to the electron, two-loop (or higher) diagrams will eventually produce some coupling, and correspondingly an EDM. These EDMs will be, of course, further suppressed by the masses of the particles in the intermediate loops, but these are typically smaller than the new particle mass. The power of these EDMs is that there is essentially *no* measurable SM background around current sensitivity [20]: due to the small amount of CP-violation in the SM, the largest a SM electron EDM can be is calculated to be 5 orders of magnitude below current experimental sensitivity [21]. Since there are no SM Feynman diagrams that contribute to this interaction to a very high degree of perturbation theory (4 loops), even very massive new particles can produce a larger-than-SM electron EDM.

We understand the more general effects of these CP violating particles by noting that CP violation is equivalent to T violation, or time-reversal symmetry violation. The CPT theorem that dictates the joint symmetry of C, P, and T must be conserved if Lorentz symmetry is locally conserved in any Hermitian QFT [5, 22]. It is easy to see that a permanent electric dipole moment violates T symmetry. To do so we first note that the EDM of a spin-1/2 particle must be aligned or anti-aligned to the spin, as other orientations would change the fundamental representation of the particle (i.e. would no longer transform like a spin-1/2 particle under symmetry operations). When such a system is placed in an electric field, it feels a Stark shift $E = -\vec{d} \cdot \vec{E}$ analogously to the Zeeman shift in a magnetic field. Unlike the Zeeman shift, however, the Stark shift for a permanent EDM reverses sign under T-reversal since $\vec{d} \propto \vec{s} \xrightarrow{T} -\vec{d}$ while $\vec{E} \xrightarrow{T} \vec{E}$. The generalization comes by noting that the EDM is not the only such T-odd electromagnetic moment; higher order P-odd electromagnetic moments are similarly T-odd, such as the magnetic quadrupole moments, electric octupole moments, etc., which can only occur in nuclei since electrons do not have large enough spin to support such moments. In fact, each of these can be linked to BSM theories via variations of the Feynman diagram in Fig. 1.3. Which particle(s) in the SM the new physics couples to most strongly will determine which of these symmetry-violating moments is largest, and thus searches for any of them in both leptons and nuclei are complementary when nothing is known experimentally about the nature of BSM physics. Though there are other potentially observable effects of BSM CP-violation, T-violating electromagnetic moments (generally referred to together as EDMs) are a generic consequence of any such interaction [5]. As such, despite our derivation of the effect from a SUSY-style symmetry violating particle, measuring any such EDM is sensitive to a broad range of CP-violating effects that may appear in a BSM the-

ory. All of these moments can arise from models with few new parameters and with extremely small SM background. Thus, all of these moments are attractive targets for measurement schemes with high sensitivity.

The existence of the EDM alone does not particularly motivate low- or high- energy experiments one way or another. However, we will show that low-energy systems (molecules, in particular) can enhance a measureable effect of an EDM in a way that is *not* replicated in collider experiments. Combined with high-precision measurement techniques, this enhancement increases the sensitivity of low-energy experiment significantly beyond what is achievable in colliders in certain regions of parameter space. Our work tries to measure the electron EDM, so we describe the enhancement factor for that explicitly. Other enhancements exist for nuclear moments in AMO systems as well [23–28].

The enhancement comes from the way in which the EDM is measured in a molecule. The naive approach to measuring an EDM would be to put an electron in a large electric field and measure the resulting Stark shift. However, such an experiment does not produce very stringent bounds: large fields necessary to generate a measurable Stark shift accelerate charged particles away quickly, correlating measurement time inversely to energy shift. A solution, as first pointed out in Ref. [28], is to instead use a bound system like an atom. That an energy shift due to EDM direction exists in such a bound system is not obvious: the bound nature of the system seems to imply that

$$\langle \vec{d} \cdot \vec{E} \rangle = \vec{d} \cdot \langle \vec{E} \rangle = 0, \tag{1.2}$$

a conclusion known as Schiff's theorem. However, this theorem can be evaded in relativistic systems, which prevents the factorization of the Stark matrix element into a

fixed dipole moment and average electric field. Roughly, length contraction changes the relative energy shift of an EDM when it is close to the nucleus versus far away, such that the total energy shift need not be zero [29]. In an atom, spherical symmetry still leads such an effect to be identically zero. However, polarization of the electronic wavefunction can create a measurable non-zero shift in the polarization frame. This effect is largest when the polarization is between s- and p- type orbitals, since higher angular momentum orbitals do not allow the electron to approach the nucleus. The resulting Stark shift is parameterized by the "effective field" defined as

$$\langle\psi|\vec{d}\cdot\vec{E}|\psi\rangle = \kappa\vec{d}\cdot\vec{E}_{eff}, \tag{1.3}$$

for some numerical constant κ of order unity, where the formula implicitly describes the effective field in the maximally-mixed case where $|\psi\rangle$ is evenly composed of s and p character [30]. Some qualitative arguments, backed up by actual calculations, show that the relativistic effects that contribute to $\vec{E}_{eff}$ scale as $1/Z^3$, where Z is the number of protons in the nucleus [22, 31]. For bound systems with heavy nuclei, the Stark shift from an EDM can be equivalent to the electron being in a $\sim 1-100$ GV/cm electric field [32–34]. This is the enhancement factor that fundamentally comes from the fact the electron is in a bound system. Lab fields cannot be realized at this strength, and hence measurement of molecular EDM Stark shifts intrinsically are capable of resolving smaller EDMs than tests of bare electrons in any measurement scheme.

Full lab-frame readout of such a Stark shift is difficult in an atom, since the large energy gap between atomic orbitals makes it difficult to highly mix s- and p- type orbitals. However, polar molecules naturally mix these orbitals to form molecular eigenstates due to chemical bonding and concomitant orbital hybridization. Field-

free molecular eigenstates are parity eigenstates; they typically have superpositions of the spin in both directions making an EDM Stark shift unresolvable in the bare states. Additional polarization of the *molecule* in the lab frame is necessary to align the molecular axis, along which the EDM shift occurs, to a lab-frame axis. This is a simpler issue to solve than atomic polarization, as molecules generically have more closely spaced states of opposite parity than atoms. For example, atomic parity only changes with electronic state, which are typically spaced by $\sim$ 500 THz. Molecular parity at least changes with rotation ($\delta E \sim 10$ GHz), and some molecules have even more closely spaced doublets due to internal angular momentum like $\Lambda-$doublets, $\ell-$doublets, or $K-$doublets ($\Delta E \sim 0.01 - 100$ MHz). This combination of considerations means that an ideal EDM measurement will use a high-mass, highly-polar molecule that is easy to polarize in the lab frame. To resolve the smallest Stark shifts possible, such experiments use Ramsey-type spectroscopy to measure the phase accumulation due to an EDM in an aligned molecule. These techniques are capable of measuring extremely small ($\ll 1$ mHz) frequency shifts, which further increases the sensitivity of an experiment. The specific details of how these schemes work is beyond the scope of this work (but can be found in Refs. [21, 35–39]); the relevant point is that molecular systems offer both intrinsic and technical advantages that enable much higher precision measurements of EDMs than any other known technique.

Some molecular states offer additional structure that is useful in rejecting systematic errors in a real experiment, so called "parity-doublets". While polarization between any states of opposite parity offers some projection of the molecular axis (and hence effective field) on the field axis, states of opposite parity that arise from the same magnitude of angular momentum in different directions offer something more. In such a case, not only will the polarized states be highly aligned with the molecular

axis, but states of both orientations along the field axis will exist [40]. Switching the relative direction of the field and $\vec{E}_{eff}$ direction can then be done *spectroscopically*, which provides an additional tool to detect non-reversing fields capable of producing a false EDM shift. There is also a third manifold of states with no lab-frame dipole moment, which could also be useful for shelving or systematic detection. The origin of these parity-doublets can be from any angular momentum around the molecular axis, and include Ω/Λ-doublets in linear molecules from electronic orbital angular momentum, $\ell-$doublets in linear polyatomic molecules from vibrational angular momentum, and K/K_a-doublets in nonlinear molecules from rotational angular momentum around a molecular axis. While not all molecules used in EDM searches have this structure, our work will focus on identifying candidates for next-generation experiments, and having such structure is beneficial if it is attainable with all other desired properties.

1.2.2 Oscillations of Fundamental Constants

The possible low-energy effects of dark matter are less well defined, in part due to the large parameter space of possible BSM theories consistent with astrophysical observation. Weakly-interacting massive particles (WIMPs) were, for a while, the favored candidate due to their compatibility with SUSY. Experiments in the last several decades have now ruled out much of the favored mass range for the most popular theories. On the other end of the mass range, there is renewed theoretical interest in dark matter models with 1 eV $> m > 10^{-22}$ eV, called "ultralight dark matter." Some such models are also capable of resolving other SM problems (e.g. the QCD axion). In this particle mass range, the field would have extremely high occupation number to be consistent with the astrophysical measurements of the DM mass density [5, 16, 19].

The DM field would then act like a superfluid or BEC; as a coherent field with synchronized oscillations. The amplitude of the field changes in time with period of the Compton frequency, $\tau \propto 1/m$. To search for candidates of these models, low-energy experiments search for corresponding oscillations of SM properties, as properties related to couplings between the DM field and a SM particle will oscillate with the field. Like is the case with EDMs, the signature of a fundamental oscillation is not reproduced by any SM process.

Which properties exactly oscillate with the DM field require some model to understand how it couples to SM particles. The many possible types of ultralight DM are accompanied by many possible types of SM couplings. The relevant ones for our work are the "Higgs portal" and dilaton couplings, in which a scalar DM particle has an interaction with the Higgs field or dresses the strength of another SM interaction [16]. Since the Higgs field gives fundamental particles mass, the existence of a Higgs coupling would cause an oscillation of the masses of fundamental particles at the DM Compton frequency. The dilaton coupling would cause oscillations of various fundamental constants, including possibly the mass of fundamental particles. Since much of the mass of nuclei is not fundamental, but predominantly arises from strong interactions (mediated by gluons), either coupling would likely affect nuclear and electronic masses differently. Thus, measuring the proton-to-electron mass ratio μ conveniently is sensitive to oscillations of either coupling[‡]. It would require an extreme coincidence for a DM particle to couple to both sources in the correct way to prevent a net oscillation of the ratio. Thus if a DM particle exists and has either dilatonic or Higgs-

[‡]We are really sensitive to the nucleus-to-electron mass ratio, but conventionally μ is the constant used in similar discussions. Nevertheless, the effects we study are sensitive to oscillations of either the neutron or proton mass with respect to the electron, and they need not be the same.

portal couplings to the SM, then the proton-to-electron mass ratio $\mu = m_p/m_e$ will oscillate [5]. Each of these interactions is motivated by large classes of BSM physics, and thus not unreasonable to search for.

Energies of different molecular states depend differently on μ, and so oscillation of the ratio will also cause oscillation of transition frequency between differently sensitive states [41, 42]. Electronic energy levels all have essentially no net dependence on μ since the energies are approximately determined by $E_{el} =\sim e^2/a^2$, where e is the electron charge and a is approximately the Bohr radius $a_0 = \hbar^2/m_e e^2$. The more accurate length scale is the reduced Bohr radius, which does depend on μ but only at the 0.01% level, so it is safe to use the heuristic that there is no substantial electronic dependence on μ. Thus transitions which only change electronic state are insensitive to variation. In contrast, harmonic molecular vibrational energies depend on $\mu^{-1/2}$, and rotational energies depend on μ^{-1}[41, 42]. The vibrational dependence seen in the first case by approximating a bond as nuclear masses M($\propto m_p$) on a spring with $k \sim E_{el}/R^2$, where R is the molecular bond length. This length scale is also typically a Bohr radius, so the vibrational energy goes as

$$E_{vib} = \hbar\omega = \hbar\sqrt{\frac{k}{M}} \sim \sqrt{\frac{\hbar^2 E_{el}}{M a_0^2}} = \sqrt{\frac{\hbar^2 E_{el} m_e^2 e^4}{M\hbar^4}} \sim E_{el}\sqrt{\frac{m_e}{M}}. \tag{1.4}$$

The rotational dependence can be understood by modelling the molecule as a rigid rotor with moment of inertia $I \approx MR^2$ and quantized angular momentum. In such a case

$$E_{rot} \sim \frac{\hbar^2}{I} = \frac{\hbar^2}{MR^2} \sim \frac{\hbar^2 m_e^2 e^4}{M\hbar^4} = \frac{m_e}{M}\frac{m_e e^4}{\hbar^2} \sim E_{el}\frac{m_e}{M}. \tag{1.5}$$

In both instances, we recover the claimed vibrational and rotational dependence on μ by using the result above that the electronic energy scale is mostly insensitive to μ

variation.

Anharmonic terms can change the dependence of an energy level further, which can lead to a enhancement in the relative sensitivity of a transition between two levels. Arguments like the above for the scaling of other parameters are more difficult, but discussions of their dependence can can be found in literature [43–45]. The power of the anharmonic terms does not come from their intrinsic sensitivity, but rather from the relationship between harmonic and anharmonic energies. In particular, it has been shown that if the anharmonic contribution to the energy difference between two states is similar in magnitude to but opposite in sign of the harmonic contribution, the fractional sensitivity of the transition frequency to μ variation is generically very large [46]. The search for UDM is then reduced to a frequency measurement between two closely-spaced levels (e.g. $\sim$GHz separation) with different intrinsic sensitivities and anharmonic contributions. This is convenient, since Ramsey-style spectroscopy is a well-established technique that is capable of high-resolution frequency measurements as noted above.

Using this principle, laboratory-based measurements of highly-sensitive transition frequencies in cold molecules can offer advantages over other techniques in a substantial part of the possible UDM parameter space. The first advantage is related to the absolute sensitivity of such an experiment. If a suitable transition can be found between two long-lived molecular states, the absolute sensitivity can be very high; limited in principle by the uncertainty in a frequency source. Microwave sources can routinely offer 10^{-16} absolute sensitivity at GHz frequencies, leading to a substantially improved absolute energy measurement compared to astrophysical measurements of molecular transitions, which have absolute energy resolution limited by $\gtrsim$ 2 K Doppler broadening and/or other large systematic errors caused by relying on distant

space objects. In addition, the ability to do these measurements over several orders of magnitude in time offers sensitivity to oscillation frequencies that are not probed at all by astrophysical measurements. In particular, the bounds from astrophysical spectra come from the fact the molecular sources are very old, and so these results limit a drift or extremely slow oscillation over universal timescales. However, lab-based experiments can be sensitive to oscillations from approximately the experimental rep rate (estimated $\sim$ 1 Hz) to the longest timescale of measurement, which can easily be weeks-to-months, and conceivably over a year. The current laboratory bounds over this frequency range are set by comparison of atomic clocks for similar reasons. However, the molecular transitions are intrinsically significantly more sensitive to μ variation than atomic species due the aforementioned structural enhancements, allowing them to probe smaller coupling strengths [46]. For instance, rovibronic transitions in molecules can have $\sim 10^3$ enhancement factors, compared to ~ 1 for atomic hyperfine transitions. In this case, if an oscillation of μ took place at 10^{-17} level, a well-chosen molecular transition would only require 10^{-14} fractional frequency sensitivity compared to the atomic system which would require 10^{-17}. Additionally, the smaller absolute transition scale (GHz) in molecules makes it easier to achieve a lower ultimate absolute frequency sensitivity than atomic sources in the 1-100 THz range. The lower transition frequency also mitigates some systematics that depend on frequency, like Doppler broadening. Thus both intrinsic and technological benefits may allow lab-based molecular searches with closely-spaced states of different sensitivity to cover parts of parameter space along both the oscillation timescale and coupling strength axes that are more difficult to probe with other measurement techniques.

1.3 Motional Control for Precision Measurement

Competitive measurement of either EDMs or UDM requires relatively few specific molecular parameters. As noted above, a molecule for an EDM will in general be heavy, polar, and with low-lying parity-doublets. A UDM candidate molecule will have closely spaced states of different fundamental sensitivity to μ variation. Though these are not trivial considerations, there are many such systems that meet these requirements.

To distinguish between systems, we can aim for additional structure benefits. In particular, though any molecule with the requisite structure will abstractly be a suitable choice for an experiment, the degree to which a generic system can be controlled is low. The greater our ability to exert control over a molecule's internal and external state, the simpler it will be to use it as a probe.

Control over internal state is more or less always a qualitative issue: simpler species have fewer internal states. There is thus a preference for the simplest molecules capable of delivering us the additional qualities we desire. There is no point in excess degrees of freedom if a molecule provides no benefits over a simpler species.

Control of an external state in this instance refers specifically to the ability to manipulate position and/or velocity. Being able to change these variables deterministically is invaluable in managing systematic and statistical uncertainty. In the extreme case, we would specifically like molecules that are fully coolable and trappable in conservative (i.e. nonradiative) traps. The low temperatures and trap volumes that have been exhibited in atomic and molecular optical dipole traps [47–49], for instance, would enable an EDM or UDM experiment to utilize long ($\gg 1$ s) Ramsey phase accumulation times and only require control of external systematics like stray fields over

$\lesssim 1$ mm^3 [50]. Even if these techniques are too complex for a given molecular species, deceleration or transverse cooling can still help increase interrogation time and flux in an experiment.

No EDM- or UDM-sensitive molecule used in an ongoing experiment is both capable of delivering all of the desired "physics traits" described above and is compatible with traditional direct deceleration and trapping techniques. For EDM molecules, this is because the "parity-doublet" structure in diatomic species can only come from nonzero electronic angular momentum, which is at odds with structural heuristics for photon-cycling. Diatomic laser-coolable EDM molecules are currently being studied ([51]), but it will likely be more difficult to do a competitive measurement without parity-doublets. Studies of μ variation in molecules typically use polyatomic molecules with convenient-to-measure vibrational transitions due to the strong μ dependence. Such species are typically studied in the lab in fast and/or warm beams with correspondingly wide velocity distributions and/or short interaction times [52, 53]. Some ongoing experiments also use molecular ions, which can be colder, will generally suffer from lower statistics than neutral species [54, 55]. There is an assembled molecule experiment using KRb molecules searching for μ variation that is complementary to our work [56]; the direct cooling and assembly pathways face different difficulties but achieve the same benefits in this application.

To what degree techniques of motional control can be extended to *polyatomic* molecules that are known to exhibit all other structural features desired for a precision measurement experiment is an evolving question. It is also the foundational question studied in our work presented here. Though light polyatomic molecules have been fully laser cooled and trapped ([57, 58]), the degree to which these techniques will be affected by more massive and complex species that are of interest to next-generation

precision measurements is as of yet unknown. Previous work in Refs. [50, 59–67] began to answer this question through initial laser cooling work on the SrOH and YbOH molecules, candidates for precision measurements identified in [50, 68]. The results in these works showed that it was possible to least exert 1D forces on these species. While such results are deeply nontrivial (indeed, unthinkable only 15 years ago), their utility alone is limited, especially since it may still be possible for similar forces to be exerted on diatomic species of interest with only modestly more experimental complexity. These results were not clearly sufficient to enable full motional control of a heavier molecule useful for a precision measurement.

This work in thesis aims to build upon these prior results. We both test the degree to which motional control is possible now on relevant precision measurement species, as well as study more complex polyatomic molecules to asses their compatibility with such techniques in the future.

1.4 Overview

We begin our discussion in Chapter 2 with a brief overview of molecular structure. We review the basic energy structure of the molecules we work with and common perturbations that appear. We end this section by explaining how this structure can be used to construct an optical cycle in a polyatomic species, the building blocks for the experimental motional control techniques in the following chapters.

From there we move to the experimental section of the thesis, which begins with a demonstration of Zeeman-Sisyphus deceleration of YbOH in Chapter 3. This technique uses large Zeeman shifts to remove $\sim$ 10 K of longitudinal kinetic energy with only a few scattered photons. Though this technique requires some optical cycling, it

is to a sufficiently low degree that our results here indicate that this technique could be used to decelerate a wide class of polyatomic molecules, including likely many useful for precision measurements.

In Chapter 4, we present results of laser deceleration and magneto-optical trapping of SrOH. These techniques are mainstays of the atomic physics world, and have hitherto only been demonstrated on a single other polyatomic molecule, CaOH. Their application to SrOH is not without technical complications due to the molecular structure, but does indicate that at least some heavier species can be successfully cooled and trapped analogously to CaOH and several diatomic molecules. Though these techniques have stringent structural requirements, these demonstrations indicates that well-behaved molecules should be compatible with this technique regardless of mass.

Our final experimental chapter, Chapter 5, studies to what degree we expect either of the previous two techniques (or indeed, any technique reliant on optical cycling) to be compatible with *nonlinear* molecules. Such species are generically of interest for precision measurements due to their *vibronic ground state* parity-doublets with significantly longer lifetimes than any other known parity-doublets, but it was not known how compatible they are with laser cooling. In this chapter, we conduct measurements of the vibrational branching fractions and study the rotational closure schemes for three Sr-containing nonlinear molecules, and identify $SrNH_2$ as a candidate for future laser deceleration and deep laser cooling. This investigation serves as a bridge between the current edge of molecular control and the future; between what we can control at the moment to a truly ideal species for precision measurement.

We conclude with a review of these works and the story they tell together about the status of molecular control techniques for species of interest to studies of BSM physics in Chapter 6. Though the existing proposals in literature for using future

polyatomic molecules are limited, the work presented here offers confidence that some of these systems can be controlled to similar degree as simpler species. This work is thus not only important in and of itself for the results included here, but also strongly motivates searches for new applications of these types of molecules so as to be able to fully utilize the rich structure they offer.

And I won't tell you where it is, so why do I tell you
anything? Because you still listen, because in times like these
to have you listen at all, it's necessary
to talk about trees.

Adrienne Rich

2

Structure of Polyatomic Molecules

Despite containing only a few atoms, the small molecules we work with are considerably complex quantum mechanical systems. Understanding this complexity is key to being able to select, control, and manipulate molecules to achieve our scientific goals. This chapter distills the relevant points of molecular structure that one needs to understand the work in the remainder of this thesis.

Since the work described for the rest of the thesis involves both linear and nonlin-

ear polyatomics, both cases are discussed when relevant. Unfortunately, the language used to describe the structure of molecules in each case is usually different, though the physics is not necessarily. We thus begin our discussions with the case of linear molecules, and then work through the nonlinear cases, making analogies to other (simpler) molecules where helpful.

A final note: though diatomic molecules are the simplest molecules, no further work in this thesis concerns them. As such, we avoid theory describing them entirely, and direct the reader to the many previous Doyle group theses and other works in literature written on them [65, 69–74]. Reference will be made to ideas in these works, though hopefully presented with just enough context for the main points to be clear without a complete review of diatomic molecular structure.

2.1 Born-Oppenheimer Approximation

The molecular Hamiltonian is actually quite simple to write down: to lowest orders in an electrostatic expansion, a molecule is just a collection of charges and dipole moments. For molecules with $I = 1/2$ or smaller, these are the *only* terms. Larger spin nuclei have higher multipole moment contributions as well, though these terms are suppressed by powers of the nuclear radius.

In the low-moment ($I = 1/2$) approximation,

$$\hat{\mathrm{H}} = -\frac{\hbar}{2}\sum_{\star=\alpha,i}\frac{1}{m_\star}\nabla_\star^2 + \sum_{\alpha\neq\beta}\frac{1}{4\pi\epsilon_0}\frac{Z_\alpha Z_\beta e^2}{r_{\alpha\beta}^2} + \sum_{i\neq j}\frac{1}{4\pi\epsilon_0}\frac{e^2}{r_{ij}^2} + \sum_{\alpha,i} -\frac{1}{4\pi\epsilon_0}\frac{Z_\alpha e^2}{r_{\alpha i}^2} + \hat{\mathrm{H}}_{es} + \hat{\mathrm{H}}_{hf}, \quad (2.1)$$

where the Greek indices indicate sums over nuclei and the Latin indices over elec-

trons. Stars are used for when a term affects nuclei and electrons symmetrically. In the Hamiltonian, m is the mass of a particle, Z_α is the charge of a nucleus, and $\vec{r}_{\star *}$ is a vector connecting two particles.

The first term is the kinetic energy of each particle. This can be separated by the usual methods into the center of mass (CM) energy and the kinetic energy relative to the CM, which allows us to work in only internal coordinates.

The second and third terms are electrostatic interactions between two nuclei or two electrons, respectively. The fourth term is the electrostatic interaction between nuclei and electrons (hence the different sign). The last two terms consist of interactions of induced and intrinsic dipoles. The fifth term, $\hat{\mathrm{H}}_{es}$, is the "electronic spin" dipolar term, which consists of terms created both by electron-electron spin-spin interactions and the interactions of an electronic spin and moving electrons and nuclei. The electron dipole-dipole terms are the familiar

$$\hat{\mathrm{H}}_{hf} = \sum_{i,j} \frac{1}{4\pi\epsilon_0 r_{ij}^3} (3(\vec{\mu}_i \cdot \vec{r}_{ij})(\vec{\mu}_j \cdot \vec{r}_{ij}) - \vec{\mu}_i \cdot \vec{\mu}_j), \tag{2.2}$$

where $\vec{r}_{ij}$ is the vector between the two electrons. The Hamiltonian terms involving the moving charges are too algebraically complex to write down in a way useful to look at, but can be found in Bunker and Jensen [75] or Brown and Carrington [72]. Nevertheless, the *physics* of these terms is intuitive: a moving charge creates a magnetic field, which can interact with either the field from another moving charge or with a permanent magnetic dipole. The sixth term, the nuclear hyperfine term $\hat{\mathrm{H}}_{hf}$, includes the nuclear equivalents of the electronic terms in the previous term; the contributions are all smaller due to a smaller nuclear magnetic moment and slower nuclear motion.

The difficult aspect of understanding molecules, as is true of many areas of physics, is solving this Hamiltonian. Indeed, it is impossible to solve it exactly for any molecule, even the simplest case of the H_2^+ ion [76]. To get any useful model for other molecules, we must begin to approximate. To do so, we first break up the full molecular Hamiltonian in the CM frame into spin-independent (robvibronic) and spin-dependent terms[75]: $\hat{\mathrm{H}}_{full} = \hat{\mathrm{H}}_{rve} + \hat{\mathrm{H}}_{es,hf}$, where

$$\hat{\mathrm{H}}_{rve} = T_0 + V_{NN} + V_{ee} + V_{eN}. \tag{2.3}$$

The potential (V) terms in this equation are the same potential energy terms in Eq. 2.1, with the N and e indicies indicating the interacting particles. The use of "rovibronic" to label this term will become clear soon. The electron spin and nuclear hyperfine ($\hat{\mathrm{H}}_{es,hf}$) term is the sum of the corresponding terms in the original Hamiltonian.

For most molecules (and certainly for our molecules of interest), the foremost approximation is to solve $\hat{\mathrm{H}}_{rve}$ first and add the spin-dependent effects as perturbations. This is not usually a bad approximation. Even when spin-dependent terms are non-negligible (e.g. the spin-orbit interaction in the $\tilde{A}$ states in SrOH and YbOH), in the molecules we study they are always small enough to be easily added as perturbations to the rovibronic basis states. Similarly, hyperfine is *always* small in our species; it is trivial to add the hyperfine energies and interactions later.

Unfortunately, even the spin-independent $\hat{\mathrm{H}}_{rve}$ is impossible to solve exactly, but at least it now looks similar to problems we have approximated before (e.g. the atomic Hamiltonian; see [77]]). Much as we solve the atomic case by separation of variables, we can do similarly here with the *Born-Oppenheimer* (BO) approximation. The BO approximation refers to the separation of electronic, vibrational, and rotational vari-

ables. The separation of the electronic degrees of freedom is motivated by the relative velocities of particles in the molecule. The nuclear motion is, on average, much slower than the electronic motion, and so the electronic eigenfunctions as functions of the electronic coordinates r, $\Phi_e(R, r)$, can be approximated as solutions to a Schrodinger equation where the non-rotating, non-vibrating nuclei are a distance R from each other[75]:

$$\Big[T_e + V_{ee}(R, r) + V_{eN}(R, r)]\Phi_e(R, r) = E_e\Phi_e(R, r), \tag{2.4}$$

.

The nuclear degrees of freedom then evolve under the difference of the robvibronic Hamiltonian and the electronic Hamiltonian:

$$[T_N + V_{ee}(R) + V_{eN}(R) + V_{NN}(R) - E_e(R)]\Phi_{rv} = E_{rv}\Phi_{rv}(R), \tag{2.5}$$

shifted such that the minimum of the potential is the electronic state binding energy[75]. A further change of coordinates into the displacement from equilibrium nuclear positions in the non-rotating axes allows a factorization of Φ_{rv} into rotational and vibrational components of the motion $\Phi_{rv} = \Phi_v\Phi_r$ for low amplitude motions, hence the name. This can be interpreted as an effect of the different energy scales of the two motions: nuclear rotations should be much lower in energy than bonds stretching, since the rotational energy is set by $\hbar/2I \sim \hbar/(m_N r)$ but vibrational motion is set by a spring constant $\sqrt{k/m_N} \sim \sqrt{E_{el}/m_N r}$ where E_{el} is the electronic binding energy. This factorization of Φ_{rv} finally allows us to write the spatial wavefunction as a product of an electronic wavefunction, a vibrational nuclear wavefunction, and the rotational nuclear wavefunction: $\Phi_{tot} = \Phi_{rve} = \Phi_e\Phi_v\Phi_r$. Each component can then be solved separately. Wavefunctions are typically most easily calculated in each case us-

ing different bases and approximations. In the following sections we just assert these approximations, but details on the mathematical transformations from the original coordinates to the more convenient rigid rotor and harmonic oscillator coordinates can be found in Bunker and Jensen [75] and Brown and Carrington [72]. Breakdowns in the BO approximation involve terms that mix the nominally separated degrees of freedom due to cross-terms in the complete Hamiltonian which effectively couple different types of BO motion (e.g. rotation and vibration). Relevant instances of such breakdowns are discussed with other perturbations at the end of this section.

Note that there is nothing about the BO approximation that is specific to any size or symmetry class of molecular structure. This approximation is used both in our discussion of linear and nonlinear molecules; the labelling of the individual components of the wavefunction, however, will differ between them.

2.2 Electronic Structure

In the BO approximation there is, by definition, no interaction between the nuclear and electronic motions. The space spanned by the constituent atomic electronic bases at equilibrium positions of the atoms is, then, a good basis for the molecular electronic structure. For example, an electronic molecular basis for the hydrogen molecule is easily formed from linear combinations of two copies of the hydrogen atomic orbitals, spatially displaced from each other by a bond length. Such linear combinations of atomic orbitals (LCAO) save us from having to solve the Schrodinger equation from first principles.

In general, finding the correct LCAO for a molecular state is still fairly tricky if there are many atomic orbitals. Finding the nontrivial ground state in such a sit-

uation is in fact famously difficult for large molecules, and a topic which quantum simulation seeks to assist on [78, 79]. However, the molecules we work with are not like this. Our molecules tend to have an alkaline-earth or alkaline-earth-like metal (Ca, Sr, Yb, etc.) bonded with a halogenic ligand (a ligand that is one electron shy of a full shell). Why this structure simplifies the electronic wavefunction can be interpreted in two ways.

The common [65, 71] way to understand the structure of these molecules is to note that the ligand, being electronegative and therefore "wanting" one electron, pulls a single valence electron from the metal to fill the valence shell. The filled-shell ligand is then negatively charged, and the ionic metal is positively charged. The two constituents then attract each other forming an ionic bond. The valence electron on the metal is polarized away from the ligand due to like-charge repulsion. Due to this repulsion, the valence electron orbitals look like linear combinations of the metallic ion's orbitals, since there is no electron density over the ligand. For intuition about the electronic structure, we need not find how the atomic orbitals of the ligand and metal mix, because they simply do not mix much. Even electronic structure calculations indicate that in molecules of this type, the electron is highly localized around the metal atom [80–83].

Though this semiclassical electrostatic picture is basically correct, it is not easy to understand how this view arises from an orbital "hybridization" picture of electronic structure that is common in physical chemistry. As a result, it is less capable of giving intuition about what happens as the ligand changes from F in diatomic species to OH, NH_2, SH, etc. An alternative view of why the molecules form can be obtained from considerations of only the atomic orbital energies, which of course already contain the information about the charge, mass, electron number, etc. of the constituent

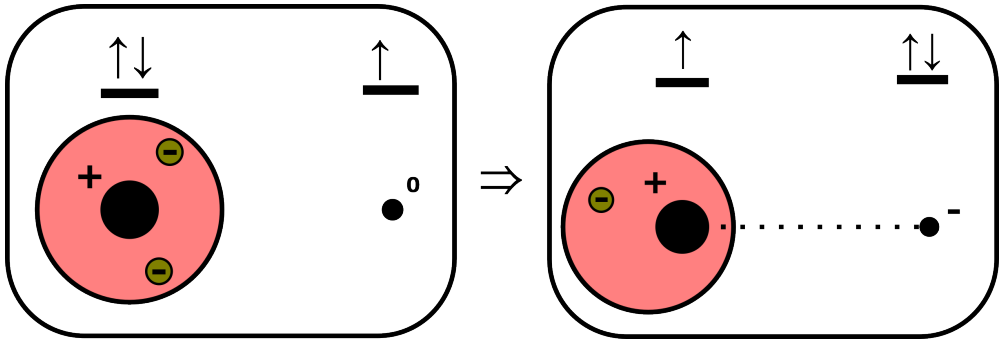

Figure 2.1: Schematic of how the ionic bonding picture explains the electronic structure. An open-shell electronegative ligand pulls a valence electron from an alkaline-earth(-like) atom, and becomes negatively charged but filled shell. The negatively charged ion then is strongly attracted to the positively-charged metallic nucleus, but repels the remaining valence electron away. This keeps electron density near the original metallic nucleus instead of spreading out over the ligand.

atoms. The critical point is the most intuitive: orbitals only mix if they are similar in energy. In our molecules, the different mass and n quantum numbers in the outer most orbitals of the ligand and metal leads to vastly different energies required to remove an electron from the metal than to remove one from the ligand. For example, in the case of SrOH, the strontium atomic orbitals are filled to the $6s$ shell, while the hydroxyl ligand has valence electrons in the $2p$ shell. The first ionization energy gives an approximate measure of the relative energies [84, 85]. In the case of SrOH, the ionization threshold of neutral Sr (i.e. gap between neutral Sr and Sr^+) is ~45,000 cm^{-1} for Sr, while the ionization energy of OH is ~100,000 cm^{-1} [86]. In this circumstance, it is much more energetically favorable to transfer the electron from the Sr atom to the OH ligand than any other configuration. This is another way of understanding why the electron fills the ligand outer shell instead of occupying some combination orbital without relying on the nebulous concept of "electronegativity". The energy gap between the then-filled ligand shell and its next open shell is typically quite large. A schematic showing the difference between the molecular orbital hybridization in the

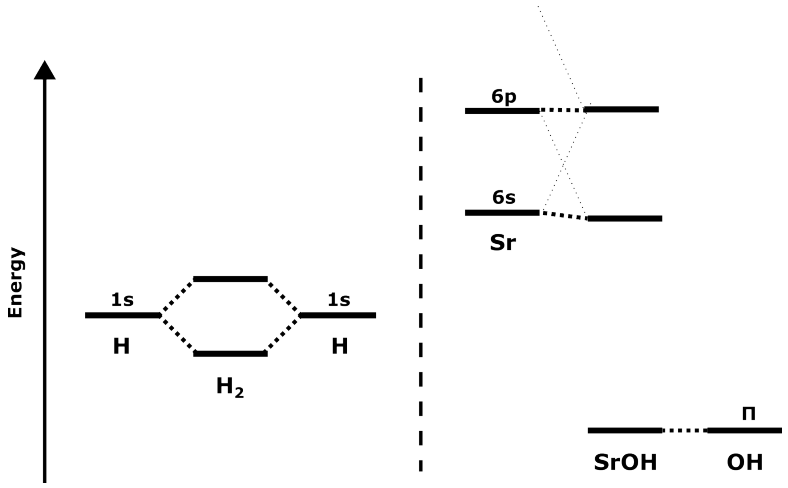

Figure 2.2: Qualitative comparison of the relative energies of the constituent orbitals for the H_2 and SrOH molecules. Because the atomic orbitals in the H_2 molecule are similar in energy, the molecular electronic levels are heavily mixed combinations of orbitals around each atom. In the SrOH case, however, the OH orbitals are much lower in energy than the Sr orbitals, and so the molecular orbitals are only slightly perturbed from the constituent bases.

H_2 molecule compared to the case of SrOH is shown in Fig. 2.2

We arrive at the same conclusion: that the valence electrons are expected to basically occupy linear combinations of the metallic atomic orbitals. Though this is the same result, it is easier in the orbital hybridization picture to understand how the ligand structure qualitatively affects the bond strength from first principles. As the ligand becomes either heavier or more complex, the electronic state density tends to increase, which increases the likelihood that states from the two basis sets will mix. When such a mixing occurs the bond becomes more covalent. This is especially useful intuition in cases of isoelectronic substitution (e.g. F→Cl), though admittedly at the expense of needing to understand the ligand electronic structure. Conversely, it is more difficult to understand why the two atoms stay together as a molecule in this picture than with the semiclassical electrostatic argument. Being able to move between the two pictures is useful to understanding the most prescient electronic charac-

teristics of our molecules.

All this is to say that the valence electrons essentially occupy states made of the metallic atomic orbital basis. Though this is what they "look like," it doesn't suffice to label the molecular states with atomic state labels since the symmetry of the molecule is different than of an atom. In particular, the label L doesn't quite make sense due to lack of molecular spherical symmetry. (Neither does n, although it is close to meaningful in our species. It still isn't used.) The convention for labelling linear molecule electronic states is more intuitive in light of the above discussion than the convention for nonlinear molecules, so we proceed in that order.

2.2.1 Linear

For linear molecules, the orbital symmetry is only broken along a single axis; the resulting system has cylindrical symmetry. This symmetry mirrors the case of an atom in an applied field. In the same manner, we can label the electronic energy levels by the projection of L onto the internuclear (quantization) axis. This label is well-defined and useful in our species. Using this heuristic, the molecular state label replaces the atomic orbital angular momentum (S,P,D,...) with the unsigned projection, Λ, of the orbital angular momentum onto the axis (designated $\Sigma, \Pi, \Delta, ...$). Similarly, the total spin s is still a useful quantum number in most cases. The magnitude of the projection of spin on the molecular axis Σ (yes, another Σ) is also frequently referenced; the relative orientation of these two quantities is sometimes also included as the quantity $\Omega = |\pm\Sigma \pm \Lambda|$ in a state label where the sum denotes the adding of the *signed* projections (note that the projections can each be negative), labelling an analogous quantity to J in atomic labels. Note that any of these angular momenta being > 0 implies a degeneracy; the doubling of a $\Lambda > 0$ state is termed "Λ-doubling", and the equiv-

alent for Ω is Ω-doubling (though this is often reserved for instances in which Λ is not a good quantum number but Ω is). These degeneracies are eventually broken by perturbations that are discussed later. The presence of a molecule-frame structurally-enforced (i.e. a result of a molecular symmetry, not random) degeneracy gives rise to lab-frame states of each parity.

In addition to the Λ and Σ labels, a new label appears with no atomic analog, but only in Σ electronic states. A $\pm$ superscript is used in this situation to denote the sign of the wavefunction under reflection in a plane containing the internuclear axis. This property does not exist separately from parity in atoms due to spherical symmetry. It is also not necessary in higher angular momentum states since both signed states exist in the degenerate manifold. Since Σ states are non-degenerate, this property must be uniquely defined, and can affect the allowed axes of transition dipole moments to other states [75]. It is not commensurate with overall parity of a state, since rotational and vibrational degrees of freedom will also affect the parity properties of an individual molecular level.

Overall, the electronic states of linear molecules have term symbols ${}^{2s+1}\Lambda_{\Omega}^{(\pm)}$, where Ω and the $\pm$ are only used when meaningful or useful. Since there is no equivalent to the atomic n label used, there is no intrinsic way of telling the relative energies of two states of identical angular momentum using this scheme alone. Additional letter labels ($\tilde{X}$, $\tilde{A}$, $\tilde{B}$, $\tilde{C}$...) are used to (typically*) denote the relative ordering of the states, with $\tilde{X}$ as the electronic ground state, $\tilde{A}$ as the first electronic state of the same spin, $\tilde{B}$ the next highest state with the same spin, etc. Lowercase labels $\tilde{a}, \tilde{b}, \tilde{c}$,... are used for excited states of different spin than the ground state. The tildes in either case just

*In older spectroscopy, these labels are related to the order in which the states were discovered. Modern spectroscopy uses these labels in order of ascending energy, when possible.

indicate the species is not a diatomic molecule.

2.2.2 Nonlinear

Just as the atomic state labels are not an accurate way to describe electronic states in linear molecules, linear molecule labels are not accurate in describing electronic states of nonlinear molecules. The linear molecules' labels were developed by understanding how the symmetry was broken from the atomic to linear case. Nonlinear molecules have still further broken symmetry, to the extent that typically no property related to L can be a strictly good quantum number for the electronic orbitals. Angular momentum conservation requires a continuous symmetry, and nonlinear molecules have none. How we describe the "shape" of the orbital must therefore be decoupled from a strict association with angular momentum, despite the correspondence in the linear and spherical cases.

As this discussion precipitates, the electronic states of nonlinear molecules are labelled by their symmetry properties. In particular, they are labelled by irreducible representations of the molecular symmetry group. For reasons that are opaque to me, and indeed to Bunker and Jensen [75], the molecular symmetry group is isomorphic to the point group of the nuclei in their equilibrium positions (i.e. not rotating or vibrating). The electronic states therefore transform as a irreducible representation of the *molecular point group*. The molecular point group is the set of discrete rotations, rotations, or inversions, which leave the systems properties identical to the original orientation (as with parity, the *sign* of a wavefunction can change, just not the probability density). An *irreducible representation* of these groups is a matrix representation of the group that cannot be decomposed into direct products of smaller-dimensional representations. Figure 2.3 illustrates an example of how two "orbitals" transform as

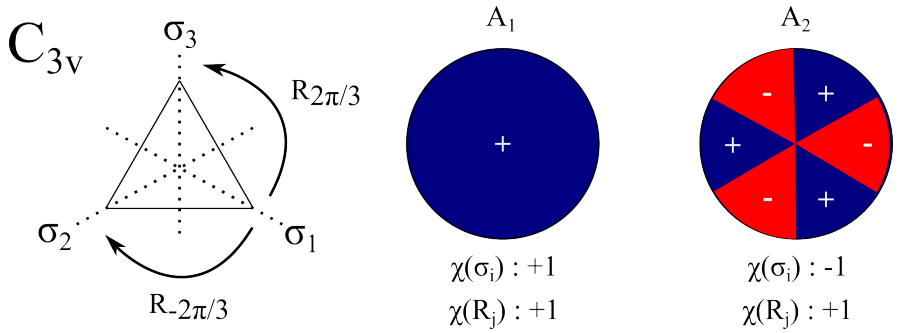

Figure 2.3: Illustration of the elements of the C_{3v} point group (left) with the top view two "orbitals" that transform as different irreducible representations (A_1 and A_2. The characters of group operations are shown beneath each orbital. The difference in the character under reflection can be used, with a character table in Bunker and Jensen [75], to label the states correctly. Note that real orbitals must have some more specific 3D structure to be in this point group, as the orbital view as drawn is consistent with an additional reflection plane symmetry.

different irreducible representations. Ref. [87] is a useful resource for more information on basic representation theory. Luckily, the representations of common point groups are already enumerated in many places. The correspondence of an electronic orbital to a particular representation is done mathematically using the "characters" of symmetry group operations acting on the state. The mathematical character of a state in a given representation is strictly defined as the trace of the matrix which completes the operation, but it can be thought of almost like an eigenvalue. For example, if an orbital switches sign under a reflection, then the character of the matrix representation it transforms like will be negative under the reflection operation. These characters are tabulated with the representations of common points groups in Bunker and Jensen [75] and other places. The character of the two orbitals in Fig. 2.3 are also shown under group operations, to illuminate how they could be used to differentiate the states even without the visual aid.

It is difficult to *apropos of nothing* assign a symmetry label to a nonlinear molecule electronic state, but there are some patterns in the molecules we use. If the symmetry

group of the molecule is capable of having degenerate states, the electronic levels that correspond to Π states in the linear limit will be E levels; doubly degenerate. If not, the degeneracy will break the state into two electronic states with one dimensional representations. Similarly, the ground states of molecules of interest to us are totally symmetric A states ($A_1, A', ...$ depending on point group). Usually the symmetry of electronic states of molecules we are interested in are already assigned by past spectroscopic work, but understanding what these labels mean makes it easier to draw comparisons with the more symmetric species. The symmetry groups of molecules and representations of key electronic states in the molecules can be found in Fig. 2.4 in a graphic demonstrating how the states correspond to SrOH levels.

These symmetry labels take the place of the Λ label in the term symbol[†]. The term symbol of a generic electronic state in a nonlinear molecule is explicitly given by ${}^{2s+1}R$ where R is the representation and s is the spin. Note that the $\pm$ label in linear Σ states is not necessary for nondegenerate representations in nonlinear species, as the representation label already differentiates states with different symmetries under molecular point group operations (of which reflection was one in linear species).

As with linear species, the states are also labelled by the $\tilde{X}$,$\tilde{A}$,$\tilde{B}$... to describe the ordering of the states. In our molecules, these will tend to correspond to the analogous label in the linear molecule. The exception is when the molecule is low-enough symmetry that there is no degenerate representation, which causes the levels that in linear species are a $\tilde{A}\ {}^2\Pi$ state to split into two electronic states $\tilde{A}\ {}^2A'$ and $\tilde{B}\ {}^2A''$ in the C_s group. No species in this thesis will ever have a more than two-fold degener-

[†]Indeed, though it is not self-evident in the least, both the atomic and linear state labels are effectively also *symmetry labels*; the L or Λ quantum numbers are labels of irreducible representations of the spherical and cylindrical symmetry groups, respectively. As such, the term symbol *always* describes the symmetry property, we just associate it foremost with angular momentum in the high-symmetry cases.

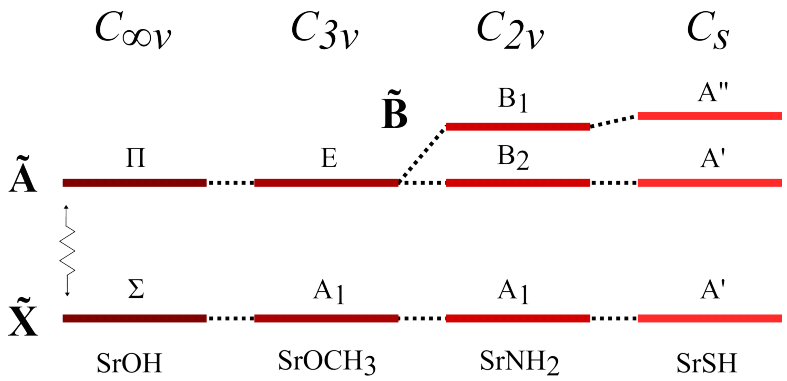

Figure 2.4: Schematic of the lowest electronic states from molecular point groups that appear in this thesis. A symmetry group label is noted at the top, with a representative example of the group at the bottom, though the labels will be generically accurate for similar species. The representation that each level transforms as are labelled by each state. The dotted lines show roughly how the states from SrOH correspond to different levels as the symmetry is lowered.

acy[‡]. This relative consistency makes it easier to understand the relationship between the linear and nonlinear analogues we work with.

2.3 Vibrational Structure

In the BO approximation, the molecular vibrations appear as substructure in an electronic manifold. The motions are approximated as harmonic excitations of the normal modes around the equilibrium structure (the harmonic approximation). The modes are the same as the classical normal modes of masses on springs. There are $3N-6$ vibrational modes in a generic molecule ($3N-5$ in linear molecules), though often several of these are degenerate thus reducing the number of differentiable modes. This degeneracy leads to a vibrational angular momentum around the internuclear axis, with corresponding parity doubling from the two projections of the angular momentum, $\pm\ell$, onto the internuclear axis. $\ell \leq n_2$, where n_2 is the quanta of excitation

[‡]High-symmetry molecules (e.g. CH_4 or C_{60}) can have higher electronic degeneracies that have no analogs in linear molecules.

in the bending mode (as described later) necessarily, since ℓ is the projection of n_2. The quanta of ℓ add like any other angular momenta, so for $n_2 > 1$ there are several submanifolds which differ by $\Delta\ell = 2$.

The vibrational modes (degenerate or not) are sometimes referred to by their symmetry properties. The *vibrational* symmetry label is assigned analogously to the electronic symmetry label, though it is more difficult to visualize. In linear molecules, if $\ell = 0$ (which includes non-bending modes) the state has Σ vibrational symmetry, $\ell = 1$ states have Π vibrational symmetry, etc., analogous to the electronic state labels with $\Lambda \leftrightarrow \ell$. In nonlinear molecules we study, degenerate modes (bending or not) have e vibrational symmetry, and nondegenerate modes have some 1D representation label (a or b with some symmetry-group specific subscript). To make the comparison explicit: $\ell \neq 0$ vibrational modes in linear molecules correspond roughly to e vibrational modes in nonlinear molecules capable of having degenerate states. $\ell = 0$ modes correspond with a or b vibrational modes in nonlinear molecules, including the bending modes of asymmetric top molecules, which are no longer degenerate.

In the BO approximation, the vibrational states are products of excitations of each vibrational mode, and can be labelled by the quanta of energy in each mode. Unfortunately, linear and nonlinear molecules have different conventions for how this information is typically presented. In linear triatomics, the states are labelled $(v_1 v_2^{\ell} v_3)$, where v_1 is the lowest energy nondegenerate stretch (e.g. Sr-O stretch motion in SrOH), v_2 is the bending motion, and v_3 is the highest energy nondegenerate stretch (O-H stretch in SrOH). The ground state, with no excitations of any mode, is identified as (000). In nonlinear species, the states are first ordered by representation (1D representations first, a-type before b-type, followed by 2D representations) and then within each set by energy from high to low. This determines the mode number i

(sometimes also written v_i). The mode numbering for the specific nonlinear molecules we study can be found in Chapter 5. The vibrational states are labelled by $n_i n_j ...$ for excitations of modes i with n_i quanta of excitation. Modes with no excitation are left out of the term symbol. For example, the state with one Sr-N stretch and one symmetric bend in $SrNH_2$ is labelled $4_1 8_1$. The only exception is the ground state, which is given the term 0_0. Though this is the dominant convention, sometimes the quanta of excitation appear in superscripts instead, especially in electronic excited states.

The energies of the states are just the sum of the individual oscillator energies. Of course, typically the potentials of the oscillators are not completely harmonic, so we add terms to produce generic anharmonic oscillator eigenvalues:

$$E(n_1, n_2, ...n_k) = \sum_i^k \omega_i(n_i + d_i/2) + \sum_{j \leq i} x_{ij}(n_i + d_i/2)(n_j + d_j/2) + \sum_{b \leq b'} g_{bb'}\ell_b \ell_{b'} + ..., \quad (2.6)$$

In this formula, the x_{ij} constants account for zero-point anharmonicicity (i.e. shifts the T_0 energy) between modes, while the $g_{bb'}$ anharmonic term specifically splits bending modes of equal excitation but different ℓ (e.g. (02^00) and (02^20) in SrOH). This term does *not* lift the degeneracy between signs of the ℓ projection; in the BO approximation they remain degenerate. Typically in our molecules $\omega_i \sim 100{-}1000$ cm^{-1}, $x_{ij}, g_{bb'} \sim 5$ cm^{-1}. Additional terms that couple three or more modes will also appear in the expansion; we will deal with one such term in our discussion of perturbations in the context of Fermi resonances.

2.4 Rotational Structure

The rotational levels form additional substructure on top of the vibronic structure. In the lowest rotational levels, the molecules are well-approximated as rigid-rotors; the

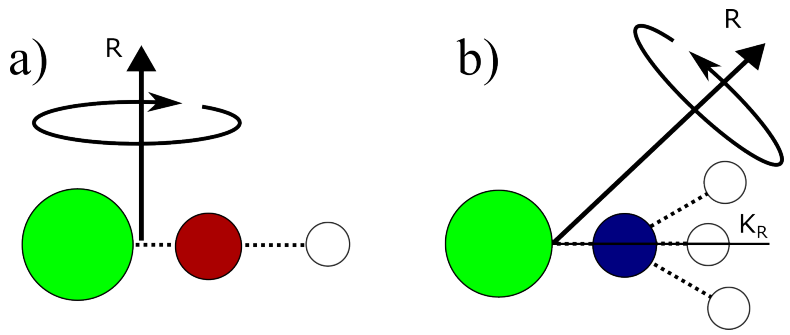

Figure 2.5: Figure showing the fundamental difference in the allowed orientation of the rigid-body rotational angular R momentum in linear and nonlinear molecules. Linear molecular symmetry prevents any angular momentum projection on the internuclear axis, while nonlinear molecules can have such a projection. In symmetric top molecules this projection is denoted K_R. The asymmetric top molecules we work with are close to prolate symmetric tops, where the K_a label approximating K_R. Since the moment(s) of inertia perpendicular to the molecular axis in the nonlinear species we work with are significantly smaller than the parallel ones, it takes much less energy to increase R without changing K_R/K_a than to change it, causing rotational levels to appear grouped into K_R- or K_a- stacks.

bond length approximately does not change due to low-energy rotations. Terms are again added to explain slight deviations from the perfect case, though they are small.

2.4.1 Linear

For linear molecules, the wavefunctions can be found by solving the rigid-rotor Schrodinger equation with the rotor being along the molecular axis with moment of intertia I. Rotation around the molecular axis does not occur in our energy range due to the extremely small moment of intertia around the axis. The wavefunctions of the rigid rotor Hamiltonian are complicated functions with polynomial prefactors multiplied by spherical harmonics. The presence of the spherical harmonics means that the parity of the rotational states alternates with increasing rotational quantum number, in the same way that the parity of atomic electronic states are given by $P = (-1)^L$. The

eigenvalues are correspondingly given by

$$E(N) = BR(R+1) + D(R(R+1))^2 + ... \tag{2.7}$$

where R is the rigid-body rotational angular momentum quantum number (Fig. 2.5), $B = \hbar^2/2I$ is the rotational constant and D is a centrifugal distortion constant which can account for small changes in bond length due to higher-energy rotation. In general, B is often implicitly a function of vibrational state and denoted B_v, where the variation of the constant with vibrational state encodes a change in bond-length. These changes are most pronounced in higher vibrational levels than are typically relevant in our experiments, so using a single constant B is sufficient, typically $\sim$ 10 GHz in our species. Similarly, the D constant can be denoted D_v in different vibrational states, though D itself is too small ($\sim 1 - 10$ Hz) to be relevant to any of the work in this thesis.

2.4.2 Nonlinear

For nonlinear molecules, there is more than one distinct moment of inertia, and so there can be rotational angular momentum around more than one axis (Fig. 2.5). The axis of lowest moment of inertia is called a axis, and the highest as the c axis ($I_a \leq I_b \leq I_c$). These molecules can then have up to three distinct rotational constants $A \geq B \geq C$. Spherical top molecules have all moments of inertia equal. None of the molecules we work with are spherical tops so we do not discuss their energy level structure, but it can be found in Bunker and Jensen [75] and Hirota [74]. Symmetric tops have two distinct moments of inertia, with one axis unique and the other two equal (and non-zero). The symmetric top molecules we discuss in this thesis are

"prolate" symmetric tops, with $I_a < I_b = I_c$. The eigenvalues of rotations are given by

$$E(N, K) = BR(R+1) + (A-B)K_R^2, \tag{2.8}$$

where B is the rotational constant for the degenerate axes, and A is the rotational constant around the molecular axis. A is typically $\sim 5 - 10$ cm^{-1} in the molecules we work with. R is the end-over-end rotational angular momentum quantum number and K_R is the unsigned projection of R onto the a axis (Fig. 2.5)[§]. When $A \gg B$ (far from the spherical top limit), as is the case in molecules we study, the rotational levels can be grouped into "K-stacks" where levels of the same K_R but different R are tightly spaced by multiples of B, compared to the spacing between K-stacks set by A. For oblate tops, in which the C rotational constant is unique, these formulae all hold with A replaced by C.

Since the energy of a level in the rigid rotor model only depends on the magnitude of K_R, each level with $K_R > 0$ is doubled (neglecting nuclear spin). Like ℓ-doublets in linear molecules, in a C_{3v} symmetric top molecule, if $K_R \neq 3$, there is an otherwise identical copy of the state of each parity[¶]. These K_R-doublets are consequently able to serve as "parity doublets" for precision measurements like the $\ell-$doublets in linear polyatomics. The $K_R = 1$ doublets in symmetric tops are degenerate until hyperfine couplings, which are not resolved in any work in this thesis. Details can be found in Butcher *et al.* [88]. The parity of $K_R = 0$ states alternates with R as in lin-

[§]This is often just denoted K, but this can be confusing because K is also used for the total projection of angular momentum excluding spin onto the molecular axis which can include electronic orbital angular momentum. K_R is never used except as the projection of the rigid body rotation onto the internuclear axis.

[¶]If K_R is a multiple of 3, the two states are *not* an e parity doublet. The two states have different rotational representations and cannot mix with electric fields. This is not obvious, but is a result of the size of the symmetry group. We do not use these states in this work; see Bunker and Jensen [75] for details.

ear molecules, determined again by the presence of spherical harmonics in the wavefunction. The rotational symmetry of symmetric top states of interest is just a_1 for $K_R = 0$ states and e for $K_R = 1$ states.

Asymmetric tops have rotational structure that is in general difficult to classify with closed form expressions. It is typical to use the symmetric top basis and express eigenstates in terms of superpositions of these states. The asymmetric top molecules we discuss in Chapter 5 were identified due to their *near-symmetry* which simplifies the situation. The molecules are *nearly* prolate tops with rotational constants $A >> B \sim C$. The degree of asymmetry is quantified using "Ray's asymmetry parameter":

$$\kappa = \frac{2B - A - C}{A - C}, \tag{2.9}$$

where $\kappa \approx -1$ indicates a near-prolate top and $\kappa \approx +1$ indicates a near-oblate top. Since the B and C constants are nearly the same in the molecules we work with, and much smaller than A, $\kappa \approx -1$ and the rotational structure is very nearly just that of a prolate symmetric top molecule. The energies are given by Eq. 2.8 with K_R replaced by K_a, signifying *approximately* the rotation around the molecular a axis. The K_a doublets in $K_a \neq 0$ are now split by the molecular asymmetry, approximately $B - C$. The two parity states are labelled by different "K_c" ($K_a + K_c = R$ or $R + 1$) which differentiate them. This label is not physically meaningful in near-prolate asymmetric top molecules. It is the value that K_R would take if the molecule were deformed into an *oblate* symmetric top, in which case K_a would analogously lose physical significance but remain a state label. These are not strictly good quantum numbers, as molecular eigenstates can generically be linear combinations of states where K_a and/or K_c differ by 2. Nevertheless, for low values of J, K_a, K_c, the K_a, K_c are ap-

proximately good, as there are few states of all the correct symmetries to mix with. In contrast to K- and $\ell-$ doublets in higher symmetry molecules, the asymmetry doublets are nondegenerate even within the BO approximation and when neglecting hyperfine effects. Again the parities of $K_a = 0$ states alternate with R. The rotational symmetry representation of different combinations of K_a and K_c can depend on both, and is not obviously related to parity. For details, see Bunker and Jensen [75].

2.4.3 Hund's Cases

The R quantum number is rarely, if ever, used to label rotational levels in a molecule. The choice of what quantum number is used depends on how the rotation is coupled to the electron orbital angular momentum and spin. The common coupling cases are called "Hund's cases". Hund's case (a) is when the electronic angular momentum and spin are both strongly coupled to the molecular axis and each other, usually due to spin-orbit coupling (see next section), such that the projections Λ, Σ, and Ω are all well-defined [72]. Ω then rotates with the axis and couples with the rigid-body rotation R. In this situation, $J = \Lambda + \Sigma + R$ is used to label rotational levels. This case describes the first excited electronic states in most of our molecules, as we will understand in the following section, and representative structure can seen in Figure 2.6. Hund's case (b) is used when the spin is not well-coupled to the internuclear axis, and in this case rotational levels are labelled by $N = J - S$ [72], as seen in Figure 2.7. Electronic Σ states trivially follow this case, as there is no mechanism to couple the spin to the molecular axis without orbital angular momentum. Though these cases are only strictly defined for linear molecules, they are approximately accurate in the nonlinear species we work with, though subtleties in low-symmetry species are discussed in Chapter 5. There are other Hund's coupling cases related to which angular

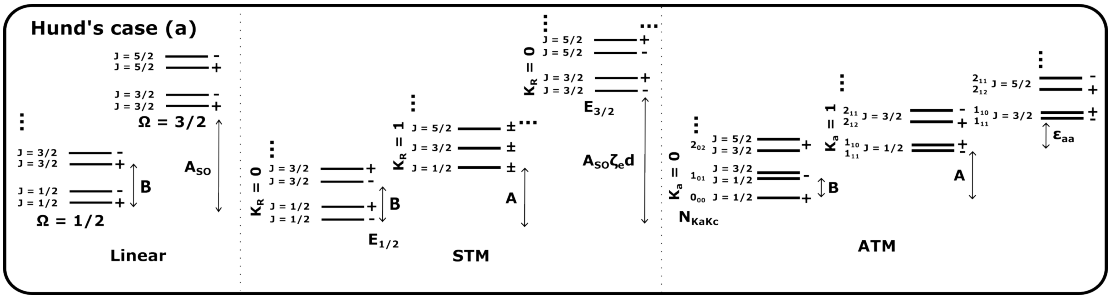

Figure 2.6: Case (a) rotational structure for linear, symmetric top (STM) and asymmetric top (ATM) molecules. The constants that set energy scales are noted next to arrows demonstrating which manifolds they split. The parity doublets in the linear case are split by $\Lambda-$doubling, which also affects $K_R = 0$ states in the symmetric top case if Λ is not quenched. Note that the parities for the asymmetric top may be different in some molecules depending on the symmetry group; these are the labellings for $SrNH_2$ $^2B_2$ electronic symmetry.

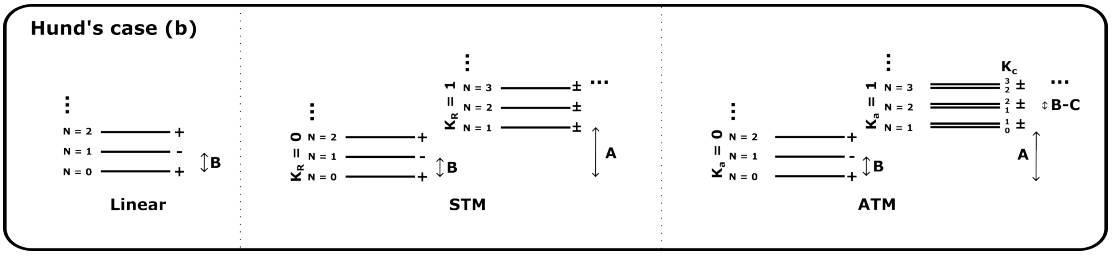

Figure 2.7: Hund's case (b) rotational structure for linear, symmetric top (STM) and asymmetric top (ATM) molecules. The constants that set energy scales are noted next to arrows demonstrating which manifolds they split.

momenta couple in which order, but they do not describe the molecules we use in this work. For details on these cases see Brown and Carrington [72].

2.5 Perturbations: life is complicated

We take perturbations to be a broad term which describes any interaction that makes the molecular structure differ from the descriptions above in meaningful ways for our work.

It is worth noting that ours is an effective-Hamiltonian view of a perturbation: *ab*

initio calculations of structure from the full molecular Hamiltonian (2.1) take all these effects into account naturally. They are simply perturbations for us because of the basis we start with in the preceding sections, which is used because it naturally gives intuition as to how the basic molecular structure is organized. Spin effects trivially fall into this category; we have ignored it up till now. More subtly, other perturbations latch on to the fact that the level structure we developed is the result of certain symmetries: structural symmetries for electronic and vibrational states, as well as spatial symmetry for the rotational states. Clearly, states of the same individual symmetries (e.g. same electronic symmetry) can mix. However, other perturbations are possible; these individual symmetries are only approximate. Only a symmetry of the complete molecular Hamiltonian must be truly and unequivocally be conserved [75]. As such, states of different individual electronic, vibrational, and rotational symmetry representations must also be able to mix, as long as the combination maintains a representation of the full molecular Hamiltonian. These perturbations are BO-breaking, by definition. This does not mean any *real* symmetry is broken, however, a point which can lead to some confusion. We discuss explicit important examples of each of these types of perturbation in the molecules we study, including some which have contributions from multiple origins.

2.5.1 Spin-orbit Effects

Just as in atoms, the presence of a spin on an electron gives rise to a coupling between its spin and orbital angular momentum. The strength of this interaction is characterized by the spin orbit constant A_{SO}:

$$\hat{\mathrm{H}}_{SO} = A_{SO}\vec{L}\cdot\vec{S}. \tag{2.10}$$

This can be separated into two components:

$$\hat{\mathrm{H}}_{SO} = A_{SO}(L_z S_z + (L_+ S_- + L_- S_+)/2), \tag{2.11}$$

where the first term produces what is typically called the spin-orbit splitting in $\tilde{A}$ states, between states with Σ and Λ aligned versus anti-aligned. In linear molecules this is set by A_{SO} directly, but in nonlinear molecules there are added "alignment" factors $\zeta_e d$ that can be interpreted as a measure of how coupled the orbital angular momentum is to the molecular axis. The total splitting between manifolds is given by $A_{SO}\zeta_e d$, with the latter two constants measured spectroscopically. The closer this combination of additional terms is to 1 gives a sense of how well the electron orbital angular momentum is still coupled to the molecular axis (if such an axis is well defined).

In our molecules, these SO constants range from $\sim$ 250 cm^{-1} in Sr species to $\sim$ 1000 cm^{-1} in Yb species. When the SO interaction is large, it tends to split an electronic manifold into submanifolds with different $\Omega = \Sigma + \Lambda$. In SrOH, the $\tilde{A}\ ^2\Pi$ state splits into $^2\Pi_{1/2}$ and $^2\Pi_{3/2}$ submanifolds. Similar things happen in $SrOCH_3$ despite some degree of L_z quenching ($\zeta_e d < 1$) [89]. This in turn also affects the rotational structure. Since Λ and Σ are strongly coupled, only J is well defined, and the rotational eigenstates are combinations of different N but same parity basis states. Such states of different N levels but the same parity and rotational symmetry to mix only necessarily exist in high-symmetry species (e.g. linear and symmetry top molecules), but can also exist in lower symmetry (e.g. C_s) species if the mixing is allowed. Case (a) states in lower-symmetry molecules may not be able to mix N sub-

levels. In the linear case, the rotational Hamiltonian in this eigenbasis gives

$$\hat{\mathrm{H}}_R = B(\vec{J} - \vec{L} - \vec{S})^2. \tag{2.12}$$

Rotational energies are dominated by the square terms in the expansion, with the cross terms contributing perturbatively to several interactions that are usually swamped by other contributions. For example, the $\vec{L}\cdot\vec{S}$ contributes to $\Lambda-$doubling, but at a much smaller level than the direct SO contribution. The size of the splitting between J components in nonlinear molecules also depends on the $\zeta_e d$ parameters as described above. Due to having too-low symmetry to define L_z, the first term of Eq. 2.11 does not affect structure in $SrNH_2$ and SrSH.

The cross terms in 2.11 also contribute to several key molecular perturbations. Notably, they give rise to splitting of $\Lambda-$doublets. Since they change Λ, they describe an interaction between electronic manifolds that differ by $\Delta\Lambda = \pm 1$. This causes the previously degenerate projections of Λ to separate. The reliance of this term on the A_{SO} constant explains why the effect tends to increase in heavier-atom-containing molecules, since the constituent metal atoms have intrinsically large spin-orbit interactions. This origin also explains why Π electronic states have the largest $\Lambda-$doublet splitting: higher Λ states require higher orders of perturbation to couple via this matrix element, and are thus suppressed.

The same SO cross terms contribute to the ground state spin-rotation (SR) splitting. The perturbation causes well-defined N states in $\Lambda = 0$ electronic manifolds of nominally degenerate S character to split into $J = N - S, J = N - S + 1, ..., J = N + S$

sublevels. This splitting is characterized by

$$\hat{\mathrm{H}}_{SR} = \gamma \vec{N} \cdot \vec{S}, \tag{2.13}$$

where γ contains the information about mixing and is usually just measured experimentally. The SO-induced contribution to this effective Hamiltonian term is much larger than the first-order "real" spin-rotation interaction caused by interaction of the magnetic moment of the rotating nuclei with the spin. This is suggested by the relative size of the SR splitting in the $\tilde{X}$ and $\tilde{B}$ $^2\Sigma$ electronic manifolds, approximately 670 MHz in $\tilde{B}$ and 110 MHz in $\tilde{X}$. This is consistent with the splitting being caused by the interaction with the $\tilde{A}$ $^2\Pi$ manifold, since the $\tilde{B}$ state is much closer in energy.

These spin-orbit cross terms also contribute to several other second-order effects, some of which are discussed in Chapts. 4 and 5. The richness of perturbations enabled by spin-orbit atomic interactions suggests a general increase of structural complexity in heavier molecules. The cross-term interactions also, in general, contribute to structure of nonlinear molecules of even very-low symmetry, like $SrNH_2$ and SrSH.

2.5.2 Coriolis Couplings

The first beyond-BO-approximation perturbation we discuss is the Coriolis-type coupling that splits the formerly degenerate projections of ℓ. This mixing occurs from rotational angular momentum weakly interacting with the vibrational angular momentum. The two motions are perpendicular to each other, and so there is no "non-rotating" frame; the effect of the rotating frame on the other motion necessarily couples the motions with a Coriolis-type effect. Figure 2.8 shows how the semiclassical Coriolis force on a nucleus moving due to both a bending motion and rigid-body ro-

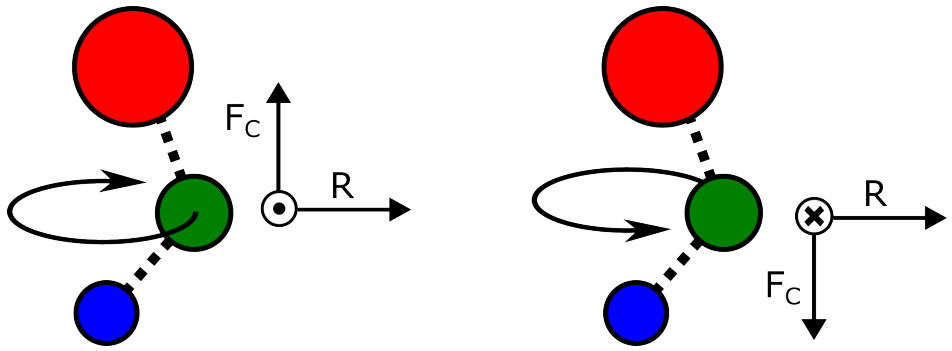

Figure 2.8: Figure comparing a semiclassical interpretation of the origin of the Coriolis splitting in the bending mode. The Coriolis force on a nucleus moving under both rigid-body rotation perpendicular to the molecular axis, R, and vibrational angular momentum around the molecular axis are shown for the two ℓ basis states. At a given point in the vibrational trajectory, nuclei in opposite ℓ states will experience a Coriolis force, F_C, in opposite directions which breaks the symmetry between them. The parity eigenstates are linear combinations of the left and right ℓ states; one combination will experience 2x the force, and the other will experience no net force. Though it is difficult to make this model quantitative, this model correctly predicts that one parity eigenstate will mix with other vibrational modes due to the net force along one of the internuclear bonds which causes a change in bond length, while the other parity eigenstate will not.

tation will experience a different magnitude of force in the two ℓ basis states. The parity eigenstates, which are even and odd linear combinations of the two, will experience either no or double the effect of the ℓ basis states. We emphasize that this is specifically a *semiclassical* way of interpreting the splitting; the actual Hamiltonian for the Coriolis coupling in the bending modes in any useful coordinates is fairly complicated (see, e.g., Merer and Allegretti [90]), but it effectively links and splits states of $\Delta\ell = 2$ as this picture suggests. The effective splitting between the $\ell = 1$ states is given by:

$$\Delta E = qJ(J+1), \tag{2.14}$$

where the q constant contains the relevant physics and is usually measured experimentally (but can be roughly calculated [65, 90]). In our molecules it is typically ~ 10 MHz in the $\tilde{X}(010)$ state, which makes it possible to mix these states with small elec-

tric fields, a useful experimental property for EDM experiments. Though we do not encounter effects of Coriolis coupling in the experimental work herein, that these parity splitting are small is vital to the motivation for using the linear species in the first place[50] since it creates parity-doublets in the ground electronic state (discussed in Chapter 1). A more detailed explanation of the Coriolis effect in bending modes of linear molecules can be found in Refs. [65, 91, 92].

2.5.3 Renner-Teller Couplings

Another BO-breaking interaction that is relevant to our experimental work is the Renner-Teller (RT) coupling (for an overview of the various Teller interactions, see Appendix A). This interaction technically is only strictly defined for linear molecules, though the effect also occurs in nonlinear species with nearly-defined L_z. The interaction mixes the electronic orbital angular momentum with a vibrational angular momentum to form states of good *vibronic* character (though the vibrational and electronic characters separately will not be well-defined).

The general RT Hamiltonian is:

$$\hat{\mathrm{H}}_{RT} = \frac{V_{11}}{2}(L_- G_+ + L_+ G_-) + \frac{V_{22}}{2}(L_-^2 G_+^2 + L_+^2 G_-^2) + ..., \tag{2.15}$$

where V_{11} characterizes the first order interaction, V_{22} the second order, etc. These constants are not usually measured themselves, but are related to spectroscopic constants as we discuss in Chapter 5. $L^{\pm}$ and $G^{\pm}$ are the electronic orbital and vibrational angular momentum raising/lowering operators, respectively.

The first order term couples states of $\Delta\Lambda = -\Delta\ell = \pm 1$, and so must operate between electronic manifolds, and between vibrational states in the two manifolds

that differ by ℓ. In our molecules, this both mixes the $\tilde{A}(010)$ state with both $\tilde{X}$ and $\tilde{B}(000)$ states and the $\tilde{A}(000)$ states with the corresponding (010) modes, and similarly in nonlinear molecules between a and e vibrational modes in E electronic states. These couplings also appear in various second-order effects, some of which appear in Chapters 4 and 5.

The second-order RT terms can directly couple levels in a single electronic manifold. These terms couple $\tilde{A}(000)$ and $\tilde{A}(100)$ to the $\tilde{A}(02^20)$ state in SrOH and YbOH, and can couple similar modes in nonlinear species. In these couplings, the term only mixes states from different spin-orbit manifolds, because the operator does not act on the spin.

2.5.4 Fermi Resonances

Fermi resonances are resonances that occur between different vibrational modes *of the same symmetry* and as such are not BO-violating but just change the vibrational basis composition of eigenstates in the BO approximation [93, 94]. Really, this effect just comes from a cubic term in the anharmonic vibrational expansion,

$$H_{FR} = x_{ijj} Q_i Q_j^2, \tag{2.16}$$

where Q_i, Q_j are dimensionless vibrational coordinate operators [75, 95]. We discuss the explicit effect of this coupling in linear molecules, and nonlinear molecules will have analogous resonances. In linear species, this term can mix two stretch modes, but more commonly appears when mixing a stretch mode with a bending mode. This mixing is allowed because n_j = even states in a bending mode j have a state with $\ell = 0$ (e.g. (02^00)) with the same vibrational symmetry as any stretch state (which

trivially have $\ell = 0$). In principle, this term mixes these $\ell = 0$ bending mode states with many other states. Luckily, most of these states are sufficiently far away that they contribute negligible fractional composition (since the mixing in nondegenerate perturbation theory depends inversely on the energy difference). However, two quanta of a bending mode tends to have similar energy to one quanta of the metal-ligand stretch mode. In this case the mixing need not be small, and the two states exchange vibrational character with each other through this Hamiltonian term. This situation occurs in many electronic states and in both linear and non-linear species. Indeed, it is so common that the specific mixing between the state with two quanta of bend and the state with one quanta of stretch is sometimes termed *the* Fermi resonance interaction, though this is not accurate. Overtones (e.g. adding the same quanta to both states) also exhibit the interaction, and indeed it can sometimes appear more strongly between higher vibrational states if other anharmonic terms bring those levels more closely together in the naïve basis before including the resonance interaction. Higher-order resonances can also occur, though they appear less commonly in our work in part due to our focus on low-lying vibrational states.

2.6 Transitions

Understanding the structure of a molecule is only useful if we can utilize it! In particular, to interact with a molecule we must be able to understand how transitions between different levels occur so as to be able to drive, or not drive, between different levels. We will focus only on electronic transitions here (i.e. between electronic states), as they are the type used in optical cycling, including the motional control techniques and spectroscopic work in Chapters 3, 4, and 5. Discussion of rotational

and vibrational transitions can be found in Refs. [72, 74, 75].

In basic quantum mechanics textbooks, electronic transitions are first discussed in the hydrogen atom. The rule for whether two electronic states can be connected via an electronic excitation is given by the "vanishing integral" rule:

$$\psi_i \leftrightarrow \psi_f \Leftrightarrow \int \psi_i^* \mu \psi_f \neq 0, \tag{2.17}$$

where μ is the transition dipole moment. Expanding the dipole moment into a series of spherical harmonics (see, e.g.Sakurai and Napolitano [77]) makes clear that the entire integral can be thought of as a sum of integrals of three spherical harmonics (with polynomial prefactors). These integrals give rise to "selection rules" on which initial and final spherical harmonics will integrate at a certain order in the transition moment expansion to a nonzero value.

Using a graphical interpretation of the spherical harmonics, we can also interpret the vanishing integral rule as a statement of a symmetry of the system. In particular, it expresses that the angular symmetry of the initial and final states must only differ by the angular properties of the transition moment at a certain expansion order to be driven by a transition of the corresponding multipole character. In Dirac notation, the equivalent rule is

$$|i\rangle \leftrightarrow |j\rangle \Leftrightarrow \langle i|\mu|f\rangle \neq 0. \tag{2.18}$$

This form is advantageous in general because it expresses that non-spatial properties can also contribute (e.g. spin) to the matrix element, but does tend to obscure the importance of symmetry under the guise of mathematical infrastructure.

The purest form of how selection rules of transitions arise uses *only* the symmetry

properties of the constituents:

$$\Gamma_i^* \otimes \Gamma_\mu \otimes \Gamma_f \supset \Gamma_1. \tag{2.19}$$

In this equation, Γ_x is the representation of a state/operator in the symmetry group of the molecule, and Γ_1 is the totally symmetric representation [75]. This form is useful in that it accounts for the relevant symmetry from all structural components while ignoring any superfluous information. The downside of this formulation of the rule is it *only* tells you whether a transition is allowed or not; it reveals nothing about the strength of such a transition. Accurate calculation of the strength does require calculation of the full matrix element.

With Eq. 2.19, we can deduce how electronic transitions can and cannot connect states differing by any quantum numbers: this equation will give all possible connected states if we use the full representational labels. The representation of the transition dipole moment for different point groups is readily tabulated (denoted Γ^* in Bunker and Jensen [75] Appendix A), as are multiplication tables of representations. Using the complete symmetry of the ground and excited states to determine if a transition between them is dipole-allowed is then quite easy, if the state representations are fully known. However, determining the complete representational label of a state is not always easy to do, and hence this process may not be possible directly.

It is often more intuitively useful to work in the BO approximation and determine transitions that are allowed in the fully separated basis. These will tend to correspond to stronger transitions as long as the molecule does not suffer from extreme BO breakdown effects. Working in this basis also offer simpler rules that are easier to remember than always working with Eq. 2.19. Nevertheless, it is important to note

that many of the simple rules derived in this way are not *strictly* good selection rules. The degree to which they break down will depend on the Ray asymmetry parameter (as discussed earlier in the chapter) and perturbations (some of which are discussed in Chapter 5).

In the BO approximation, the wavefunction is completely separable into electronic, vibrational, and rotational components. In this case, each component separately must obey an equation like Eq. 2.19. The symmetry action of the dipole moment on each coordinate gives rise to the selection rules for each subsystem. The process of determining these rules is not shown here for brevity, but can be found in Chapter 14 of [75]. We discuss the results here.

The electric dipole moment operator on the electronic coordinates can produce either $\Delta\Lambda = 0, \pm 1$ selection rules in linear molecules. $\Delta\Lambda = \pm 1$ transitions are called "perpendicular" transitions, as they must be driven by a transition dipole moment perpendicular to the molecular axis. Analogously, $\Delta\Lambda = 0$ transitions are "parallel" transitions because the transition dipole connecting the states is parallel to the molecular axis. There are similar rules for nonlinear molecules that change the electronic symmetry. These selection rules also depend on the axis of the transition dipole, with parallel and perpendicular transitions also in symmetric top molecules, and $a-$, $b-$, and $c-$ type transitions in asymmetric tops, each referring to the axis the transition dipole occurs along. The selection rules in the last cases is not able to be written down in a succinct form; it depends on the representation of the operator along the axis x, $\Gamma(T_x)$, in the molecule's point group. These are tabulated in Bunker and Jensen [75] Appendix A. How electronic symmetry changes for each type of transition can be seen in Table 2.1.

Rotational selection rules are determined by conservation of angular momentum

Species	Transition	Electronic	Additional Rotational	Exceptions
Linear	$\parallel$	$\Delta\Lambda = 0$	-	$\Delta N \neq 0$ if $\Lambda = 0$
Linear	$\perp$	$\Delta\Lambda = \pm 1$	-	
STM	$\parallel$	$\Delta\Gamma_e = 0$	$\Delta K = 0$	$\Delta N \neq 0$ if $\langle L_z \rangle$ or $K = 0$
STM	$\perp$	$\Delta\Gamma_e = E$	$\Delta K = \pm 1$	
ATM	$a-$type	$\Delta\Gamma_e = \Gamma(T_a)$	$\Delta K_a = 0$, $\Delta K_c = \pm 1$	$\Delta N \neq 0$ if $K_a = 0$
ATM	$b-$type	$\Delta\Gamma_e = \Gamma(T_b)$	$\Delta K_a, \Delta K_c = \pm 1$	
ATM	$c-$type	$\Delta\Gamma_e = \Gamma(T_c)$	$\Delta K_a = \pm 1$, $\Delta K_c = 0$	$\Delta N \neq 0$ if $K_c = 0$

Table 2.1: Table of selection rules on electronic and rotational angular momentum for various molecular electronic transitions. The electronic selection rules for nonlinear molecules are best expressed as changes in the electronic representation due to the representation of the transition dipole moment along the relevant axis of the molecule; in the cases of asymmetric top molecules, these representations $\Gamma(T_x)$ need to be looked up for each symmetry group. The rotational selection rules all include the typical $\Delta N = 0, \pm 1$, so only additional rules are noted. Exceptions are due to conservation of angular momentum; *some* angular momentum must change by ± 1. The asymmetric top selection rules are not strict since the K_a and K_a are not strictly good quantum numbers; they will be approximately good in the species we work with.

and the Wigner D matrices (the representations of the rotation group in spherically-symmetric free space) [75]. The Wigner D matrices appear from transforming the molecule-frame dipole moment into the lab frame. For all species, this transformation gives a $\Delta N = 0, \pm 1$ selection rule, with the typical exceptions that transitions which do not change *any* angular momentum are not allowed; e.g. $N'' = 0 \not\to N' = 0$ in parallel transitions between $\Lambda = 0$ states. Since this transformation depends on the symmetry character of the transition dipole moment, different electronic transitions also give rise to additional rotational selection rules in nonlinear species. The resulting selection rules can be found in Tab. 2.1. Parity always must change for a dipole-allowed transition, and must be considered in addition to the rules in this table. The typical exceptions for low-angular momentum cases still arise due to the conservation of angular momentum.

The electronic transition dipole moment is to leading order completely symmetric in the vibrational coordinates [75]. As such, there is *no selection rule* on vibra-

tional quantum number during an electronic transition, though there is an approximate conservation of vibrational symmetry. The strength of a transition between vibrational states of the same symmetry in different electronic states is dictated only by the overlap of the vibrational wavefunctions (e.g. the vibrational matrix element 2.18 is reduced to $\langle v_i'| \mathbf{1} |v_f''\rangle$). This overlap is called a Franck-Condon factor (FCF), and a schematic illustration of the principle is shown in Fig. 2.9. FCFs are not, in general, particularly close to 0 or 1 for generic molecules on generic electronic transitions. Since the modes are determined by equilibrium geometry in the electronic states, which changes as the electron occupies different regions of space, the resulting vibrational bases are always different. This has a few implications. Upon excitation, the strength of an electronic transition is affected by how similar the initial and final vibrational states in the electronic manifolds are. This both simplifies and complicates life: it makes very few transitions forbidden but none necessarily strong. The converse is much more relevant: upon decay, a change in vibrational quantum number is *entirely* statistical. This lack of selection rule leads to unavoidable branching to various vibrational modes in the ground electronic state upon decay from any vibrational mode in an excited electronic state.

This vibrational branching is the root of the difficulty of extending atomic control techniques to molecules. As we will see, electronic and rotational structure can be well-managed. The vibrational structure is intrinsically different; it is impossible to completely control due to the lack of selection rules. Nevertheless, understanding how and why this part of molecular structure arises has allowed substantial progress to be made by identifying how intelligently choosing a molecule can allow *management* of vibrational structure to a degree sufficient for many optical cycling applications, including laser cooling.

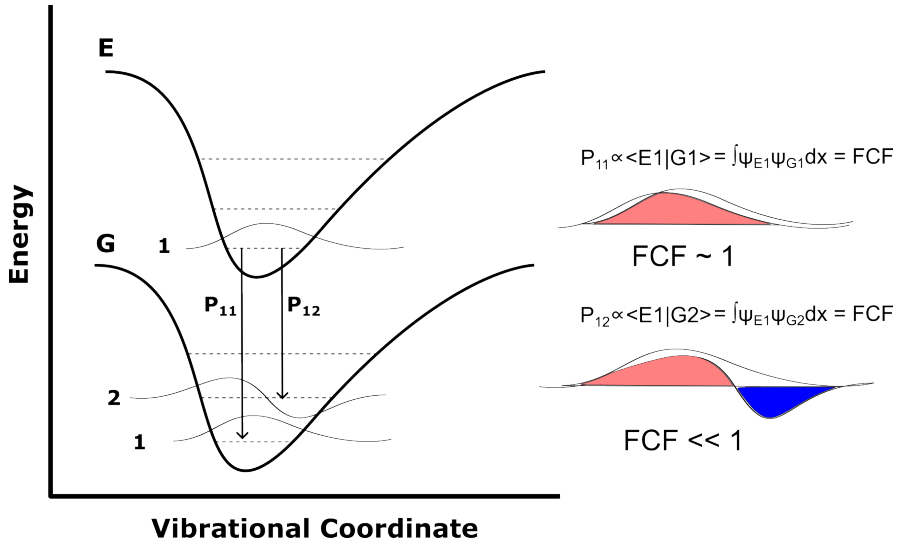

Figure 2.9: Schematic of how vibrational transition probability from an excited electronic state, E, depends on the FCFs between the vibrational states of the initial and final states. These FCFs are calculated by the overlap of the vibrational wavefunction as schematically shown on the right. In this example, the transition to state G1 is vastly more probable than to G2 because of the wavefunction similarity to the excited state. However, the FCFs will never be exactly 1 or 0, and so decays to both states will occur at the statistical ratio.

2.7 Optical Cycling

Control of atomic systems has often relied, to some degree or another, on the ability to *optically cycle*, i.e. to use a single frequency (or small number of frequencies) of light to repeatedly excite an atom and have to decay to the same ground state(s). This process is useful for detection, imparting momentum, and quantum state control/preparation, without which nearly all of modern atomic physics would be impossible.

Extension of these techniques to molecular systems requires constructing an optical cycle in more complex molecular systems. The complications arise from the additional vibrational and rotational degrees of freedom compared to atomic systems. Maintaining closure of these and the electronic degree of freedom is nontrivial, and requires analysis of each separately. To that end, we here review the basic concepts important in attaining electronic, rotational, and vibrational closure. The specifics of generating a closure scheme in a real polyatomic molecule (SrOH) are expounded upon in Chapter 4.

2.7.1 Electronic Closure

Electronic angular momentum is governed by strict selection rules, derived from the angular momentum of the photon and the symmetry of the molecule. the molecule. Driving an electric dipole allowed electronic transition ($\Delta\Lambda = 0, \pm 1$) ensures that the excited state is always allowed to decay to the same state via a dipole allowed decay. Choosing dipole transitions in the optical regime also ensures a *rapid* decay time, important for applications that require fast optical cycling. Of course, many molecules do not have any dipole-allowed optical transitions below their dissociation

energy, so the existence of any such transitions in the first place is nontrivial. If such transitions do exist, complications can arise from intermediate electronic manifolds between the ground and excited states of the optical cycle.

Complications can either effect the speed of the optical cycle, break rotational selection rules, or both. Those intermediate states that could alternatively be used for optical cycling (in particular, that only differ by $\Delta\Lambda = 1$, or an electric dipole symmetry, from the ground state) by definition decay quickly, and so should not significantly increase the cycling time. However, such intermediaries can add decay channels to the wrong parity rotational levels in the ground state, which will spoil the rotational closure scheme. Though this is not really an issue of electronic closure (the final electronic state is the same as the initial), it is at least an issue of total optical closure related to electronic structure. In our molecules, possible cycling electronic states are much closer in energy to each other than to the ground state, and so luckily such decays are suppressed by a $1/\omega^3$ factor (in the Einstein A coefficient) compared to decays directly to the ground state. Nevertheless, avoiding this issue entirely requires optical cycling on the lowest possible excited electronic state.

Intermediate states that differ by too much electronic character (i.e. more than a dipole-symmetry difference) from the ground state to be used for optical cycling can be more problematic. Such metastable states, like the Δ electronic manifold in BaF/BaOH [96, 97], or the "f-state excitations" in YbF/YbOH [98, 99], can be populated at a low level either by electric-dipole-allowed decays out of or perturbations in the cycling excited electronic state. Since these states cannot decay via electric dipole-allowed electronic transitions (by definition) down to the ground state, they in general change some other angular momentum in the molecule when they *do* decay. This will almost certainly spoil rotational closure and could increase decays to vibra-

tional bending modes. In addition, these perturbative decays can also be quite slow, which can limit the average scattering rate in the optical cycle, making certain applications like laser cooling very technically difficult to do in reasonable times or over reasonable lengths. Similarly, low-lying electronic manifolds, even if they are of correct angular momentum to be compatible with optical cycling, will limit the overall scattering rate of the cycle due to the $1/\omega^3$ suppression of spontaneous emission and cause effective electronic leakage. These complications can be seen as a genuine issue of electronic closure, as the population may not return to the original electronic state quickly enough to be useful. Such low-lying electronic states also affect photon cycling in complex atoms (e.g. [100]). In either case, these leakage channels can be dealt with using additional lasers or applied fields, but the efficacy of doing so depends on how strongly the state in question can couple to the cycling excited state.

Ideally, molecules are chosen that lack any of these problematic intermediate electronic configurations. Indeed, the molecules we use tend to intrinsically minimize electronic complications, since the orbital structure appears similar to that of an alkali atom. In these species, the valence electron occupies an s-like orbital with the natural first excited electronic state being a p-like orbital. If the ligand is chosen sufficiently electronegative, there are naturally no electronic states due to the bonding that lie intermediate to the atom-like orbitals. For Mg-, Ca-, and Sr- molecules bonded with many ligands (F, OH, OCH_3, CH_3, SH) there are no metastables at all, thanks to this simplification. In such cases electronic closure is *guaranteed* for the $\tilde{X}$–$\tilde{A}$ transitions.

However, the same is not true of heavier-atom analogs, even though in species containing Ba and Yb, there are still no metastable states due to ligand modes. Unfortunately, these heavy species, and other species most useful for precision measurements, do tend to have *atomic* metastable states between cycling levels. In these cases, the

question is not if these intermediate levels affect cycling, but to what degree. Some techniques to manage the existence of these metastable states in a functional optical cycle include adding powerful additional lasers to optically pump out of the states themselves at a high enough Rabi frequency to prevent problematic spontaneous emission [101], or alternatively microwave remixing additional ground states caused by decays from them [102]. These techniques are nontrivial to experimentally implement and difficult to generalize, but have been found to be effective in some instances.

Sr containing species have no known metastable electronic manifolds, and can thus support electronic closure at arbitrary precision. These species thus make an ideal platform for experimentation of new techniques while maintaining some degree of new physics sensitivity. Accurate demonstration of control techniques in Sr molecules also motivates future investigations in how to efficiently accommodate the more complex species without requiring a complete reinvention.

2.7.2 Rotational Closure

Rotational closure is straightforward in linear molecules. Because total angular momentum excluding nuclear spin (i.e. rotation + electronic orbital + electronic spin) is a very-nearly-perfect quantum number in the molecules we use, the selection rules on how it changes upon electronic excitation and decay are quite rigorous. The simplicity of rotational structure in combination with the selection rules provide a simple outline for maintaining a closed cycle. For a $\Sigma - \Pi$ electronic transition, we start our transitions out of an $N'' = 1^-$ state, and we drive to a $J' = 1/2^+$ state, shown in Fig. 2.10. Though the case (a) nature of the excited state means this level has both $N' = 0, 1$ character, the $N'' = 0, 2$ ground states are positive parity, and thus an electric dipole

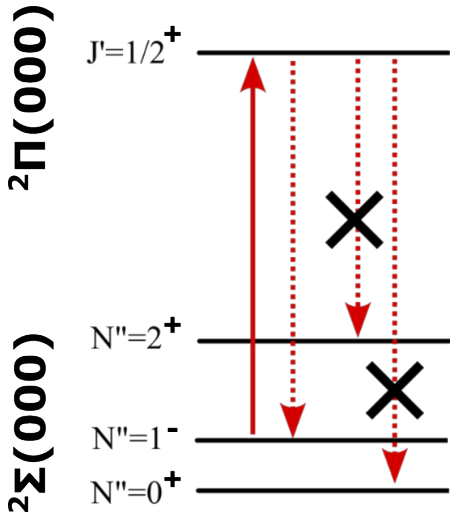

Figure 2.10: Schematic showing rotational closure scheme for a linear molecule between a $^2\Sigma$ ground state and a $^2\Pi$ excited state. The combination of angular momentum and parity selection rules prevent decay from the excited state to any other rotational ground states.

transition cannot connect them. The only decay that is allowed by the combination of conservation of angular momentum and parity is back to the $N'' = 1$ state. For a $\Sigma - \Sigma$ electronic transition, the $N'' = 1^-$ state is driven through an $N' = 0^+$ excited state, which similarly can only decay back to $N'' = 1$. Both of these schemes are parity protected, and so are not perturbed until weak interactions are taken into account, which is at far higher precision than we ever need to experimentally utilize optical cycling.

Rotational closure in nonlinear molecules is substantially more complicated. These classes generically have multiple rotational levels with the same angular momentum and parity in the vibronic ground state due to the K_R or K_a angular momenta. These channels provide additional leakage channels for *any* electronic excitation, making rotational closure generally impossible in physically relevant isomers with a single frequency. In very low symmetry species (e.g. C_s or C_1 symmetry), the excited state's

rotational character can also be heavily mixed, which in turn creates allowed decays to even more states. Special symmetry cases can still support rotational closure with a single ground state, but in general multiple rotational ground states will need to be connected to a single excited rotational level. The details of rotational closure in three low-symmetry molecules is discussed in Chapter 5.

2.7.3 Vibrational Closure

Though rotational and electronic closure are difficult to ensure perfectly in an arbitrary species, in our molecules it is possible to pick a scheme with few electronic and rotational decay channels. The same cannot be said, unfortunately, of vibrational closure. The lack of selection rules on vibrational quantum number indicates that decay from an excited state is dipole-allowed to decay to *any* vibrational mode of the same symmetry. Perturbations often mix vibrational symmetry (see above), which can increase the available decay channels further. The only mechanism of *experimentally* controlling the vibrational decay is to add lasers to "repump" the population back into the main optical cycle. To cycle 10^4 photons in an arbitrary molecule, as is necessary for some laser cooling techniques, one would require dozens or more laser frequencies to account for all the decays which occur above $\sim 10^{-4}$ probability. In order for vibrational repumping to be a feasible mechanism, the molecule of study must be chosen carefully. That such a choice is even possible was the insight that sparked the approach to the first molecular laser cooling [103].

The key is that Franck-Condon factors (FCFs) depend on how similar the vibrational bases are in the ground and excited states. Electronic states with similar bond lengths will naturally have similar vibrational structure, and transitions between such states will have much stronger propensity to "maintain" the vibrational quantum

number than a random molecular transition. Such a situation we refer to as having "diagonal" FCFs, as the table of FCFs between states of each basis will have larger elements along the diagonal.

A class of diagonal molecules had coincidentally already been identified by chemists studying molecular bonds: again, M-L type molecules where M is a alkaline earth (-like) metal atom and L is an electronegative ligand. The resulting isolation of the electron means that even upon excitation the rest of the molecule remains relatively unaffected, and in particular the bond length. As such, the normal modes, and hence the vibrational motions, in the electronic manifolds are similar. Of course, even in this instance, *perfect* vibrational closure is not maintained on a single transition, but this sort of "diagonal" vibrational structure limits the number of decay channels populated at $\sim 10^{-5}$ probability. Indeed, this heuristic seems to hold even for quite large molecules [82, 104], though the number of populated channels still increases with atom number. This intelligent choice of molecule is the key to enabling vibrational repumping as a useful technique: optically pumping out of previously dark vibrational states works arbitrarily, but limiting the number of instances in which it needs to be used is what makes molecular photon cycling possible.

A complication that arises out of this method of closure is that the branching fractions from the main cycling excited state need to be identified to extremely high precision. Few molecular properties are known this well (to be fair, few need to be known this well). The branching fractions are also difficult to calculate accurately (though techniques are improving rapidly [46, 105, 106]). As such, these branching channels typically need to be measured experimentally in order to provide the level of accuracy needed to make decisions about an experiment (e.g. whether to pursue, how practical, which lasers to buy...). A method we use for in-house measurements

of branching fractions is discussed in Chapter 5. Similar work was done (often with the help of collaborators or by other spectroscopists) for *all* laser cooled molecular species(e.g. [46, 99, 105, 107–111]). Very few of these measurements exist at high resolution for molecules not already in use for laser cooling. This lack of necessary information is a major hurdle to extending techniques that requires a high degree of cycling. For many next generation techniques, the existence of fewer previous spectroscopic studies make quick measurements of vibrational branching more difficult, as it may need to be preceded by rotational or even electronic spectroscopy of some poorly-understood species (e.g. RaOH). Until theory is reliably predicting the relevant decay channels, these properties will need to be measured for each species under consideration. There is no clear way around this problem, though it has generated interest in stimulated control techniques (e.g. pi-pulse slowing [112–119]) which avoid it entirely by forgoing spontaneous emission. Such techniques suffer their own technological limitations, although future engineering may surmount some of them. We discuss these and similar ideas briefly in Chapter 6.

2.8 Summary

In this chapter, we describe the basic molecular structure that is referenced in the remainder of this thesis. We begin with Born-Oppenheimer approximation, which allows us to understand molecular energy levels as products of independent electronic excitations, nuclear vibrations, and molecular rotations. A brief discussion of relevant perturbations modifies this simple picture slightly through the inclusion of spin and several effects which perturbatively break the BO approximation. Transitions between electronic states are then reviewed, emphasizing the maintenance of symmetry as a

prognostic for assessing transition strength.

We end the chapter by outlining how the molecular structure and theory of transitions can be used to design an *optical cycle* in molecules, the building block of the experimental techniques both in the following chapters and in the field of direct cooling of molecules as a whole. We discuss how choice of molecule allows for true electronic and rotationally closed cycles in some linear species, with only slight modifications necessary for a much broader selection. Vibrational loss channels are closed through brutish but manageable "repumping", though this technique unfortunately innately links experimental complexity to molecular complexity.

Many of the topics are elucidated further in the following chapters; the information included herein is included to present an unfamiliar reader sufficient material to make sense of the more detailed discussions later. For more thorough treatment of the basics of molecular structure, however, readers are enthusiastically directed to any of the various books (but especially [74, 75]) for more quantitative understanding.

I leave Sisyphus at the foot of the mountain! One always finds one's burden again. But Sisyphus teaches the higher fidelity that negates the gods and raises rocks. He too concludes that all is well. This universe henceforth without a master seems to him neither sterile nor futile. Each atom of that stone, each mineral flake of that night filled mountain, in itself forms a world. The struggle itself toward the heights is enough to fill a man's heart. One must imagine Sisyphus happy.

Albert Camus

3

Zeeman-Sisyphus Deceleration of YbOH

Traditional radiative slowing and trapping techniques tend to rely on the momentum of imparted photons to decelerate and cool molecules. Such methods are, in general, less efficient for higher mass species due to redder cycling transitions and lower recoil velocities. Conversely, many of the molecules that are good for tests of fundamental physics necessarily contain heavy atoms: as previously discussed, EDM searches rely on molecules with minimally Sr-mass atoms, and indeed preferring something

much heavier such as Ba, Yb, or Ra. In addition to the basic mass-related considerations that make it harder to laser cool heavy-atom-containing molecules, the more complex electronic structure in the constituent atoms further complicates the corresponding molecular structure making it difficult to cycle as many photons as in lower-mass nominally isoelectronic species [96–99]. Complications (similar or otherwise) may also arise as molecular complexity increases, for instance in many-atom and lower-symmetry species.

These considerations naturally inspire searches for deceleration and cooling methods that require fewer scattered photons to achieve the same net effect as Doppler methods. To improve the efficiency of photon-cycling based motional control, one must either increase the number of photons a system can scatter without rovibrational loss or increase the energy removed per photon scatter. The former concept has been manifested in exhibitions of the bichromatic force and Pi-pulse deceleration [113, 115, 116, 118, 120, 121]. These ideas have been experimentally demonstrated on several species, but suffer from either technological or theoretical shortcomings which have so far prevented their efficient realizations in arbitrary systems. The latter heuristic is the purview of so-called "Sisyphus" methods, which utilize electromagnetic fields in various configurations to increase the "heft" that a photon imparts on the molecule upon scattering. The first discovered, and most commonly used of these, rely either on the intensity or polarization gradient of the electric field of light to AC Stark shift certain ground states up in energy and others down as the molecule travels through a standing wave [122]. At the peak Stark shift, transitions through excited states which decay to oppositely shifted ground states are driven, upon decay removing $\sim 2\times$ the magnitude of Stark shift per photon scatter. Even with modest laser powers, this energy removal can be many times the recoil energy of a single pho-

ton. If experimental parameters are tuned correctly, the molecule/atom appears to be constantly climbing an increasing potential and is periodically returned to the bottom after scattering a photon, hence the appellation. Though these optical Sisyphus methods are powerful and commonplace, they are not generically applicable to warm or hot samples of molecules: AC Stark shifts in many molecular species of interest are simply too small to exert "large" (even K) energy shifts.*

Zeeman-Sisyphus (ZS) deceleration aims to replace AC Stark shifts with Zeeman shifts. In many molecular species, indeed any species with $S > 0$, laboratory Zeeman shifts can easily reach several K regime. If one can remove Kelvin of energy per photon scatter, in analogy to the Stark-based Sisyphus methods, then in principle one can fully decelerate molecules with only a few scatters. The main scheme is as follows (and illustrated in Fig. 3.12). First, molecules in a weak-field seeking (WFS) state enter the decelerator and slow down by exchanging kinetic and magnetic potential energy as they move towards the first magnetic field maximum. Near the maximum field, they are optically pumped through an excited electronic state into a strong-field seeking (SFS) ground state, removing $2\mu\mathcal{B}$ magnetic potential energy from the system. The molecules then decelerate further as they leave the high field region and bring the internal energy back to 0 (allowing them to travel in free space). This process removes a total of $2\mu\mathcal{B}$ kinetic energy from any molecule that makes it all the way through the magnet. The process can be repeated as many times as necessary. The first reference to the ZS idea was put forth by Comparat briefly in a 2014 manuscript [124], with the first actual design proposed in 2016 by Fitch and

*Electro-optical Sisyphus configurations, using static electric fields, have also been used for trapping molecular species if the height of the electric potential can be made larger than the kinetic energy of the molecules [123]. These are difficult to mode-match CBGBs and have only been demonstrated so far on "out-of-the-bottle" species. Future work may extend the applicability of this method.

Tarbutt [125]. The Fitch and Tarbutt proposal consisted of a ∼meter long decelerator of ∼50 permanent magnet stages which was capable of removing ∼10K of kinetic energy if molecules were correctly flipped between magnetic sublevels via scattered photon between each stage.

Building on these early ideas and our own areas of expertise, we designed, constructed, and used a novel type of ZS decelerator that improved upon certain aspects of the Tarbutt design. In this chapter we describe each of these aspects of the decelerator. Though the first application was on CaOH molecules [126], these molecules are not of interest to precision measurement. Additionally, the material has already been described in detail in other work [65, 126]. As such, we focus on the design principles, important points of construction, and application of ZS deceleration to YbOH. We make particular note of the complexity of applying the method to YbOH, making comparisons to CaOH ZS deceleration when relevant. In this process, we emphasize aspects of molecular structure that deserve attention when designing future ZS decelerators of heavy molecules to avoid several pitfalls we encountered.

3.1 Design and Construction of A Superconducting Zeeman-Sisyphus Decelerator

To understand many aspects of our ZS decelerator design, it is necessary to first review why we did not simply build the previously proposed design. There were two main concerns with the Tarbutt design ZS decelerator. First, the long set of permanent magnet stages would have a very small inner bore. This would not only poorly mode-match a typical CBGB, limiting the number of molecules that entered the decelerator, but could also lead to pressure build up due to low conductance from the

helium buffer gas to vacuum pumps. Second, the design required the optical pumping light to be sent longitudinally down the bore of the decelerator. This alignment would make it necessary to spectroscopically resolve the spin flips at different stages of deceleration, which could be difficult due to the large magnetic moment and relatively steep field gradients in the device. It would also make possible coincidental driving of the wrong transitions at intermediate field strengths if degeneracies occur.

Our solution was capable, in principle, of resolving both issues: use superconducting magnets. Superconducting magnets could produce much higher field homogeneity over a larger volume without requiring either large permanent magnets nor water-cooled high-current systems. The larger field and homogeneity would allow a larger bore, which would better accomodate the CBGB cross section. A larger bore would also increase the pumping speed of helium in the bore, as well as cryopumping almost any other gas, ensuring good vacuum throughout the slowing process. We could also leverage the larger field by leaving a gap in the coil near the center of each magnet. This gap could be used to transversely pump The high-field spin-flip transitions can be driven through these gaps, at areas of relatively low field gradient, to avoid the need to spectroscopically resolve different points on a steep $\mathcal{B}$ slope. Last, but certainly not least, the higher fields created by even technologically simple superconducting magnets reduce the number of magnet stages needed to slow a CBGB dramatically from dozens to "a few".

With these intentions in mind, we designed a of a magnetic field capable of delivering these desires and a coil form capable of housing a magnet capable of delivering such a field. Though we had American Magnetics Inc. wind the actual coil, we provided both a field profile and physical coil bobbins on which to wind them to them to ensure optimal compatibility with the ZS scheme.

3.1.1 Designing The Magnetic Field

The design of our magnets was, of course, primarily dictated by scientific consideration. First and foremost, the apparatus needed to be capable of removing $\sim$ 8K = $\mu\mathcal{B}/\frac{1}{2}k_B$ of kinetic energy, around the typical energy of previously optimized CBGBs [127]. This energy removal corresponds to the molecules climbing a total field of 12T for spin-1/2 species. The maximum field value for single stage was limited to some degree by technical limitations on how easy it was to wind a magnet ("easy" at $\sim$5 T or below). It was also limited by molecular structure concerns. Though we did not plan on cycling many thousands of photons, we still wanted to utilize the electronic and rotational closure afforded by the $\tilde{X}(000)$, $N'' = 1$ – $\tilde{A}(000)$, $J' = 1/2^+$ cycling line, which would enable cycling enough photons for the process. Unfortunately, the N" = 1 low-field seeking (LFS) states and N" = 3 high-field seeking (HFS) levels meet at an avoided crossing around 3 T in both CaOH and YbOH. At such a crossing, the nominal N" = 1 population will be lost from a rotationally closed scheme. We designed around these constraints to avoid over-engineering to a point that would not be useful with our molecules of interest.

In addition to field strength constraints, there were mechanical constraints for the experiment to work as desired. As mentioned above, the field configuration was to be compatible with a large (1") bore and maintain a few percent field homogeneity over the innermost centimeter in order to keep as many molecules as possible in similar fields. Similarly, keeping a longitudinal gap in the middle of the magnet would allow spin-flip optical pumping of many molecules without spectrally broadening the laser. Lastly, we desired to minimize the field strength as close as possible to end of the slower, so as to not lose molecules nor complicate future cooling or trapping down-

stream due to stray fields.

Practical constraints, predominantly from considerations around safely and easily operating the magnets, also determined aspects of the design. Specifically, we didn't want to have a magnet design that would require >100A or long ramping times, both of which could negatively affect quality of life and safety. Housing the magnets would be easiest with the entire system in a single cryogenic chamber, which also constrained the maximum radius and length.

These considerations were used to model field configurations in the Biot-Savart program. The final profile is visible in Fig. 3.1 and Fig. 3.2. We opted for two 3T stages, which allowed us to use magnets small enough to produce a large-bored, homogeneous, field with <50 A of current. This field was also low enough to avoid ground state rotational mixing in CaOH. To minimize the field tails, we added shim coils in an anti-Helmholtz configuration referenced to the main coils, which could produce a near magnetic field zero about 50 cm away from the end of the magnet. The configuration was kept as short as possible to minimize ultimate experiment length.

3.1.2 Coil Form Design

With a field design, we then created a physical mount for AMI to wind the coils on. We wanted to make this piece ourselves to ensure the relevant physical qualities were realized accurately. In particular, we wanted to maintain the 1" bore size, maximize the open gap at the center of the magnets, and minimize the overall length while maintaining structural integrity. The first two concerns were easy to manage: with a bore thickness of 0.230" we were able to keep a 1" open area with minimal decrease in field strength, and we used four solid spacers that bolted to the individual half-coil holders that would easily be able to withstand the slight compression from the

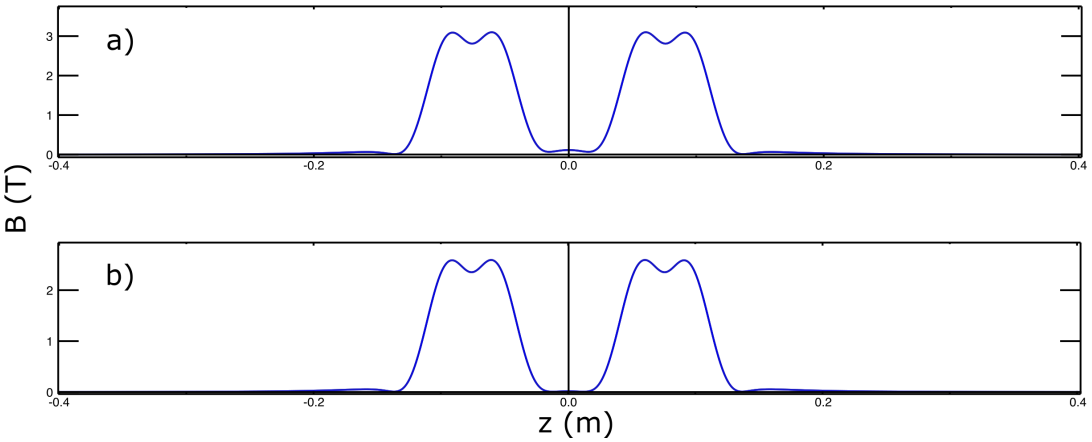

Figure 3.1: Plots of the calculated on-axis magnetic field along the ZS decelerator in a) original configuration and b) YbOH configuration. The main differences in YbOH case are the lower peak field value and additional shim coils reducing the field in between the two magnets (both discussed in text).

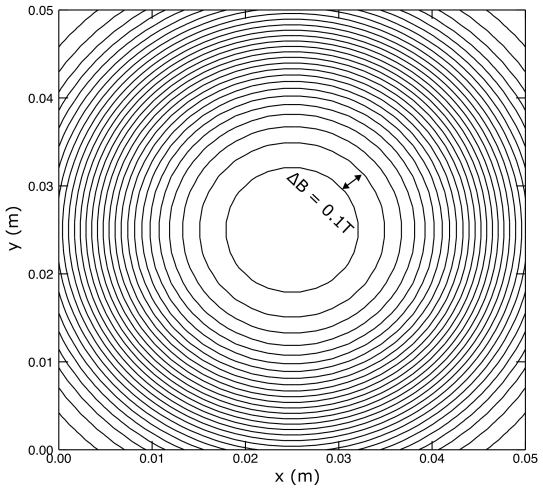

Figure 3.2: Cross section of the field at the middle of one of the magnets in the ZS slower with 0.1T contours as generated from the BiotSavart program with the final magnet design. Note the relatively large area within the inner contour, increasing the compatibility with the CBGB.

Helmholtz pair and allowed optical access to the center of the magnet.

Minimizing the length was not so trivial; we wanted to make the walls of the coil form as thin as possible without risking plastic deformation due to magnet operation. To test the strength and malleability of our designs as we iterated, we modelled the stresses in the coil forms due to the magnetic forces using COMSOL simulation software. Using this modelling, it quickly became apparent that the stress was highly concentrated around the inner radius of the coil, as seen in Fig. 3.3. To minimize the negative effect of this stress, we modelled stress as a function of inner edge cut radius, two examples of which are shown in Fig. 3.4. Unsurprisingly, the stress decreases as the cut radius becomes larger. However, we also had a constraint that once the radius is on the same scale as the magnet wire, the field distortion compared to the ideal would increase. As such, we chose modest radii to focus on, and looked for cryogenic-friendly materials that had large enough yield strengths to not plastically deform under the repulsion. Two materials stood out as contenders, Grade IV CP Ti and Aluminum 6061. Both were strong enough to maintain a small inner radius, and both are thermally conductive enough to cool the magnets by connecting the coil forms to a pulse tube 4K state with heatlinks. The main difference between the two came down to thermal expansion. Since the coils themselves would likely be wound from some high-copper alloy and epoxy, they would thermally contract significantly when cooled. Matching the contraction of the form close to this rate was vital to prevent the magnet from cracking or pulling away from the coil form during this process. On this issue, the clear choice was Al 6061-T6. Though the yield strength of Ti IV is slightly higher than Al 6061-T6 (70 ksi and 40 ksi respectively[†]), Aluminum 6061-T6 contracts about 30% more than copper, and about 4x more than Ti IV. With this

[†]Information found on MatWeb, a useful website for many material properties.

material, we modelled the final coil radius again, with results for the final 0.030" radius visible in Fig. 3.4. We settled on 2.0 mm of an outer edge. In this design, the peak stress is $\sim$ 10 ksi, a factor of $\sim$4 below the yield strength. As additional deformation protection, we also added rods between the faces of the half coils near the outer radius of the forms, which would be slightly pre-stressed during construction so the magnetic forces returned the system closer to an equilibrium. To accommodate heatlinks and thermometer attachment we added small through and tapped holes on the outer coil faces wherever possible. CAD files of the coil form (with stand-in magnet coils) can be seen in Fig. 3.5. The machine drawings for the coil forms can be found in Appendix B. The total length of an assembled coil was 4.96".

We sent AMI the desired field profile and machined coil forms. They wound three coil sets for us (two for the ZS slower and a backup). Details of the construction are "trade secrets", but they did provide datasheets from their tests of the final magnets (see Appendix B). Of particular note are the the maximum field of 2.8T at a typical current of 40 A. Upon delivery, we conducted measurements of the low-current longitudinal field profile with a gaussmeter before installing the coils. These measurements qualitatively agreed with specifications; we attribute small discrepancy to the test being done at room temperature and low current.

3.1.3 Coil Mounting and Installation

Unfortunately, the magnets from AMI were not accompanied by a fully constructed cryogenic chamber to connect to our beam source! As such, we had to also design a dewar capable of holding two magnet sets and a pulse tube. Unlike in the CBGB source, where stability and thermal dissipation are essentially the only relevant concerns, the magnet dewar would also require high-current electrical connections down

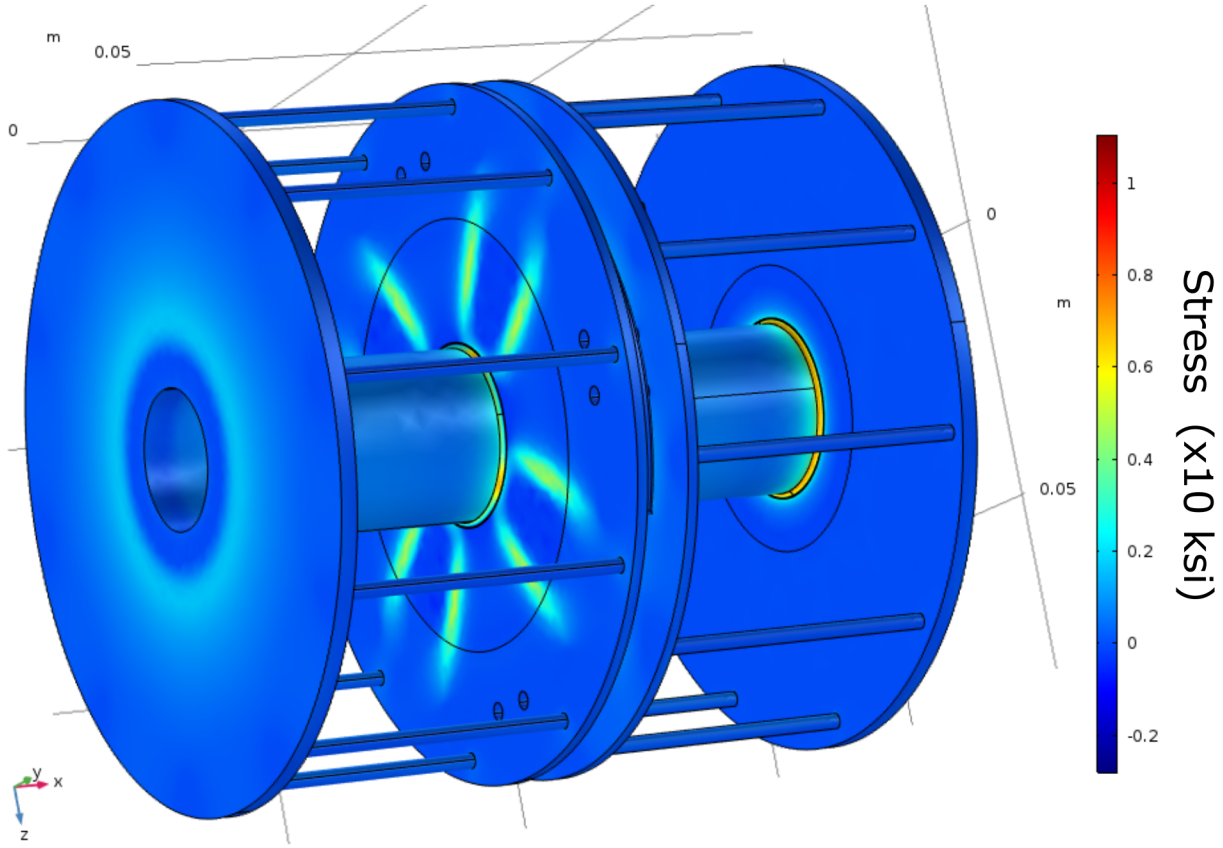

Figure 3.3: COMSOL simulation showing the stress distribution over the entire magnet assembly. The highest stress is clearly on the outer wall edge and against the spacers between half coils, with the latter not being a concern for deformation since the stress is compressive. Fig. 3.4 shows the corner stress at higher resolution and as a function of radius of curvature.

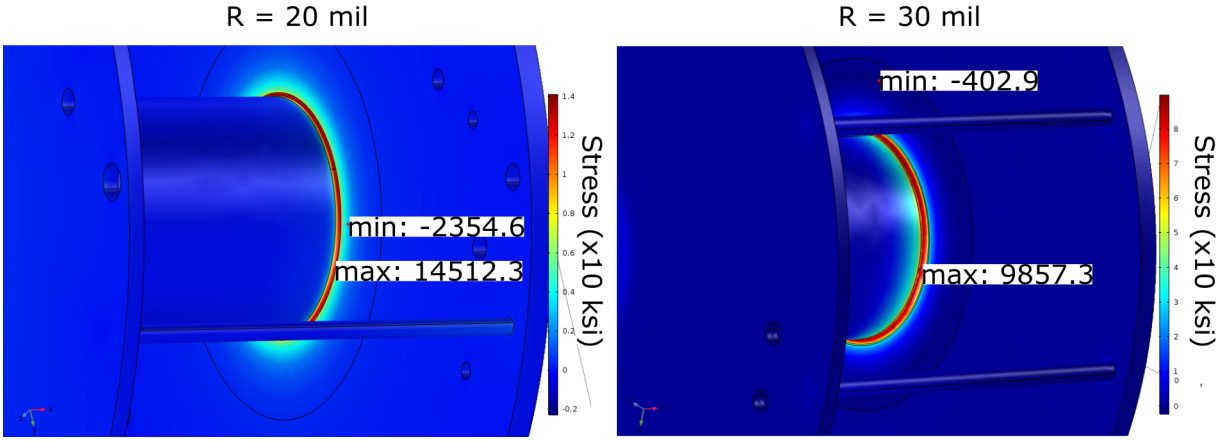

Figure 3.4: Comparison of maximum and minimum stress on the ZS coil form between a 20 mil and 30 mil radius of curvature along the outer wall as calculated by COMSOL simulation software. The change in radius decreases the maximum stress by approximately 50% giving a safety factor of 4 below the Al6061-T6 yield strength of 40 ksi.

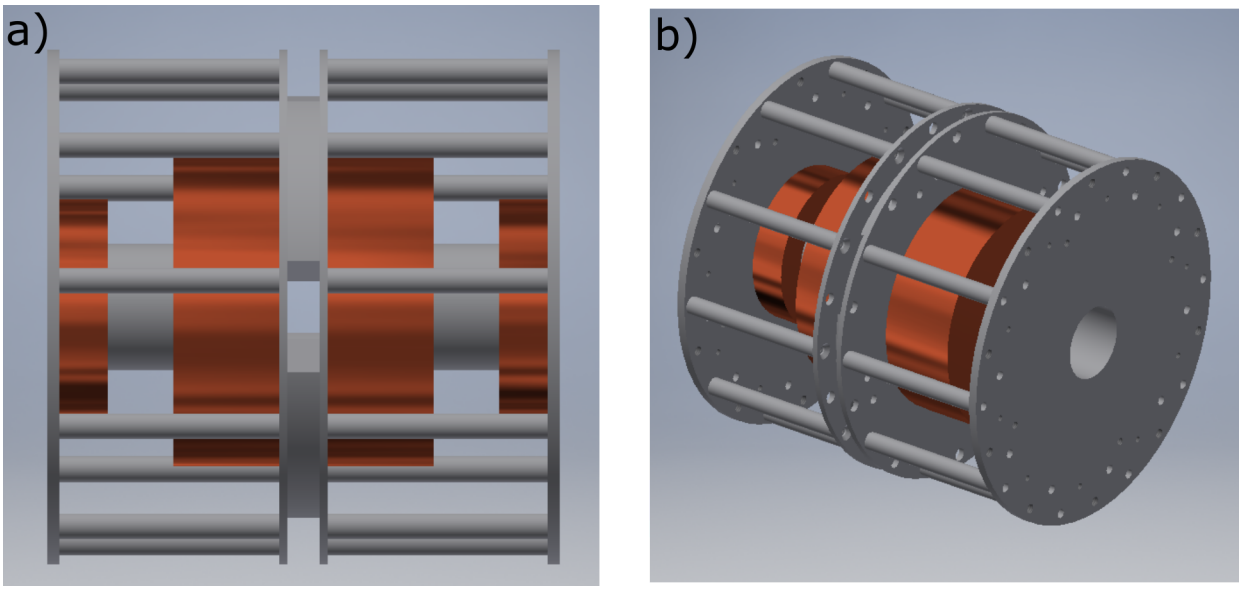

Figure 3.5: Side and angle view of the designed coil forms with stand-in copper coils. The two sub-assemblies are bolted into solid aluminum spacers to hold them together, and the half-coils each have longitudinal pre-stressed rods between faces to counteract the anti-Helmholtz repulsion of main and bucking coil.

to cryogenic temperatures since we needed to supply high current to the magnets. We describe both the mechanical and electric aspects of the design here.

Mechanically, the dewars' design needed to allow the molecular beam to pass through the slower, have sufficient optical access for the ZS optical pumping, and maintain the magnet temperature at 4K. Except for these details, the cryogenic shields, temperature monitoring, and cryopumps were done in the same manner as in our CBGB sources. We omit details here due to plentiful descriptions elsewhere [65, 69, 71, 94].

Adding ∼1 cm holes on all the downstream and upstream cryogenic shields was sufficient alteration to allow the molecules to pass cleanly through the decelerator. The hole size was chosen to balance the molecular flux entering the slower and the blackbody load from 300K radiation on the 4K stage. Even with this balancing, these holes were still the limiting source of blackbody radiation on the cryogenics. Future iterations could extend the 40K cryogenic shielding between the beam source and ZS slower to reduce the solid angle of blackbody incident on the magnet dewar pulse tube.

Ensuring optical access was also simple: long, 0.375" thick windows over the whole length of the slower on both the 40K and 4K cryogenic shielding. COMSOL simulations indicated that this thickness is sufficient to keep the entire bulk of the window within 1K(?) of the shield temperature, indicating that, provided the thermal contact was done correctly, these windows should not add to the heat load on the pulse tube. See [71] and Bao [69] for details on mounting windows cryogenically.

The magnets were connected to the cryogenic refrigerator through a combination of a rigid aluminum mount and a copper braids to the 4K stage of the pulse tube. The mount alone was more structural than thermal, as it was kept narrow to maintain access to the tapped holes on the flange faces. To provide a robust thermal connection

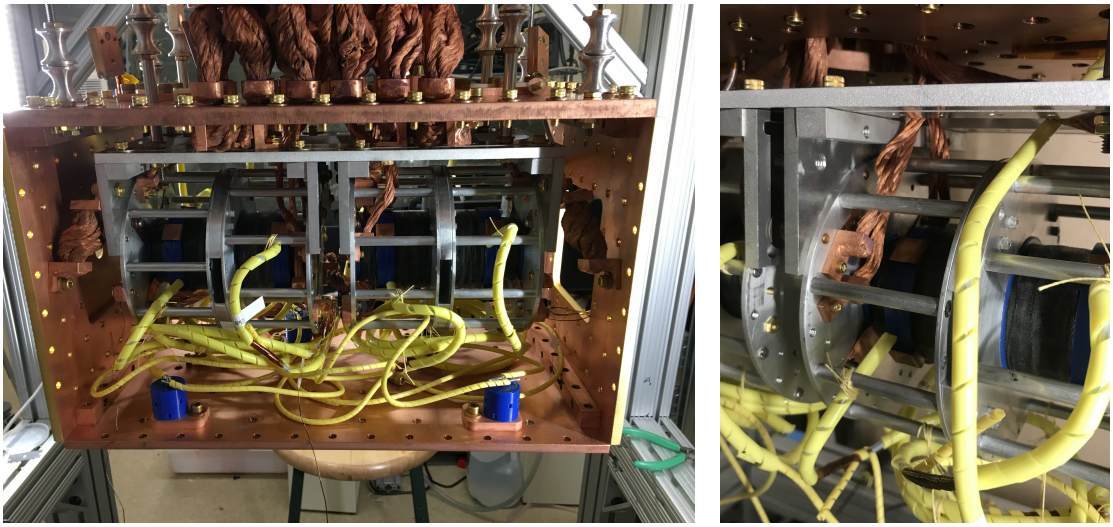

Figure 3.6: Images of the mounted magnets. On the left, a view of both magnets in the 4K cryogenic shielding, with optical access slits seen in the middle of each set. The blue packages are quench protection diodes, which were removed for the experiments described in the text. On the right, a close-up of the inner wall of one of the magnets, showing the copper braids bolted to the inside face. These braids were also clamped to the 4K stage of the pulse tube to cool the magnets.

between the 4K pulse tube stage and the magnets, we connected them with ∼15 thin copper braids per magnet. These assemblies were mounted inside nested 40K and 4K cryogenic shields, as visible in Figure 3.6. The two magnet sets' bores were coaligned to 0.02" concentricity using a machined macor rod. Longer decelerators likely require more accurate alignment to avoid transverse oscillations off-axis resulting in molecule loss, but simulations show this alignment was sufficient for our experiment.

The electrical connections for the magnet coils were trickier. The quandry arises from the fundamental tension between resistive heating and thermal conductivity. Outside the cryogenic chamber, there is no issue. From the power supply to the ZS chamber, 4 AWG copper cables can easily carry many 10s of amps of current. Inside the chamber, however, thick copper wires cannot be used from the feedthrough to the

magnets because they are also very thermally conductive: an 8 AWG wire (rated *in air* for 40 A) from the feedthrough to the magnets would have to be almost 2.5 meters long long to not add >500 mW to the pulse tube load. This is a long length of a quite thick wire to fit in a tight space. Even this heat load on the 4K stage is really a strict maximum: in combination with other heat loads it would come close to overwhelm the 2W cooling capacity of the PT420 model, which would prevent superconducting operation of the magnets. On the other hand, using thin copper wire in this capacity is also not reasonable, since resistive heating goes inversely with the cross sectional area and would melt the wire. Such heating would also add significant thermal load to the cryogenics. Higher thermal resistivity regular metals magnify the resistive heating issue further. An alternative to these options uses high-temperature superconducting (HTS) components, which as ceramics are able to both electrically conduct and thermally isolate in their superconducting phase.

The 150 mm long HTS leads were produced by GMW Associates. The superconducting component was a filament of HTS (non-disclosed, likely YBCO) with a critical temperature of >64 K. The leads also had a thin sheet of stainless steel along the length as a "shunt" which reroutes the current in case of a LTS magnet quench to prevent damage to the HTS material itself. We used these as the electrical connection between the 40K and 4K states of the ZS dewar, as they would add essentially zero heat load to the magnets themselves and both temperatures are comfortably below the T_C. Normal copper wire was used between the room-temperature feedthrough and the 40K stage. The electrical connections between the normal and superconducting sections was done by bolting both to a ∼1/2" thick copper block to minimize junction resistance. To avoid electrically shorting the cryogenic shields, these blocks were mounted to the shields on a 0.002" kapton sheet, the bolting holes were

rimmed with G10 tubing, and G10 washers kept the bolts themselves from touching the blocks. This combination allowed us to use large enough copper blocks to provide sufficient thermal contact even across the kapton sheet to remove most of the heat that was conducted through the normal wire from room temperature. These blocks were surrounded, to the best of our ability, by 1/8" copper thermal shielding to prevent blackbody from heating the top of the leads. Pictures of these heatsinks and connections can be seen in Fig. 3.8. Thermometers mounted on the connection blocks showed that although the combination of thermally conducted and blackbody heat load was sufficient to keep the HTS leads superconducting, the temperature routinely sat >15K above the shield temperature. Future iterations should improve the conductive heat load by improving thermal shielding robustness, further increasing the size of the connection block, shrinking the kapton sheet thickness, and increasing the gauge of the bolts.

The lower temperature ends of the HTS leads were clamped to another large copper block, seen in Fig. 3.8. The LTS magnet leads were adapted with copper lugs which also clamped to this block, documented in Fig. 3.9. This configuration provided good electrical connection between the HTS and LTS sections, while preventing torques or forces from moving the HTS leads, which are comparatively fragile to the other materials involved. These blocks were tightly clamped through an electrically-insulating layer of Kapton to the 4K shield to remove heat. This heatsinking was important to prevent the ends of the LTS leads from going normal, as their critical temperature was only $\sim$ 10 K. Previous iterations of electrical connection with less heatsinking area proved unable to remove the conductive heatload through the HTS leads (rated by GMW to be 72 mW/lead), likely due to the stainless shunts. In the final configuration, thermometers on these blocks showed only a slight (<1K) temper-

Figure 3.7: Picture of the electrical connection between the regular conducting lead (top left) to the HTS lead (silver, to the right). The block which they are connected through also serves as a heatsink, and is tightly clamped to the 40K shield through a sheet of kapton (not visible).

Figure 3.8: Electrical and thermal connection at the bottom of the HTS leads. The HTS leads are clamped tightly to the large copper blocks, along with the LTS lugs (3.9) to eleectrically connect the two. The block itself is tightly clamped to the 4K shields to remove heat conducted through the HTS lead shunts and prevent the LTS lead from going normal. To prevent electrically shorting the block to the shields, a kapton sheet is placed between the block and shield, and a G10 sheet separates the top of the clamping bolts from the block.

ature difference across them to the 4K stage.

3.1.4 Magnetic Guide

The last new (i.e. not used in typical Doyle group experiments) part of our ZS decelerator, the magnetic octupole guide, is not actually involved in the deceleration at all but was necessary for accurate detection. In particular, since the molecules exit a ZS cycle in a SFS state, they are susceptible to off-axis acceleration due to fringing fields, an effect that is magnified at slow velocities. To prevent these molecules from getting lost (and therefore not detected), the octupole guide was added after the second ZS magnet to ferry the molecules safely out of the strong stray field region. The design of a single stage of the guide, including relevant dimensions, can be seen in

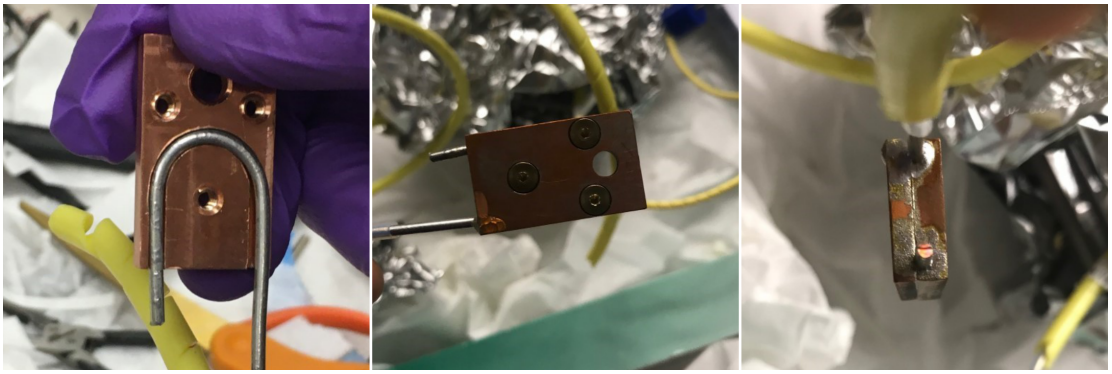

Figure 3.9: Assembly of the lugs used to connect the LTS magnets to the rest of the electrical circuit. The LTS leads were fit and clamped into copper endpieces, which were then soldered to ensure optimal electrical connection. These lugs were then clamped to the heatsinks along with the HTS leads (3.8).

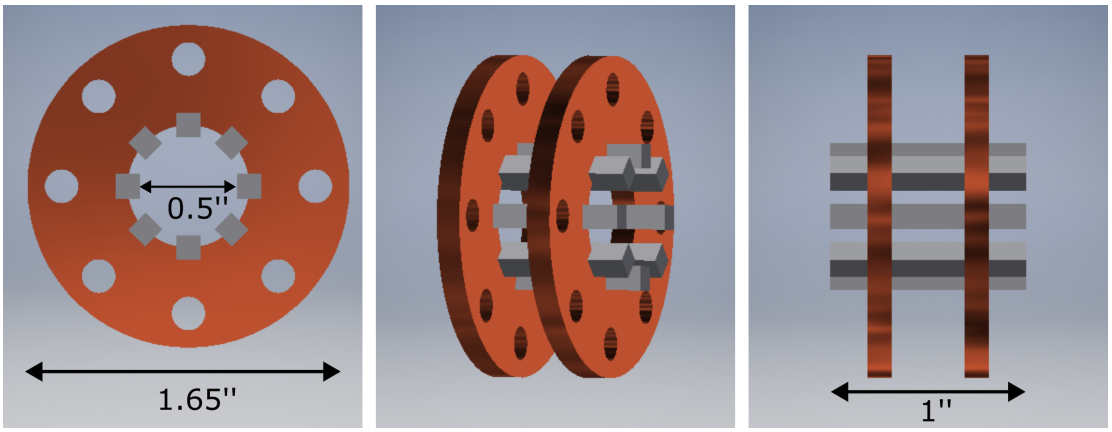

Figure 3.10: CAD views of a segment of the magnetic guide. The design is 1" long. ∼15 of these were used to bridge the distance between the end of the ZS magnets and the detection region. The magnets were affixed to the copper holders with epoxy.

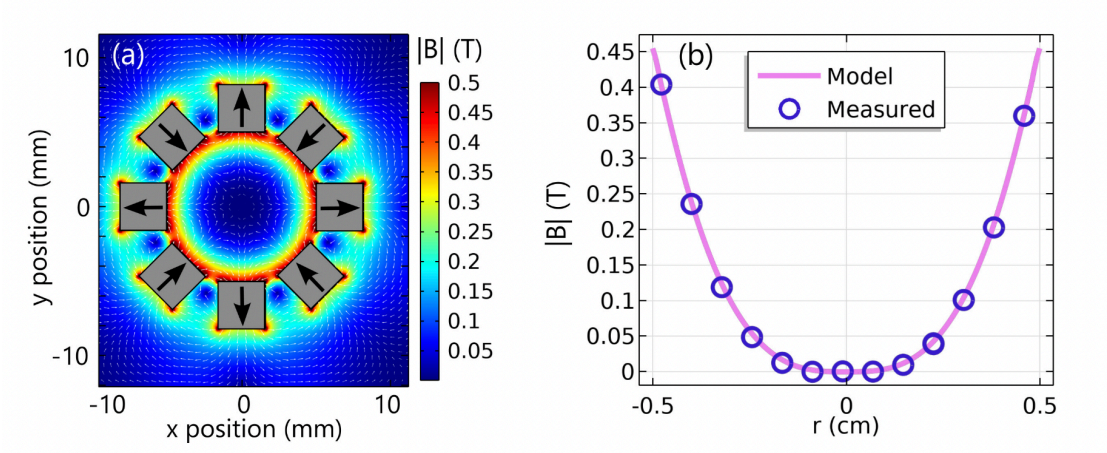

Figure 3.11: Field strength inside the magnetic guide, figure borrowed from Augenbraun [65]. On the left (a), an end-on view of the individual permanent magnet orientation and a COMSOL-generated profile of the field. On the right (b), a comparison of the radial field strength as measured (dots) and simulated with COMSOL (line).

Fig. 3.10. The final construction used $\sim$ 15 1" long, 0.125"x0.125" cross section, 1.3 T N42 NdFeB magnets[‡] epoxied[§] into Cu mounts. These subassemblies were held evenly spaced on #10 Ti threaded rods with aluminum nuts to cover the whole length from ZS magnet to detection region. The field was simulated COMSOL and measured via gaussmeter (Fig. 3.11). This field corresponds to $\sim$ 250 mk depth for $s = 1/2$ species. This depth is more than sufficient to contain the estimated 1 m/s transverse velocity the CBGB should have a meter downstream from the source through the cell, shield, and magnet apertures.

[‡]BX022 from K&J Magnetics, Inc.

[§]Masterbond EP30-2 epoxy or Stycast 2850, for room temperature and cryogenic parts respectively

3.2 Zeeman Sisyphus Deceleration of YbOH

In this section, we describe in detail the ZS deceleration of YbOH [¶]. Though the method was ultimately successful in decelerating molecules, the YbOH scheme fundamentally differed from the simple picture outlined earlier in this chapter. We begin our discussion with an outline of the YbOH ZS experiment including the apparatus above and the relevant optical pumping. To ultimately make the ZS scheme work as outlined, we had to better understand the molecular structure of the involved states. To that end, we then discuss the high-field Zeeman spectroscopy, optical pumping modelling, and technical upgrades that were necessary to achieve deceleration. We end with discussion of the results and limitations of this work. Throughout the section, we raise attention to aspects of the work that require attention for future ZS deceleration of other heavy molecules.

3.2.1 Experimental Setup

YbOH molecules are produced by laser ablation of a pressed powder target of a stoichiometric mixture of Yb and $Yb(OH)_3$. This ablation occurs inside a buffer gas cell held at $\sim$2 K and filled with He_4 buffer gas at a typical density of 10^{15} cm^{-3}. The buffer gas quickly thermalizes the molecules to the cell temperature, and the combination is hydrodynamically extracted from the cell through a 7 mm diameter aperture [129]. The molecules then enter a 20 mm long second stage "slowing" cell [129, 130] held at 0.9 K by a pumped ^{3}He pot (see Augenbraun [65] for details). The gap between the two stages was tuned to 2 mm to optimize the molecular beam's

[¶]Portions of this section are taken and/or adapted from the publication "Zeeman-Sisyphus Deceleration for Heavy Molecules with Perturbed Excited-State Structure" [128].

forward velocity and flux. Typical peak forward velocities after the second cell are between 30 and 50 m/s (equivalent kinetic energy $\sim$ 15 K). The appearance of molecules at the lower end of the velocity spectrum was extremely dependent on small changes to ablation energy and pointing, and even cell construction. Advancements in reliable low-velocity molecules in a CBGB would increase the efficiency of this method substantially.

After leaving the cell, the molecules fly 55 cm to the decelerator described above. Before entering the first magnet ("S1" region), molecules are optically pumped into the WFS manifold by a state-preparation laser (7 mm diameter, 100 mW) tuned to the $|\tilde{X}\,^2\Sigma^+, SFS\rangle \rightarrow |\tilde{A}\,^2\Pi_{1/2}, J' = 1/2, p' = +\rangle$ transition. The molecules then enter the first magnet and decelerate as they climb the magnetic potential. At the center of the first magnet (region "D1", $B \approx 2.4$ T), molecules are optically pumped toward the SFS manifold by a laser beam tuned to the $|\tilde{X}\,^2\Sigma^+, WFS\rangle \rightarrow |\tilde{A}\,^2\Pi_{1/2}, J' = 1/2, p' = +\rangle$ transition. The pumping in the D1 region is done by a 400 mW laser beam that is cylindrically expanded to $\sim$ 20 mm$\times$5 mm, nearly the maximum size compatible with magnet design (the slits can be seen in Figure 3.6, and dimensions of the spacers can be found in Appendix B). The molecules, now in the SFS manifold, continue to decelerate as they exit the first magnet. When the molecules finally leave the magnet, they are driven back to the WFS manifold via the $|\tilde{X}\,^2\Sigma^+, SFS\rangle \rightarrow |\tilde{A}\,^2\Pi_{1/2}, J' = 1/2, p' = +\rangle$ transition (in the "D2" region). The laser beam in D2 has a power of 200 mW and is also expanded to $\sim$ 20 mm$\times$5 mm.

In addition to the apparatus as describe above, an extra pair of compensation coils are installed to ensure $B < 500$ G in this region so as to maximize optical pumping efficiency, as explained in Section 3.2.2. The high-field pumping step is repeated in the second magnet as molecules pass through the second field maximum ("D3"). Immedi-

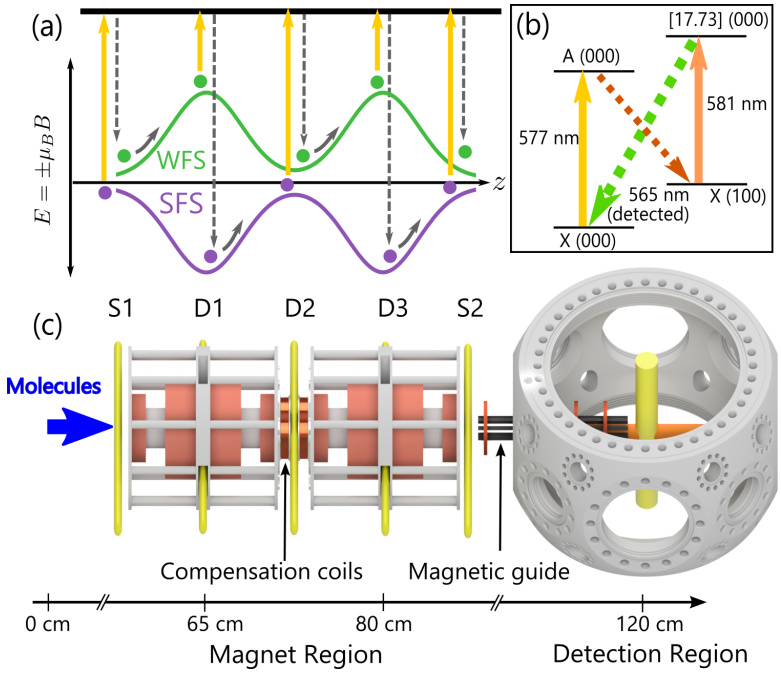

Figure 3.12: Overview of the ZS deceleration scheme. (a) Simplified representation of the magnetic field tuning for an ideal $^2\Pi - ^2\Sigma^+$ electronic transition. (b) Level diagram indicating the background-free detection scheme. (c) Schematic rendering of the decelerator magnets and detection region.

ately after exiting the second magnet, a final spin-flip transition is performed ("S2"), to putting the molecules into the WFS state so they can enter the magnetic octupole guide. The molecules then traverse the guide into the detection chamber.

Molecules are detected using a (nearly) background-free laser induced fluorescence (LIF) detection scheme. We simultaneously drive the $\tilde{A}\,^2\Pi_{1/2}(000) \leftarrow \tilde{X}\,^2\Sigma^+(000)$ (577 nm) and $[17.73](000) \leftarrow \tilde{X}\,^2\Sigma^+(000)$ (581 nm) transitions[‖] while detecting fluorescence from $[17.73](000) \rightarrow \tilde{X}\,^2\Sigma^+(000)$ at 565 nm.[**] The 581 nm laser beam can

[‖]The [17.73] state is an electronic excited state in YbOH that arises from excitations of the Yb($4f$) shell. It is mostly of $\Pi_{1/2}$ character and predominantly decays to the $\tilde{X}\,^2\Sigma^+(000)$ and (100) levels.

[**]A small magnetic shim coil is used to keep the magnitude of the field in the detection region $\lesssim 1$ G so the Doppler-sensitive light is only resonant with a single set of molecules.

either be sent transverse to the molecular beam, to detect all molecules, or sent partially counterpropagating against the molecular beam to provide velocity-sensitive detection. In the Doppler-sensitive configuration, the 581 nm beam is chopped at 500 Hz and sequential comparison of time bins with the laser on and off are used to reduce the noise associated with remnant scattered light from the 577 nm beam, which is the dominant source of noise despite the off-diagonal detection scheme.

3.2.2 Zeeman Spectroscopy

The observant reader will note that many of the field values noted above are lower than the nominal design specifications of the ZS magnets. These values were chosen as a result of the Zeeman spectroscopy we describe in the section to ensure minimal loss of molecules in the presence of a $\mathcal{B}$ field.

We performed optical pumping measurements using segments of the complete ZS decelerator to characterize the YbOH Zeeman structure in magnetic fields up to 2.5 T. In these measurements, molecules are first prepared in the WFS manifold in region S1 and enter region D1 in which a (variable) magnetic field is applied. The molecular flux transmitted to the detection region is monitored as the frequency of the optical pumping laser is scanned over resonance features for various magnetic fields.

Because SFS states are unable to traverse the octupole guide (see Fig. 3.12), transitions that drive population from the WFS manifold to the SFS manifold are detected as a decrease in fluorescence in the detection chamber.

Figure 3.13(b) shows optical pumping spectra recorded at various magnetic fields between 0.2 T and 2.4 T. By subtracting the known ($1\mu_B$) ground state Zeeman shifts from the raw data, we isolate the $\tilde{A}\,^2\Pi_{1/2}$ energy level structure in Figure 3.13(b). The $|\tilde{A}\,^2\Pi_{1/2}, J' = 1/2, p' = +\rangle$ manifold displays significant Zeeman tuning. More-

over, the nonlinear Zeeman shifts indicate significant rotational mixing with $|\tilde{A}\,^2\Pi_{1/2}, J' = 3/2, p' = +\rangle$. The appearance of a third resonance, marked by (*) in Figure 3.13, is due to the $|\tilde{A}\,^2\Pi_{1/2}, J' = 3/2, p' = +\rangle$ level, which tunes strongly toward the lower energy $J' = 1/2$ states. We fit the observed transitions to the Hamiltonian model of Ref. [131]. Holding all constants other than g_S and g_l' in the $\tilde{A}\,^2\Pi_{1/2}$ state fixed, we determine $g_S = 1.860(9)$ and $g_l' = -0.724(4)$. g_S significantly differs from the bare electron value, although this is not unexpected given perturbations between the $\tilde{A}\,^2\Pi_{1/2}$ state and nearby $Yb^+(4f^{13}6s^2)OH^-$ states (see supplemental material of Sawaoka *et al.* [128] for additional details). The measured g_l' value is close to that predicted by a Curl-type relationship [132], which predicts $g_l' = -0.865$. The fitting method and obtained values are discussed in detail in supplemental material in the same supplement [128].

The ground state also experiences level crossings that lead to rotational mixing. At fields greater than ~ 0.01 T, the two Zeeman manifolds of the $|\tilde{X}\,^2\Sigma^+, N'' = 1\rangle$ level tune linearly with a slope of $1\mu_B$. Near 0.5 T, the $|\tilde{X}\,^2\Sigma^+, N'' = 1, \mathrm{SFS}\rangle$ manifold crosses the $|\tilde{X}\,^2\Sigma^+, N'' = 0, \mathrm{WFS}\rangle$ manifold and near 1 T, the $|\tilde{X}\,^2\Sigma^+, N'' = 1, \mathrm{WFS}\rangle$ manifold crosses the $|\tilde{X}\,^2\Sigma^+, N'' = 2, \mathrm{SFS}\rangle$ manifold. However, these crossings do not affect the $|\tilde{X}\,^2\Sigma^+, N'' = 1\rangle$ manifolds because the neighboring rotational states have opposite parity. On the other hand, near 2.5 T, the $|\tilde{X}\,^2\Sigma^+, N'' = 1, \mathrm{WFS}\rangle$ manifold crosses the $|\tilde{X}\,^2\Sigma^+, N'' = 3, \mathrm{SFS}\rangle$ manifold and these levels *can* mix due to dipolar hyperfine terms. For YbOH, 2.5 T is the practical maximum field that can be used for the peak field of a deceleration stage. In general, the crossing between the $|\tilde{X}\,^2\Sigma^+, N'' = 1, \mathrm{WFS}\rangle$ manifold and the $|\tilde{X}\,^2\Sigma^+, N'' = 3, \mathrm{SFS}\rangle$ manifold happens at a magnetic field of $5B/\mu_B$, where B is the rotational constant.

This Zeeman spectroscopy thus limited our field strength below the maximum value

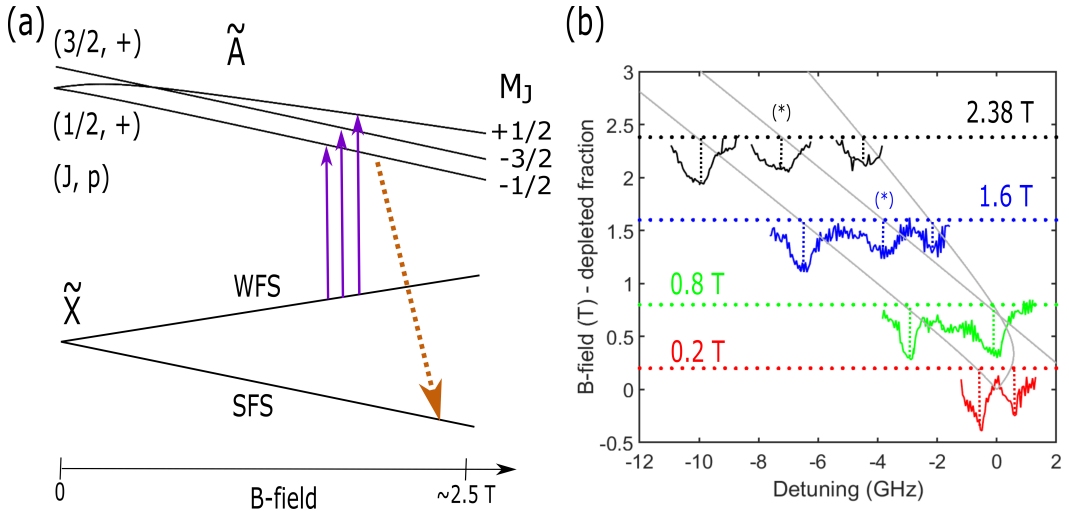

Figure 3.13: Overview of the $\tilde{A}\,^2\Pi_{1/2}$ (000) Zeeman structure and optical Zeeman spectroscopy. (a) Energy levels and excitation/decay pathways involved in the optical pumping transitions. (b) Magnetic tuning of the low-J $\tilde{A}\,^2\Pi_{1/2}$ (000) energy levels inferred from the optical pumping measurements Data recorded at different magnetic fields are offset vertically for clarity. Lines overlaid on the spectra indicate computed energy levels using optimized fit parameters. The vertical dotted lines are guides to the eye for indicating the center of the depletion features at each magnetic field values. (*) denotes the resonance due to the $|\tilde{A}\,^2\Pi_{1/2}, J' = 3/2, p' = +\rangle$ level.

of the magnets. Additionally, it illuminated the strong rotational mixing in the excited state. Both the lower field and the excited state contributed to the lower efficiency in this work compared to Augenbraun *et al.* [126]. We note that both of these issues are likely not specific to YbOH, since related heavy species will generically have similar ground state rotational constants and congested excited state structure. Understanding the Zeeman structure in other species will be paramount to designing a future ZS scheme with minimal loss.

3.2.3 Optical Pumping Efficiency

Efficient spin-flip transitions are of central importance to ZS deceleration. For this reason, the initial proposals [124, 125] and demonstration [126] for the ZS decelera-

tor focused on molecules whose lowest electronic excited states are nearly ideal $^2\Pi_{1/2}$ states. The large spin-orbit coupling, small g-factor, and the presence of rotationally-closed cycling transitions between these states and $^2\Sigma$ ground states makes them ideal targets for ZS deceleration.

In the $^2\Sigma$ ground state, the electron spin is uncoupled from the molecular axis, giving rise to WFS and SFS states with well defined values of M_S, the projection of the electron spin along the external field. Transferring population between these states requires flipping the projection of the electron spin. The large spin-orbit coupling of a $^2\Pi_{1/2}$ state facilitates driving these spin flips because the eigenstates in such a manifold are a nearly even linear combination of M_S values.

By driving transitions from the $|\tilde{X}\,^2\Sigma^+, N'' = 1\rangle$ to the $|\tilde{A}\,^2\Pi_{1/2}, J' = 1/2, p' = +\rangle$ state, parity and angular momentum selection rules ensure that molecules always decay back to the $N'' = 1$ manifold. The rotational closure of a cycling transition is crucial to minimize loss during the repeated optical pumping steps. This situation, which has been used in previous ZS deceleration of CaOH [126] and molecular laser cooling experiments [133], relies on the $|\tilde{A}\,^2\Pi_{1/2}, J' = 1/2, p' = +\rangle$ states being negligibly Zeeman-mixed with higher-J states. Of course, any optical pumping scheme also requires that transitions that decay to other rotational states are not accidentally co-resonant with the desired transition.

The primary challenge in extending ZS deceleration to YbOH molecules comes from the complex structure of its $\tilde{A}\,^2\Pi_{1/2}$ excited state. This state has an effective g-factor, $g_J = g_l'/3 \approx -0.25$, that is over an order of magnitude larger than that of CaOH [126, 131], due to mixing with nearby electronic states. Furthermore, the large Λ-type doubling in YbOH places the $|\tilde{A}\,^2\Pi_{1/2}, J' = 1/2, p' = +\rangle$ and $|\tilde{A}\,^2\Pi_{1/2}, J' = 3/2, p' = +\rangle$ levels of the $\tilde{A}\,^2\Pi_{1/2}$ state within about 0.1 cm^{-1} of one another. Thus,

the $\tilde{A}\,^2\Pi_{1/2}$ states of YbOH experiences both large, non-linear Zeeman shifts and significant state mixing among the $\tilde{A}\,^2\Pi_{1/2}$ rotational levels. The ZS deceleration scheme must be re-examined in light of these features, both of which may reduce the optical pumping efficiency between ground state spin manifolds. These features are likely not unique to YbOH but instead representative of many heavy-atom containing molecules, as the number of excited states near the cycling excited state tends to increase with mass.

Even in low fields, where the mixing among these rotational levels is not significant, care must be paid to avoid accidental resonances to lossy transitions through the $|\tilde{A}\,^2\Pi_{1/2}, J' = 3/2, p' = +\rangle$ states. In particular, at $\sim$ 1000 G, the field used in region D2 for our previous ZS deceleration of CaOH [126], a transition from the WFS manifold to the $|\tilde{A}\,^2\Pi_{1/2}, J' = 3/2, p' = +\rangle$ state is nearly degenerate with the D2 transition frequency. Driving such a transition produces near-unity loss to excited rotational states. This loss was observed prior to installing the compensation coils (see Appendix B) in D2. After installing the compensation coils, we no longer observed this loss as indicated in section 3.2.4. The construction of these coils will be covered in H. Sawaoka's thesis.

Regions S1, D2 (after compensation), and S2 operate at fields under 500 G. In this low-field regime, the 10% vibrational branching ratio from $\tilde{A}\,^2\Pi_{1/2}(000)$ to the $\tilde{X}\,^2\Sigma^+(100)$ limits the optical pumping efficiency [99]. Simulations show that below $\sim$ 1T, the population can still be almost entirely transferred between WFS and SFS manifolds using $\lesssim$ 4 photon scatters per molecule. Without vibrational repumping lasers, calculations show $\sim$ 75% efficiency in transferring SFS to WFS molecules with 4 scattered photons, with the vast majority of the remaining 25% of the population lost to $\tilde{X}(100)$. Less than 5% of the population remains in the SFS mani-

fold after passing through any of these regions. The major difference in efficiency in these stages when compared to CaOH is due to the larger vibrational branching to the $|\tilde{X}\,^2\Sigma^+, v_1 = 1\rangle$ manifold.

The situation differs qualitatively at magnetic fields above $\sim$ 1 T, i.e. in regions D1 and D3. In this regime, the Zeeman shift is much greater than the rotational energy spacing, leading to significant rotational mixing between the $|\tilde{A}\,^2\Pi_{1/2}, J' = 1/2, p' = +\rangle$ and $|\tilde{A}\,^2\Pi_{1/2}, J' = 3/2, p' = +\rangle$ manifolds. The lower state in the $|\tilde{A}\,^2\Pi_{1/2}, J' = 1/2, p' = +\rangle$ manifold retains dominant $J' = 1/2$ character, but the upper state in the manifold gains significant $J' = 3/2$ character. This rotational mixing induces a $\sim$ 10% decay to the $|\tilde{X}\,^2\Sigma^+, N'' = 3\rangle$ state. Additionally the large effective g-factor g_l' causes the states that correlate to $|\tilde{A}\,^2\Pi_{1/2}, J' = 1/2, p' = +\rangle$ at zero field to be split substantially. At 2.4 T, they are split by 5.6 GHz and transitions to both components must be driven to drive the entire ground-state WFS manifold toward the SFS manifold. This frequency splitting is bridged in the experiment by a high-frequency electro-optic modulator (EOM), but pumping through both excited states still requires $\sim$ 4 cycles to spin flip all possible ground-state population.

In a high-field regime, not only must we still cycle several photons to drive all possible molecules from WFS to SFS states, but also the loss per cycle is nearly double the low-field value due to the additional loss channel. At 2.4 T, $<$ 60% of the population can successfully transfer from the WFS to the SFS manifolds at all, due to the substantial rotational and vibrational loss. Calculations show that four scattered photons are sufficient to transfer $\sim$ 55% of the population, with only $\sim$ 5% remaining in the WFS manifold.

Combining the efficiencies for each individual region, and assuming sufficient transit time in all optical pumping regions (i.e. maximally allowed photon cycling), the

Table 3.1: Comparison of experimentally measured pumping efficiencies to the optimal values calculated from theory for different combinations of pumping light. The measurements approach the best efficiencies our scheme is capable of as described in Section 3.2.3.

Light on	Detected Pop. (%)	Optimum (Calc.) (%)
S1	100	100
S1 + D1	25(3)	20
S1 + D1 + D2	55(4)	66
Round Trip Pop.	30(5)	41

inefficiencies described in this section imply that $10 - 15\%$ of the population that enters the ZS slower can be successfully decelerated. In principle, this fraction could be significantly increased by recovering population lost to rovibrational dark states. Though the loss channels are dominated by only two rotational levels ($|\tilde{X}\,^2\Sigma^+, v_1 = 1, N'' = 1\rangle$ and $|\tilde{X}\,^2\Sigma^+, v_1 = 0, N'' = 3\rangle$), both of these rotational levels will split into separate SFS and WFS manifolds (each with multi-level substructure), making rotational repumping a complex task. We thus find that the complex Zeeman structure of the $\tilde{A}\,^2\Pi_{1/2}$ state in YbOH significantly impacts both the number of optical cycles necessary to spin-flip population in a high-field ZS decelerator and the amount of loss that those cycles induce.

While we have focused specifically on YbOH, some or all of the structural features that complicate ZS decelerator appear to be generic to many heavy molecules that have been proposed for next-generation precision measurements, including YbF [134, 135], BaF [136, 137], and BaOH [138, 139].

3.2.4 Deceleration of YbOH

Overcoming the complications described above, we successfully demonstrated ZS deceleration of YbOH. To characterize the overall efficiency associated with the scheme,

we first studied each optical pumping step. We compared the ratio of detected WFS signal in various pumping configurations, as shown in Table 3.1. For these measurements, the state preparation light S1 was always on. First, we turned on the high-field pumping region D1, which lead to depletion of the WFS population. Then we kept the D1 light on and added the low-field pumping region D2, reviving the population that was depleted by D1. The ratios we measured are similar to what calculations predict for optimum pumping efficiencies as described in 3.2.3. By combining similar measurements with D3, D4, and S2, we found that approximately $\sim$ 10% of the population successfully completed two full ZS cycles, in good agreement with the calculations.

After optimizing the optical pumping efficiency in each region, we detected individual velocity classes of molecules exiting the decelerator using Doppler-sensitive laser excitation. Figure 3.14 shows a representative laser-induced fluorescence signal for the velocity class at 18(3) m/s. Accounting for optical collection efficiency and quantum efficiency of our detector (a photomultiplier tube), we determined that $\sim$ 100 molecules per pulse in this single velocity class are decelerated. As expected from the slowing mechanism, the molecules arrived in the detection region earlier than an arrival time that would be expected for molecules that were produced in the beam source at this velocity. This early arrival necessarily means that the detected molecules originated at a higher velocity, providing further confirmation that the detected molecules were decelerated. The molecules detected at 18 m/s originate at velocities near 30 m/s, as expected from the known magnetic potential energies experienced by the molecules. Note that this 12 m/s decrement of velocity would have required $\sim$3,000 photons if radiative slowing were used, while the average molecule undergoing ZS deceleration scattered $\lesssim$ 10 photons. This $>$ 100$\times$ gain in efficiency

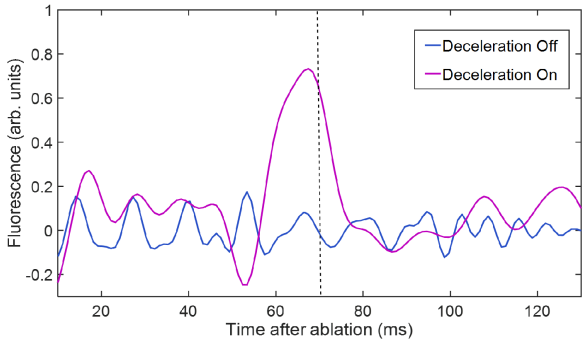

Figure 3.14: Demonstration of Zeeman-Sisyphus deceleration of YbOH molecules. Both traces are taken in Doppler-sensitive configuration looking at the 18(3) m/s velocity class. The blue trace was taken with only S1 light on, so no deceleration occurs. The purple trace was taken with the full ZS pumping scheme, and reveals decelerated population in this velocity class. The dashed line demonstrates the earliest time of arrival for molecules produced at this speed.

per optical photon scatter would be critically important for molecules that do not have high closed optical cycles.

3.2.5 Conclusion

In this chapter we describe the design and construction of a Zeeman-Sisyphus decelerator and its application to YbOH molecules.

For the decelerator itself, we discuss the relevant considerations around field strength, magnet type, magnet size, and cryogenic housing. While we did not wind the magnet coils ourselves, we designed the field profiles and coil forms to ensure compatibility with the molecular and optical pumping beams, minimize long-range field strengths, and ensure electrical and mechanical robustness. Though many of our final choices were made to suit our particular needs, we believe that the discussions cover the most relevant concerns for future ZS deceleration schemes more generally.

After these discussions, we move on to describe the ZS deceleration of YbOH molecules. We begin by outlining the nominal experimental setup, including production, optical

pumping transitions, and detection. This outline looks similar to the ZS deceleration of CaOH [65, 126]. However, there were several complications that made the realization of deceleration significantly more complex. To understand the complications, we then examined the Zeeman structure of YbOH and investigated the effects of this structure on the ZS scheme. With improvements to the pumping scheme and magnetic field strength, we finally realize deceleration of YbOH molecules. The deceleration observed represents the largest velocity change produced in a YbOH beam yet, and could be further improved with a lower beam source velocity (e.g. by lower cryogenic temperatures), more rovibrational rempumping, and/or adding a few more magnetic stages (conveniently at lower field). Modeling shows that closing the rotational and vibrational loss channels with additional frequencies would increase the number of molecules below 20 m/s by an order of magnitude. Laser-induced chemically enhanced production of YbOH[140] and an optimized initial beam velocity would increase the number further to $\geq 10^4$ decelerated molecules. With this improved decelerator performance, and typical trap capture efficiencies for polyatomic molecules [57], it is likely possible to capture $\gtrsim 100$ molecules in an optical dipole trap, a number that is sufficient to obtain an electron EDM sensitivity that surpasses the current limit of $d_e \lesssim 10^{-29}$ e cm [36].

These results provide insight into the deceleration dynamics of complex molecules. In particular, it is quite common for heavy species to have excited-state g-factors sufficiently large to produce Zeeman splittings comparable to Λ-doubling splitting at modest fields. Molecules in this class will likely require additional repumping lasers to avoid inefficiencies in Zeeman-Sisyphus deceleration schemes that involved high-field optical pumping. This class includes many molecules of broader interest, such as YbF [134, 135], BaF [136, 137], BaOH [138, 139], and WC [141–143]. Many other

experimentally relevant heavy species (e.g. $YbOCH_3$ [107], $YbCH_3$ [144], YbSH [145], $BaCH_3$[144], RaF [146], RaOH[147], HgF [148], HgOH [149]) require further examination of excited state structure to assess the feasibility of Zeeman-Sisyphus deceleration. In contrast, light species of general interest for precision measurements and/or quantum computation (such as MgF [150, 151], MgNC [152–154], $CaOCH_3$ [155, 156]) generally have small Λ-doubling and will not suffer from the observed Zeeman-induced rotational loss channels, even at higher magnetic field strengths.

To eliminate the observed problematic optical spin-flip transitions, one could replace the high-field optical pumping with microwave transitions. For essentially any molecule with a $^2\Sigma^+$ ground state, this would mean replacing the D1/D3 (see Figure 3.12) light with a microwave source to drive population from the WFS to the SFS manifold directly. For decelerators operating below 3 T, the required microwave tone is in a convenient technological range of $f \lesssim 80$ GHz. Optical pumping in the low field regions, where optical spin-flips are more efficient and do not lead to rotational loss, maintains the irreversability of the method. This modification would be species independent, as any $^2\Sigma^+$ ground state will have similar Zeeman tuning and could be decelerated similarly, opening the door to simultaneous Zeeman-microwave deceleration of multiple species.

Though the process of Zeeman-Sisyphus decelerating YbOH was significantly more complex than CaOH, the complications were in the end understood and overcome. With a tested understanding of both apparatus construction and how molecular structure affects the scheme, ZS deceleration should be seen as a viable option for future slowing of molecular beams. Indeed, the deceleration of YbOH shows that the method can be used to motionally control even very complex molecules, since the decelerated molecules scattered only 15 photons. There are significantly many more species capa-

ble of scattering $\mathcal{O}(10)$ photons than $\mathcal{O}(10,000)$! If future photon-efficient trapping techniques can be developed, ZS deceleration can play a vital role in the control of a much wider class of molecules than is currently accessible with contemporary technology. Even by itself, ZS deceleration could be utilized to significantly increase coherence time in beam experiments of molecules or even atoms not amenable to other techniques.

The low yellow

moon above the

Quiet lamplit house.

Jack Kerouac

4

Radiative Slowing and Magneto-Optical Trapping of SrOH

Though experimentation with novel slowing and trapping techniques is useful for pushing on the frontier of complex molecular control, it is undoubtedly a slow process. While Zeeman-Sisyphus deceleration of YbOH was now understood, there were still major open questions about the remaining steps necessary to use the molecule

in a precision measurement. In particular, while a bit of Doppler cooling could bring the ZS beam to a trappable velocity, the molecule could not (and still cannot) be put into a magneto-optical trap. Previous work had identified the first few vibrational repumping transitions, but only enough to cycle around a thousand photons. Furthermore, Yb molecules (including YbOH) were discovered to have generic intermediate electronic states that are long lived, difficult to repump, and capable of spoiling rotational closure. These issues prevent further use of YbOH without months-to-years of additional exploratory work in either 1) vibrational spectroscopy or 2) novel trapping techniques.

As such, the decision was made to pivot to SrOH as a target molecule. SrOH was chosen because it could both support either an EDM or UDM measurement ([46, 50]) and was plausibly close to well enough understood [46, 63, 64] to immediately begin full laser cooling. Radiative slowing and magneto-optical trapping are previously demonstrated techniques that have been applied to atomic, diatomic, and polyatomic systems isoelectronic to SrOH. As such, our effort could be entirely dedicated to understanding how this molecule differed from previous use cases to modify these techniques, instead of simultaneously developing them from scratch.

In this chapter, we review the laser cooling and trapping of SrOH. We begin with the theory of operation for both techniques, including key points of departure between polyatomic and diatomic molecules. Then we review the previous work done on SrOH to establish the existing information that made the current work possible: high-resolution rotational spectroscopy, 1D Sisyphus cooling, and high-resolution vibrational branching ratio measurements [46, 61, 63, 64, 157–166]. Having established the prior work on the molecule, we then explain how the full SrOH photon cycling scheme was developed. From there, we move on to the layout and results of the SrOH

radiative slowing demonstration. Then, we discuss a preliminary MOT of SrOH and the ongoing modifications to improve the stability of the experiment as well as increase the trapped number and lifetime. Finally, we discuss remaining steps between the existing experiment and a future Ramsey-style precision measurement in a conservative trap.

4.1 Theory of Radiative Slowing, and Magneto-Optical Trapping

Radiative slowing and magneto-optical trapping are both foundational techniques in atomic and molecular physics based strongly on using photon cycling as a source of momentum recoil. In particular, each scattered photon can remove momentum $p = h\nu/c$ on average opposite to the direction of absorption. Photon cycling allows repeated absorption from a single or few lasers which in turn, given sufficient scattering, allows large reduction of momentum along arbitrary axes. Radiative slowing makes use of this to decelerate a beam along its direction of motion. Adding a magnetic quadrupole potential allows the scattering force to also be made spatially dependent, giving rise to magneto-optical trapping. Despite the technical complexity required to accurately characterize these techniques in polyatomic systems, most of the qualitatively important features can be gleaned from simple models. From there, the subtleties involved in applying the techniques to real molecular systems can be more easily understood as perturbations on the underlying concepts. By and large, the most important addition for applying either method to molecules is maintaining sufficient optical closure. Analysis of each method can give an approximate figure for how closed the cycle must be, which in turn can lead to identifying and closing more vibrational channels as described in Chapter 2.

4.1.1 Radiative Slowing

We begin with a simple two-level system moving at a velocity $\vec{v}$ in the lab frame, with ground and excited states $|g\rangle$,$|e\rangle$ connected by a laser with wavevector $\vec{k}$ and Rabi frequency Ω. The laser is detuned from resonance by δ (defined as $\delta>0$ for red-detuned light), and the excited state has a spontaneous emission rate γ.

Knowing that the force applied on the molecules originates from photon recoils allow us to write $\vec{F} = \hbar\vec{k}\gamma_s$ where $\gamma_s = \frac{|\Omega|^2}{\gamma}\frac{\gamma^2}{\gamma^2+2|\Omega|^2+4\delta'^2}$ is the scattering rate of a two-level system; it is simply the net number of photon momenta absorbed per unit time. In this formula, $\delta' = \delta - \vec{v}\cdot\vec{k}/(2\pi)$ is the effective detuning. From this formula, it is easy to see three characteristics of the radiative force. First, the force is linearly dependent on the momentum of the photon in the limit of small detuning, as one would naively expect. Unfortunately, there are not many ways to tune this parameter in an experimental system, but it nevertheless affects the Doppler force between molecular systems depending on the wavelength of the transition being driven. Second, the force saturates at $F_{max} = \hbar k\gamma/2$ in the limit of large Rabi frequency, again expected from a simple understanding of the effect: in this regime, the molecule can be expected to spend about half of its time in the excited state, limiting the rate of a total cycle to half the spontaneous emission rate. In a multilevel system with n_g ground states and n_e excited states, the force saturates to $F_{max} = n_e/(n_e+n_g)\ \hbar k\gamma/2$, again as expected from a simple rate-equation model [167]. Lastly, for a given red-detuning and molecular speed, the force is largest when the two are counterpropagating. This matches an intuitive picture of how the method is actually decelerating the molecules, but it is nevertheless good to have explicitly come out of an equation. This is the simple picture of radiative slowing.

One may wonder why the emitted photon does not sometimes counteract the repeated absorption of the laser beam and reduce the net force. This actually does happen, but because the emission is in a random direction, the *average* force is just given by the aforementioned formula. Put another way, if we say a molecular absorbs N photons from a laser beam, only an RMS of $\sqrt{N}$ emitted photons will counteract the laser momentum assuming a true 3D random walk. Thus the total momentum change is $\delta p = Np_\gamma - \sqrt{N}p_\gamma \approx Np_\gamma$ for nearly all molecules in the limit of large N. At very low velocities, of course, the diffusive recoils become important too, but such situations are outside the scope of this thesis and can be reviewed elsewhere [167–169].

Up to this point, there is an obvious limitation. Given the above formulas only, one may notice that for $\delta' \gg \gamma$, the radiative force is greatly reduced. Indeed, for a beam resonant with nonmoving molecules and a Rabi frequency $\Omega \sim \gamma$, the force 10 linewidths away is already a factor of 20 below the maximum force. In the molecules we work with, this detuning corresponds to Doppler shifts of molecules <100 m/s, much slower than the average initial velocity of CBGB. The radiative force from a single-frequency laser is insufficient to decelerate a beam of molecules.

There are two commonly-encountered options to resolve this issue. "White-light" slowing involves adding a broad pseduo-continuum of sidebands to the slowing light [170, 171]. Then, even though the power of an individual sideband is low, there is always a sideband nearly resonant in the molecular frame during the entire trajectory, from the initial to final velocity. This spectrum produces a fast scattering rate, and therefore high force, over the complete interaction time. The other option is "chirped" slowing, where the slowing beam remains single-frequency, but the absolute frequency is quickly swept from a detuning resonant with molecules at the initial velocity to resonant at the final velocity [172–174]. The former option is usually technically eas-

ier to implement initially, but the latter anecdotally tends to lead to more captured molecules in a MOT or other trap. In either case, the key to utilizing the radiation pressure effectively lies in not relying on far-off-resonant scattering, which would be very slow and would require unreasonably (spatially and temporally) long experiments.

For most molecules that have been laser cooled, initial translational temperatures tend to be $\sim 8 - 10$ K and cycling transitions are in the 600 - 700 nm range. These numbers imply $\sim 10^4$ photon scatters are necessary to remove the full kinetic energy of a molecule. Higher precision simulations can determine photon budget more accurately, but 10^4 is a remarkable good ballpark figure for many species of interest both historically and at present, with species requiring from $5 \times 10^3 - 2.5 \times 10^4$ scatters to fully decelerate.

So far, we have essentially ignored any internal structure of the molecule by assuming a two-level system. However, SrOH (and CaOH, CaF, SrF, etc.) are *not* two-level systems. Indeed, they are type-II systems, meaning the optical cycle is done on a transition with an equal or greater number of ground states than excited states. Such a system has a lower fundamental maximum scattering rate than a Type-I system, as noted above. However, an excess of ground states also affects radiative forces more qualitatively. A single polarization of light will only drive a single ground eigenstate to a single excited eigenstate. It follows that for a single polarization of slowing light, some of the molecules in the ground state manifold will not get excited; they will not be subject to a radiation force. Furthermore, the molecules that *do* absorb light will, with some probability, decay to these dark states as well. A conceptually easy way to get rid of these dark states is to time average: rapid switching of the polarization will quickly remove population by changing which states are "dark" as a

function of time [110, 175–177]. This turns out to be experimentally simple to do as well (4.1.1). Managing these dark states is really the only conceptual deviation from a simple model of radiative slowing we encounter.

4.1.2 Magneto-Optical Trapping

A magneto-optical trap (MOT) uses radiation pressure with an additional magnetic potential to create a force that is both velocity and position dependent. To understand magneto-optical trapping we actually cannot begin with a two level system. The simplest model for a "type-I" trap (most atomic MOTs) requires a J $\rightarrow$ J+1 transition. Such a case does not occur in molecular MOTs, at least not any of those so far demonstrated, intrinsically because the rotational closure scheme (see Chapter 2) requires the opposite case, a J+1 $\rightarrow$ J variety "type-II" transition. There is much written about type-I MOTs (see, e.g. [168]), so we only focus on type-II here, because they are the relevant case for both our work on SrOH and any other molecular MOT (so far). Let us then continue with our toy model consisting of four ground states $|g_{-3/2}\rangle$, $|g_{-1/2}\rangle$, $|g_{+1/2}\rangle$ and $|g_{+3/2}\rangle$ and two excited states $|e_{-1/2}\rangle$ and $|e_{+1/2}\rangle$. The subscripts indicate an m_J projection of some angular momentum J.

The trap light consists, in the most common case, of three pairs of counterpropagating beams; one pair along each orthogonal axis. The polarizations of the counterpropagating pairs are circular and oppositely handed to each other. The detuning of these beams depends on the MOT scheme being used; in the "RF MOT" configuration, the beams are both red-detuned from the zero-field resonance transition frequency. Note that in this polarization configuration, with no magnetic field, there is no "trapping" force that keeps molecules in a fixed region of space. There is a "molasses" effect that does compress the velocity distribution, however, since molecules

moving radially outward at any angle will see light shifted towards resonance and preferentially absorb photons opposite the direction of motion. In such a molasses, and indeed later in a MOT configuration, there is an obvious issue with what has been described so far. There is a broken symmetry in the polarization/ground state structure: only one ground state has a transition dipole moment to each excited state for a given nonzero velocity. Remixing of the other ground states will happen due to stray fields and transitions driven by perpendicular beams, but these are not in general very fast mechanisms compared to the scattering rate in ambient conditions. This problem is similar to the dark states that appear in radiative slowing, and the solution again is time averaging: fast ("RF") switching of the polarization of each beam will allow the molecules that accumulate in the instantaneous dark state to quickly absorb more light after a switch. If this switch is around the same timescale as the scattering rate (∼1-10 MHz), the time spent in dark states is small. Switching polarization much faster or slower than a scattering time can lead to a reduction in efficiency [178]. Even with the dark states resolved, there is still no trapping force, and we are left with a fluffy Doppler molasses.

To get a trap, we add a magnetic quadrupole field with the poles aligned with the laser beam axes. Now, while there remains a velocity dependent force from the laser detunings, the ground state energies also depend on the position of a molecule in the trap due to the strength and direction of the $\mathcal{B}$ field. There are a lot of subtleties in understanding the trapping in the full 3D case, and it is not even clear if there is accurate intuition for all the details in this case. However, the 1D case is both tractable and offers useful qualitative descriptions of how the force depends on $\mathcal{B}$ field strength, laser detuning, and laser polarization that agree with more detailed 3D models. As such, we analyze a single axis of the full setup and ignore the light and field along the

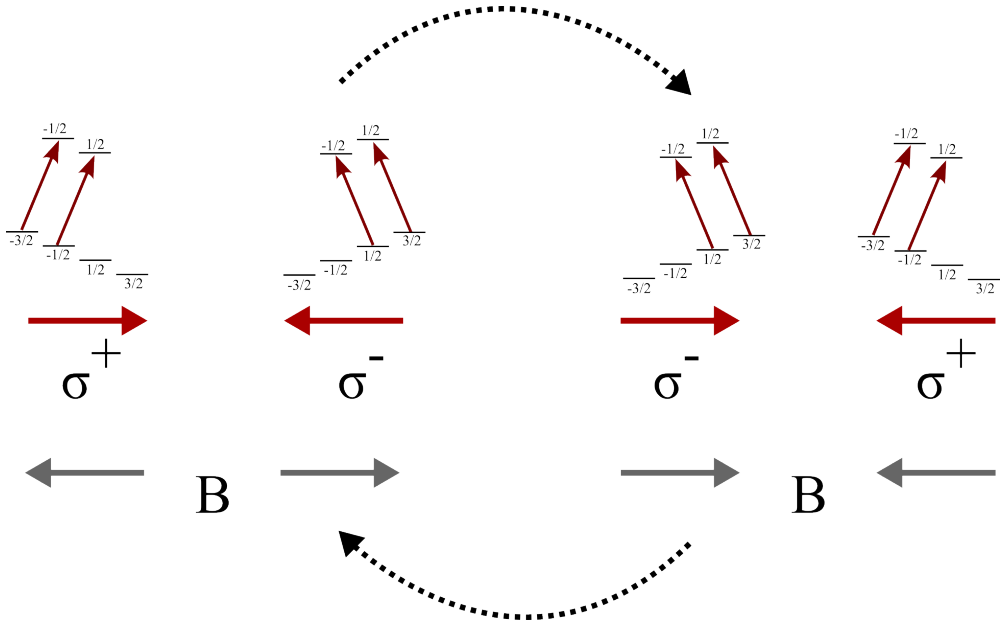

Figure 4.1: Schematic of one dimension of an RF magneto-optical trap showing m_J sublevels of a typical molecule of interest as long as the instantaneous polarizations and magnetic field orientation. In the initial configuration, on the left, the polarizations and magnetic field only allow fast emptying of some of the ground states. In order to maintain a radially-inward force, the direction of the magnetic field gradient and the polarizations of the two beams must be synchronously switched. If this switching is repeated on a similar timescale to the scattering rate, the time-averaged force will continue to be towards the center, maintaining a trap.

other axes. A schematic of this subsystem can be seen in Fig. 4.1.

On this axis, the Zeeman levels will shift in a way that the red-detuned light becomes closer to resonant with transitions out of one sign of magnetic sublevel on one side of the center. With a static field and switching polarizations of light, half the time, the light will also be the correct polarization to drive the near-resonant transitions. In these instances, molecules displaced from the center will preferentially absorb photons pushing them inwards from the laser beams. In the other polarization, the light will preferentially push the molecules on the opposite side of the center outward, producing zero net force at any given position. To resolve this, the direction

of $\mathcal{B}$ is reversed synchronized with the polarization. Then, one orientation of polarization and field looks as the trapping case discussed above: molecules in one Zeeman sublevel feel a net force towards the center of the field. When the polarization switches, the field direction does also, so instead of the beams pushing radially outward on the opposite edge of the trap, the light again pushes radially inward. As long as the switching is done slowly enough for sublevels to empty, this scheme produces what is desired: a time-averaged spatially dependent radiative force, always towards the center of the trap. This configuration also maintains some velocity-dependent component due to the red-detuning of the light. The effective detuning depends both on velocity ($\delta_v = -\vec{v} \cdot \vec{k}/(2\pi)$) and position ($\delta_x = g_{FB} m_F B(x) \langle e|\sigma_i|g\rangle$ where σ_i is the polarization of the beam in question).

We can also estimate the "capture velocity" of the MOT to estimate how slow we need to decelerate a beam to be able to trap. From the maximum scattering rate $\gamma/2$ and the size of the laser beam D:

$$1/2 m v_c^2 = F_{max} D = \hbar D k \gamma/2 \Rightarrow v_c = \sqrt{\hbar k \gamma D/m}. \tag{4.1}$$

Intuitively, larger MOT beams (at a fixed intensity!) and higher scattering rates are most conducive to the trapping faster molecules. This scattering rate is best approached when detuning of the MOT light matches the Zeeman shift on the edge of the trap. This simple model suggests capture is possible with $v_c \approx 10$m/s, and simulations usually agree to within a factor of two. Similarly as was done to estimate the photon budget necessary to radiatively slow the molecular beam, one can calculate the photon budget necessary to cool a molecule from the capture velocity to zero as ∼few thousand photon recoils. The temperature of a MOT is set by the balance of

cooling and momentum diffusion from photon emission. Naively, these considerations give $T_c = \hbar\gamma/(2k_b)$, where γ is the spontaneous emission rate of the excited state. Molecular RF MOTs tend to treat this as somewhat of a lower bound, and tend to be hotter due to only approximating these models. Indeed this is more or less true for all of these estimations. Nevertheless, while not necessarily numerically correct in the full 3D case, the dependence of quantities on parameters like spontaneous emission rate, detuning, field strength, and molecule mass remain qualitatively true, according to more sophisticated modelling [179, 180]. As such, these simple ideas often serve as starting points for scans of parameters in the experiment, often to good agreement.

A note on lifetime: there is no intrinsic relationship between capture velocity and MOT lifetime. However, there often is an emergent interconnection in systems with finite photon budgets, like molecules. In particular, too high intensity will lead to a very short trap lifetime because of loss to vibrational dark states. On the other hand, too low intensity will not capture many molecules since the radiative force is small. Experimentally, the MOT beam intensity is usually chosen to capture as many molecules as possible while still being able to cool them to near the base temperature. It remains true, however, that a sufficiently closed optical cycle could both trap more molecules and for a longer time. The theoretical maximum scattering rate in these situations is still lower than in type-I systems due to the additional ground states, but it is often difficult to fully optimize both parameters even to their type-II maximum.

4.2 Previously Existing Work on SrOH

Before delving in to the current SrOH experiment, it is useful to give an overview of the existing knowledge of the molecule before we began. This is a substantial col-

lection of research, and indeed enabled much of the other work through its existence. The convenience of this existing information cannot be overstated. The relative dearth of similar work on some of the molecules we will encounter in Chapter 5 poses some not insignificant barrier to their use. The complete lack of even basic spectroscopy on more exotic species is a substantial impediment to continued exploration.

It is a bit of a coincidence that there was extensive spectroscopic work on alkaline-earth monohydroxides for almost exactly the same reason they are useful for laser cooling: the highly polarized bond and diagonal Franck-Condon factors. The chemists cared about what these features could reveal about chemical bonding in radicals as a simple test case. We, of course, see these as tools that enable laser coolablity and sensitivity to BSM physics.

In any case, from the 1980s to the mid 2000s, there were many studies done on electronic, vibrational, and rotational spectroscopy of SrOH. These studies established the electronic structure of the molecule, measured vibrational energies, and assigned rotational features down to low N/J in some vibronic states. Prior to any laser cooling work on SrOH, the laser cooling rotational line was observed and well-characterized, and the ground and excited states were assigned at high resolution for many of the vibrational repumping transitions. Even for states that had not been identified at high resolution, there was sufficient spectroscopic data (rotational constants, vibrational anharmonic constants, etc.) to predict their positions within a few cm^{-1} which enabled relatively quick determination via later in-house spectroscopy (Appendix C). A overview of the previously existing data useful to our work can be found in Tab. 4.1.

This set of data would have been sufficiently convenient alone to approach further work on SrOH. Indeed, it is much more substantial than the set of previously-

Table 4.1: Tabulation of what spectroscopic data on SrOH existed prior to our experimental work and the sources that contain the information.

Information	Sources
$\tilde{X}$, $\tilde{A}$, $\tilde{B}$ electronic structure	[157, 158, 161, 163, 165]
$\tilde{X}$(000),(100),(010),(200),(02^{0}0),(02^{2}0) assignment	[157, 161, 163, 165]
$\tilde{A}$(000),(010),(100) assignment	[158, 163, 165]
$\tilde{B}$(000),(010),(100),(02^{0}0),(02^{2}0) assignment	[157, 161]
$\tilde{X}$(000),(010),(100),(02^{0}0),(02^{2}0),(200) rotational structure	[157–159, 161, 163–165]
$\tilde{A}$(000),(010),(100) rotational structure	[158, 163, 165]
$\tilde{B}$(000),(010),(100),(02^{0}0),(02^{2}0) rotational structure	[157, 161]
$\tilde{X}$, $\tilde{A}$, $\tilde{B}$ (000) Stark and Zeeman shifts	[160, 166]
$\tilde{X}$(000) hyperfine constants	[162]

measured data on YbOH before work on that molecule was undertaken. However, old spectroscopy was not even the sum of work on the molecule before our radiative slowing and MOT work began! Predecessors in the Doyle group had already experimented on the molecule before, due in large part to the spectroscopic base. A CBGB of the molecule had already been produced (which also measured its collisional cross-section with He buffer gas), photon cycling was demonstrated, and 1D Sisyphus cooling had been done [59–61, 63]. Application of a bichromatic force was also demonstrated [64]. This set of work did not provide additional knowledge of molecular structure per se, but it did take care of a stage of trial-and-error in production and provided nearly foolproof evidence of the molecule's ability to be experimentally laser cooled. Work of this quality and impact on laser-cooling cannot be expected of nearly any other species prior to large-scale experimentation, but was extremely convenient and was instrumental in ensuring a fast scaling-up of our projects.

4.3 Establishing a Closed Optical Cycle in SrOH

With a large existing dataset, the molecule was chosen for full radiative slowing and magneto-optical trapping. The major difficulty in applying these methods to a molecule is maintaining the optical cycle. Since these methods are reliant essentially only on photon recoils to slow and cool the sample, it is not surprising that a meager photon budget strongly affects how well laser slowing and magneto-optical trapping are applied.

In Chapter 2, we reviewed how vibrational closure is an unavoidable necessity in molecular laser cooling. In the earlier discussion in this chapter, we establish the need for such a cycle to be able to scatter $> 10^4$ photons to successfully radiatively slow and MOT a molecule. In this section, we describe how such a cycle was created for SrOH. First, we review measurements of the vibrational branching ratios that identified the relevant loss channels. Then, we identify transitions suitable for repumping these channels through a combination of theory and spectroscopy (both previously existing and new). We also discuss changes or additions that can increase the robustness of the optical cycle in the future. Throughout, we identify changes that may occur in heavier linear analogues like YbOH and RaOH.

4.3.1 Vibrational Branching Ratios of SrOH

To scatter 10^4 photons, the vibrational branching ratios (VBRs) need to be identified down to a few 10^{-5} probability*. Though calculations are rapidly improving, these branching ratios still must be experimentally measured to ensure all channels

*There needs to be $< 10^{-4}$ total vibrational branching left, so the largest individual loss channels below 10^{-4} will still combine to a relevant level.

Table 4.2: Calculated and experimental VBRs for decay from $\tilde{A}$,$\tilde{B}$(000) and $\tilde{A}$,$\tilde{B}$(100) from Ref. [46]. The assignment of $\tilde{X}(210)$ in the $\tilde{B}$ data is tentative, but not important to the work herein.

	A(000)		A(100)	
States	Calc.	Exp.	Calc.	Exp.
(000)	94.767	95.63(20)	6.30	5.15(28)
(010)	0.034	0.037(2)	-	-
(100)	4.933	4.14(20)	83.83	86.88(45)
(02^00)	0.012	0.008(1)	-	-
(02^20)	0.037	0.027(2)	-	-
(110)	0.002	0.006(3)	-	-
(200)	0.203	0.148(8)	9.14	7.44(37)
(12^20)	0.003	0.003(1)	-	-
(300)	0.008	0.006(1)	0.57	0.54(15)

	B(000)		B(100)	
States	Calc.	Exp.	Calc.	Exp.
(000)	96.787	97.116(11)	3.29	1.73(15)
(010)	0.360	0.209(11)	-	-
(100)	2.636	2.32(11)	91.05	93.57(26)
(02^00)	0.037	0.125(6)	-	-
(110)	0.010	0.039(2)	0.34	0.20(5)
(03^10)	0.013	0.013(1)	-	-
(200)	0.078	0.077(4)	4.95	4.30(21)
(12^00)	0.008	0.015(2)	-	-
(210)	< 0.001	0.006(2)	-	-
(13^10)	0.001	0.010(1)	-	-
(300)	0.002	0.020(1)	0.22	0.20(6)
(22^00)	0.001	< 0.001	-	-
(05^10)	0.063	0.047(2)	-	-
(15^10)	0.003	< 0.003	-	-

are found. To this end, Lasner *et al.* [46] conducted such measurements in a modified CBGB source (similar to the apparatus described in Chapter 5). The experimental details are withheld here because they are reviewed in Ref. [46] and later in Chapter 5. These early measurements were accompanied by *ab initio* calculations by Lan Cheng, the results of which are also presented in this section, to document the rapidly improving state of these calculations. Additionally, later measurements of these VBRs were done during radiative slowing work which agree well with the original measurements in most cases.

The branching ratios from the lowest and first excited stretch states in the $\tilde{A}\,^2\Pi_{1/2}$ and $\tilde{B}\,^2\Sigma$ manifolds can be found in Table 4.2. Measurements for the first vibrationally excited states were measured to make sure the states were diagonal enough to use as repumping excited states; the ground vibronic state tends to have the most controlled branching in all laser cooled molecules so far.

From the data, the choice between electronic manifolds for the main cycling tran-

sition is clear: the $\tilde{A}\,^2\Pi_{1/2}$ (000) state only has 8 populated vibronic levels at the relevant level, whereas the $\tilde{B}\,^2\Sigma$ has 11. While theoretically the number of channels has no impact on the efficacy of laser cooling if they are all closed, each vibrational leakage requires at least one laser to repump. Every additional populated vibrational state thus increases the cost and experimental complexity significantly. The $\tilde{B}\,^2\Sigma$ state is still useful in repumping pathways, as the more exotic vibrational decays from it occur with low enough probability that they will not enter a scheme that only rarely populates the state. The wavelengths for repumping through the $\tilde{B}$ state are also experimentally more convenient than corresponding transitions through the $\tilde{A}$ state.

With electronic state chosen, understanding the decays from $\tilde{A}\,^2\Pi_{1/2}$ (000) is important to not only choose an adequate repumping pathway but also to understand how polyatomic laser cooling differs from diatomics. The large decays to (100), (200), and (300) are exactly analogous to the M-F stretch in CaF, SrF, YbF, etc. Their relative strengths are similar to, though typically larger than, the branching in their diatomic analogues. These decays arise predominantly from differences in the bond length, and are a good measure of how similar the ground and excited electronic potentials are.

The other decay channels have no analogues in diatomic species. The branching to $\tilde{A}\,^2\Pi_{1/2}$ to $\tilde{X}(01^10)$ is the example *par excellence* of qualitatively novel interactions. These channels are enabled by so-called Renner-Teller (RT) interactions, as discussed in Chapter 2. Two matrix elements appear due to terms the RT Hamiltonian. One is the direct first order linear vibronic coupling to $\tilde{B}(01^10)$,

$$\frac{|\langle\tilde{B}(010)|H_{RT}|\tilde{A}(000)\rangle|^2}{(\Delta E_{AB}-\omega_2)^2} \approx \frac{g_K}{\omega_2(1-\omega_2/\Delta E_{AB})^2}, \tag{4.2}$$

where g_K is a measured constant with units of energy related to the V_{11} parameter (see Chapter 2), ΔE_{AB} is the energy between electronic manifolds, and ω_2 is the vibrational frequency of the $\tilde{A}$ bending mode. The second RT matrix element comes from a second order interaction between $\tilde{A}(000)$ and $\tilde{A}(01^10)$ mediated by a combination of RT coupling and cross-term SO coupling to the $\tilde{B}(010)$ and (000) states:

$$\begin{aligned}
&|\langle\tilde{A}(010)|H'|\tilde{A}(000)\rangle|^2 \\
&\approx 2\left|\frac{\langle\tilde{A}(010)|H_{SO}|\tilde{B}(010)\rangle\langle\tilde{B}(010)|H_{RT}|\tilde{A}(000)\rangle + \langle\tilde{A}(000)|H_{SO}|\tilde{B}(000)\rangle\langle\tilde{B}(000)|H_{RT}|\tilde{A}(010)\rangle}{\omega_2\Delta E_{AB}}\right|^2 \\
&\approx \frac{4g_K A_{SO}^2}{\omega_2^3},
\end{aligned} \tag{4.3}$$

where A_{SO} is the spin-orbit constant (see Chapter 2). In the middle term of the equation, the factor of two accounts for the two vibronic components of $\tilde{A}(010)$. In SrOH, $\Delta E_{AB} \approx 1703$ cm^{-1}, $\omega_2 = 388.5$ cm^{-1}, $g_K = 0.196$ cm^{-1} and $A_{SO} = 263.7$ cm^{-1} [163]. These numbers give a first order overlap of 8.4×10^{-4} and a second order overlap of 9.3×10^{-4}. Weighting the contributions appropriately shows the total decay is dominated by the direct vibronic coupling, as in CaOH and calculational work [94, 105]. The ratio is in large part determined by the large SO coupling that splits the two interacting $\tilde{A}$ states in the second-order interaction, and so this trend is expected to remain qualitatively true in heavier molecules, though the same calculations do show larger contribution in YbOH than SrOH [105]. It is not clear if mechanism of RT mixing affects VBR convergence more generally, but it is clear that RT mixing is relevant in similar molecules and generically induces decays above the 10^{-4} level to $\tilde{X}(010)$.

Despite only differing by ℓ, the two decay channels from $\tilde{A}\,^2\Pi_{1/2}$ (000) to

(02^00) and (02^20) (and similarly (12^00) and (12^20)) are enabled by completely separate mechanisms. Decay to (02^20) is forbidden in the BO approximation by the $\Delta\ell = 0$ vibrational symmetry selection rule. It is made allowed by the quadrupolar Renner-Teller vibronic mixing in the $\tilde{A}\,^2\Pi_{1/2}$ manifold, which directly mixes $\tilde{A}\,^2\Pi_{1/2}$ (000) and $\tilde{A}\,^2\Pi_{1/2}$ (02^20):

$$|\langle\tilde{A}(02^20)|H_{RT}|\tilde{A}(000)\rangle|^2 \approx \frac{(\epsilon\omega_2/\sqrt{2})^2}{(\Delta E_0 - 4g_{22})^2}, \tag{4.4}$$

where ϵ is the "Renner parameter" related to the V_{22} RT coupling constant (see Chapter 2), ΔE_0 is the difference in vibrational origin energies, and g_{22} characterizes the ℓ-dependent anharmonicity. In SrOH, $\epsilon\omega_2 = -30.7$ cm^{-1} and $g_{22} = 7.5646$ cm^{-1}, both close to the values of CaOH [94, 161, 181]. The similar values of $\varepsilon\omega_2$ in SrOH and CaOH (-36.3 cm^{-1} in CaOH) are consistent with decays to the corresponding ground state occurring at about the same probability in the two molecules [163, 182]. This interaction, suppressed by a $\Delta v_1 = 1$ factor, is also responsible for the decay to $\tilde{X}(12^20)$.

On the other hand, $\tilde{X}(02^00)$ is the same vibrational symmetry as $\tilde{A}(000)$, and so the decay is not symmetry forbidden, but still nominally suppressed because $\Delta v_2 = 2$. This decay is enhanced above a naive prediction likely by a Fermi resonance (see Chapter 2) interaction with the $\tilde{X}(100)$ state. A matrix element for the mixing can be found in Ref. [94], but the relatively weaker decay to $\tilde{X}(02^00)$ compared to CaOH is simply explained by the significantly larger energy spacing between the Fermi-interacting states. A similar Fermi resonance is responsible for a decay to $\tilde{X}(12^00)$ state, which is bounded to be smaller than

in CaOH [46, 105].

These perturbative effects are expected to be generic in heavier analogs to SrOH. The magnitude of the RT-induced mixings can be expected to be similar in size to as in SrOH thanks to similar electronic spacings in other molecules (unless the structure is heavily perturbed), but the decays enabled by Fermi resonance are not easily predictable without vibrational spectroscopy. Of course, decays to the stretching mode will also be generic in heavier M-OH molecules, though again strengths will need to be determined from measurements (or theory) of bond length differences. Most of the additional decay channels from the $\tilde{B}\,^2\Sigma$ state in SrOH seen in Tab. 4.2 are due to bond length difference, characteristically to higher excitations of stretching modes. Resonances with $\tilde{A}\,^2\Pi_{1/2}$ excited vibrational levels (e.g. $\tilde{A}(05^10)$) also contribute new channels. These additional perturbations are also expected in heavier polyatomic molecules' higher electronic states, due to the larger density of states even at the vibronic origin. Indeed, the $\tilde{B}(200)$ state was not found at all in SrOH, indicating perturbations that are not fully understand even in the relatively low excited vibrational states of this molecule. For this reason, if technically feasible, optical cycling on the lowest excited electronic state seems to be the safest route to minimizing excess perturbative decays. Such a choice comes at the cost of lower scattering rate and redder scattered photons, but may be the only option for heavier and/or more structurally complex molecules.

4.3.2 Constructing an Optical Cycle

Once the vibrational decay channels are known to the desired precision, it is possible to design an optical cycling scheme. Though of course recovering population is paramount, a good scheme for laser cooling will also 1) maintain a high scattering rate, 2) quickly return population to the *main* cycling transition, and 3) operate using strong(-ish) transitions. These three considerations concentrate the time a molecule spends in the optical cycle to the most diagonal transition, which in turn allows minimization of power (and therefore cost) of repumping lasers. Identifying transitions that meet these goals is nontrivial, and in several cases requires explicit understanding of the perturbations discussed above. Since SrOH was relatively well studied in the past, most of the excited states had been previously characterized in literature. Many had sufficiently assigned rovibrational levels to determine repumping transition frequencies to 100 MHz precision. In a few cases, higher rotational states in the relevant vibronic manifold had been studied but not at sufficiently low J. For two vibronic states of interest, nothing had been documented at all. Spectroscopic identification of the laser cooling rotational lines in these last cases is discussed in Appendix C.

The main cycling transition ("main line") was easy to choose based on the discussion in the previous section: only $\tilde{X}(000)$–$\tilde{A}(000)$ is vibrationally diagonal enough to cycle many times without populating an excessive number of vibrational states in the $\tilde{X}$ manifold. The problem of constructing a cycle is then somewhat simplified into the issue of returning population quickly to the $\tilde{X}(000)$ state, in particular. We discuss the vibrational repumping transitions in

approximate order of importance; how quickly they enter the optical cycle.

The $\tilde{X}(100)$ state is populated after only around 20 photon scatters. As such, it can be expected to be populated $>$ 500 times during a 10^4 photon cycle. To maintain a high scattering rate, it must be repumped very efficiently. As a baseline, if population is emptied out of $\tilde{X}(100)$ at 1/20th of the main line scattering rate, the overall scattering rate would be reduced by a factor of 1.5. Ideally, the first repumper does not limit the scattering rate even this much. Luckily, the $\tilde{X}(100)$ state connects strongly to all the states in Tab. 4.2. Repumping through $\tilde{B}(000)$ was chosen as the best option, as it returns the population back to $\tilde{X}(000)$ in a single photon scatter, has a strong linestrength ($\sim$few percent of main line), and is at a convenient wavelength for high-powered sum-frequency generation (SFG) laser systems. Note that repumping through $\tilde{A}(000)$, even with high power, would still cut the scattering rate by $\sim$ 2 because doing so doubles the number of ground states connected to the same excited state.

$\tilde{X}(200)$ is similarly repumped through $\tilde{B}(100)$. Only populated every 100 photons, the scattering rate requirement is much less stringent. The transition to $\tilde{B}(100)$ is still quite strong, which enables the use of less power on this laser. This population does take an extra photon scatter through $\tilde{B}(000)$ to return to $\tilde{X}(000)$, but that transition is already driven strongly with a fast scattering rate.

According to our later measurements, $\tilde{X}(010)$ is the next most populated vibrational level (similar to $\tilde{X}(02^20)$). Modes with $\ell > 0$ are tricky because of the parity doublets: all rotational levels have sublevels with both parities. As

such, our nominal rotational closure scheme is somewhat spoiled since both N" = 1 and N" = 2 will be populated. These two repumpers are slightly too widely spaced ($\Delta E \approx 4B = 40$ GHz) for a typical EOM to modulate. We originally tried producing them by double-seeding an SFG system, which would allow repumping the two rovibrational states through a single excited state. Difficulties with beam recombination of the similar wavelengths prevented us from delivering enough power to the experiment to saturate either line. In the current scheme, we repump the N" = 1 level through $\tilde{B}(000)$, as it is more populated and there is no intrinsically stronger transition that creates a quick path back to $\tilde{X}(000)$. The N" = 2 level is repumped through the $\kappa\tilde{A}(010)$ state, which decays often enough to $\tilde{X}(010)$ N" = 1. This scheme adds additional pressure on the $\tilde{X}(010)$ N" = 1 repumper, since the $\tilde{X}(010)$ state is now populated more frequently, but not so much that it is intractable.

$\tilde{X}(02^20)$ is difficult to repump in SrOH. The decay is only enabled by small perturbations, implying intrinsically weak transitions. Yet, it is a frequent enough decay, being reached every $\sim$ 1500 photons, to require several kHz scattering rate. Driving the population through to a (010) excited state is not sufficient, as the transition is weak due to the $\Delta\ell = 1$ selection rule, compounded by the fact that the molecules would still later need to be pumped through the fairly weak $\tilde{X}(010)$ – $\tilde{B}(000)$ transition before returning to the main line. Initially, we tried using a transition through $\tilde{A}(100)$. This transition was initially chosen because it is analogous to the line CaOH uses in their optical cycle. However, this turned out to be possible only because of an excited state Fermi resonance

between $\tilde{A}(100)$ and $\tilde{A}(02^20)$ in CaOH. Calcuations indicated that similar power to the main line should repump the state with similar efficiency as in CaOH, but later scattering rate measurements show that the SrOH transition was too weak to drive without limiting the overall scattering rate significantly. This discrepancy is consistent with only an order unity miscalcuation in branching, and thus not indicative of a physical misunderstanding. Nevertheless, the transition through $\tilde{A}(100)$ proved sufficient to demonstrate radiative slowing of SrOH with >1.5W of laser power, though was later replaced for the MOT work. At the time of this writing, we repump the $\tilde{X}(02^20)$ through $\tilde{A}(02^00)$. This transition is substantially stronger than other options due to RT mixing that gives it some (02^20) character (see Chapter 2). This transition does dump population into $\tilde{X}(02^00)$, a nominally later repumped state, but the transition out of this state turns out to be sufficiently strong to support the extra population burden.

$\tilde{X}(02^00)$ suffers some of the same problems as its $\ell-$rich sibling, but its lack of angular momentum makes it intrinsically easier to couple to non-bending modes. It is both convenient technically and possible to strongly drive the transition to $\tilde{B}(000)$. Since the $\tilde{X}(02^20)$ population is dumped into this state as well, more power is required on this repumper than with an alternative pumping scheme, but still much less than the main line and $\tilde{X}(100)$ repumper thanks to its relatively rare occurrence in the cycle.

The remaining occupied states, $\tilde{X}(300)$ and $\tilde{X}(11^10)$, are the lowest likelihood states to be occupied during the cycle. Each is only reached a few times in a cycle of 10^4 scatters. $\tilde{X}(300)$, another stretch mode, we repump through

$\tilde{A}(200)$. After spectroscopy to find the excited state state (see Appendix C), we measured the VBRs of it to low resolution, and found that it had a few times stronger $\Delta v_1 = 1$ decays than the $\tilde{A}(000)$,(100) states. Thus not only is the $\tilde{X}(300)$–$\tilde{A}(200)$ repumper not require a high scattering rate due to its late appearance in the cycle, but it also benefits from a larger transition dipole moment than its stretch-repump counterparts. Indeed, we later find that the transition is driven sufficiently fast with $\sim 100\mu W$. The $\tilde{X}(11^10)$ vibrational state has both N" = 1 and N" = 2 populated. Since these states are so late in the cycle, they only require modest scattering rates. The N" = 1 state is repumped through $\tilde{B}(100)$, akin to the N"=1 $\tilde{X}(010)$ pathway. N"= 2 is driven through $\tilde{B}(010)$, which is a strong transition and only marginally increases the population in $\tilde{X}(010)$. These transitions are strong enough to easily repump the population without significantly decreasing the total cycle scattering rate.

Though not part of our experimental cycle at the moment, the last remaining reasonable states to consider adding are $\tilde{X}(12^00)$ and $\tilde{X}(12^20)$. Investigations are underway to identify suitable transitions to repump both. As they are now both a stretch and two bends away from the ground state, transitions to excited states "close" to the fundamental are all intrinsically weak. The $\tilde{X}(12^00)$ can likely be driven to an excited (02^00) state with sufficient strength. The comparable transition out of $\tilde{X}(12^20)$ through $\tilde{B}(02^20)$ would break rotational closure since $J'' = 3/2$ is the lowest rotational state in the excited manifold. Driving through $\tilde{A}(02^20)$ would add load to an already burdened $\tilde{X}(02^20)$ repumper, which may or may not be possible for it to accommodate. For either ground

state, it remains an open question as to which transition will be used in the future.

The initial and current photon cycling schemes for SrOH can be seen in Fig. 4.2. Effective VBFs that treat all excited states as a single manifold were calculated using the known VBFs and the cycling scheme, and can be found in Table 4.3. These branching fractions, including rotational branching in the bending modes, allow calculation of the number of photons it takes to enter a given level, which roughly corresponds to a photon budget for cycle without repumping a given state. Estimates of these numbers for the next vibrational states in the cycle are also included.

State	Effective VBF	Scatters to Enter	T_{in} (ms)
(000)	0.955	-	-
(100)	0.042	24	1.2×10^{-2}
(200)	1.5×10^{-3}	650	0.325
(010) N = 1	3.6×10^{-4}	2800	1.4
(02^00)	2.3×10^{-4}	4300	2.2
(02^20)	1.6×10^{-4}	6500	3.3
(010) N = 2	8.0×10^{-5}	12600	6.3
(300)	7.0×10^{-5}	14200	7.1
(110) N = 1	6.3×10^{-5}	15800	7.9
(120) (both $\ell = 0, 2$)	3.5×10^{-5}	28500(?)	14.3
(05^1) (both N = 1,2)	2.1×10^{-5}	50000(?)	25

Table 4.3: Effective branching fractions for states in the optical cycles in Fig. 4.2, where the VBFs out of specific excited states are weighted by the number of scatters through them using data from Tab. 4.2. The measurement uncertainty of the VBFs is near the level of the next two states, and hence the numbers are speculative for the (120) and (05^10) states. The T_in number is the time it takes to enter the state assuming a 2 MHz scattering rate. These numbers are used to determine an appropriate scattering rate later in Tab. 4.4.

Analogs of the repumping transitions are likely useful in laser cooling other alkaline-earth(-like) analogs to SrOH, as they have been chosen on fairly gen-

eral considerations of molecular structure. Some, such as those through excited bending modes, may even be stronger in heavier species since spin-orbit, and therefore $\Lambda-$doubling, will increase the direct vibronic type RT mixing and add transition strength [163]. This is in contrast to some transitions in the CaOH scheme that are only useful due to specific resonances in the molecule. While such resonances are difficult to predict, they should be considered for their utility in cycling schemes if they occur.

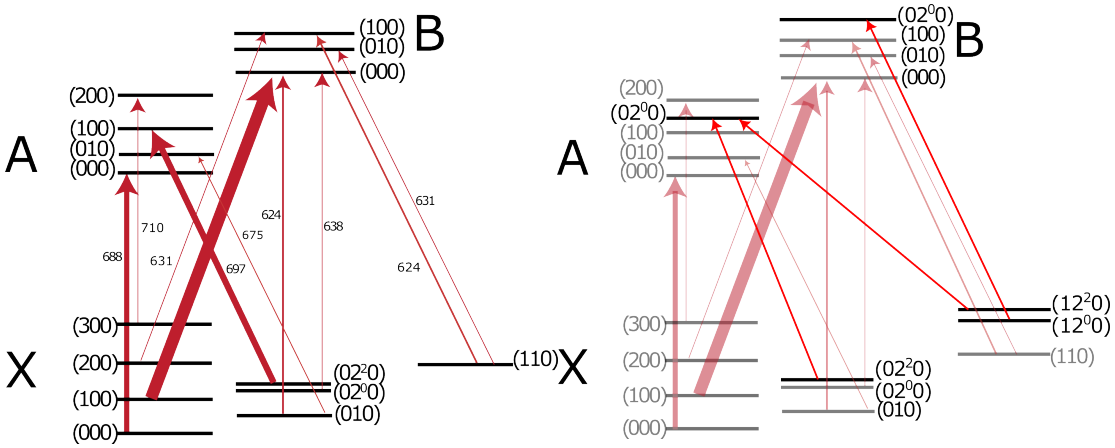

Figure 4.2: The two photon cycling schemes used in this work, with transitions that did not change muted in color in the latter diagram to view the changes more easily. The left scheme was used for radiative slowing, which was capable of producing results but suffered from a limited scattering rate due to the weak $\tilde{X}(02^20)$ repumper. This was replaced in the MOT work with a much stronger transition through $\tilde{A}(02^00)$. The scheme on the right also includes soon-to-be-added repumpers for states not necessary to repump in the original slowing and MOT work.

4.4 Apparatus and Laser Systems

The most difficult part of radiatively slowing a molecule is fully realizing the photon budget of the complex optical cycle. In this section, we outline the experimental implementation of laser slowing on SrOH. We briefly describe the

cryogenic buffer gas beam source and beamline construction, and provide detailed exposition of the laser systems and optics used to produce the slowing light.

4.4.1 Apparatus

Molecules are produced in a two-stage 1.7" bore cryogenic buffer gas cell by ablation of a strontium metal target in the presence of water and helium. The water is introduced at a rate of 0.2 sccm via a 280 K hot fill line directed at the target. The helium enters via a 4 K fill line in the back of the cell at ∼3-10 sccm to maintain an ambient density of $10^{14}/\text{cm}^3$. At this density, the buffer gas both quickly thermalizes the molecules after ablation and entrains them in a beam that exits the first stage via a 7 mm aperture. The molecules pass through a 2 mm gap into the 20 mm long second cell, where a final few thermalizing collisions reduce the forward velocity of the beam to ∼100-130 m/s. They exit the second cell via a 9 mm aperture to the rest of the experiment. There is no mesh on the front to maximize molecule extraction, but there is 30% closed mesh on the top and bottom of the second cell. The cell, with labelled features, can be seen in Fig. 4.3. We note that almost all of these parameters of the CBGB source were chosen to optimize the combination of flux and forward velocity. They should be tuned for new sources as appropriate.

After leaving the second cell, the molecules traverse ∼15 cm further out of the beam box and then down a ∼1.5 m beamline, where they will interact with counterpropagating slowing light. The beamline consists of three sections. The

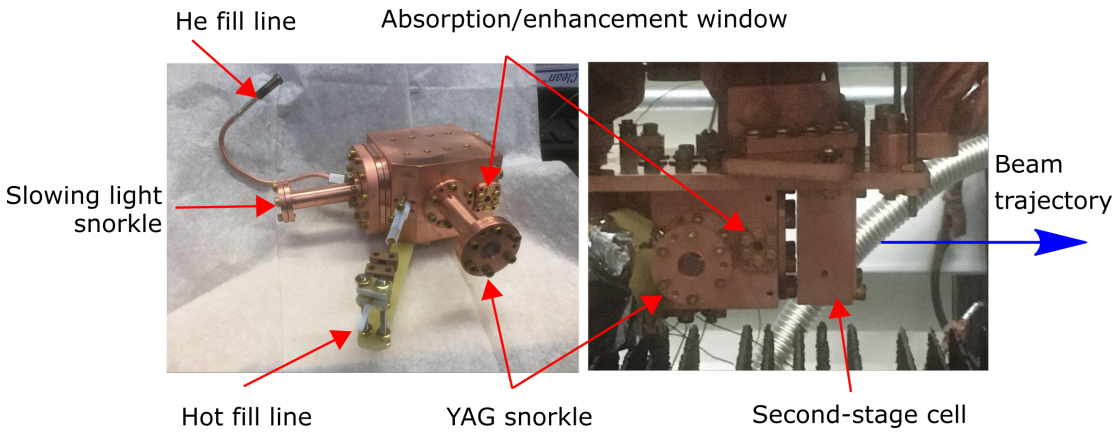

Figure 4.3: Picture of the cryogenic buffer gas beam cell. On the left is an assembled, but not mounted cell on which you can see several key components. On the right, the cell is mounted in the beam box, in the orientation we use experimentally.

first is a $6'' \times 6'' \times 12.5''$ aluminum chamber, the "transverse cooling" region. It is so named because of the long windows along the length, which are capable of supporting a transverse cooling setup in the future. There is a Uniblitz VS14 in-vaccum shutter at the end of this chamber, which blocks excess helium buffer gas from making it to the rest of the beamline. An 80 L/s Pfeiffer turbo maintains vaccuum in this region. The next region, the "intermediate region," is 50 cm long and constructed of CF 6" nipples, with several tees and crosses along the length. This region is differentially pumped by a 300 L/s Pfeiffer turbo on one of the offshoots. Two pairs of viewports along the length enable transverse optical pumping along this section, which is used for spectroscopy and/or signal monitoring. Finally, the molecules enter the detection chamber (soon, "MOT chamber"), a Kimball 12" spherical square chamber. This chamber is also differentially pumped by a 700 L/s Pfeiffer turbo on a 10" tee off the bottom of the chamber. Molecules can be detected via fluorescence imaging in either a

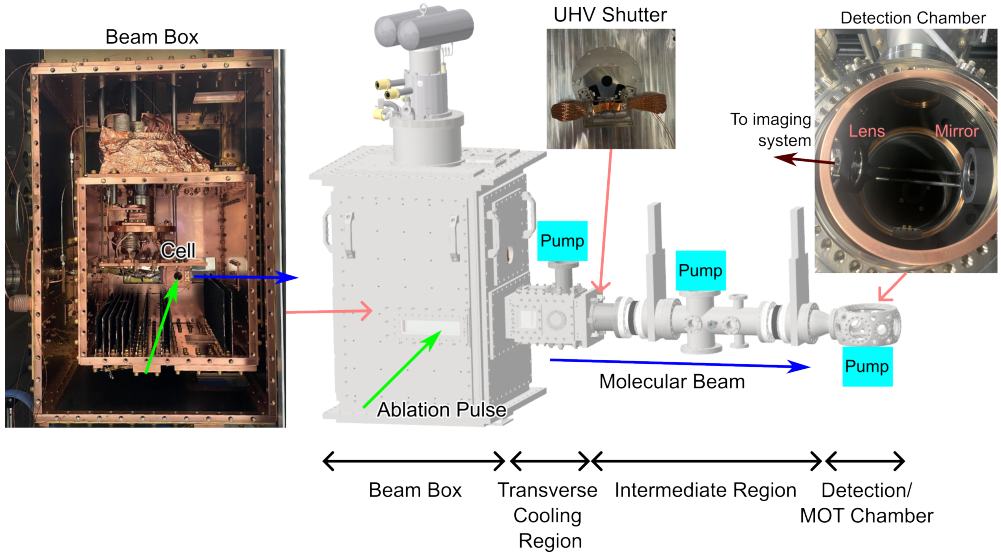

Figure 4.4: Schematic of a CAD file of the complete beamline, with regions labelled as discussed in text. Positions of turbo pumps are noted with cyan boxes. Photographs of the inside of the beam box, UHV shutter mounted at the end of the transverse cooling region, and detection chamber are also included.

transverse or Doppler-sensitive configuration. The transverse detection beam is sent vertically through windows on the top and bottom of the chamber, and the velocity-sensitive detection beam is sent through windows at 45 degrees to the molecular beam. A 2" lens and retroreflecting mirror were mounted symmetrically around the molecule beam axis to collimate the emitted fluorescence towards an imaging stack. A schematic of the assembled beamline and pictures of some of these components can be seen in 4.4.

The imaging stack for slowing consisted of spectral bandpass filters, a focusing lens, and an imaging device. For the slowing work, photons were collected on a R7600U-200 PMT, but later work on the MOT would use an Andor iXon Ultra DU-897U camera. The PMT produces $\sim$100 μA pulses from photons,

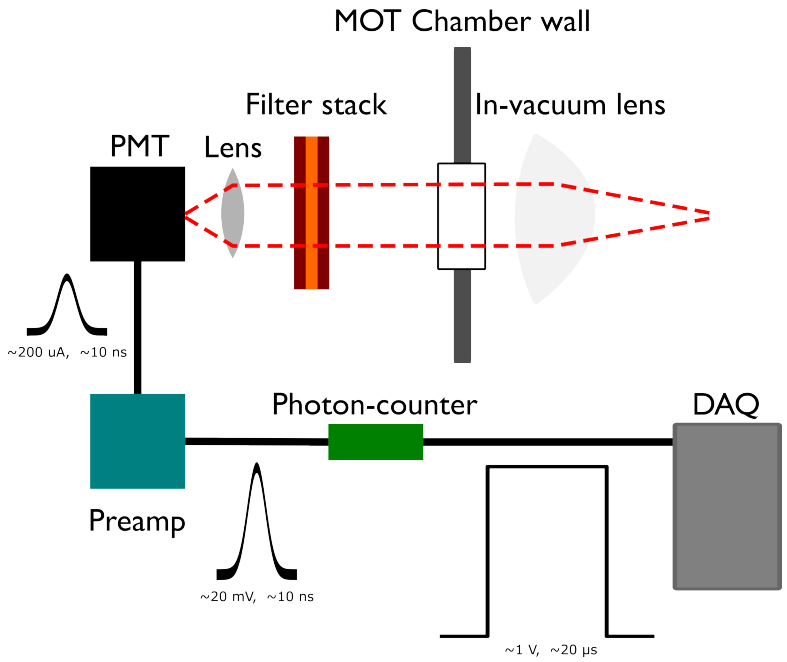

Figure 4.5: Schematic showing the image acquisition pathway used for the radiative slowing work. An in-vacuum lens collimates molecular fluorescence out of the chamber, through a filter stack to block background light, and though a final lens that focuses on the PMT. Photons incident on the PMT produce $\sim$ 1 mV, $\sim$ 10 ns electrical pulses which are amplified by a factor of 50 in a fast preamp. The amplified pulses are then counted in 20 μs time bins on a photon counting board, which outputs TTL pulses with heights proportional to the number of incident photon counts that are subsequently collected by a DAQ system.

which are amplified by an SRS SR445A 350 MHz preamp to $\sim$ $1 - 10$ mV pulses. A photon-counting board converts these fast pulses to TTL pulses in larger timebins (200 μs) that are easily read in by our DAQ. A schematic of this sequence can be found in Fig. 4.5.

4.4.2 Laser Systems

Unfortunately, SrOH is not a molecule with easy-to-generate optical transitions. All transitions through the $\tilde{A}$ state are 670 nm or above, for which there are no

("cheap") high-power diode laser sources available. Repumpers through the $\tilde{B}$ state are between 610–630 nm, over which region there are slightly more options for light generation (e.g. Rhodamine 610 and 640 dyes, some low power diodes). Nevertheless, for the highest-power transitions, there is still a dearth of affordable options for hundreds of mW to W of power.

The caveat to this difficulty is that all of our wavelengths *are* relatively convenient for sum-frequency generation (SFG). All transitions used in the experiment can be generated by readily available ∼2000 nm (Thulium) or 1550 nm (Erbium) + 1040-1080 nm (Ytterbium) high power fiber amplifiers. The downside of exclusively using such systems is financial, as fiber amplifiers are still significantly more expensive than diode lasers. Nevertheless, there are few other options capable of delivering sufficient power. To minimize cost, we only purchase two full SFGs systems, and purchase the amplifiers and crystals separately for the other systems. To maximize amplifier utility, some amplifiers are double-seeded, and the light is passed consecutively through multiple SFG crystals (i.e. "daisy-chained"), when transitions don't require utilization of the full amplifier output for a single frequency. Eight transitions are covered by either purchased or assembled SFGs. The remaining two transitions in the slowing optical cycle are filled with low power ECDLs or are temporarily pumped by a Ti:Sapph (while ECDLs are ordered/built). Identification of how each transition light is generated follow, with SFG construction details found in supplemental material of the in-process publication of this work. Powers noted in these discussions are at the source laser.

The two high-powered transitions through the $\tilde{A}$ state in our slowing cycling scheme are the main line ($\tilde{X}(000)$–$\tilde{A}(000)$) and the $\tilde{X}(02^20)$ repumper ($\tilde{X}(02^20)$–$\tilde{A}(100)$). These transitions are both addressed with fully-assembled Precilasers SFG systems to ensure high output without having to manage unfamiliar 2μm optics. The main line is produced by summing sin 1942 nm and 1064 nm, with a total output of 7W (not all for slowing, but also for MOT light later). The $\tilde{X}(02^20)$ laser is a sum of 2051 nm and 1055 nm, with a total output of > 4 W.

The $\tilde{X}(100)$ repumping ($\tilde{X}(100)$–$\tilde{B}(000)$) light is produced with a home-built SFG system, combining light from 1550 nm and 1064 nm fiber amplifiers. Since this transition requires a lot of power to maintain the necessary scattering rate (see Tab. 4.4), this laser is not double seeded or daisy chained. When optimized, the system can produce 7W of red light.

The $\tilde{X}(200)$, $\tilde{X}(02^00)$, and $\tilde{X}(110)$, N"=2 repumpers ($\tilde{X}(200)$ – $\tilde{B}(100)$, $\tilde{X}(02^00)$–$\tilde{B}(000)$, $\tilde{X}(110)$, N"=2 – $\tilde{B}(010)$) are all similar wavelengths ($\Delta v_1 = 1 \sim \Delta v_2 = 2$) and have significantly lower power requirements. These three SFGs share a single 1550 nm amplifier. The $\tilde{X}(02^00)$ is produced from combination of some 1550 nm light and a standalone ∼1084 nm light from a 1064 nm fiber amplifier to produce ∼638 nm light. The other two are generated in two daisy-chain SFGs of a double-seeded $\sim$ 1064 nm amplifier (around 1060 nm) and the 1550 nm light to produce light at ∼631 nm. The $\tilde{X}(110)$ laser is second in the daisy chain due to the low power requirement in the cycle, and can output >100 mW. Each of the other two lasers achieve >500 mW. The relative power between the

three outputs is adjustable to a degree by tuning the ratio of 1550 nm to each setup as well as the seed power ratio in the double-seeded amplifier.

A final daisy chain is used for the $\tilde{X}(010)$ N"=1 and $\tilde{X}(110)$ N"=1 repumpers, again since they are similar wavelengths ($\tilde{X}(010)$ N"=1 – $\tilde{B}(000)$, $\tilde{X}(110)$ N"=1 – $\tilde{B}(100)$). Again produced from a 1550 nm amplifier and a double-seeded 1064 nm amplifier seeded at $\sim$ 1045 nm, the $\tilde{X}(010)$ light is produced first due to the higher power requirement. This laser produces >400 mW, and the $\tilde{X}(110)$ component produces >100 mW.

The $\tilde{X}(010)$ N" = 2 repumper ($\tilde{X}(010)$–κ $\tilde{A}(010)^{\dagger}$) is a fairly strong transition. It is conveniently possible to drive with a home-built ECDL with a Thorlabs HL6750MG diode that produces >50 mW. The $\tilde{X}(300)$-$\tilde{A}(200)$ repumper is also accessible by ECDL, though near a difficult region of the spectrum (711 nm), so we use a Moglabs LDL which produces >40 mW. Some slowing work was done using a Ti:Sapph to drive this transition.

The output of each slowing laser is passed through an AOM as a method of fast switching, using the first-order diffracted path to reach the apparatus. After the AOMs, the beams go through several white-light EOMs. In some cases several lasers are combined on OptiGrates, dichroics, or beamsplitters before the EOMS. The EOMs are 50mm x 1mm x 1mm strongly overdriven $LiNbO_3$ crystals that produce closely spaced sidebands over a width of $\sim$300 MHz which cover both SR sidebands over the complete range of possible Doppler shift up $\sim$100 m/s. A cross-section of the white-light EOM can be seen in Fig. 4.6. An

†The κ $\tilde{A}(010)$ is approximately the $\tilde{A}$ $^2\Pi_{3/2}(010)$ state, dressed by Renner-Teller interactions.

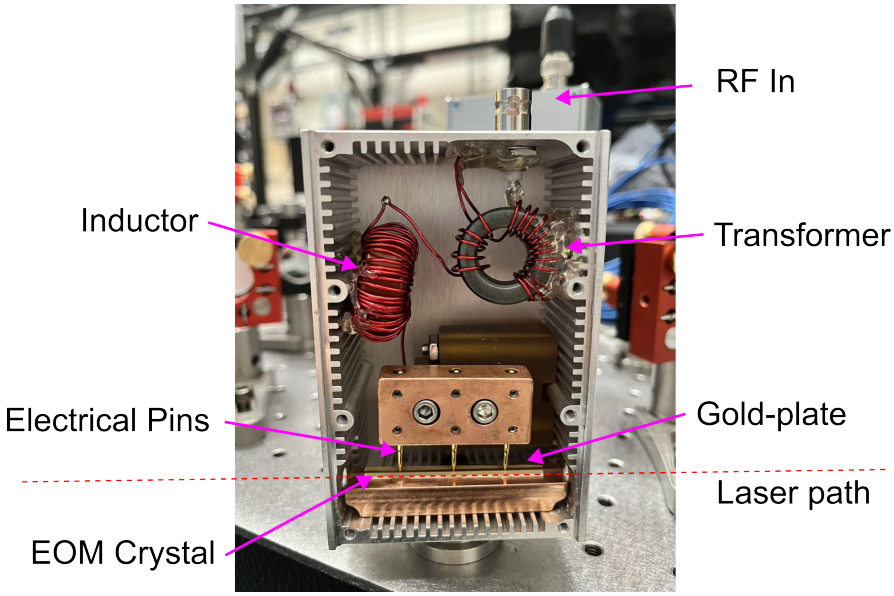

Figure 4.6: Cross-section of one of the white-light EOMs used to add frequency sidebands to the slowing light. The 50 mm long crystal is near the bottom of the box, and has a stripe of gold-coating on the top and bottom of it (which acts as a capacitor). The RF signal comes in through a BNC on the top of the box, and is impedance matched at ~ 1.4 MHz to the crystal capacitance with a home-wound inductor and transformer.

example of measurements of the broadening from the EOM can be seen in Fig. 4.7. The spectral broadening widths for all the lasers are tabulated in Tab. 4.5. After the EOMs, the light from each subsetup travels by fiber to the experimental table, where it is combined via a combination of PBS and dichroics into a single beam. This beam is then passed through a Pockels cell which rotates the polarization back and forth by ∼90 degrees at 1.4 MHz, as described in 4.1. After the Pockels cell, the light is expanded by a telescope to a 1" diameter, and directed down the bore of the beamline. The powers that enter the combination board can be found in Table 4.4, with differences from initial laser power dominated from repeated fiber coupling along these optical setups.

Figure 4.7: Oscilloscope trace of laser light passed through a white-light EOM and passed through a beat-note relative-frequency measurement setup. The individual frequency peaks are spaced by $\sim$ 4 MHz, and the total width of the spectrum is $\sim$ 350 MHz in this image. Measurements like this allowed tuning of the white-light broadening for all of the slowing lasers. Later measurements with a cavity, instead of the beat-note setup, were also done later as the measurement scheme turned out to be quicker.

4.5 Radiative Slowing Of SrOH

Having described the construction of laser cooling scheme and experimental apparatus, we now continue on to how the radiative slowing of SrOH was accomplished. Though we will end this section with the results of optimized slowing, they end up looking very similar to the slowing data of other molecules, and are therefore not particularly enlightening in and of themselves. It is more useful to understand how the experiment was developed to produce these results, so we begin the with the process of identifying and optimizing the relevant slowing parameters. Then, measurements of each laser's scattering rate ensure sufficient slowing time to decelerate the molecules specifically. Detuning scans similarly ensure that the white-light broadened light is able to interact with the

molecules strongly over the entire velocity range. We finally present the results of slowing SrOH, possible only with these optimizations: the peak of the distribution slowed from ∼110 m/s to < 50m/s, and an order of magnitude increase in population below 10 m/s. These results are sufficient to produce a trappable population of molecules.

4.5.1 Scattering Rate Measurements

Except for the main line laser, which of course we want to scatter as quickly as possible to efficiently decelerate molecules, the requisite intensities of the lasers are not immediately obvious. Clearly, the total scattering rate in the cycle should be as similar to the main line as possible, but the vibrationally-excited ground states are not populated nearly as often. As such, the repumping transitions need not maintain the same scattering rate individually (indeed, this is excellent news, as some of the transitions would require 10s of watts of power to do so). A naive model assumes that a repumper should empty a vibrational state on the same timescale as it is populated ("time in = time out"). In this case, a molecule would spend most of the time in vibrationally excited states, and so cut the effective scattering rate significantly. More precise Markov chain calculations suggest emptying the vibrational states $\sim 10x$ as fast as they are populated only minimally alters the overall scattering rate. The goal is to therefore achieve scattering rates as far below this number as possible. The "times to enter" each state are listed as T_{in} in Table 4.3.

There are two ways of experimentally ensuring the overall scattering rate is

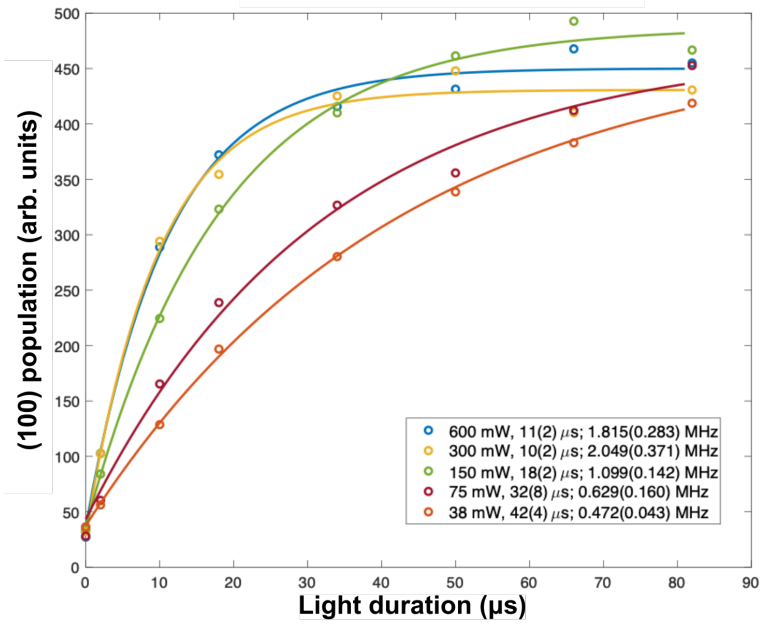

Figure 4.8: Data of the type taken to measure the saturation curves in Fig. 4.9. The laser being tested (in this case the main line) is pulsed for several increments, and then for different powers. The population in a later vibrational state in the cycle is monitored, from which the decay constant of the tested state's population can be extracted. These time constants are then plotted as a function of power which makes it easy to see if a laser is highly saturated (Fig. 4.9).

maintained as the optical cycle is extended. The simpler way is to measure the total scattering rate as repumps are added. This can be done by dividing the known photon budget for the included transitions by the time it takes for molecules to get pumped into dark states. We used this scheme to measure the scattering rate early in the cycle. For the scattering rate of just the main line, we pulsed the main line light down the bore for 2-160 μs in increments of ~ 20 μs starting a few ms after the ablation pulse. These pulses push molecules into the $\tilde{X}(100)$ state proportional by scattering rate and pulse length. In the detection region, the $\tilde{X}(100)$ repumper intersects the molecular beam transversely and excites population to the $\tilde{B}(000)$ state, which upon decay produces

observable fluorescence that is collected on the imaging system. In this orientation, the $\tilde{X}(100)$ population increases as the main line light is kept on longer. A time constant can be extracted from this curve (Fig. 4.8), which is proportional to the scattering rate divided by the photon budget. As long as the data is extracted from after the main line light is off, the detection light does not alter the length of the cycle. Scattering rates were extracted as a function of laser power to determine if the transition was saturated or not: a linear relation as a function of power indicates an unsaturated transition. Power fluctuations in lasers driving unsaturated transitions will produce scattering rate fluctuations; the same is not true for high saturation. The main line power scan can be found in Fig. 4.9. 600 mW in the slowing beam was found sufficient to maintain a 2 MHz scattering rate and the transition was highly saturated. A scan of the scattering rate as a function of frequency was used an approximate measurement of the width of the white-light broadening[‡]. The main line broadening was confirmed to be ∼300 MHz (Tab. 4.5), which was used later in setting the laser detuning correctly. A similar process was used to extract the scattering rate of the combination of main line and $\tilde{X}(100)$ lasers. The main line laser was left on down the bore of the beamline, while the $\tilde{X}(100)$ repumper was pulsed for various times. The corresponding *decrease* in fluorescence in the detected state can be used to calculate the total scattering rate of the joint $\tilde{X}(000)$+$\tilde{X}(100)$ laser system. The rate is found to be ∼1.5 MHz, highly saturated when the first repumper has over 800 mW of power (see Fig. 4.9). Frequency scans were used

[‡]This broadening was also measured on a scanning Fabry-Perot cavity.

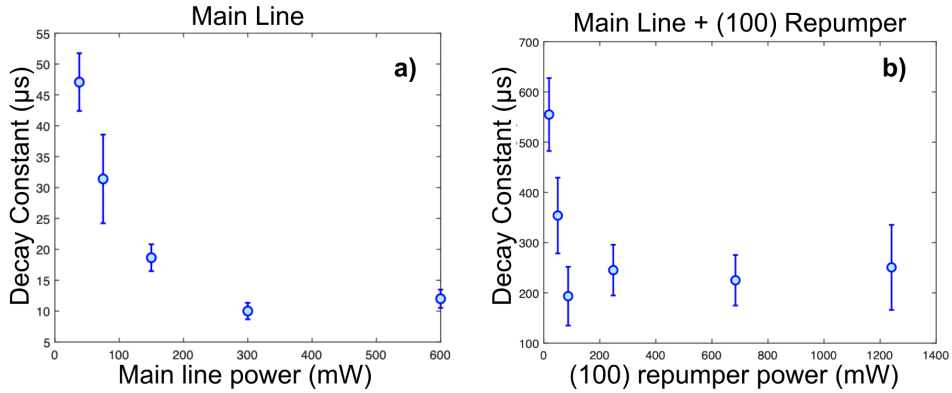

Figure 4.9: Measurements of the power saturation for (a) the main line and (b) (100) repumpers. As discussed in text, the lasers are pulsed for various amounts of time at different powers as shown in Fig. 4.8. The time constant to pump population out of the measured states are then plotted as a function of power to determine at which power the scattering rate is saturated. These curves show the main line can achieve a $\sim$ 2 MHz scattering rate with $\sim$ 600 mW (since it cycles 20 photons) and the (100) repumper with $\sim$ 700 mW (since the two cycle >600). Both lasers are operated as far above these powers as possible to ensure maximal scattering rate. Similar measurements were done for all lasers in the optical cycle. Powers for all the lasers can be found in Tab. 4.4.

to tune the broadening of the first repump to ∼300 MHz. Though this method of measuring scattering rate worked well for these early lasers, it becomes intractable once the photon budget is high and not precisely known. In particular, the pulse time must continually get longer to fully empty the optical cycle as lasers are added. After only a few more repumps, the pulse time must be long enough that molecules reach the detection region while the cycling light is still on. Only fluorescence from after the pumping light pulse is off is useful, but this becomes a very small portion of the signal. We initially tried continuing with this way but we found it difficult to extract reliable numbers from the tail.

An alternative is to measure the individual scattering rates of repumping lasers, and then calculate the total rate as a weighted average of each ground

Table 4.4: Table showing the $T_{in} = T_{out}$ power ($P_{Ti=To}$) and operation powers (P_{op}) for each laser. The $T_{in} = T_{out}$ powers were determined from the scattering rate measurements and the estimated T_{in} (Tab. 4.3) from a Markov chain model of the optical cycle. The powers for the main line and (100) repump were kept as high as possible to maximize the total overall scattering rate. Ideally, all lasers are 10x higher power than for $T_{in} = T_{out}$ to not significantly slow the optical cycle speed. This was not possible on a few lasers, which limited the rate.

Laser	$P_{T_i=T_o}$ (mW)	P_{op} (mW)
(000)	-	1000
(100)	<100	1200
(200)	5	170
(010) N = 1	50	240
(02^20)	100	750
(02^00)	50	390
(010) N = 2	<1	3.5
(300)	<1	50
(110) N = 1	<10	80

state's scattering rate by the time spent in each state. Since the repumpers are necessarily off diagonal transitions, even comparatively slow rates are easy to measure because only one-few photons are scattered before loss. In contrast to the previous method, here the main line and early repumps are pulsed for a fixed time, long enough to populate the vibrational state of interest with at least some molecules (∼ms). Then, the repumper of interest is pulsed after this light is off, again for various increments of time over multiple ablations. If the repumper being studied pumps population into $\tilde{X}(100)$, the $\tilde{X}(100)$ repumper alone is used for detection. If the population is pumped into some other state, other repumpers are added to get population into $\tilde{X}(100)$ first. The scattering rate can be extracted again via exponential fit of the pumped population versus pulse length. For some repumpers, like out of $\tilde{X}(010)$, N"=2, this number is not really the "single-photon" scattering rate since some cycling occurs on

the transition itself, but is still <10x the value. However, it is the relevant scattering rate to return closer to the main cycling transition. These rate measurements is done for the remaining repumpers as a function of power and frequency to determine saturation parameters and white-light broadening. The results of these measurements can be found in Tabs. 4.4 and 4.5. All transitions except a few are found to be $> 10 \times P_{T_i=T_o}$ at the powers delivered to the experiment. The most important exceptions are the (010), (02^20), and (02^20) laser. Some of these transition are replaced with a better option for MOT work, but one or multiple of these probably limited the total scattering for our slowing demonstration. If not already, the white-light broadening for all lasers was adjusted to be $\geq$ 300MHz to cover an adequate velocity range. With these measurements, we estimate a ~ 2 MHz overall scattering rate.

4.5.2 Detuning

After ensuring each laser was scattering sufficiently well to utilize the entire photon budget, the detuning of each had to be set to be able to maintain the full scattering rate over the course of deceleration. There are a few subtleties to setting it correctly. The broadening occurs symmetrically around frequency of the laser as measured on the wavemeter. The spin-rotation components of SrOH are spaced by 110 MHz. The Doppler shift of molecules on the main line at 110 m/s is -160 MHz. Knowing these three things, we can set the central frequency of the lasers ~ -150 MHz detuned from resonance of the higher frequency Sr component. At such a setting, the sidebands go down to approxi-

mately -300 MHz, which is enough to interact with the lower sideband at 110 m/s (since -120 MHz + -160 MHz > -300 MHz). Similarly, the light will still interact with the upper sideband at 0 m/s, since EOM broadening also reaches the zero-velocity resonance. It is clear from this discussion that molecules much faster than 110 m/s will only be able to interact with the slowing light in the lower energy (higher frequency transition) SR component. If a laser has sufficient power to maintain sufficient scattering rate with wider broadening, we increased it, which allows some interaction with faster molecules. Nevertheless, more laser power can improve this "capture velocity" further by allowing wider broadening. The central frequency can be set in the same method to maximize the velocity range over which the light interacts with both spin-rotation components. Note that this is not an issue in the N" = 2 repumpers, since only one SR component is populated in the cycle. The broadening can be smaller than 300 MHz on these lasers, but the other considerations remain. Additionally, the detuning of each laser is iterated when slowing is operational to make small (<15 MHz) adjustments to these setpoints based on optimal deceleration. The final detunings can be found in Tab. 4.5.

4.5.3 Laser Deceleration of SrOH

With the lasers properly operational and detuned correctly, we were ready to slow SrOH. To decelerate the molecules, the combined laser beams were pulsed down the bore of the molecular beam line for 10-30 ms synchronized with the ablation pulse. The molecules were detected in the velocity-sensitive configu-

Repump	Resonance - AOM Shift (THz)	$\Delta\nu$ (MHz)	Slowing ν (MHz)
(000)	435.968146'	275	435.968137
(100)	475.171755*	275	475.171600
(200)	475.508750*	325	475.508750
(010) N = 1	480.074300*	400	480.074300
(010) N = 2	444.478850*(?)	400	444.479000
(02^00)	469.887050'	400	469.887000
(02^20)	430.228810*	275	430.228900
(300)	421.360450*	400	421.360500
(110) N = 1	480.480550'	325	480.480500

Table 4.5: Table of the resonance values for each laser used in slowing (see the left-hand cycling scheme in Fig. 4.2) and the detunings used during the slowing work. Resonance frequencies are noted for the *lower* frequency spin-rotation component. Additionally, the resonance frequencies differ from the true resonance values because of AOM switches in the path. * indicates an 80 MHz AOM shift, and ' signifies a 110 MHz AOM shift. The frequency broadenings, as measured on a beat-note setup, are also included. This combination is used to choose the freuqencies used for slowing.

ration, with several averages taken every 10 MHz from 0 to -110 MHz detuning (corresponding to 0-80 m/s). Evidence of deceleration was obtained in two ways. First, the integrated signal as a function of velocity could be compared to data taken when the slowing light was off, Figure 4.10. The accumulation of molecules at lower velocities is clear in the slowed molecule trace. A skeptic could/would argue that there is a (admittedly very small) chance that the ablation or some other parameter just happened to change between the two datasets that produced molecules with different velocity distributions. Data of this first type is unable to disprove this idea explicitly, even though it is quite unlikely. The integration turns out to be discarding the relevant information. Instead of integrating the velocity-sensitive traces, we can also plot all of the traces together in a velocity versus time of arrival plot. These "2D" plots for

both slowed and unslowed molecules show not only the velocity of molecules but also, crucially, the arrival time of those same molecules, as seen in Fig. 4.11. A kinematic trace can be overlaid on these plots corresponding to ballistic trajectories of molecules leaving the cell within a few ms of ablation. Molecules cannot organically arrive to the left or below this trace without violating causality. Molecules fluorescing in this region in the slowing data therefore *cannot* arise from anything except deceleration. Sure enough, Fig. 4.11 clearly shows a large accumulation of molecules in this region of phase space when the slowing light is on. These two figures are the final slowing results, but analysis of figures like these was what guided optimization. In addition to small changes in detuning, the start time and end time of the slowing light were also separately varied. The slowing was found to be most effective when starting 4 ms after ablation and with a 27 ms duration. These parameters were revisited when looking for a MOT, as it is not clear if the optima of both should coexist.

4.5.4 Looking forward

Using a new apparatus and 10 lasers, we successfully demonstrated deceleration of molecules and, importantly, accumulation below 15 m/s. This work was done in new cryogenic buffer gas beam source attached to a 1.5 m long differentially pumped beam line and a detection chamber. The light was produced from a combination of SFG systems and ECDLs, both home-built and pre-assembled. The laser light was white-light broadened, combined into a single slowing beam, and passed through a polarization-switching Pockels cell. These preparations

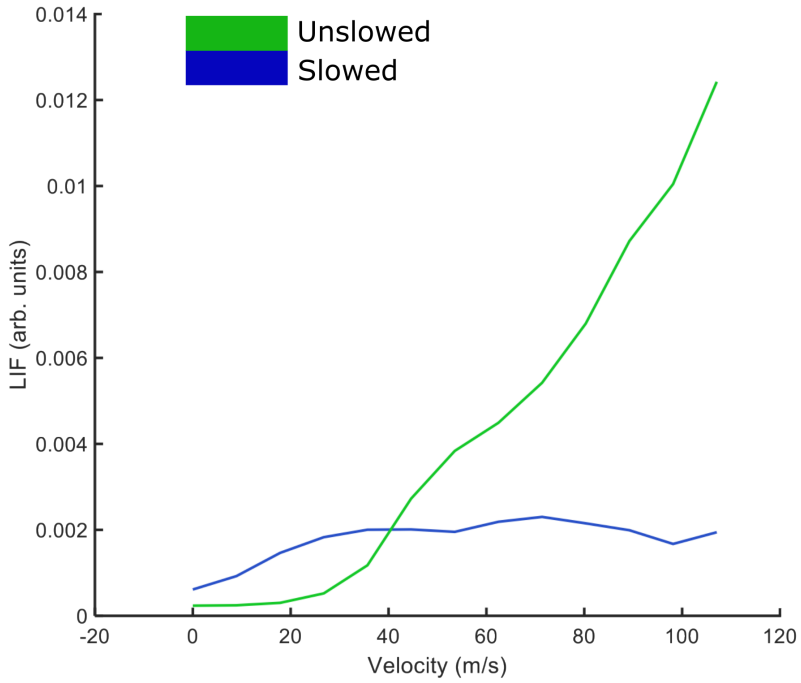

Figure 4.10: Integrated slowing signal as a function of velocity. For each point, a Doppler-sensitive laser fluoresced off molecules in a given velocity class. At each velocity setting, the signal was integrated. Not integrating the data produces Fig. 4.11. In this figure, we can see accumulation of molecules below 40 m/s in numbers larger than in the unslowed beam.

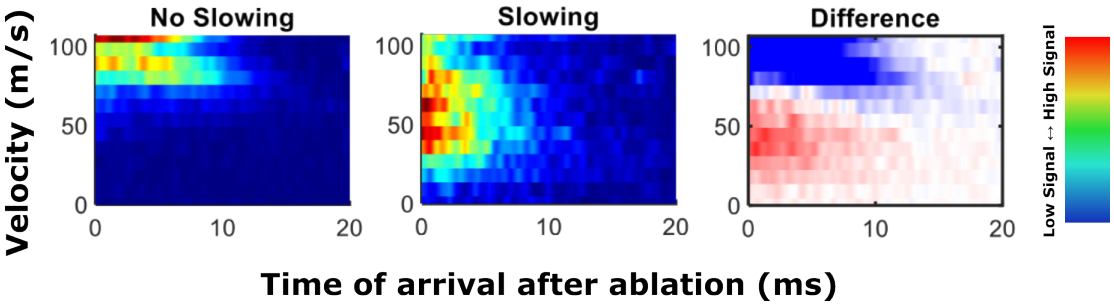

Figure 4.11: 2D traces of slowing data. The plots are made of individual velocity-sensitive traces. The comparison of the population concentration with and without slowing demonstrates that the slow molecules must originate at higher velocities than they end, indicating deceleration is taking place.

destabilize dark states and allow the light to interacting with the molecules over both the entire spacial length and velocity distribution from ∼110 m/s to rest. Optimization of laser detuning and light pulse duration resulted a large fraction of decelerated molecules, with many below 15 m/s.

The most technical aspects of this work were, of course, related to managing the many lasers. If the stabilization, frequency modulation, and combination can be managed for more lasers, there is nothing intrinsically different about the physics in extending radiative slowing to more complex molecules. Further technical complications may arise, however. Heavier molecules, like Ba- or Ra-containing species, have redder cycling transitions and therefore require longer experiments, which may increase pluming loss. Conversely, lighter metal containing species with bluer transitions are more amenable to shorter beamlines, but are in general less interesting for precision measurement (with a few exceptions, e.g. [153]). It will also be more difficult to combine all the lasers for complex species with congested rotational closure schemes due to many closely-

spaced lines. Nevertheless, these are definitively "technical" complications; if light for a sufficiently closed optical cycle can be assembled, any molecule can be slowed [71]. The number of species that this is possible for is neither large nor zero.

4.6 Preliminary Magneto-Optical Trapping of SrOH

Radiative deceleration of molecules is complex enough that the effort involved is not justified by slowing alone. Indeed, there is no reason to stop at this step anyway! The photon budget required to magneto-optically trap (MOT) a species is comparable to the radiative slowing budget. In the case of SrOH, scientific considerations also weigh in: an EDM or μ-variation experiment of SrOH in a beam would not have statistics or systematic control necessary to compete with exisiting state-of-the-art measurements. Cold trapped samples, however, will be competative. A MOT is the first step to achieving these conditions.

The theory of a general RF MOT has been earlier described in 4.1. In this section, we present the implementation of these considerations to realize the first MOT of SrOH. We begin by describing the additions to the apparatus required to MOT: most vitally, a set in in-vacuum RF magnetic field coils and trapping light. Then discuss early attempts at trapping, and modifications to the laser cooling scheme that were implemented to reconcile instabilities. With these improvements, we present early results of a MOT of SrOH. We end with notes about current limitations of the MOT and future improvements to improve lifetime and temperature towards loading molecules into an optical dipole

trap.

4.6.1 MOT Coils

The RF field needed for a MOT poses an interesting technical dilemma. The field gradient need not achieve more than $\sim$ 10 G/cm at the trap location, which is trivial at DC. However, RF switching of such a field is not, and either requires in-vacuum coils with modest inductances (but which are at risk of substantial heating and/or large electric fields mixing opposite parity states) or out-of-vacuum coils with are easily to cool but require much larger inductances. The in-vacuum approach has been tested and gradually developed by past experiments in the Doyle lab, so we too use this approach to take advantage of the technical knowledge of our predecessors. In particular, we use the design used in the Doyle group CaF and CaOH experiments [69, 71], where a more detailed description of the coils can be found.

The coils are made from photochemically etched 1/32" thick OFHC copper. They are 8 turns each, with a wire width of 0.03" and a gap of 0.02" between turns. The ID is 0.85", which allows for optical access through the coils. The inductance of the coils is 60-70 μH. The copper coils are on aluminum nitride boards that maintain the bore optical access. These coils can produce 10 G/cm field gradient with 4.6 A.

Driving the coils at RF frequencies (1.4 MHz) leads to a small skin depth: the current only passes through the outer $\sim$ 50 μ m of the wires [71]. As a result, the resistance ($R \propto 1/A$) increases substantially from the DC value. The

current through this resistance produces 10s of watts of heat. If the coils were isolated in vacuum, this heat would quickly cause problems, and indeed this has been the case in past iterations of design [71].

To remove this heat from the vacuum chamber, the coil mounts were made as thermally conductive as possible. Indeed, the choice of aluminum nitride was determined partially by thermal considerations (as there are few materials that are electrically insulating but thermally conductive). The high thermal conductivity (200 W/(m·K)) helps to spread the heat load across the board. There is a conductive copper ring on the edge of the board which allows good thermal contact to copper rods between boards and finally to thick copper feedthroughs out of the chamber. These feedthroughs are then water-cooled outside the chamber to continuously remove heat from the system. The mounted coils can be seen in Fig. 4.12.

RF electric fields between the plates can arise due to asymmetry between the two tank circuits. Since the currents are changing very quickly, if the two coils are driven with different current the potential across each coil will be different as well. As a result, there will be an RF electric field between the two coils. To avoid this, current probes on the electrical feedthroughs into vacuum allow the current in the coils to be tuned to match, and the leads from the feedthroughs to the coils are made as close to identical as possible. The current must be in phase to within a few percent of the duty cycle and of equal magnitude to avoid E fields. Such E fields have been observed in previous versions of the MOT coil design [71]. These fields severely limited the trap lifetime by inducing mixings of

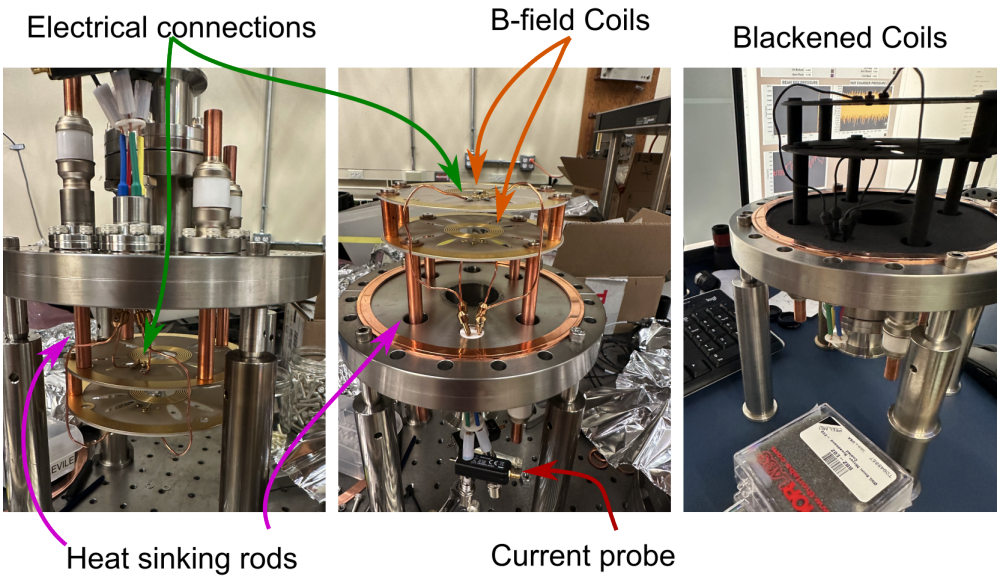

Figure 4.12: Pictures of the MOT coils mounted on the MOT chamber flange. Arrows show the actual RF coils, the electrical connections to feedthroughs, a current probe attached to one of the electrical lines, and thermal rods which can be heatsunk outside of the chamber. The coils are also shown after being blackened by MH2200 spray paint.

opposite-parity states, and solving the problem immediately resulted in significantly longer MOTs.

The RF signal is originally generated by a Siglent SDG 2042X function generator. The signal is first amplified by ENI 550L RF amplifiers by 50 dB (up to 150 W). To impedance match the coils to the RF amplifiers and cabling we electrically integrate the MOT coils into "tank circuits". The tank circuit is schematically just a series LC circuit. The MOT coils themselves are the main inductor, and a variable vacuum-gap capacitor in series changes the resonance by small amounts. A small fixed air core inductor is used for larger tuning. The quality factor ("Q factor") of the circuit is set by parasitic resistance throughout the circuit. The MOT coils have an inductance of 30 uH each, and we use 500-

1500 nF tunable capacitors and 16:3 transformers. The Q-factor is measured to be 2200 on one coil, and 1800 on the other. The field strength is experimentally changed by the amplitude of the function generator output.

4.6.2 MOT Light

The other necessity for a MOT is light (duh). As described in 4.1, the radiative force is exerted by three pairs of counterpropagating red-detuned laser beams, one pair along each cartesian axis. Ideally, the detuning can be quickly changed to be able to rapidly modify the depth (and therefore temperature) of the MOT. The in-plane beams must also be circularly polarized in the relative configuration noted in Fig. 4.1, with the absolute polarization quickly switching handedness to destabilize magnetic dark states. The vertical axis beam polarizations are reversed due to the opposite direction of the magnetic gradient along the axis.

The MOT laser light is taken from the same SFG system than generates the main line slowing light. After optimizing slowing, there is $\sim$1.5 W of excess available. This light is fibered from this laser to an auxiliary table for frequency and polarization dressing. This table has three sub-assemblies for fast frequency tuning, SR sideband generation, and polarization switching. The first, frequency tuning, consists of a large-aperture double-pass AOD from Gooch & Housego. The AOD is set up in a cats-eye configuration, schematically outlined in Fig. 4.14. With the collimation lens placed such that the AOD is in the focal plane of the lens, this orientation maintains the output alignment of the light as the diffrac-

tion frequency of the AOD changes. The AOD is controlled by a VCO and a VVA, which in turn can be remotely controlled to change both the frequency and strength of the diffracted order. To ensure robustness against small fluctuations in power, the VVA is ultimately controlled by an SRS SIM960 PID box. The PID reference is a power-monitoring photodiode on one of the MOT beams. The frequency is controlled by an NI-DAQ system so fast patterns can be remotely programmed in the experimental cycle. After the AOD, the again light travels via fiber to a Pockels cell. The Pockels cell is set up in a polarization-switching configuration, with high enough intensity to rotate the input linear polarization 90 degrees, as measured on a fast photodiode after a PBS. It is driven by a Conoptics 302RM driver with a square wave. The output linear polarizations are aligned to the axes of another fiber leading to a SR sideband setup. On this final board, the light is split by an 110 MHz AOM to address the two ground-state SR components of the transition and again polarization-aligned into optical fibers to travel back to the experiment. Unlike a typical spectroscopic SR sideband setup, the sidebands cannot be recombined on a PBS, as they are downstream of the Pockels cell and a PBS would dump the entirety of light in one switching phase. Instead, each sideband is separately fiber coupled, and these two output fibers are combined in a 2x4 evanescent fiber splitter from Evanescent Optics. Three of the four fibers out of the splitter go to the experiment, while the fourth is attached to a photodiode which serves as the PID power monitor. A schematic showing the ordering and elements of frequency and polarization control of the MOT light can be seen in Fig. 4.13.

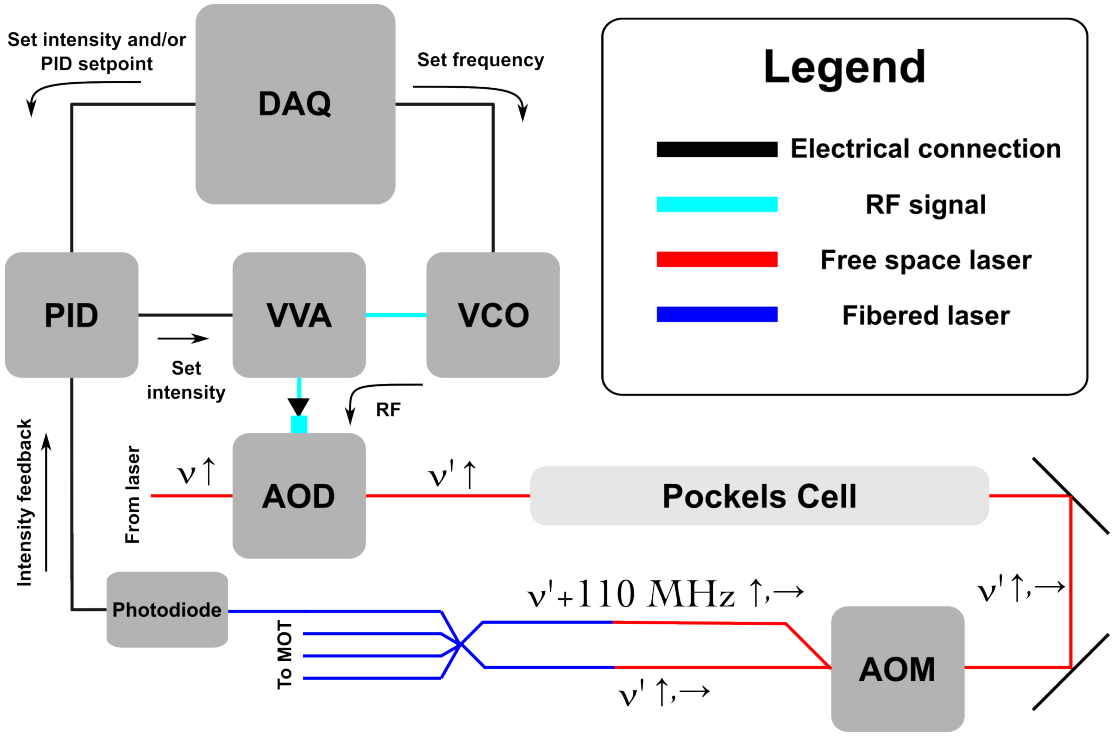

Figure 4.13: Schematic showing how the MOT light intensity and frequency are controlled by electronics and optical elements. The intensity the light through the AOD is set by the variable-voltage amplifier (VVA), which in turn is set by the PID box. The frequency of the AOD shift from $\nu' - \nu$ is set by a voltage-controlled oscillator (VCO). The PID box can either feed back on the MOT light intensity or relay a setpoint directly from the DAQ. The VCO frequency is set by the DAQ as well. The light then passes through a Pockels cell to switch polarization quickly, and an AOM which adds a spin-rotation sideband. The two sidebands are then coupled into a 2x4 fiber splitter, with one output used as a signal for PID feedback and the other three as the MOT beams.

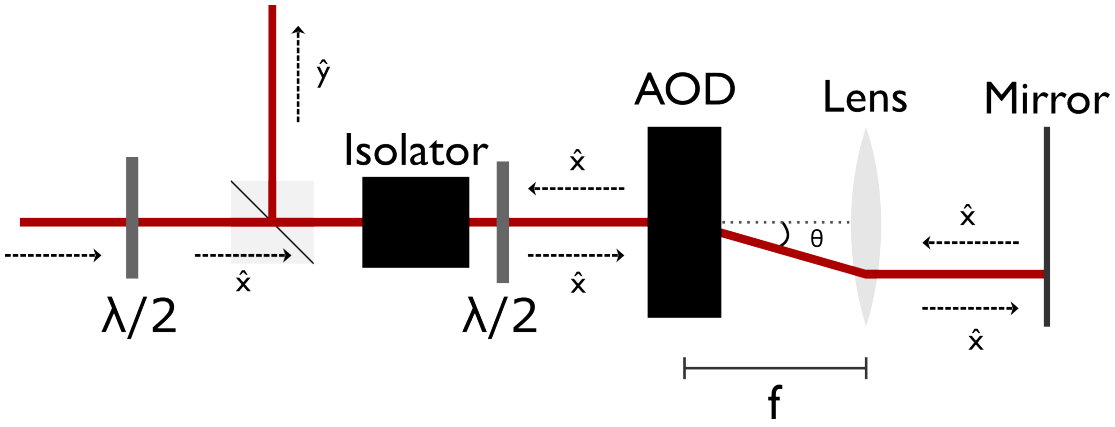

Figure 4.14: Schematic of the cat's eye AOD setup. The optical elements and laser path are noted. The input polarizations are noted below the beam, and the retroflection polarizations are noted above. The first half-waveplate tunes the polarization to be linear in the x direction, which then passes through a PBS unobstructed. The quarter-waveplate then converts the linear polarization to right-hand circular polarization, which is efficiently diffracted through the AOD by an angle θ. If the lens is placed a focal distance f from the AOD diffraction plane, the light will always be collimated after the lens. The collimated light then exactly retroreflects through the system overlapped with the input beam until the quarter-waveplate, where the phase shift from the mirror reflection results in the opposite linear polarization than the input beam. The PBS then splits the input and output beam so the frequency shifted light can be utilized.

At the MOT chamber, the light from each fiber passes through a quarter-wave plate to give the input beam along each axis the correct polarization (e.g. when not swtiching σ^+ along the horizontal axis and σ^- along the vertical axis) and is directed into the MOT chamber. The waveplate angles are set by minimizing the transmission of the light through circular polarizers. The two horizontal beams are ± 45 degrees from the molecular beam axis to avoid crosstalk and congestion with the slowing beams. The vertical beam passes through the center of the chamber and hole in the MOT coils. Instead of generating three more beams for the counterpropagating light, each of these initial three MOT beams passes through another quarter-wave plate after exiting the chamber and is retroreflected back along the same path. The quarter-wave plate gives the retroreflected beam the opposite circular polarization as the input beam. Counterpropagation is ensured by back-coupling the retroreflection into the fiber splitter. Absolute alignment of the light is done by observing fluorescence of molecules passing through the chamber with the magnetic field on with both the regular imaging camera and a separate camera looking down the vertical axis of the MOT coils. The beams are aligned to center on the molecule fluorescence when the light is on resonance, since in this condition the molecular signal corresponds to the region of smallest field value. The retroreflected beams are blocked and re-aligned after this process to avoid broadening. Small improvements of alignment are possible once a MOT is visible, but this process was vital in obtaining a good initial alignment. Centering the beams on the windows was not sufficient, likely due to small offsets of the MOT coils from the cham-

ber axes and/or imprecise normality of the flanges on the spherical square. Repumping was initially done by the slowing beam repumpers, though the main line light was turned off for the MOT to prevent trapped molecules from being pushed out of the trap.

4.6.3 Synchronization of Polarization and Magnetic Field Switching

Ensuring the synchronicity of the $\mathcal{B}$ field and laser polarization is paramount to constructing a trapping force for the molecules. Obviously, if the two switches are 180 degrees out of sync, there is an anti-trapping force. Even slight misalignments ($\sim$10 degrees) can cause substantial decrease in the trapping force in an unoptimized system.

The $\sim$1.4 MHz RF for both is generated by a Siglent SDG 2042x signal generator. For low-frequency signals, external generation would be sufficient to ensure close-to-synchronicity. However, given the high frequency of the signal, and the fact that MOT Pockels cell and MOT coil electronics were located across the room from each other, this was not ensured. To monitor the phase between the two signals, the Pockels cell controller "sync out" signal and current monitors on the MOT coil electrodes were connected via identical BNC cables to an oscilloscope. The travel time from the signal generator to the devices, as well as differences in electronics, was found to produce large (>20%) phase shifts between the two. Using this monitor, we were able to minimize the relative phase. This monitor also served to ensure that experimental cycles were running as

they were supposed to, as MOT versus anti-MOT configuration are obvious when the phases can be seen by eye.

4.7 Early Tests

With the light and magnetic field ready, we began searching for evidence of trapped molecules. Since the number of initially trapped molecules was expected to be small, we searched for parameters which gave difference between in-phase and out-of-phase magnetic field and light configurations. The out-of-phase ("anti-MOT") configuration, while nominally anti-trapping, is also capable of producing a molasses-type effect, but this was seen to be much broader than the MOT volume. As such, locating the center of the MOT was necessary to correctly compare signals, and signal was only integrated over this small region of the whole images.

Several parameters' optimal values need to be experimentally scanned to produce an observable difference between the two configurations, especially for an unoptimized MOT. These include $\mathcal{B}$ field gradient, relative timing of extinguishing the slowing beam, and MOT beam intensity and detuning. A high $\mathcal{B}$ field gradient results in a dense and bright MOT with a short lifetime, while a low gradient creates a fluffy MOT with a smaller scattering rate and correspondingly less fluorescence and shorter lifetime. Though the gradient was changed a few times, most searches were done with a relatively high $\sim$ 15 G/cm gradient to maximize MOT brightness. The timing of the slowing is important because turning it off too early can result in molecules not decelerating enough for MOT

capture, but turning it off too late will start to push molecules backwards out of the MOT. Scans of the end time were done in increments of 2-3 ms, from 10-35 ms with an optimum close to the previously observed 27 ms of slowing. The MOT beam detuning was regularly scanned alternating with the slowing timing, as the detuning should change the capture velocity and size of the MOT. Typical values were from -3 MHz to -10 MHz, with an optimum eventually found around -7MHz for the high $\mathcal{B}$ gradient. A ramp to the MOT beam intensity was added to prevent too-fast initial scattering from impeding a MOT from forming. The typical ramp began at the maximum 30 mW/beam and decreased to $\sim$ 8 mW over 5 ms. These remained the ramping parameters for the remainder of the work; though it was scanned occasionally no other parameters seemed obviously better.

Iterations of these parameters were done, not haphazardly, but certainly without much direction. In certain configurations, there were short-lived excesses of fluorescence in the MOT configuration compared to the anti-MOT. However, these signals were not repeatable and seemed to be highly sensitive to ablation spot and fluctuations in slowing power. When it did occur, the MOT signal also appeared offset from the field minimum.

The latter problem was attributed to a radiative force from the first repumper, which is populated enough in the optical cycle to plausibly exert a force on weakly trapped molecules. To remedy this, an $\tilde{X}(100)$ repumping beam was overlapped and retroreflected with the vertical MOT beam, in which configuration no net force is possible.

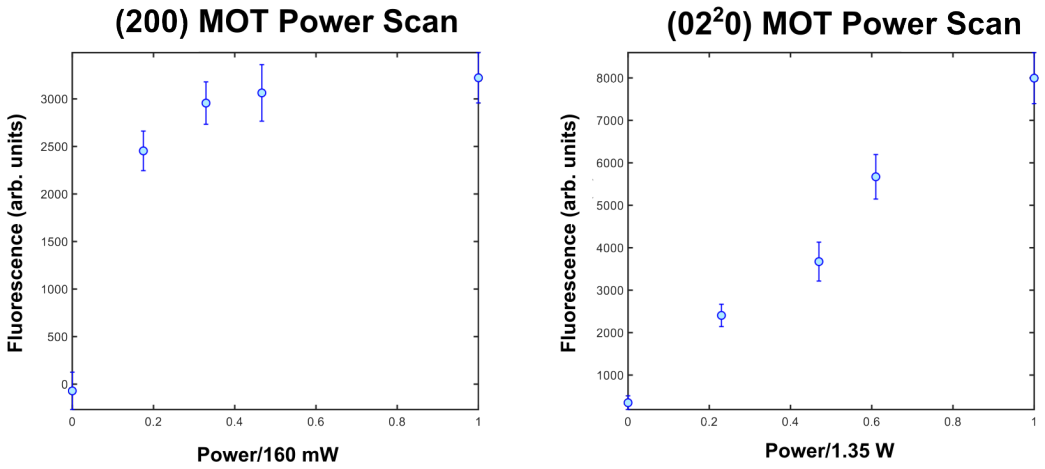

Figure 4.15: Comparison of two repumper power scans done with the MOT-type signal. The (200) repumper, when operating at full power, is insensitive to fluctuations. In contrast, fluctuations of the (02^20) repumper caused linear shifts in fluorescence signal. This data led to replacement of the (02^20) repumper with a different transition, as discussed in text.

The MOT depending on laser power fluctuations was a result of a low overall scattering rate leading to a variable number of both slowed and trapped molecules. Scattering rate measurements in the slowing beam (as in 4.1.1) indicated that the (02^20) repumper was not participating in the cycle optimally but was sufficient to not significantly limit the rate. Similar scattering rate measurements were done in the early MOT where the fluorescence signal was monitored versus laser power. In these measurements, the signal did not seem to strongly depend on repumper fluctuations (of course, it depended on main-line power strongly) except for the (02^20) repumper, with which the MOT fluorescence roughly linearly improved with power. Fig. 4.15 compares the scattering rate measurement of the (02^20) and the (200) repumpers, and shows the qualitative difference in dependence.

As a result of these measurements, the decision was made to replace the (02^20) repumper with a stronger transition. There are no "good" transitions out of this vibrational state that both have strong transition dipole moments and greatly reduce vibrational quanta. Indeed the only reason the $\tilde{X}(02^20)$–$\tilde{A}(100)$ transition works in CaOH is a combination of ground and excited state Fermi resonances (which is to say, basically luck). Without these resonances, the transition was predicted to be at least 2× weaker, and measured to be at least 5x weaker in SrOH. At this linestrength, this factor of a few made the transition impossible to drive sufficiently fast. Other transitions with $\Delta v_2, \ell \neq 0$ (e.g. to $\tilde{A}(010)$ or $\tilde{A}(000)$) are intrinsically weak since they must also be due to perturbations, and changes in quanta of multiple modes (e.g. to $\tilde{A}(110)$) are always weak. This left us with essentially one option, another (020) state. $\tilde{B}(020)$ was ruled out, since, as a Hund's case (b) state, such a transition does not change ℓ, and so the dominant decays will maintain $\ell = 2$. $\tilde{A}(020)$ states avoid this issue because of their Hund's case (a) character and the $\tilde{A}\ ^2\Pi$ electronic character leads to mixing of the nominal $\tilde{A}(02^00)$ and $\tilde{A}(02^20)$ states. Even though the effect is small, the mixing between the states turns out to produce a larger transition dipole between the $\tilde{X}(02^20)$ and $\tilde{A}(02^00)$ than any other "useful" excited state. This transition replaced the old repumper in the slowing cycle. Scattering rate measurements showed that 3 mW of power saturated this transition more than the 2 W did on the original line. This change was sufficient to observe a more reliable MOT-like signal. It did increase the power requirement of the $\tilde{X}(02^00)$ repumper since this ground state was more frequently populated,

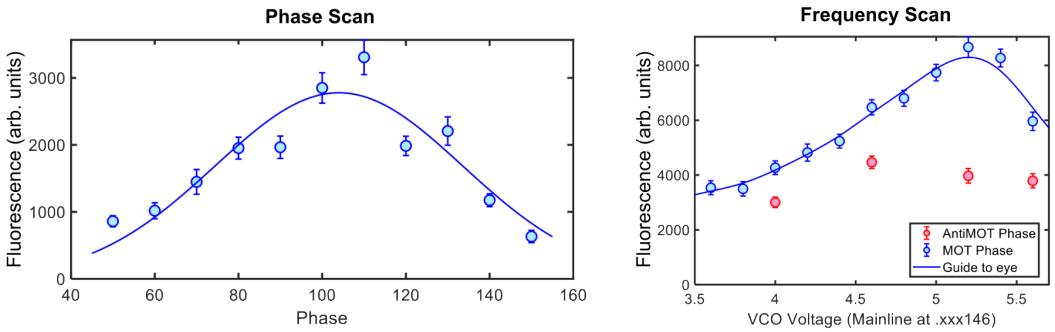

Figure 4.16: Two scans of MOT parameters and how the fluorescence signal changes as a result. On the left, a scan of the relative phase on the function generator between the MOT current and Pockels cell signals. The phase was chosen at the peak of the fluorescence. On the right, a scan of the VCO frequency, and correspondingly MOT frequency. The difference between the in-phase light and magnetic field ("MOT phase") and out-of-phase curves are clear.

but this was accounted for by rearrangement of amplifier power as noted above.

The initially optimized MOT-like signal indicated an estimated lifetime of <20 ms and contained an estimated 1000 molecules. The signal acted as expected as a function of detuning and relative phase, as shown in Fig. 4.16. The SNR was >10 between MOT and anti-MOT configurations after optimization. However, no matter which parameters we tuned, the lifetime was stuck around 20-25 ms and numbers remained low.

To figure out what was going on, we adopted stochastic-wavefunction based simulation code from the CaOH experiment (modified from their calculations in [58]). To our surprise, these simulations indicated that the apparently limited lifetime could be due to a convolution of signal from semi-trapped molecular samples entering the trap with the actual MOT. Basically, many molecules seem to be able to scatter enough photons to remain in the MOT region for several ms, but are moving too quickly to be trapped. These molecules enter and exit

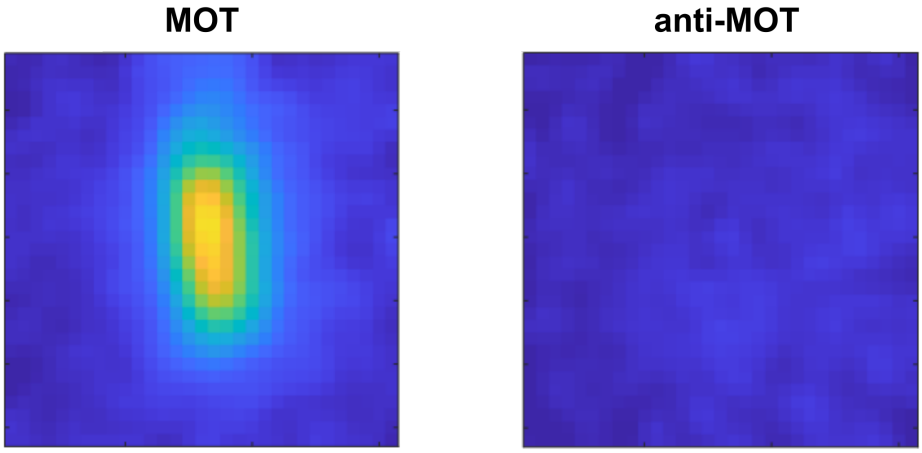

Figure 4.17: Images compiled of 1000 camera averages with the MOT field and light in-phase (MOT) and out-of-phase (anti-MOT). The color scales are equal, making clear the excess of molecular fluorescence in the MOT configuration. Imaging system calibration indicates the fluorescence comes from an average of $>$1000 molecules per shot. Though not all of these molecules are trapped, the latest work suggests that a substantial portion are.

the MOT as the entirety of the molecular beam passes through the region, and obscure the lifetime of the more consistently trapped molecules that entered the trap at lower velocity.

To disentangle the signal from the untrapped/loosely trapped molecules and the MOT we worked on developing a better imaging technique. As part of this, we also replaced our detection camera with a high-QE ($\sim$ 15%) Hamamatsu GaAs R943-O2 PMT to have higher resolution. This PMT increased our intrinsic SNR by a factor of 5 from the old PMT or camera. Then, to understand what portion of the signal in MOT configuration were long-lived trapped molecules, we took data in two configurations that would affect trapped and untrapped molecules differently. In particular, both MOT and anti-MOT configuration was taken (1) with the MOT light on as normal and (2) the MOT light only turned on at the end of the previous ramping (at the low intensity of 8 mW). In this configuration, molecules trapped during the loading/ramping time contribute fluorescence signal to the data taken in case (1), while transiently-fluorescing molecules passing through the MOT at late times will contribute to signal in both cases. Hence subtraction of case (2) data from case (1) can isolate trapped molecules that originated in the MOT before the ramp endpoint.

Data taken in this way showed a statistically significant and long-lived ($\sim$ 30 ms) excess in the trapping configuration, confirming the existence of a MOT separate from the transient signal. The comparison can be seen in Fig. 4.18. These results indicate that about half of the fluorescence originates from trapped molecules, indicating at least 500 molecules in the MOT at the time of writing

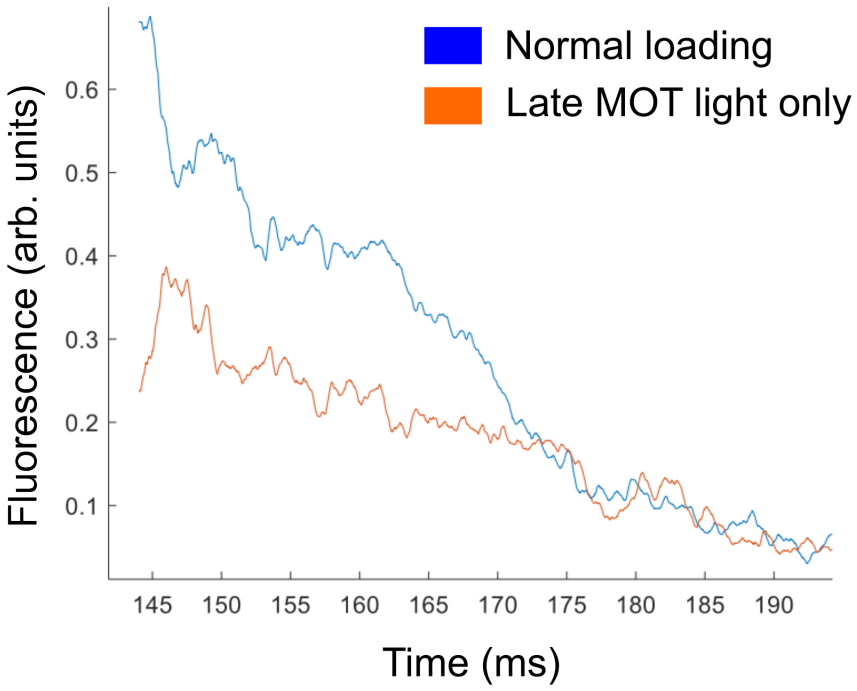

Figure 4.18: Comparison of MOT fluorescence data taken in normal configuration versus the trap light only being turned on late. The difference in signal indicates a trapped sample of molecules originating at early trap times with a lifetime ~ 30 ms.

based on earlier calibration.

4.8 Future work on SrOH

The next steps on SrOH are simply to increase the number of trapped molecules. There are several ideas on how to do so. The simulations indicate a shorter lifetime due to smaller trapping forces compared to CaOH. Larger beams should increase the net force per molecule, and so we are expanding our beams from 1 cm to 2 cm. The MOT beam intensity will be scanned with the larger beams to ensure optimal use of the photon budget.

The simulations also show that the larger spin-rotation splitting (110 MHz) compared to CaOH (50 MHz) seems to negatively affect the trapping force. Unfortunately, the origin is not understood at the time of this writing, so the existence of a solution, or not, is unknown. Adding additional SR sidebands to the MOT light and changing the frequency between the existing sidebands may be attempted to see if they show any effect.

In addition to these simulation-motivated changes to improve the magnitude of the MOT force, addition of the next repumper, out of $\tilde{X}(120)$, will increase the photon budget $\sim 2\times$ (Tab. 4.3). An improved photon budget should increase the number of molecules absorbing enough photons to be trapped, even with the current MOT force. Identification of a repumping pathway for the states ($\ell = 0, 2$) is currently underway, and the lasers will be added after the decided transition is identified spectroscopically.

Electronics are also being constructed to switch from white-light to chirped

slowing [183]. Past molecular experiments have seen improved MOT loading out of a chirped beam [179]. The chirping seems to compress the velocity distribution of the molecular beam, which also helps us decrease the population being pseudo-loaded out of an extended beam.

In the longer term, a "push beam" in combination with transverse 2D Sisyphus cooling will be added to our slowing path. Simulations of this combination of techniques in literature indicate that adding these should improve MOT loading by 20× [184]. Preliminary experimental results from the same group only show an increase of only 30%, but work in ongoing to determine where the discrepancy lies. In any case, any improvement in number of molecules will make it easier to detect the MOT.

Additionally, moving to a DC or blue-detuned MOT should increase the number of trapped molecules as well as lowering the temperature and increasing the density. Recent work on blue-detuned MOTs have demonstrated near-unity loading from a MOT into an ODT [58]. Simulation work is also being done to see if such a blue-detuned MOT can be loaded from either a short RF MOT, or no RF MOT at all.

When there are sufficient molecules trapped in the MOT, the next experimental step is to do sub-Doppler (typically Sisyphus) cooling to allow molecular transfer into an optical dipole trap (ODT) (e.g. as in Refs. [49, 57]). Once SrOH is loaded in the ODT, work can begin on testing measurement schemes and characterizing systematics effects for either EDM or μ-variation experiment.

4.9 Conclusion

In this chapter, we described the theory, design, and implementation of radiative slowing and magneto-optical trapping of the SrOH molecule for use in precision measurement experiments. The bulk of the experimental complexity for both techniques lies in the maintenance of an optical cycle capable of scattering $\sim 10^4$ photons. A cycle of this size is necessary to remove to sufficiently decelerate and cool the molecules, respectively.

The initial steps towards creating such an optical cycle predate this work. Decades old spectroscopy assigned many useful transitions at high resolution and was vital in identifying the molecule as a candidate for laser cooling in the first place. More recent work confirmed cycling on the main line and first few repumping transitions, and demonstrated application of this cycling in 1D Sisyphus cooling. Immediately before the work herein began, measurements of the vibrational branching ratios down to parts in 10^5 identified all the relevant vibrational leakage channels necessary to construct a scheme capable of scattering enough photons for full radiative slowing and magneto-optical trapping.

Using this data, we created an optical cycle capable of repumping the necessary ground states quickly and efficiently back to the main transition. These considerations were relevant to realizing the scheme in the lab in a cost-effective manner. The cycle is still being updated as properties of the molecule continue to be understood, but currently consists of 10 transitions out of 8 vibrational states. The light for 7 of these are produced by sum-frequency generation with

high-powered optical amplifiers. Two transitions are driven by ECDLs, and the last is driven by a Ti:Sapph, though soon to be replaced by enough ECDL.

For radiative slowing, the light is then dressed with ∼300 MHz of closely-spaced sidebands to address the entire range of Doppler shift during the process. The beams are combined into a single slowing beam and polarization-switched to destabilize instaneous magnetic dark states. The combined slowing beam counterpropagate against the molecular CBGB to decelerate the molecules. Optimization of laser power, detuning, and timing results in evident slowing of SrOH. The peak of the molecular distribution is reduced by > 50 m/s and trappable population is accumulated below 20 m/s.

To trap the decelerated molecules, RF MOT coils and MOT light are added at the end of the apparatus. The light polarization and RF magnetic field are synchronously switched to produce a time-averaged trapping force. To increase MOT stability, it was necessary to replace a transition in the cycle with a stronger line. Repeated tuning of magnetic field strength, light detuning, and relative timing of slowing light resulted in a preliminary MOT-like signal. Simulations indicated our data was a convolution of trapped and un-trapped molecules. More recent experimental data has identified approximately 50% of the MOT signal comes from trapped molecules with a lifetime $\sim$ 30 ms. The consistently low number of trapped molecules (<1000) and lifetime requires improvement before continuing on towards a precision measurement.

To improve population in the trap, simulations indicate we should change the MOT intensity, ramping speed, and beam size to increase the trapping force.

In addition, several experimental upgrades will increase the photon budget and molecular flux in the MOT region which will also increase the number of trapped molecules. Simulation-guided parameter searches will continue in parallel to identify other ways of increase the MOT force.

From such an enhanced MOT, it will then be possible to further compress (via a blue MOT or sub-Doppler cooling) the molecule distribution and load into an optical dipole trap. In such a trap it will be possible to conduct a measurement of either the eEDM or μ variation.

This work demonstrates that, though it is more complex than for CaOH, laser slowing and trapping of SrOH is possible, and likely not ultimately limited to SrOH. For an eEDM search, a heavier metal is preferable to Sr, such as Yb, Ba, or Ra. The considerations outlined in this chapter will be useful in slowing and trapping these species, as very few aspects are molecule-specific. Indeed, even constructing our optical cycle was done with fairly general structural considerations that likely remain valid in heavier species. Nevertheless, these heavier species can be expected to bring new complications with them. In particular, heavier metals tend (though are not necessarily guaranteed) to have more congested electronic structure, which can lead to perturbed excited state structure and metastable levels, both of which can increase the number of decay channels in the optical cycle and decrease the scattering rate. Many heavier species will also have lower-energy electronic states, which will decreases the recoil of a scattered photon further and requires longer experimental slowing distances or modification of the technique. It is the hope of the author that the work here

provides a stepping stone from which accommodating these perturbations can feel manageable, as previous demonstrations of slowing and trapping diatomic molecules and CaOH provided for us. It does not seem that there are fundamental incompatibilities with heavier linear molecules and these techniques of control, and as such, effort into understanding the differences in applying these techniques compared to now both SrOH and CaOH is well-warranted.

"Hope" is the thing with feathers -

That perches in the soul -

And sings the tune without the words -

And never stops - at all -...

Emily Dickinson

5

Towards Laser-cooling Nonlinear Molecules

Linear polyatomic molecules lie at a convenient intersection for current precision measurement experiments: similar enough to diatomics to make sense of the most difficult aspects of working with them, but novel enough to contribute

new structure and possibilities. Nevertheless our eyes turn towards the future: what is next*? The advantage of linear polyatomic molecules in EDM experiments over simpler laser-coolable diatomic molecules stems from their low-lying bending-mode "parity doublets" [5, 23, 185–187]. This structure allows for the full polarization of these species in the lab frame, and hence the full realization of their intrinsic sensitivities to new physics, as well as being powerfully useful in suppressing systematic errors in precision searches for symmetry violation [188, 189].

A disadvantage of using parity doublet states in a vibrational excited state is the shorter spontaneous lifetime compared to diatomic rotational states, $\tau \lesssim 1$ s (e.g. see Ref. Hallas *et al.* [49]). Symmetric and asymmetric top molecules, which we refer to as nonlinear molecules, feature many of the same desirable properties as vibrationally excited linear polyatomic molecules (low-field polarizability, parity-doublet-like structure, and compatibility with laser cooling [83, 187, 190]) in the vibronic ground state, with correspondingly long intrinsic lifetimes $\gtrsim$ 10 s. The benefits of nonlinear molecules for BSM searches, including the possiblity for very long coherence times, have been pointed out previously [83, 187, 190], but key elements of laser cooling them are less explored than for linear counterparts. While 1D laser cooling of a symmetric top species has been demonstrated [191], and an extension to asymmetric top species has been proposed [83] with initial studies already performed in $CaNH_2$ [70], further work is required to establish a road map to full 3D laser cooling and trap-

*This chapter takes and adds to the publication "Vibrational Branching Ratios for Laser-Cooling of Nonlinear Strontium-Containing Molecules"

ping of such molecules. In addition, the few extant studies of laser cooling low-symmetry molecules have focused predominantly on relatively light molecules. While these species are of interest for quantum information applications, many proposals for BSM physics searches rely on constituent atoms at least as heavy as Sr [5, 23, 185–187, 189, 192–194]. The effect of mass-dependent perturbations on laser cooling low-symmetry species is not well understood. As such, studying heavier molecules, even in the same symmetry group, provides vital information for precision measurement experiments that is not easy to generalize from existing work. The same or similar molecules are also of interest for quantum information platforms [195–198] and the study of low-temperature chemical reactions [199, 200].

As noted in Chapter 4, to laser cool any molecule, vibrational loss channels need to be identified to sufficient resolution to be able to create a sufficiently closed optical cycle. Computational techniques are rapidly improving [46, 99, 105, 201–205], but predictions of low-probability ($\sim 10^{-4}$–10^{-5}) decay channels have not yet been benchmarked against experimental results for heavy, nonlinear polyatomic molecules where vibronic perturbations are challenging to quantitatively model. As such, *ab initio* methods cannot be solely relied upon to assess the laser coolability of a complex molecule and direct measurements of the vibrational branching fractions (VBFs) must be experimentally recorded.

Though vibrational branching occurs during photon cycling in any molecular species, rotational loss may qualitatively differ in nonlinear species compared to their linear analogs. In linear species, rotationally closed transitions are simple

to identify based on parity and angular momentum selection rules, and the ability to drive a single rotational transition for most vibrational repumping levels is ensured [103, 206, 207]. Such rotationally closed transitions are not generally possible when laser cooling nonlinear molecules [83, 190, 191]. Rotational leakage channels for laser cooling schemes have not been previously analyzed on the basis of general symmetry-group properties. In particular, whether or not there are nonlinear symmetry groups which have "sufficient" symmetry to maintain rotational closure in reasonable perturbative limits is an open question.

To address these questions, we measure the VBFs of the lowest excited electronic states in three strontium-containing molecules: $SrOCH_3$, $SrNH_2$, and SrSH. We measure vibrational branching fractions as small as 0.01%, and by doing so investigate the mid-resolution vibrational branching of heavy species in three distinct symmetry classes (C_{3v}, C_{2v}, and C_s). Our measurements also invite an analysis of the rotational structure of the laser cooling transitions proposed for these molecules, and we expand upon ideas presented in Ref. Augenbraun *et al.* [83]. We also point out known perturbations in the Sr-containing species that exacerbate rotational leakage channels compared to the previously studied Ca species.

Through these analyses, this work provides a side-by-side comparison of the technical complexity required to laser cool isoelectronic species as a function of molecular symmetry. The combination of rovibrational analyses indicate that the easiest molecule to laser cool among those studied here is likely $SrNH_2$, the species of *intermediate* symmetry C_{2v}. Correspondingly, molecules from the C_{2v}

point group such as $SrNH_2$ (or heavier analogues such as $BaNH_2$, $YbNH_2$, and $RaNH_2$) appear to be the most preferable species for a next-generation laser-cooled EDM-sensitive nonlinear molecule—having fewer vibrational modes and rotational leakage channels than $SrOCH_3$, but greater symmetry protection against internal perturbations than SrSH. This highly motivates future work to measure VBFs in $SrNH_2$ at the $\sim 10^{-5}$ level, similar to prior work on SrOH [46], which should be possible with a few additions to our current methods.

Nevertheless, our work does not show the *impossibility* of laser cooling in any of these species, suggesting that with sufficient motivation laser cooling even C_s (and more easily, C_{2v} or C_{3v}) molecules is realizable, in agreement with previous proposals [83, 190, 208].

5.1 Method And Apparatus

We measure the VBFs of the three molecular species using the dispersed laser-induced fluorescence method and apparatus used in Ref. Lasner *et al.* [46] for SrOH. A schematic of the apparatus can be seen in Fig. 5.1.

The molecules are produced in a cryogenic cell ($\sim$8 K) by ablating a strontium target in the presence of both a species-specific reactant gas and a helium buffer gas. Sr atoms released by ablation react to form the molecules of interest, which are then quickly thermalized to the cell temperature by collisions with the buffer gas.

Methanol is used as the reactant gas to produce $SrOCH_3$, ammonia for $SrNH_2$, and 1,3-propanedithiol for SrSH. The reactant fill line temperature was kept at

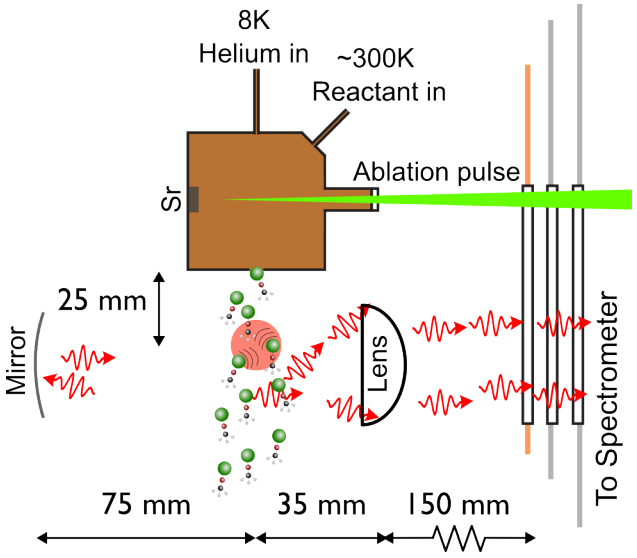

Figure 5.1: Schematic showing the apparatus as viewed from above. A strontium metal target, located inside a cryogenic copper cell, is ablated by an Nd:YAG laser. The strontium atoms then react with the reactant gas to form the molecule of interest. The molecules are thermalized to the cell temperature by helium buffer gas, and exit the cell rotationally cold. A laser beam excites molecules to the lowest excited electronic state, and the fluorescence from the subsequent decay is collected into a spectrometer.

$275 - 310$ K in all cases, despite differences in vapor pressure, to prevent clogs forming in the hot fill line due to ambient contamination in the system. The gas pressure immediately upstream of the fill line was approximately 3 Torr for methanol, 10 Torr for ammonia, and 1.8 Torr (approximately the vapor pressure) for 1,3-propanedithiol. Increasing the vapor pressure for methanol and ammonia did not drastically improve molecular production, but did coincide with a higher rate of clog formation that necessitated warming up the cryogenic system to near room temperature.

About 1" downstream of the production cell, the molecular beam is intersected by a $\sim$50 mW, $\sim$5 mm diameter beam of excitation light, tuned to the

rovibronic transition of interest (discussed in Section 5.2). The excitation light is generated using a Matisse tuneable Ti:Sapph laser, and is locked to ∼5 MHz with a High Finesse WS7 wavemeter. This light is directed into the chamber via cryogenically-mounted mirrors. These mirrors direct the light down and under the 4K shield to avoid a line-of-sight from the input window to the collection optics (therefore reducing scatter in the detection). At the lower height, the light traverses the 4K stage until it is beneath the production cell aperture, where another mirror directs it upward to vertically intersect the molecular beam. A mirror mounted off the cell-holding plate retroreflects the light back through the setup, which both increases interaction time and is useful for optical alignment without being able to see into the box.

The fluorescence from the molecular decays is collimated with a 50 mm in-vacuum lens (focal length 35 mm) and directed out of the chamber into another optical setup to direct it into a 0.67 m Czerny-Turner style spectrometer. The setup consists of mirrors to direct the light correctly through the spectrometer aperture and a long focal length lens to roughly focus the light as it passes through the spectrometer. The overall collection efficiency is limited by the spectrometer's numerical aperture of 0.11. An optical low-pass frequency blocks off-resonant scatter from entering the spectrometer. In the spectrometer, a 2400 line/mm grating disperses a ∼40 nm region of the spectrum onto an EM-CCD camera. We adjust the grating angle throughout the data taking process to select different subsets of the spectrum and thus cumulatively image over the entire wavelength range of interest for each molecule. The spectrometer tuning

knob is calibrated by McPherson to center light at the camera at a wavelength of (0.4 × knob value) nm.

Calibration of the spectrometer and camera system using known frequencies allows us to infer the wavelength and thus vibrational identity of the decays. The relative intensity combined with the spectral response of the spectrometer and camera allows us to obtain the relative probability of each decay.

Off-resonant scatter from the ablation laser, fluorescence from strontium atom decays, and EMCCD signal offsets can all contribute to the fluorescence signal as false molecular decays. We therefore take images of all combinations of ablation laser on/off and excitation light on/off for a given data point. A linear combination of images from these four configurations provides only the spectrum of the light emitted by the target molecules. We collect data using this method long enough to reach an ultimate VBF sensitivity of $0.01 - 0.1\%$.

5.2 Rotational Structure and Excitation Transitions

Since much of the literature on laser cooling molecules is focused on diatomic and linear triatomic species, here we outline the structural considerations of each of the molecules studied in this work. These considerations are relevant to both identifying the excitation transitions used to measure the relevant VBFs, as well as for evaluating the robustness of rotational closure. The basic structure is reviewed in Chapter 2.

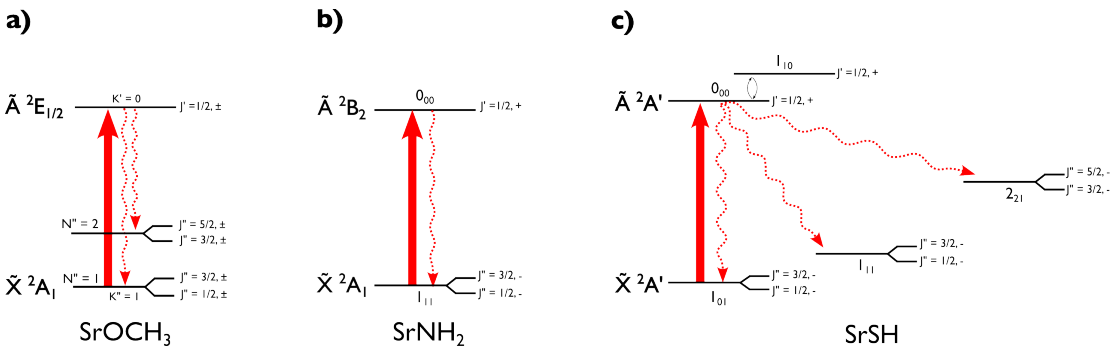

Figure 5.2: Schematics showing the relevant rotational structure in a) $SrOCH_3$, b) $SrNH_2$, and c) SrSH. Dashed lines show known rotational decay channels, and identify states that will need to be addressed in order to photon cycle in each species. The asymmetric top states are labeled as $N_{K_a K_c}$. In these molecules, the opposite parity states are not shown due to strict parity selection rules. Note also that these are only the confirmed decay channels; see Appendix D for all possible loss channels given the excitations used here. Even when perturbations are taken into account, $SrNH_2$ requires the fewest rotational repumps per vibrational decay channel.

5.2.1 $SrOCH_3$

$SrOCH_3$ is a C_{3v} symmetric top molecule. The ground electronic state is described as a $^2A_1$ representation [209, 210]. Levels in this state are well-represented by Hund's case (b). Since the end-over-end rotational constant, B (0.084 cm^{-1} [89]), is much smaller in $SrOCH_3$ than the symmetry-axis rotational constant, A (5.185 cm^{-1} [89]), the rotational levels labeled by N are grouped into ladders of distinct values of $K = |K^{\S}|$, where $K^{\S}$ is the projection of $\mathbf{N}$ onto the symmetry axis, a; for clarity, we employ a superscript silcrow to distinguish signed angular momentum projections from unsigned ones. The spacing between K manifolds is set by $A - B$. In states with $K \neq 3n$, each N level has a rotational E representation and possesses nearly degenerate opposite-parity states, known as a K-doublet, split only by weak hyperfine interactions [88]. Thus any state in these rotationally excited K manifolds will be easily polarized and therefore of

interest for EDM or quantum science experiments.

The lowest electronic excited state is described as a ^2E representation [209, 210], analogous to the $^2\Pi$ state in SrOH. As in SrOH, there is large spin-orbit coupling that splits the manifold into $^2E_{1/2}$ and $^2E_{3/2}$ manifolds; we drive transitions only to the former. This state is Hund's case (a), so that each rotational eigenstate has significant admixtures of distinct N values.

We use the notation $(N, K; J)^{\pm}$ to label rotational states in $SrOCH_3$, where the $\pm$ sign denotes parity. In the situation of Hund's case (a) states where N is a bad quantum number, we omit the N label. Likewise, we omit J and parity labels unless necessary.

For molecules in the C_{3v} point group, rotational closure schemes have been previously identified [190, 191, 208]. We reiterate the main points with a slightly modified discussion that emphasizes the structural selection rules in C_{3v} molecules, which will elucidate the comparison with the C_{2v} and C_s cases. The differentiating factors between rotational closure in linear versus C_{3v} molecules arise for states with non-zero rigid body rotational angular momentum about the a-axis, K_R, which have no analog in linear species.

Since there is no electric dipole moment perpendicular to the symmetry axis, rovibronic transitions do not change K_R (up to small perturbations such as the Jahn-Teller and pseudo-Jahn-Teller interactions that couple rotational and other angular momenta [202, 211, 212]) and an optical cycle must occur between states with the same value of K_R. The parity doublet structure of interest to symmetry violation experiments is not found in the $K = K_R = 0$ manifold

of $\tilde{X}^2A_1$, so we focus on the optical cycles available with $K_R = 1$.

A given $\tilde{A}^2E_{1/2}(N', K')$ component of an eigenstate may decay to $\tilde{X}^2A_1(N'', K' \pm 1)$ where $N'' = N'$ or $N' \pm 1$, subject to $N'' \geq K''$ and $K'' \geq 0$, a double-prime denotes a ground state label, and a single-prime denotes an excited-state label. Ideally, the $N' = K' = 0$ state, with $J' = 1/2$, would be targeted so that only $N'' = K'' = 1$ can be populated. Clearly, a $\tilde{A}^2E_{1/2}(0, 0; 1/2)$ state may mix with the $\tilde{A}^2E_{1/2}(1, 0; 1/2)$ state of the same parity while respecting J and parity conservation. Such a mixing will contribute additional decays to $\tilde{X}^2A_1(2, 0)$, necessitating a rotational repumping transition as demonstrated in Ref. Mitra *et al.* [191] for the $CaOCH_3$ laser cooling cycle originating from $K'' = 1$.

We now present a brief heuristic argument for why the C_{3v} molecular symmetry offers no *additional* protection against rotational state mixing in the $\tilde{A}^2E_{1/2}(K' = 0)$ manifold beyond that afforded by angular momentum and parity selection rules. States with distinct N components within the $\tilde{A}^2E_{1/2}(K' = 0)$ manifold essentially arise from different combinations of $(N'_R, K'_R = 1)$ states, where we have denoted the rigid body rotational angular momentum by N_R to distinguish it from the total angular momentum excluding spin, N. Since *all* of the $(N'_R, K'_R = 1)$ rotational states have an E representation in the C_{3v} point group, it follows that there cannot be a symmetry-based prohibition against mixing $N' = J - 1/2$ and $N' = J + 1/2$ states of the same parity within the $K' = 0$ manifold (which has $K'_R = 1$). Since the $\tilde{A}^2E_{1/2}$ state is Hund's case (a), the symmetry-allowed mixing between $(0, 0; 1/2)$ and $(1, 0; 1/2)$ components is of order unity and the $(0; 1/2)$ state decays with comparable strength to both

$\tilde{X}^2A_1(1,1)$ and $\tilde{X}^2A_1(2,1)$.

To study the vibrational branching fractions from the excited state used for laser cooling, we drive $\tilde{X}^2A_1(1,1;1/2)^{\pm} \rightarrow \tilde{A}^2E_{1/2}(0;1/2)^{\mp}$, as shown in Figure 5.2. Here the parity is denoted with $\pm$ ($\mp$) in the ground (excited) manifold because the parity doublets are split by a smaller energy gap than the natural linewidth of the transition. The $\tilde{X}^2A_1(1,1)$ state is significantly populated in our CBGB despite having a relatively large absolute rotational energy (owing to the large rotational constant $A = 5.2$ cm^{-1} [210]) because it is the ground rovibronic state of the para-$SrOCH_3$ isomer [191].

5.2.2 $SrCH_3$

We also attempted to study $SrCH_3$ as part of this work. However, we were unable to observe $SrCH_3$ in our CBGB using either chloromethane or methane as a reactant gas. This molecule has been observed in room temperature sources [213], though even in that work it was unobserved without Sr atom excitation light present. It has never been observed in cryogenic sources. Further work is needed to identify whether the production is merely suppressed by lack of atomic excitation or whether at cryogenic temperatures production is suppressed via some other mechanism (which would preclude the use of the molecule at all in a laser cooling experiment). Even in the former case, all other laser cooled species that report enhanced production from atomic excitation have some non-negligible production without it, and it thus seems questionable whether production could match the output of SrOH or the other species studied here. In light of this, we

suggest that this molecule does not appear especially promising for EDM measurements due to a substantial challenge with production.

5.2.3 $SrNH_2$

With a slightly lower degree of symmetry, $SrNH_2$ belongs to the C_{2v} point group. The ground state is described by the $^2A_1$ representation [214, 215]. As in $SrOCH_3$, this state is Hund's case (b) [216]. Individual rotational levels are again described by N. The projection K is no longer a good quantum number, but we can identify states with the additional labels K_a (K_c), denoting the value of K that would describe the state if the molecule were adiabatically deformed to a prolate (oblate) symmetric top. Because $A \gg B \approx C$ in $SrNH_2$, the level structure closely resembles that of a prolate symmetric top with K_a corresponding to K [216]. In the relevant case where the symmetry axis is along the a inertial axis, the parity of a state alternates with even vs. odd values of K_c and in the vibronic ground state, the parity is given by $P = (-1)^{K_c}$. The allowed values of K_c are $N - K_a$ and $N - K_a + 1$. The states comprising an effective parity doublet are therefore the two allowed states with the same N and $K_a \geq 1$ but different K_c. These states are inherently split by an amount set by the rotational constant asymmetry $B - C > 0$. In $SrNH_2$ the splitting between opposite-parity states in the $N = K = 1$ manifold (in the rigid rotor model neglecting details of hyperfine and spin-rotation structure) is ∼130 MHz [217], large enough to be spectroscopically resolvable but small enough to be easily polarized.

The $\tilde{A}^2B_2$ state differs qualitatively from the first excited state in SrOH and

$SrOCH_3$ because in the lower symmetry group there are no doubly-degenerate electronic manifolds. Physically, the degeneracy of the Π orbital is broken by the orientation of the hydrogen nuclei, and the in-plane vs. out-of-plane electron orbitals acquire distinct energies. However, there is still a moderately strong spin-orbit interaction, so the $\tilde{A}^2B_2$ state is described by Hund's case (a) just as in SrOH [216]. Rotational states are labeled by $(N_{K_a,K_c}; J)^{\pm}$, where as before $\pm$ denotes the parity of the state. J and parity labels are omitted unless necessary.

Routes to rotational closure for C_{2v} molecules have been previously identified [83]. For b-type transitions like $\tilde{X}$–$\tilde{A}$, the optical cycle proceeds on $\tilde{X}^2A_1(1_{11})$ $\leftrightarrow$ $\tilde{A}^2B_2(0_{00}; 1/2)^+$. Because parity alternates with K_c, a $(1_{10}; 1/2)^+$ rotational state from any B_2 vibronic manifold (possibly but not necessarily $\tilde{A}^2B_2$) has the same J and parity values as the excited laser cooling state. As seen for the case of C_{3v} molecules, the possibility should be considered that such a (1_{10}) state could mix with $\tilde{A}^2B_2(0_{00})$, leading to rotational leakage channels such as to $\tilde{X}^2A_1(1_{01})$ or $\tilde{X}^2A_1(2_{21})$. However, such a mixing is strictly forbidden in C_{2v} molecules, up to hyperfine or Coriolis-like interactions that couple states of different rotational symmetries (and which are expected to be very weak). Specifically, the (0_{00}) rotational state has the A_1 representation, while the (1_{10}) state has the B_1 representation; thus the (0_{00}) excited state rotational label must be highly pure. This behavior guarantees much stronger protection against rotational leakage channels than in C_{3v} or (as we will see) C_s molecules. See Appendix D for more details. We note that any rotational leakage channel introduced by the weak rotational-symmetry-violating perturbations mentioned

above is likely to require repumping for only the strongest vibrational decays, if at all, in order to cycle $\sim 10^4$ photons.

To study the laser cooling transition, we drive $\tilde{X}^2A_1(1_{11};1/2)^-$ $\rightarrow \tilde{A}^2B_2(0_{00};1/2)^+$, as seen in Figure 5.2. The molecular symmetry enforces a relationship between the rotational and hydrogen nuclear states, and (as discussed in Appendix D) $\tilde{X}^2A_1(1_{11})$ is the ground state of the $I_{H_{\text{tot}}} = 1$ isomer, where $I_{H_{\text{tot}}}$ is the total hydrogen nuclear spin. Since the nuclear spin is not efficiently changed during buffer gas cooling, this state thus has a significant population in our CBGB despite being at a relatively large energy (set by $A = 13.5\text{cm}^{-1}$ [217]) compared to the absolute ground $\tilde{X}^2A_1(0_{00})$ state.

We note that the nuclear spin state associated with the nitrogen atom is always in the totally symmetric representation of the C_{2v} group and thus has no effect on the selection rules or naturally populated states of $SrNH_2$. Furthermore, the hyperfine interaction arising from coupling of the nitrogen spin to the electron spin can be expected to be approximately an order of magnitude weaker than in SrF owing to the smaller nuclear magnetic dipole moment of both naturally abundant nitrogen isotopes, ^{14}N (with $I_N = 1$, $\mu = 0.40\ \mu_N$ where μ_N is the nuclear magneton) and ^{15}N (with $I_N = 1/2$, $\mu = -0.28\ \mu_N$), compared to ^{19}F (with $I_F = 1/2$, $\mu = 2.63\ \mu_N$) [218]. Based on our *ab initio* calculations we have estimated the splittings arising from the nuclear electric quadrupole moment interaction (which does not occur in SrF) between ^{14}N and the electric field gradients in the molecule to be $\sim$1 MHz. The hyperfine interactions arising from the hydrogen nuclear spins are also expected to

be only ∼1 MHz due to the large distance between the metal-centered valence electron and the hydrogen atoms. We therefore expect all hyperfine splittings to be $\lesssim$10 MHz, approximately within a natural linewidth of the $\tilde{X}$ – $\tilde{A}$ transition and not requiring additional frequency sidebands to address during laser cooling. To date, no hyperfine splittings in $SrNH_2$ have been observed. Thus only a single low-frequency sideband is required to address the spin-rotation splitting in order to achieve rotational closure in $SrNH_2$.

5.2.4 SrSH

With only a single reflection plane, SrSH belongs to the C_s point group [219]. Also an asymmetric top, the electronic and rotational structure is similar to $SrNH_2$. However, the point group is smaller, and as a result there are only two allowed representations. The ground electronic state transforms as the A' representation, and is analogous to the ground states of the other molecules studied here [219]. The rotational structure in $\tilde{X}$ is the same as in $SrNH_2$, and we employ the same rotational state notation. In the rigid rotor model (i.e., neglecting the full structure including spin-rotation and hyperfine splittings), the nominal parity splitting in the $N = K_a = 1$ rotational state manifold proposed for laser cooling of SrSH is ∼30 MHz [220].

The lowest electronic excited state of SrSH also transforms as the A' representation, but is again described as a Hund's case (a) state [219, 221]. Though the first-order rotational structure of this state is the same as in $SrNH_2$, the reduced symmetry is compatible with rotational state mixing even in $J = 1/2$

states. Specifically, in vibronic A' manifolds the rotational states with $K_c = +1$ transform as A' and those with $K_c = -1$ transform as A''. As a result, $A'(0_{00}; 1/2)$ and $A'(1_{10}; 1/2)$ states have the same rotational symmetry and may, under the influence of perturbations, generically mix with each other. Provided such a mixing exists, the laser cooling scheme suggested in Ref. Augenbraun *et al.* [83] for the predominantly *b*-type $\tilde{X}^2A'$–$\tilde{A}^2A'$ transition will be limited by rotational leakage from the $\tilde{A}^2A'(1_{10})$ admixture to $\tilde{X}^2A'(1_{01})$ and $\tilde{X}^2A'(2_{21})$ ground states.

The proposed laser cooling transition, $\tilde{X}^2A'(1_{11})^- \rightarrow \tilde{A}^2A'(0_{00}; 1/2)^+$, could not be directly excited in our CBGB because of the large rotational energy of $\tilde{X}^2A'(1_{11})$, set by the rotational constant $A = 9.71\text{cm}^{-1}$ [220], and correspondingly low thermal population. In principle, the $\tilde{X}^2A'$–$\tilde{A}^2A'$ transition dipole moment contains a small "*a*-type" amplitude, so that $\tilde{A}^2A'(0_{00})$ can also be populated from $\tilde{X}^2A'(1_{01})$. We therefore drive $\tilde{X}^2A'(1_{01}; 1/2)^- \rightarrow \tilde{A}^2A'(0_{00}; 1/2)^+$ in order to measure rovibrational branching fractions from the proposed laser cooling excited state, as shown in Figure 5.2. We find this transition to be of comparable strength to *b*-type transitions in the $\tilde{X}^2A'$–$\tilde{A}^2A'$ band, consistent with the reports of Ref. Sheridan *et al.* [221] where strong transitions were observed between $K_a'' = 0$ and $K_a' = 0$ states due to a large excited-state perturbation. Though a concrete physical origin of the perturbation was not identified in that work, and cannot be inferred from our measurements, we interpret these results as supporting the existence of the mixing suggested above between $\tilde{A}^2A'(0_{00})$ and $\tilde{A}^2A'(1_{10})$. We note that Ref. Sheridan *et al.* [221] observed less evidence

of perturbation in the excited state of CaSH, highlighting that although mixing between (0_{00}) and (1_{10}) would be *permitted* in the excited state of any C_s molecule, its actual prevalence must be assessed on a case-by-case basis. We provide additional evidence for this mixing in SrSH, and discuss its implications for laser cooling, in Sec. 5.4.

5.3 Results

By driving transitions to the relevant rovibrational levels in the first excited electronic states of $SrOCH_3$, $SrNH_2$, and SrSH, we record VBFs out of these states at or below the $\sim$0.1% level. The resulting dispersed fluorescence spectra can be seen in Fig. 5.3.

We use the calculated vibrational energies and branching fractions to help identify each decay channel. We denote the i-th vibrational mode v_i, identified for each molecule of interest in Table 5.1. Vibrational energy levels are labeled according to the convention $i_{n(i)}j_{n(j)}\cdots$ to denote the state with $n(i)$ quanta of excitation in mode v_i, and so on. Modes with $n(i) = 0$ are omitted, and the special case of the vibrational ground state is denoted 0_0. We do not measure or assign rotational branching fractions to vibronic levels where multiple *rotational* levels are populated. Peak intensities are computed by integrating the signal over the width of a feature. The resulting calculated VBFs done by our collaborator Lan Cheng can be found in Tables 5.2–5.4 (see [106] for details of the calcuational methods).

$SrOCH_3$

Number	Description	Representation
1	C–H sym. stretch	a_1
2	CH_3 umbrella	a_1
3	C–O stretch	a_1
4	Sr–O stretch	a_1
5	C–H asym. stretch	e
6	Scissor	e
7	Rock	e
8	Sr–O–C bend	e

$SrNH_2$

Number	Description	Representation
1	N–H sym. stretch	a_1
2	NH_2 bend	a_1
3	Sr–N stretch	a_1
4	Sr–N–H out of plane bend	b_1
5	N–H asym. stretch	b_2
6	Sr–N–H in plane bend	b_2

SrSH

Number	Description	Representation
1	S–H stretch	a'
2	Sr–S stretch	a'
3	Sr–S–H bend	a'

Table 5.1: Ground state vibrational mode labels and representations for each of the species studied here.

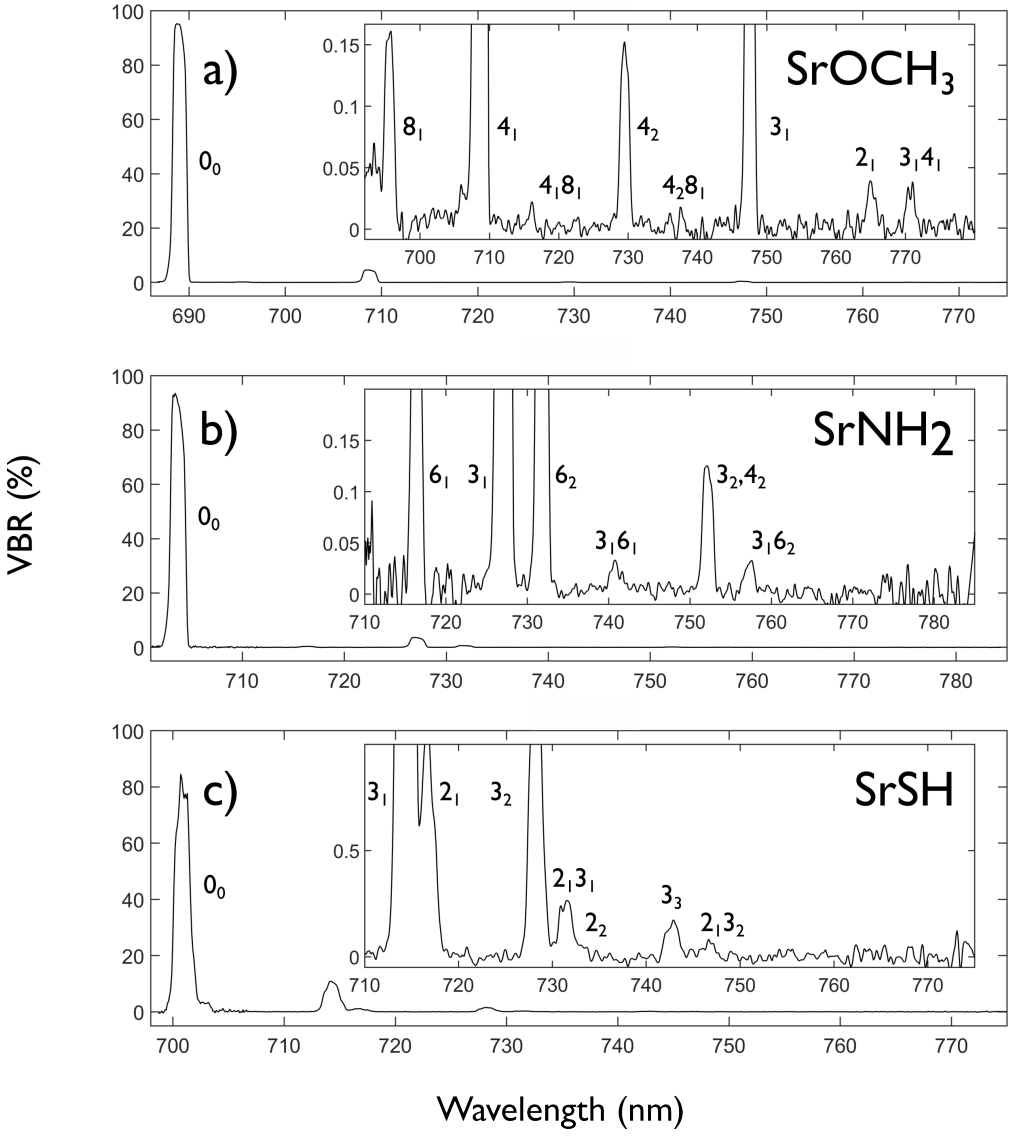

Figure 5.3: VBF data for (a) $\mathrm{SrOCH_3}$, (b) $\mathrm{SrNH_2}$, and (c) SrSH. Insets show the same spectra at higher resolution. Accompanying VBFs are found in Tables 5.2–5.4. States are labeled according to the modes in Table 5.1. State labels separated by commas indicate transitions to different states that are unresolved by the spectrometer.

5.4 Discussion

5.4.1 $SrOCH_3$

We measure the vibrational branching fractions of $SrOCH_3$ over a range of 80 nm. We reach an ultimate VBF sensitivity over this range of $\sim$0.01%. We find qualitatively worse scaling of vibrational branching than in the isoelectronic linear molecule SrOH; see Table 5.2. We note two contributions to this difference.

First, the decay to a single quantum of the Sr–O–C bending mode (8_1) is about an order of magnitude larger than to the analogous (010) state of SrOH. This bending state is also accompanied by higher-probability decays to some combination states ($4_1 8_1$ and $4_2 8_1$). Two vibronic coupling mechanisms contribute to these decays. One is the Jahn-Teller effect (JTE), which mixes 0_0 and 8_1 in the $\tilde{A}$ state, making these decays no longer vibronically forbidden [75]. The other mechanism is vibronic coupling between the $\tilde{A}^2E$ states and the $\tilde{B}^2A_1$ state. This is essentially the same as the "direct vibronic coupling" (DVC) mechanism [105, 204] in CaOH and SrOH that borrows the intensity for the VBFs to (010) states. In the following we also refer to this vibronic coupling mechanism as the DVC mechanism.

These effects similarly contribute to enhancing the strength of decays in $CaOCH_3$ to the 8_1 mode compared to (010) in CaOH [65, 94, 202]. In the present computational treatment, the inclusion of spin-orbit coupling has been shown to quench the JTE; the first excited state with spin-orbit coupling has the C_{3v} structure as a minimum on the potential energy surface. We have included the

DVC contribution via perturbation theory using the formulation reported in Ref. Zhang *et al.* [204]. The VBF to 8_1 thus computed agrees reasonably well with the measured value. The VBF to 8_1 in $SrOCH_3$ is larger than that to the first excited bending mode in SrOH. This is readily attributed to that the value of around 120 cm^{-1} for the linear vibronic coupling constant [222] between the $\tilde{A}^2E$ and $\tilde{B}^2A_1$ states in $SrOCH_3$ is larger than the value of 70 cm^{-1} between the $\tilde{A}^2\Pi$ and $\tilde{B}^2\Sigma$ states in SrOH [46].

The second cause of increased branching channels is simply that there are more modes (of both allowed and nominally forbidden symmetry) to decay to than in smaller molecules. In particular, in addition to the a_1 symmetry Sr–O stretch (v_4), $SrOCH_3$ also has an a_1 symmetry C–O stretch (v_3). We find decay to both the 3_1 and 3_14_1 states above our measurement sensitivity. Two other a_1 vibrational modes also exist, the CH_3 "umbrella" mode (v_2) and the C–H symmetric stretch (v_1). Near the noise floor we tentatively assign a small decay to 2_1, though as expected it is suppressed compared to the modes more closely coupled to the Sr atom. The decay to 1_1 lies beyond our measured wavelength range, but calculations predict the decay to this mode to be below our measurement sensitivity of $\sim$0.01%. Decays to the three remaining modes in the molecule—namely, the C–H asymmetric stretch (v_5), CH_3 scissor (v_6), and CH_3 rock (v_7)—would be accompanied by infrared fluorescence outside of our measurement range but are all nominally symmetry forbidden. Our computational work supports the negligibility of these modes at the sensitivity of the present work. Thus several (though not all) modes in $SrOCH_3$ without any analog in

$SrOCH_3$ $\tilde{A}^2E_{1/2}$ 0_0

	Energy (cm^{-1})		VBF (%)	
State	Calc.	Exp.	Calc.	Exp.
0_0	0	0	92.688	94.7(2)
8_1	144	138(5)	0.145	0.18(8)
8_2	286	—	0.066	<0.02
4_1	406	404(2)	6.369	4.5(2)
4_18_1	553	547(3)	0.009	0.017(7)
4_2	810	807(2)	0.123	0.145(10)
4_28_1	960	965(5)	0.000	0.010(6)
3_1	1177	1138(2)	0.509	0.38(2)
2_1	1472	1446(4)	0.055	0.037(7)
3_14_1	1582	1542(2)	0.023	0.033(6)
2_14_1	1878	—	0.005	—
3_2	2339	—	0.002	—
1_1	2799	—	0.006	—

Table 5.2: Predicted and observed vibrational state energies and branching fractions from the $SrOCH_3$ $\tilde{A}^2E_{1/2}$ ground vibrational state. The predicted decays to 2_14_1, 3_2, and 1_1 lie outside of the measured wavelength range toward the infrared.

smaller species such as SrOH or SrSH contribute relevant vibrational decays around the 0.01% level.

One surprise in the spectrum is the lack of an observed 8_2 decay. Calculations predict that it should occur around the 0.07% level, as it is vibronically allowed. However, we see no such decay, and bound the decay to $< 0.02\%$. We know of no technical reason that a peak larger than this would not appear in our dataset.

In all, we find at least 9 vibrational levels populated above 0.01% probability, compared to 5 in SrOH. The measurements and predictions are in generally good agreement. We therefore tentatively extrapolate from the computed re-

sults that approximately 11 vibrational states will be populated in a photon cycle with $\gtrsim$15,000 scatters, compared to 8 in SrOH [46]. In addition, as noted in Sec. 5.2, most of these vibrational repumpers will require addressing two well-separated rotational states, increasing the experimental challenge significantly further. Since the production rates of SrOH and $SrOCH_3$ are comparable, these factors unambiguously indicate a much more challenging laser cooling scheme for $SrOCH_3$. Nevertheless, as the rotational closure is well understood and the VBF measurements identify the relevant peaks to the $\sim$0.01% level, we expect $SrOCH_3$ to be realistically fully laser coolable with sufficient effort.

5.4.2 $SrNH_2$

We measure VBFs for the $SrNH_2$ $\tilde{A}^2B_2$ 0_0 state over a similarly wide range of $\sim$80 nm. Due to lower production, however, our ultimate sensitivity is limited to $\sim$0.05% branching fraction. We find a similar number of states populated at our ultimate sensitivity as in SrOH (see Table 5.3). However, there are several important differences between $SrNH_2$ and its linear analog. Most notably, the Sr–NH_2 bending motions, which in a linear species are doubly degenerate, are separated by $>100\text{cm}^{-1}$ and belong to different 1D representations. Decay to the in-plane vibrational bending excitation, 6_1, can be induced by vibronic perturbations between $\tilde{A}^2B_2 0_0$ and $\tilde{C}^2A_1 6_1$, owing to the b_2 symmetry of the v_6 mode. This decay is much stronger than the analogous (010) decay in SrOH. The out-of-plane v_4 mode is predicted to be populated in the 4_2 level near our measurement resolution, though we do not observe a corresponding peak. Thus,

$SrNH_2$ $\tilde{A}^2B_2$ 0_0

	Energy (cm^{-1})		VBF (%)	
State	Calc.	Exp.	Calc.	Exp.
0_0	0	0	94.024	95.1(2)
6_1	260	252(4)	0.351	0.35(3)
3_1	454	459(1)	4.627	3.7(2)
6_2	531	547(2)	0.869	0.63(3)
3_16_1	699	717(9)	0.019	0.04(1)
3_2	904	918(4)	0.048	0.10(1)
4_2	888	∼918	0.012	0.03(1)
3_16_2	965	1007(2)	0.030	0.03(1)
6_4	1083	—	0.002	<0.03
2_1	1540	—	0.014	—
1_1	3331	—	0.003	—

Table 5.3: Predicted and observed vibrational state energies and branching fractions from the $SrNH_2$ $\tilde{A}^2B_2$ ground vibrational state. We tentatively assign the observed 918cm^{-1} peak to the sum of unresolved decays to 3_2 and 4_2. The ratio of VBFs to these two components is assumed to match the calculated ratio. The expected decays to 2_1 and 1_1 lie outside of the measured wavelength range.

despite the lack of bending degeneracy, the lower symmetry of $SrNH_2$ compared to SrOH does not seem to induce more loss channels at the 0.05% level.

Another difference from SrOH is that the NH_2 bend is predicted to be populated around the 0.01% level, though it is outside of our measured wavelength range. This is a significantly higher level than ligand modes in SrOH, and indicates a less polar bond, which is supported by spectroscopic analysis [215]. The branching fraction to the N–H stretch mode is predicted to be around 0.003%, smaller than that of the C–H stretch in $CaOCH_3$. This is likely not limiting for a target photon budget of $\sim 10^4$ scatters. Overall, the loss channels introduced by the amine group are manageable though nonzero.

In addition to these structural differences, there are also several resonances that appear to perturb the ground state vibrational manifold substantially. In particular, the 3_1 and 6_2 states are close in energy and of the same symmetry, and so are mixed by a strong Fermi resonance. Overtones and combination bands will also be mixed (e.g., 3_2 and 3_16_2). Consider the transitions to the 3_1 and 6_2 states as examples. The computed branching fraction to the 6_2 state within the harmonic approximation is less than 0.1%. We thus infer that the branching fraction of 0.6% for the transition to 6_2 observed here predominantly arises from the mixing with the 3_1 state due to the Fermi resonance. The VPT2 calculation that explicitly diagonalizes the 2×2 matrix expanded by the 3_1 and 6_2 harmonic oscillator wave functions shows that the 6_2 state has around 15% contribution from the 3_1 harmonic oscillator wave function. This gives rise to the $\sim$1:5 intensity ratio between the decays to the 6_2 and 3_1 states. Since these states would likely be populated in 10^4 optical cycles even in the absence of Fermi resonances, these ground state resonances should not substantially affect the complexity of laser cooling the molecule. A similar Fermi resonance appears in CaOH between the (100) and (020) modes and does not significantly impact the number of states needed for full photon cycling [57, 94].

We also note that the present calculations may not have captured the resonances among the overtones accurately. The computed levels for 3_1 and 6_1 agree well with the measured values. However, the computations substantially underestimate the level positions for the 3_16_1 and 3_16_2 states. Future computational work will be focused on improving the potential energy surfaces and per-

forming variational calculations of vibrational structures to go beyond VPT2.

We find only 7 vibrational states populated at the ∼0.05% level, slightly more than in SrOH. Extrapolating to the $\gtrsim$15,000 photon scatter level using computed branching fractions, only 9 vibrational states are expected to be populated. At the same branching probability level there are 8 populated vibrational levels in SrOH. However, because every vibrational decay is rotationally closed in $SrNH_2$ (unlike for the bending mode excitations in SrOH), remarkably we tentatively anticipate one fewer repumping laser to be necessary to achieve the same degree of rovibronic closure. Thus $SrNH_2$ appears a strong choice for full laser cooling in a future precision measurement, as it is significantly simpler both rotationally and vibrationally than $SrOCH_3$, while possessing long-lived parity doublet structure in the ground state.

5.4.3 SrSH

In SrSH we see evidence of decay to *all* K_a manifolds allowed by selection rules on J from the $\tilde{A}^2A'(0_{00};1/2)^-$ excited state. We find this well-explained by the symmetry-allowed mixing suggested previously between $\tilde{A}^2A'(0_{00})$ and $\tilde{A}^2A'(1_{10})$. Sheridan *et al.* also suggested a large perturbation (of unclear fundamental origin) in SrSH that mixes $K_a' = 0$ and $K_a' = 1$ states.

To test the effect of the perturbation more rigorously, we recorded the fluorescence spectrum for excitations to several rotational levels in the $\tilde{A}^2B_20_0$ state. We narrowed the spectrometer slit to ∼5 μm to resolve the decays to distinct K_a manifolds, which are spaced on a scale set by the a-axis rotational

SrSH $\tilde{A}^2A'$ 0_0

	Energy (cm^{-1})		VBF (%)	
State	Calc.	Exp.	Calc.	Exp.
0_0	0	0	88.383	85.2(5)
3_1	268	268(2)	10.206	10.9(5)
2_1	323	315(4)	0.629	1.85(9)
3_2	540	536(2)	0.499	1.51(8)
2_13_1	604	596(3)	0.113	0.29(2)
2_2	634	∼623	0.102	0.07(4)
3_3	815	805(2)	0.013	0.17(3)
2_13_2	889	875(2)	0.008	0.07(3)
2_23_1	928	—	0.010	< 0.03
1_1	2895	—	0.036	—

Table 5.4: Predicted and observed vibrational state energies and branching fractions from the SrSH $\tilde{A}^2A'$ ground vibrational state. A shelf toward the red side of the peak arising from decays to 2_13_1 is tentatively assigned to 2_2; however, a reliable energy estimation for 2_2 cannot be made due to the partially unresolved spectrum. The predicted decay to 1_1 lies outside of the measured wavelength range.

constant, $A = 9.71\text{cm}^{-1}$, and thus resolvable [220]. Branching to different N and J levels within each K_a manifold remains unresolved.

In particular, we measured the decay patterns to the $\tilde{X}^2A_10_0$ vibrational state for excitations to $J' = 1/2$ and $J' = 3/2$ states in both $K'_a = 0, 1$ manifolds. The results can be seen in Fig. 5.4. There are clearly more decay channels from the nominal $\tilde{A}(1_{10}; 3/2)$ state than from either of the $\tilde{A}(0_{00}; 1/2)$ or $\tilde{A}(1_{11}; 1/2)$ states, indicating a dependence of K_a branching fractions on J. At the simplest level, this behavior occurs because an excited $J' = 1/2$ state can mix with other $J' = 1/2$ states, implying at most $N' = 0, 1$ components. Since $K_a \leq N$, consequently a $J' = 1/2$ state has at most contributions from the $K'_a = 0, 1$ manifolds. For a b-type transition, these components can populate

$K_a'' = 0, 1, 2$ upon decay. On the other hand, a $J' = 3/2$ state can have components with $N' = 1, 2$ and therefore $K_a' = 0, 1, 2$, which are allowed to decay via b-type transitions to $K_a'' = 0, 1, 2, 3$.

Though parity and angular momentum selection rules would allow $\tilde{A}(2_{02}; 3/2)$ to mix with $\tilde{A}(2_{20}; 3/2)$, the decay spectrum of $\tilde{A}(2_{02}; 3/2)$ does not show a significant decay to $K_a'' = 3$, which would be expected from any $\tilde{A}(2_{20}; 3/2)$ admixture. Thus not *every* pair of states with the same J and parity have order-unity mixing even in the presence of this perturbation.

Clearly, the admixture of the "leaky" rotational state $\tilde{A}^2A'(1_{10}; 1/2)$ into the nominal optical cycling excited state, $\tilde{A}^2A'(0_{00}; 1/2)$, is of order unity and will therefore meaningfully affect decays to all higher vibrational branches in $\tilde{X}^2A'$ as well. This behavior can be contrasted with any rotational leakage channels that could plausibly be induced in $SrNH_2$ by Coriolis or hyperfine interactions, where few if any vibrational states should require rotational repumping. The three K_a manifolds populated in each of the SrSH vibrational decays are also too widely spaced ($\gtrsim$300 GHz) from the optical cycle origin to be bridged by typical frequency modulation techniques.

Since the perturbations indicate that laser cooling this species is likely exceedingly difficult, we only measure VBFs to $\sim$0.1% and examine a fluorescence wavelength range of 60 nm. Nevertheless, we can still analyze the VBFs, compare the computations and experiment, and compare to the other species studied here. We find poor vibrational branching for photon cycling, with 6–7 states populated above 0.1%—significantly worse than SrOH, $SrOCH_3$, or $SrNH_2$. This

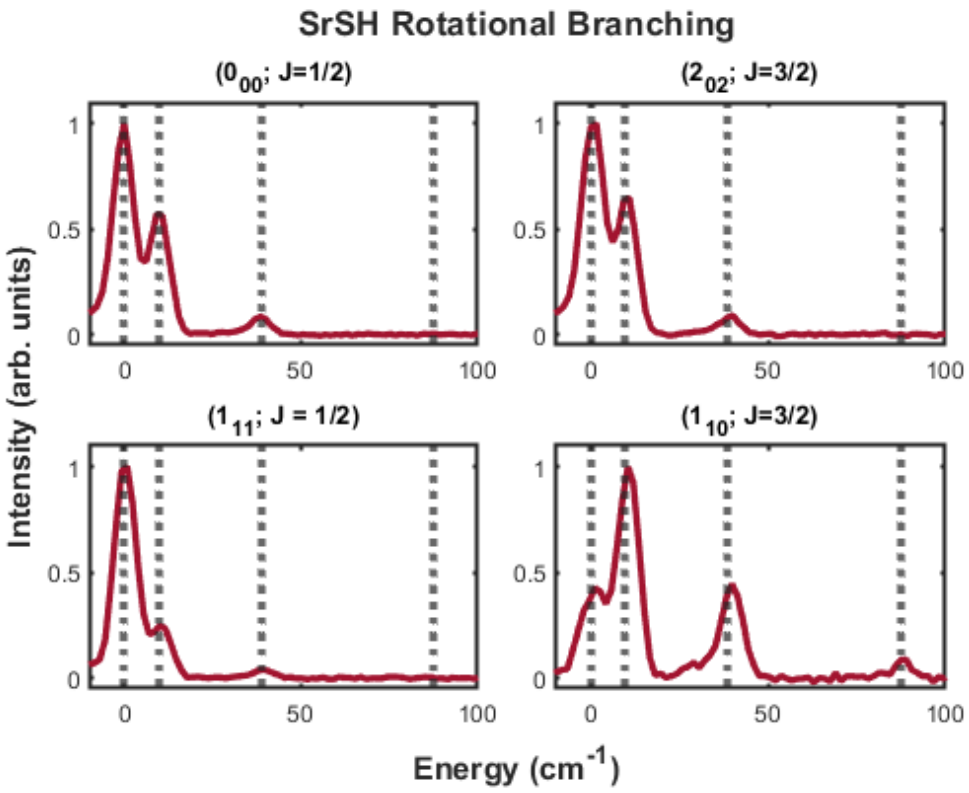

Figure 5.4: Comparison of rotational branching for four rotational levels in the SrSH $\tilde{A}^2A'$ 0_0 state to the $\tilde{X}^2A'$ 0_0 state. Each peak corresponds to a decay to a different K_a level in the ground state. Dashed lines indicate the energies of K_a levels using the measured A constant [216]. Note that four decays only happen for $K_a' = 1$ *and* $J' = 3/2$. The other states show only three decays.

comparison is well-explained by the difference in structure of the vibrational modes compared to the other species. Particularly of note, the C_s point group has only two representations, both one-dimensional. All vibrational modes are a' symmetry. Furthermore, the most relevant modes—the Sr–S–H bend, v_2, and the Sr–S stretch, v_3—are close in energy and thus decays to one are typically accompanied by decays to the other due to mixing between vibrational states. This effectively introduces a similarly strong bend or combination mode for every Sr–S stretch, which matches the factor of ∼2 difference in number of populated decays at the 0.1% level compared to SrOH.

As shown in Table 5.4, the computed vibrational frequencies agree well with the measured ones. The double harmonic approximation tends to underestimate the VBFs to the overtones of the Ca–S stretching mode. This is consistent with the observation for the Ca–O stretching modes of CaOH [204]. In addition, we mention that the VBF to the S–H stretch mode, 1_1, in SrSH is predicted to be 0.036%, an order of magnitude larger than that for the C–H stretch in $SrOCH_3$ and the N–H stretch in $SrNH_2$. This is also unfavorable for laser cooling.

We thus attribute both the poor rotational and vibrational branching in SrSH to the low symmetry of the species. In particular, the absence of higher symmetry is what allows the K_a mixing to occur in the $\tilde{A}^2A'$ state, as such a mixing is forbidden in higher-symmetry analogs (specifically, in C_{2v} species). Similarly, mixing between all vibrational states is symmetry-allowed, unlike in higher-symmetry species, substantially increasing the number of significant decays beyond SrOH. Given that a single vibrational repumper requires at least three

widely-spaced laser frequencies to address all populated K_a'' manifolds, and many more vibrational states would be populated in an optical cycle of sufficient depth to fully laser cool the molecule, these findings indicate that molecules in the lowest symmetry groups (C_s and C_1) pose significant challenges and are less favorable candidates for laser cooling experiments unless there is a strong specific motivation to use such a species (for example, many chiral molecules, including SrOCHDT [83], belong to the C_1 point group). However, such a motivation is not apparent for precision measurement applications such as EDM experiments, where these lowest symmetry groups possess states of only similar polarizability and lifetime as C_{2v} and C_{3v} molecules, which are likely simpler to control.

5.5 Conclusion

We measure the vibrational branching fractions of three nonlinear strontium-containing molecules: $SrOCH_3$, $SrNH_2$, and SrSH. Each of these species has sensitivity to BSM physics searches similar to SrF and SrOH. The lower structural symmetry of these species offers parity doublets in the vibronic ground state, thus combining the polarizability in small electric fields and parity doublets of linear triatomics with the long lifetime of rotational states in diatomics. We measure VBFs and further elucidate to what degree these nonlinear molecules are laser coolable.

There is evidence in the literature of severe perturbation in higher electronic states for all three molecules [89, 216, 221], suggesting that the simplest path to

photon cycling is likely through the $\tilde{A}$ states. Side-by-side comparisons of laser coolability as a function of molecular point group are studied for these excited states in particular.

We identify complications with rotational closure related to the respective symmetry groups. The low symmetry of SrSH allows perturbations that result in ≥ 3 rotational decays of comparable strength for each vibrational excitation. The greater molecular symmetry in the C_{3v} and C_{2v} point groups prevents these perturbations from appearing at low order in $SrOCH_3$ and $SrNH_2$. Conversely, there is one fewer symmetry-allowed rotational loss channel for the laser cooling excitation in $SrNH_2$ than in $SrOCH_3$ due to the lower symmetry of the former.

To asses vibrational loss channels, we measure the VBFs out of each molecule's $\tilde{A}$ excited state to at least the 0.1% level. We find that the number of vibrational loss channels at this precision are similar between SrOH, $SrOCH_3$, and $SrNH_2$. SrSH is found to have significantly more loss channels than SrOH. All loss channels for the three molecules are measured to at least the 0.1% level, sufficient to implement one-dimensional laser cooling in the style of Refs. Augenbraun *et al.* [66], Mitra *et al.* [191]. Full 3D laser cooling in the typical configuration [57] will require $\sim$10$\times$ higher-resolution VBF measurements for $SrOCH_3$ and $SrNH_2$, and $\sim$100$\times$ higher-resolution for SrSH.

Looking toward a future polyatomic molecule for the most precise BSM searches, the choice of species to pursue further is clear. In particular, the simplicity of rotational closure in the C_{2v} point group and controlled vibrational branching at the 0.05% fractional level make $SrNH_2$ the most promising candidate

for a next-generation search for the electron electric dipole moment. Comparison of Table 4.2 and Table 5.3 illustrates that cooling the $SrNH_2$ molecule be very similar in complexity to the work on SrOH in Chapt. 4. Further investigation of the $SrNH_2$ VBFs to the 10^{-5} level is thus warranted to identify whether there are any perturbations that appear at higher resolution, which might prevent straightforward full laser cooling and control of the species. These measurements will be possible with the addition of Sr chemical enhancement light [140, 210, 216] and spin-rotational closure. Such work would enable full laser cooling of $SrNH_2$ and make possible an EDM experiment in a long-lifetime conservative trap, reducing the volume over which a high degree of systematic control is necessary. Similar work on $CaNH_2$ could be useful in quantum information experiments. To this end, a comparison of $SrNH_2$ and $CaNH_2$ versus their linear polyatomic counterparts can be found in Tab. 5.5.

Comparison of Linear and C_{2v} Varieties of Sr and Ca Molecules

		CaOH	$CaNH_2$	SrOH	$SrNH_2$
Cycling excited electronic manifolds		2	?	2	?
Main Lines (nm)	$\tilde{A}$	625	647	688	703
	$\tilde{B}$	555	630	611	682
1× Stretch repumper (nm)	$\tilde{A}$	650	670	711	726
	$\tilde{B}$	575	652	631	704
Current VBF accuracy		10^{-5}	10^{-3}	10^{-5}	10^{-4}
Repumpers known to <5 cm^{-1}		>11	3	9	5
Est. repumpers for 10^4 photons		11	?	9	9-10
Observed in a CBGB		Yes	Yes	Yes	Yes
Enhancement known		Yes	Yes	Yes	Yes
Literature		[57, 223]	[224]	(see Chapt. 4)	

Table 5.5: Comparison of laser-cooling considerations between linear and C_{2v} molecules of Ca and Sr.

We expect very similar behavior for other metal containing molecules (e.g. $RaNH_2$, $YbNH_2$, or $BaNH_2$) that have significantly higher BSM sensitivity [204], though spin-orbit-related complications will likely affect the electronic structure of these heavier species. Investigations into the effect of increasingly heavy optical cycling centers on laser cooling in such nonlinear species is therefore highly motivated.

The woods are lovely, dark and deep,

But I have promises to keep,

And miles to go before I sleep,

And miles to go before I sleep.

Robert Frost

6

Conclusion and Outlook

In this thesis, we have demonstrated deceleration, cooling, and trapping of linear polyatomic molecules useful for BSM physics experiments. Through these demonstrations, we have identified complications that arise when applying these techniques compared to diatomic and lighter polyatomic species. First, we found that the efficacy of Zeeman-Sisyphus deceleration is, in general, reduced in heavy

molecules compared to lighter species due to a combination of congested excited state structure in very heavy molecules greatly decreases the efficacy of Zeeman-Sisyphus deceleration due to smaller rotational constants and congested excited state structure. Then, we found that laser deceleration and magneto-optical trapping was possible with SrOH molecules. Though both techniques acted qualitatively similarly to their use on CaOH, the redder cycling photons and higher mass did require a longer slowing distance and led to a slower initial MOT trap depth. This work suggests that still heavier molecules with still redder cycling transitions will suffer similarly, though the techniques should still be broadly applicable.

We finish by analyzing the prospects for controlling the motion of nonlinear species of interest in light of these experiments. To that end, we measure vibrational branching fractions and analyze rotational closure in three nonlinear Sr-containing molecules. We find that $SrNH_2$ is likely compatible with full laser deceleration and trapping, with only slightly more complexity than SrOH. This is surprising and encouraging, as it insinuates the work on the simpler species is almost directly transferable to this more complex molecule, and indeed likely more complex molecules in the future. In parallel, advancement in optics technology can help to democratize the field; more accessible lasers can enable more experimentation of how these techniques can be appplied more broadly.

However, the VBF measurements and rotational closure analyses also show that such techniques would be significantly more complicated in $SrOCH_3$, and nearly impossible in SrSH. Combined with the complications identified the laser

deceleration and MOT work, it is clear, as has always been clear, that many molecules are simply too complex to laser cool using traditional AMO techniques. ZS deceleration can begin to fill the control gap; it is likely applicable to many more complex species even with the aforementioned complications. Even so, application to very heavy species will likely involve significant technical challenges. Furthermore, if a species can only cycle enough to ZS decelerate, it remains impossible to cool and trap, limiting the ultimate utility of the technique alone. Our work thus continues to motivates investigations into new or less-explored slowing and cooling techniques in order to be able to control more generic species.

We conclude with prospects for some such methods as have been proposed or previously demonstrated, and note what particular aspects need improvement before being generally applicable.

6.1 Other Methods of Motional Control

6.1.1 Some Scattering

In the same vein as ZS deceleration, there are some methods of motional control that have been developed to optimize the force applied per spontaneously-scattered photon. A unique example is "pi-pulse" slowing, in which intense pulses of laser light successively excite and coherently de-excite a beam of molecules in times less than the spontaneous decay time of the excited state [114, 116–118]. Each pulse sequence then removes $2 \times h\nu$. If the timing can be optimized, a molecule could scatter *many* photons coherently before spontaneous emission.

If a species has somewhat diagonal FCFs, then the stringency is relaxed. This technique has been demonstrated on atom beams, but not on molecules, so the effects of the additional structural complexity are not understood. Nevertheless, proposals exist for application to species, so there is some effort to understand the feasibility. However, the intensities required to reach high-enough Rabi frequencies are not compatible with current laser technologies for molecules produced in CBGBs, thus limiting the species of interest it can be applied to. Nevertheless, this technique should become more broadly viable as the technology improves.

An other example of a low-scattering control method is opto-electric Sisyphus cooling [123]. Like other Sisyphus methods, it relies on a cyclic process of potential-climbing to repeatedly remove potential energy. In this case, strong electric fields are used to create the potential, with optical pumping used to move between manifolds. As with the pi-pulse slowing above, this technique has been demonstrated in chemically stable species. It is not known how effective it will mode-match to cryogenic molecular sources, but requires only $\sim 10^2$ spontaneously-emitted photons to cool from K to 500μ K, and so is, in principle, broadly applicable to a wide class of molecular species. A potential downside is that this method can take a very long time and requires significant technical complexity, but neither of these imply application to new species would not work. The efficiency of such a method is unknown, since its previous applications have been on again, "bottle molecules" like formaldehyde.

6.1.2 Nonradiative

On the other hand, there is also interest in methods of motional control which do not require any spontaneously scattered photons at all. These methods will be intrinsically less sensitive to certain molecular structure, but often suffer their own difficulties.

Similar to the pi-pulse slowing discussed above, optical Stark slowing (OSS) is an established method of deceleration using short, intense, pulsed light. Instead of driving stimulated transitions, though, OSS used spatially overlapped pulses of red-detuned light as deep, moving, optical dipole traps [225–232]. If set up correctly, these traps enclose the moving molecules and the dipole force decelerates the molecules as they encounter the trap wall. This method has again been demonstrated on stable species. Though the wavelength requirement is looser than for the pi-pulse method, the power requirement is higher. Mode matching to a cryogenic source has also never been demonstrated, and laser powers are still at least an order of magnitude beyond viable as of a few years ago. Nevertheless, the simplicity of the method makes it attractive, and more accessible higher-powered pulsed lasers may lead it back to the forefront of molecular control.

Relatedly, there is ongoing work to use an in-vacuum, in-cryogenic optical cavity to make an enormous, very deep ($\sim$ 10 K) dipole trap in or near a cryogenic buffer gas cell [233]. The cavity and resulting trap depth will allow direct loading of molecules into the trap with no additional deceleration or cooling. While this method is expected to work for a some species, calculations raise

concern about the extremely high intensities leading to dissociation or ionization of a large number of molecules in such a trap. Additionally, the trap depth will result in the trapped molecules being quite hot, and the prospects of cooling inside such an ODT are not well-understood. The upside is that since the work is ongoing, answers to these open questions are expected in the near term, and the broader applicability should become clearer.

Some nonradiative motional control methods do not use light at all, as is the case with the "cryofuge." First demonstrated at MPQ [234], the cryofuge decelerates molecules through a rapidly-rotating curved guide. The molecules enter at an edge, and to leave must climb the centrifugal barrier and decelerate. The first generation was made from an electric guide, which, though functional, required extreme technical expertise and as such has not yet been replicated. However, there is work beginning towards creating such a machine with a magnetic guide, which would still be capable of decelerating many species (just need a magnetic moment!) but would be technically simpler to build. Another concern is that the previous demonstrations were again on stable, plentiful molecules, and so the compatibility with CBGBs will need to be studied. Nevertheless, the ongoing and imminent work provides hope of near-term resolutions to these uncertainties.

6.1.3 Fin

These methods are by no means exhaustive, and each suffers already from fundamental limitations in applicability. Nevertheless, they represent a real effort

to move beyond the same techniques of control that have basically been inherited *as are* from their first demonstrations on atoms. These old techniques, though powerful, are inherently limiting, not only on the molecules we can control, but indeed on the species in our collective subconscious.

Though there are some 100-odd atoms in the universe, there are infinitely more molecules. Less than two dozen atomic species can be trapped, and only a handful of molecules. We have only begun to explore the possibilities which are afforded to us through the richness of our universe, and it is clear now that we will need to be more clever to continue to explore more deeply. Both the knowledge and limitations uncovered in the work here are opportunities and invitations to strive towards a much broader world of molecular physics.

A

X-Teller Interactions

Lots of interactions are thrown around with Teller's name attached to them. We here provide a *very* brief overview of what each is and when it is relevant. Most are not relevant to any of our molecules, with the exceptions between Renner-Teller and pseduo-Jahn Teller, but it is good to have a sense to what each term refers to.

A.0.1 Renner-Teller

The Renner-Teller (RT) effect is a rovibronic mixing that mixes electronic and rovibrational angular momentum. The interaction is used to explain electronic structure both in nominally linear molecules (in which the effect breaks linearity) or in nonlinear molecules (in which the effect can explain why the structure is nonlinear). The RT effect predominantly appears in our work as nearly a vibronic interaction (see Chapters 2 and 4) that splits the vibrational bending modes in $^2\Pi$ electronic states by mixing vibrational and electronic angular momentum. The rotational structure is also, in general, affected, but we work with low rotational states anyway. The RT effect is also responsible for various intensity-borrowing mechanisms that allow the rovibrational ground state of excited electronic manifolds to decay to nominally-forbidden vibrational states upon decay.

A.0.2 Jahn-Teller

The Jahn-Teller effect (JTE) is a true vibronic mixing that refers to the breaking of electronic degeneracy in nonlinear molecules by nuclear distortion. In particular, a non-totally-symmetric nuclear coordinate (e.g. the bending coordinate in $SrOCH_3$) will cause splitting of nominally degenerate electronic states. This interaction also mixes nominally symmetric vibrational states with non-totally-symmetry modes, which can lead to intensity borrowing on vibronic transitions.

The true JT effect does *not* appreciably occur in the $\tilde{A}$ states of $SrOCH_3$ or $CaOCH_3$, as noted in literature.

A.0.3 pseduo-Jahn Teller

The pseudo-Jahn Teller effect (pJTE) is not really a single effect, but a term used to describe mixings that mimic the state mixing one would see in the Jahn-Teller effect but enabled by mixings between different electronic manifolds, not between degenerate electronic states. The symmetry of the electronic states is not necessarily significantly broken by such an interaction.

In $SrOCH_3$, the pJTE is responsible for decays from the $\tilde{A}(^2E)0_0$ state to $\tilde{X}^2A_18_1$ vibrational state, which is nominally vibrationally forbidden. This aspect mimics the effect of a *true* JTE, hence the "pseudo" in the name. However, the pJTE is caused by mixing between the $\tilde{A}(^2E)$ and $\tilde{B}^2A_1$ electronic manifolds as noted in Chapter 5, not a direct vibronic mixing between the degenerate states. The lack of true JTE is evident by the maintained near degeneracy of the parity-doubled states in the $\tilde{A}^2E$ manifold in spite of the intensity borrowing of decays.

A.0.4 Herzberg-Teller

The Herzberg-Teller (HT) effect is vibronic mixing that causes nominally forbidden electronic transitions to become allowed. It can also be understood as the electronic transition dipole moment having a strong dependence on the nuclear coordinates. Bunker and Jensen [75] show the two descriptions imply the same physical effects; the dependence of the transition moment on nuclear coordinates can be understood as necessarily a result of vibronic mixing. In our species, we almost exclusively drive electronically *allowed* transitions, and so typically the

HT effect is not encountered. An argument could be made that transitions to some electronic manifolds in YbOH are strengthened by such interactions, but the electronic character is not extremely well-defined in the first place in these cases, so the verdict is not clear to the author.

B

Magnet Details

We compile useful drawings and datasheets for the superconducting magnets in this Appendix.

B.1 Coil Form Design

The magnet coils were designed to house the magnets. The bore of the form was made to be 1", with the overall length minimized. Two half-forms are bolted together with ~ 8 mm spacers between. The spacers are not solid disks, but instead made of four separate pieces that allows optical access through the bore of the magnet at the region of highest field. This gap is important to being to optically pump transversely, at a single field value, in comparison to longitudinal pumping. There are also tapped and through holes on the outer faces of the forms, useful for heatsinking and thermometer mounting. The machine drawings are displayed here.

B.2 AMI Data

We provide the public data provided to us by AMI about the magnets. These include a rough outline of the magnet construction in the coil form, as well as datasheets for the two magnets used. Field profiles were also provided, but they are not reproducible here.

B.3 Compensation Coils

The field between the two ZS coils was originally too high to drive only rotationally-closed transitions (see Chapter 3). To make the field smaller, two superconducting compensation coils were wound on the Doyle lab coil winder. The details of construction will be covered in later students' theses.

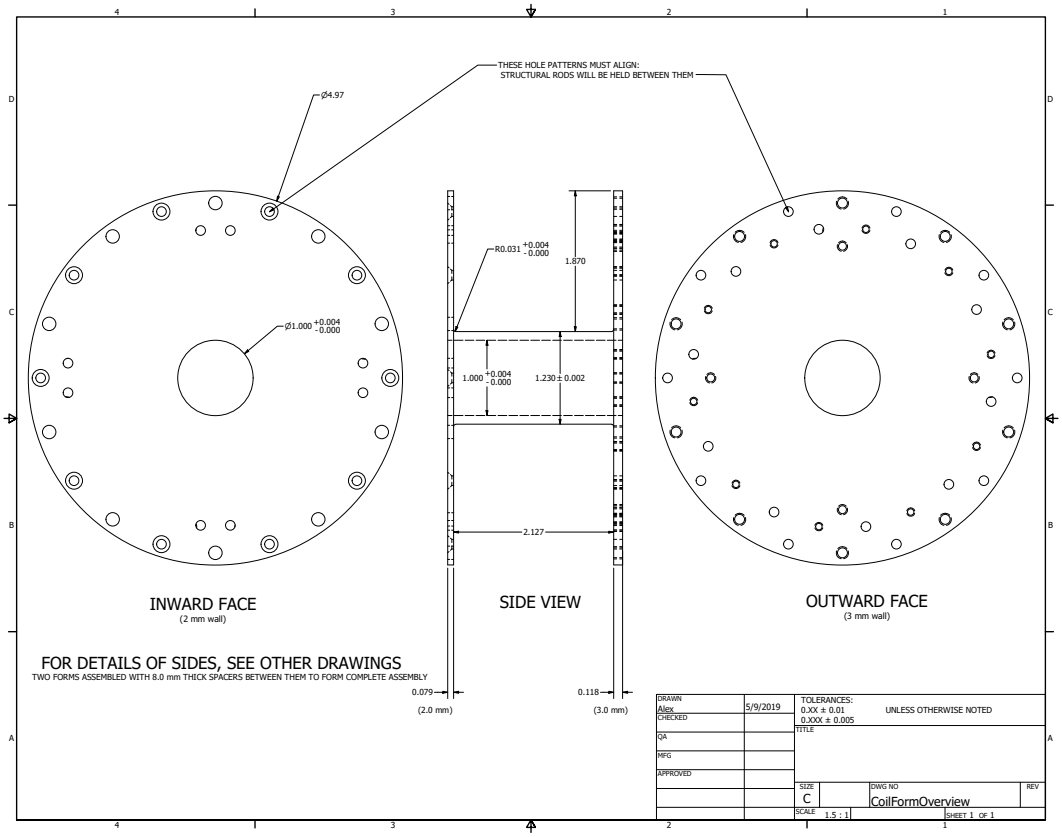

Figure B.1: Machine drawing of the side profile and side views of a half-coil form.

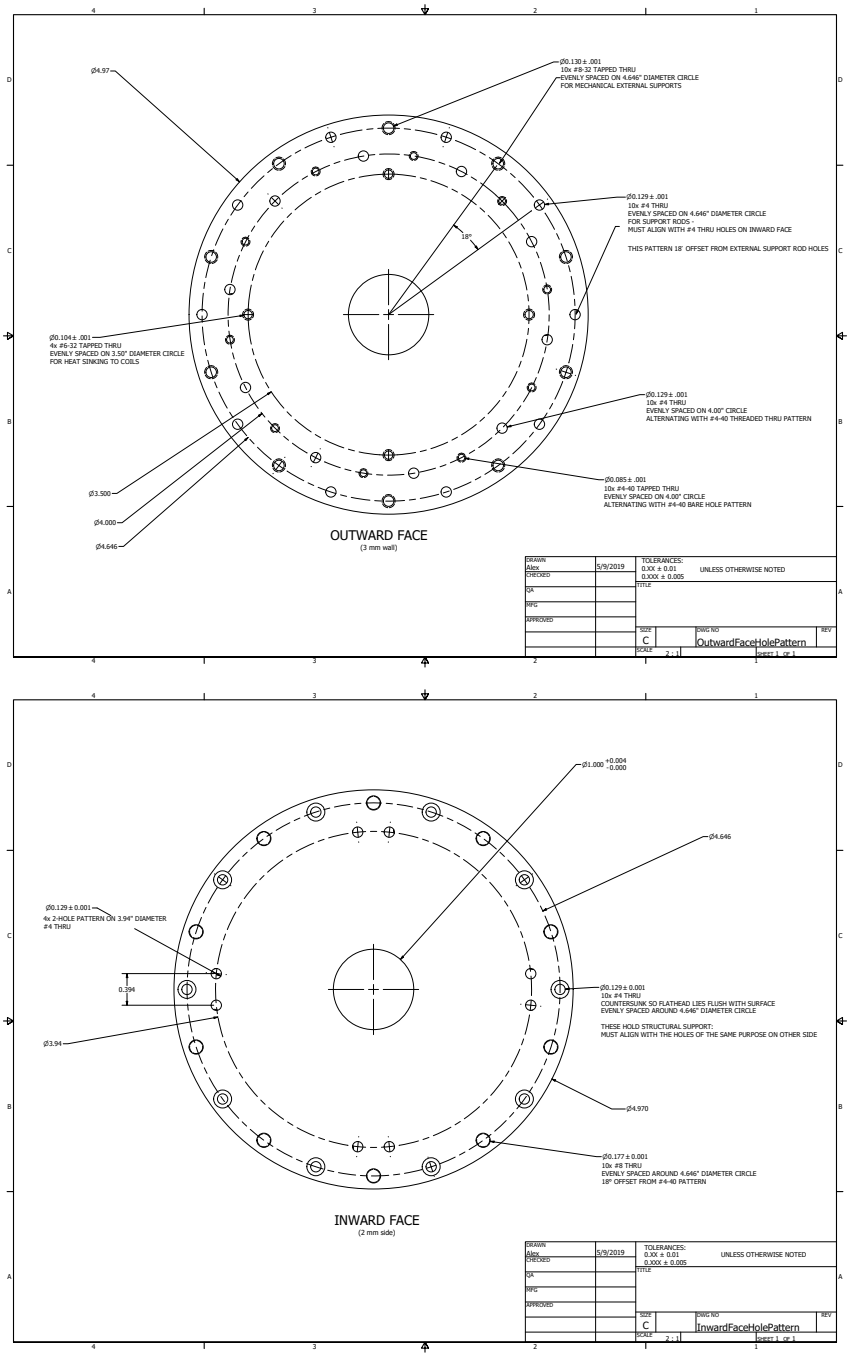

Figure B.2: Machine drawings of the hole patterns on the inner and outer faces of the half-form.

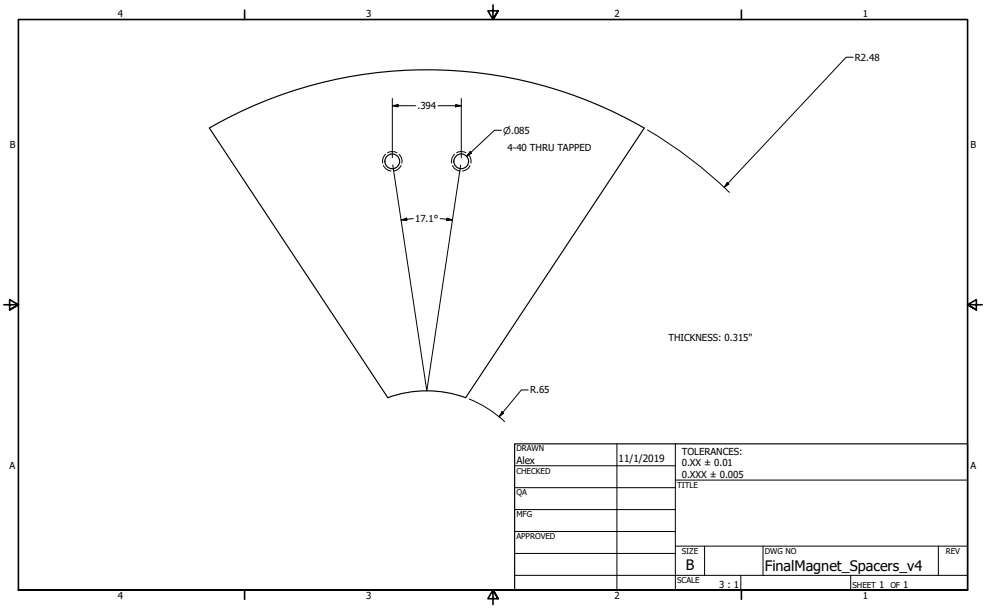

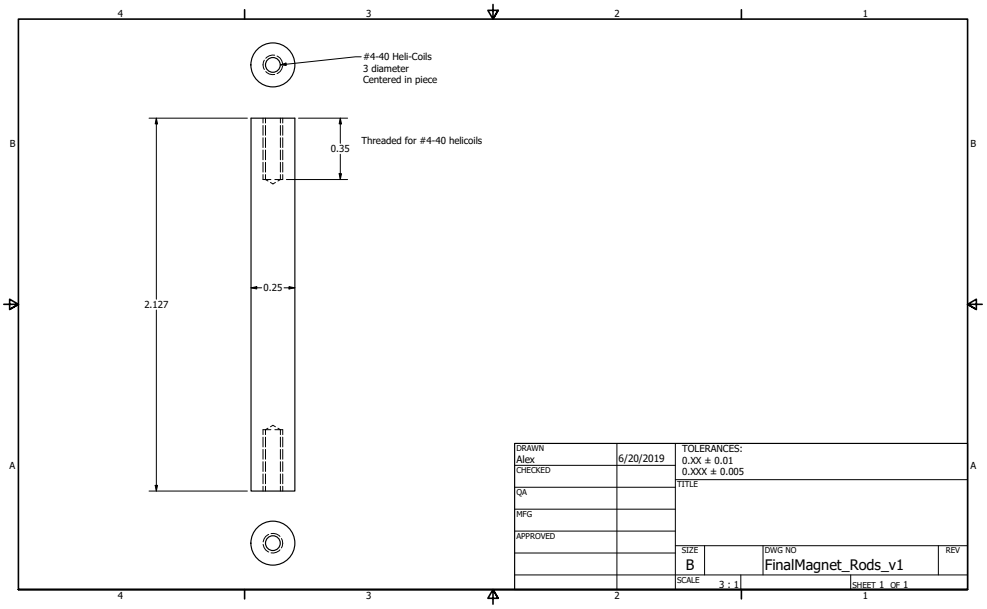

Figure B.3: Machine drawings of the spacers and pre-stressing rods used in magnet assembly. The spacers go between two half-forms, and the rods go between the two faces of a single half-form (as seen in Figure 3.5.

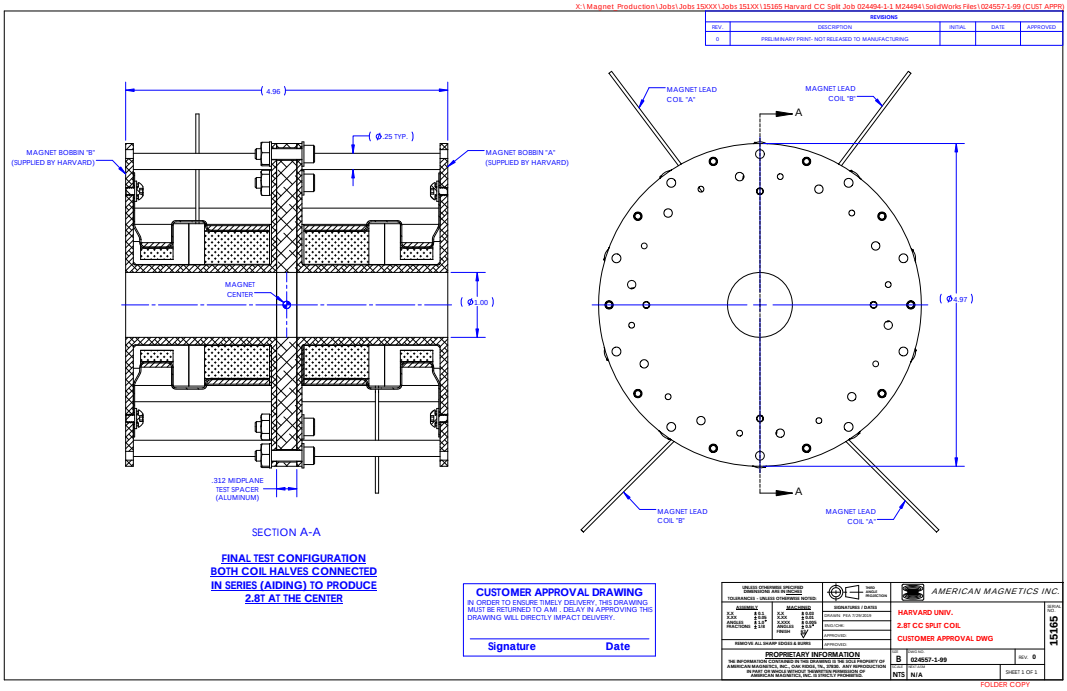

Figure B.4: Machine drawing of the magnet design as created by AMI. The magnet windings are represented by the space filled by dotted patterning. The bolts on the insides of the panels are used to heatsink the coils; they bolt a piece of copper to the form that is also intertwined with the coil windings. The other materials in the magnet construction are not noted and are proprietary.

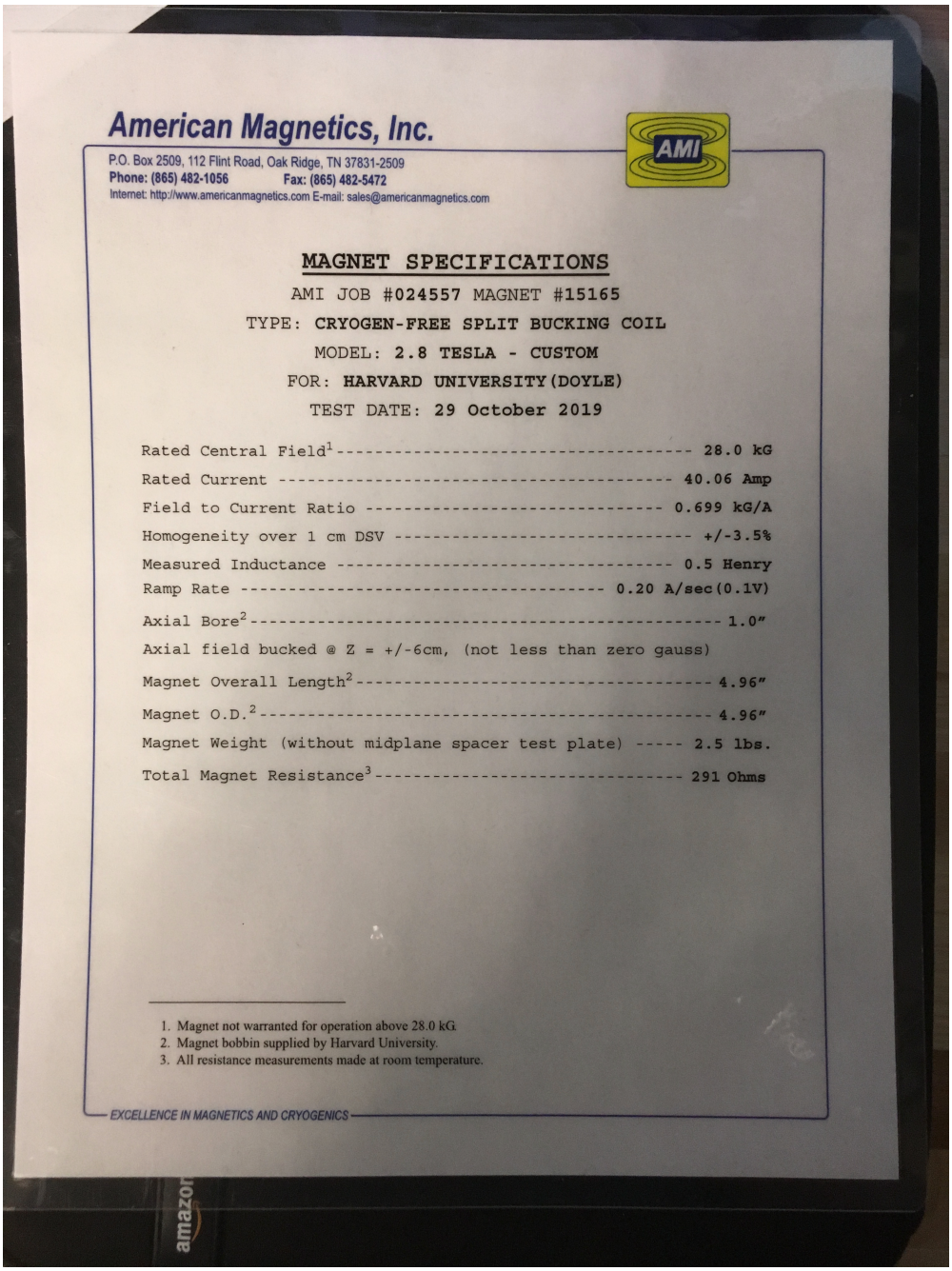

American Magnetics, Inc.

P.O. Box 2509, 112 Flint Road, Oak Ridge, TN 37831-2509
Phone: (865) 482-1056 Fax: (865) 482-5472
Internet: http://www.americanmagnetics.com E-mail: sales@americanmagnetics.com

AMI

MAGNET SPECIFICATIONS

AMI JOB #024557 MAGNET #15165

TYPE: **CRYOGEN-FREE SPLIT BUCKING COIL**

MODEL: **2.8 TESLA - CUSTOM**

FOR: **HARVARD UNIVERSITY(DOYLE)**

TEST DATE: **29 October 2019**

Rated Central Field[1]	28.0 kG
Rated Current	40.06 Amp
Field to Current Ratio	0.699 kG/A
Homogeneity over 1 cm DSV	+/-3.5%
Measured Inductance	0.5 Henry
Ramp Rate	0.20 A/sec(0.1V)
Axial Bore[2]	1.0"
Axial field bucked @ Z = +/-6cm, (not less than zero gauss)	
Magnet Overall Length[2]	4.96"
Magnet O.D.[2]	4.96"
Magnet Weight (without midplane spacer test plate)	2.5 lbs.
Total Magnet Resistance[3]	291 Ohms

1. Magnet not warranted for operation above 28.0 kG.
2. Magnet bobbin supplied by Harvard University.
3. All resistance measurements made at room temperature.

EXCELLENCE IN MAGNETICS AND CRYOGENICS

Figure B.5: Datasheet for one magnet used in the ZS slower.

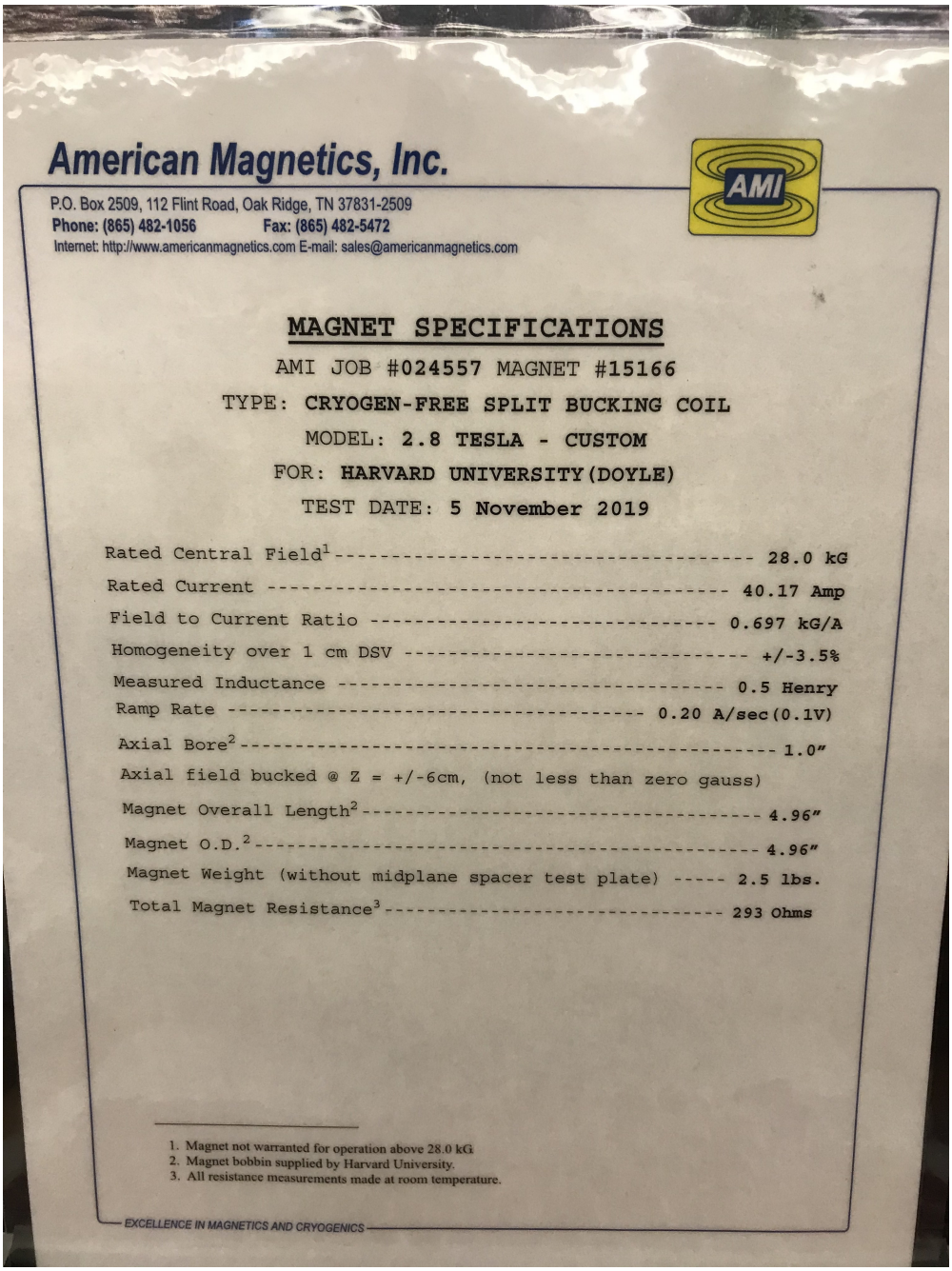

American Magnetics, Inc.

P.O. Box 2509, 112 Flint Road, Oak Ridge, TN 37831-2509
Phone: (865) 482-1056 Fax: (865) 482-5472
Internet: http://www.americanmagnetics.com E-mail: sales@americanmagnetics.com

AMI

MAGNET SPECIFICATIONS

AMI JOB #024557 MAGNET #15166

TYPE: **CRYOGEN-FREE SPLIT BUCKING COIL**

MODEL: **2.8 TESLA - CUSTOM**

FOR: **HARVARD UNIVERSITY(DOYLE)**

TEST DATE: **5 November 2019**

Rated Central Field[1]	28.0 kG
Rated Current	40.17 Amp
Field to Current Ratio	0.697 kG/A
Homogeneity over 1 cm DSV	+/-3.5%
Measured Inductance	0.5 Henry
Ramp Rate	0.20 A/sec(0.1V)
Axial Bore[2]	1.0"
Axial field bucked @ Z = +/-6cm, (not less than zero gauss)	
Magnet Overall Length[2]	4.96"
Magnet O.D.[2]	4.96"
Magnet Weight (without midplane spacer test plate)	2.5 lbs.
Total Magnet Resistance[3]	293 Ohms

1. Magnet not warranted for operation above 28.0 kG.
2. Magnet bobbin supplied by Harvard University.
3. All resistance measurements made at room temperature.

EXCELLENCE IN MAGNETICS AND CRYOGENICS

Figure B.6: Datasheet for the second magnet used in the ZS slower.

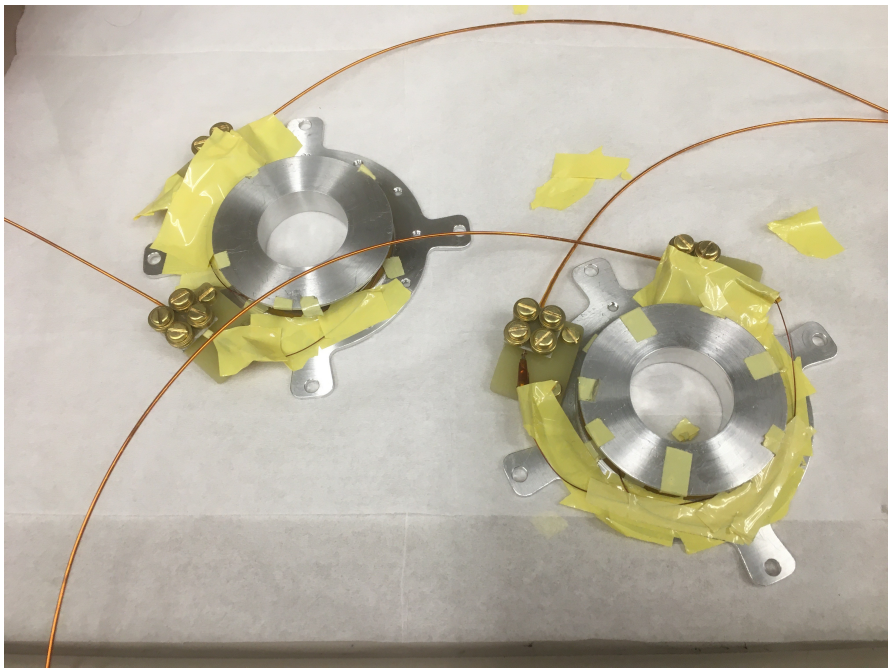

Figure B.7: Compensation coils just after winding. The superconducting wire is stabilized and clamped to a normal conducting lead on the G10 connectors on each coil, which also serve as a heatsink.

Figure B.8: Mounted coil in between the two ZS magnets. The current lead heatsink is bolted to the ZS magnet face in the lower anterior of the photograph.

C

Spectroscopy of Previously Unobserved States in SrOH

Though many rovibrational states in the optical cycle had previously been observed, there were six that had not been identified. In this supplement, we discuss how each of these states was characterized to $\sim$ 10 MHz resolution using

various spectroscopic techniques. Four of the states were identified using the apparatus described in Lasner *et al.* [46], and the remaining two in the apparatus described in the main text used for the slowing and trapping of SrOH. The state energies of the laser-cooling rotational levels can be found in Table C.1.

State	Energy (cm^{-1})
B(010) $N = 1$	16778.74
A(200) $J = 1/2^+$	15621.93
A(02^00) $J = 1/2^+$	15275.84
Aκ(010) $J = 1/2^+$	15191.15
X(300) $N = 1$	1566.86
X(110) $N = 2$	884.74
X(110) $N = 1$	883.75

Table C.1: State energy of the previously-unobserved rotational levels identified with a combination of DLIF and depletion-revival spectroscopy. The absolute uncertainty is conservatively estimated to be $\lesssim 0.03$ cm^{-1} through comparison of wavemeter frequencies of transitions previously observed in our apparatus to literature transition values.

C.1 Dispersed Laser-Induced Fluorescence Spectroscopy

We briefly reiterate the main aspects of the spectroscopy apparatus described in [46]. The molecular source is a cryogenic buffer gas beam source (CBGB). The molecules are produced in a copper cell held at $\sim$ 8 K via laser ablation of a strontium metal target in the presence of $\sim$ 300 K water vapor and helium buffer gas thermalized with the cell. The SrOH molecules formed from the water vapor and ablated metal are thermalized with the cell by collisions with helium. The cold molecules are then in entrained in a beam of helium that exits the cell through a 7 mm aperture. About 2.5 cm downstream, the molecular beam is vertically intersected by a laser beam (where the laser source and ad-

dressed transition depends on the specific spectroscopic search). When the light is resonant with a transition, the molecules are excited to an electronic excited state. Fluorescence from the subsequent decay is collected and collimated by a 50.8 mm diameter lens in the cryogenic chamber, subsequently propagating out of the beam source and into a Czerny-Turner style grating spectrometer that disperses the fluoresced light. The wavelength resolution of the dispersion is controlled by an adjustable slit aperture at the input to the spectrometer. This dispersed laser-induced fluorescence (DLIF) is imaged in 40 nm spans by either an EMCCD camera or gated ICCD camera, for CW and pulsed laser excitation, respectively. The wavelength range is tuneable over ∼300 nm by adjusting the angle of the diffraction grating. The wavelength axis of the collected fluorescence is calibrated using known transitions.

High-resolution $\tilde{B}^2(010)$ spectroscopy

The $\tilde{B}^2(010)$ state is used to repump the $\tilde{X}^2(110; N = 2)$ state. The excited vibronic manifold had previously been observed ([161]), but only for higher rotational states. It was thus necessary to identify the energy of the $\tilde{B}^2(010; N = 1, J = 1/2^+)$ state at high resolution.

To find this state, a CW dye laser was used to drive rotational lines on the $\tilde{X}^2(000)$–$\tilde{B}^2(010)$ vibronic transition. The $\tilde{B}^2(010)$ state remains vibrationally diagonal like other low-lying vibrational states in the $\tilde{A}^2$ and $\tilde{B}^2$ manifolds, and so upon excitation predominantly decays to $\tilde{X}^2(010)$. The frequencies of the excitation scatter and decay light differ by ~ 360 cm^{-1}, a splitting easily resolv-

able on the spectrometer, even with a low-resolution widely-opened slit.

Since the $\tilde{X}^2(000; N = 1)$–$\tilde{B}^2(010; N = 1, J = 1/2^+)$ transition had not been observed, we first identified the $\tilde{X}^2(000; N = 3)$–$\tilde{B}^2(010; N = 3)$ line in our apparatus, which is listed in Ref. [161]. We found a $\sim$ 300 MHz offset between our frequency reference and the published value, well within the uncertainty of the absolute wavemeter accuracy.

To identify the $\tilde{X}^2(000; N = 1)$–$\tilde{B}^2(010; N = 1, J = 1/2^+)$ transition, we calculated the energy using Eqs. 3 and 4 in Ref. [161] and the constants in the previously work, accounting for the observed frequency offset. The line was identified almost exactly where this calculation predicted, with strong fluorescence observed over a few hundred MHz. The width is attributed to both Doppler broadening and the partially resolved ground state spin-rotation (SR) splitting of $\sim$110 MHz.

The energy of the $\tilde{B}^2(010; N = 1, J = 1/2^+)$ state (found in Table C.1) is somewhat surprising given that Refs. [90] seems to imply that the rotational energy formulae in Ref. [161] are only valid in the high-N limit. Nevertheless, several peak positions out of low-N that had been observed in this reference were also observed with similar wavemeter frequency offsets to these other peaks, and the assignment based on spacings between lines is only consistent with our assignment matching these formulae.

$\tilde{A}^2(200)$

The $\tilde{A}^2(200)$ state is used to repump population out of $\tilde{X}^2(300)$. This vibrational manifold had never been previously observed at any resolution, so the search began with pulsed-dye laser DLIF, since a pulsed dye laser has a larger linewidth ($\sim$0.1 cm^{-1}) and extremely high intensity which enabled driving of comparatively weak transitions. The dye laser was a HyperDye-300 pumped by a 10 ns, $\sim$ 100 mJ YAG. The dye laser routinely produced more than 2 mJ/pulse over the wavelength range studied. The dispersed fluorescence was collected by an ICCD in this stage, with the intensifier on the camera gated a few ns after the excitation pulse was fired to avoid blinding the sensor.

We estimated the position of the $\tilde{A}(200)$ manifold from the $\tilde{A}(100)$ position and the ground state x_e anharmonic constant. We then centered the dye laser in the vicinity of this prediction, and scanned the frequency in $\sim$ 0.1 cm^{-1} steps. By recording the fluorescence spectrum as a function of excitation frequency, we could deduce the nature of the transitions we were driving again by the separation between the excitation and decay light frequency, and additionally by the pattern of decay peaks. In particular, the $\tilde{A}(200)$ manifold was identifiable by a strong decay $\sim$ 1000 cm^{-1} higher energy that the excitation light, *and* weaker decays to $\pm \sim$ 500 cm^{-1} from this dominant decay, indicating stretching character with few percent decays to $\Delta v_1 = 1$ stretch modes. The state was quickly discovered.

Low resolution ($\sim$ 1%) vibrational fractions (VBFs) were measured with the dye laser frequency parked at the low frequency edge of the feature. These

measurements suggest an 80% diagonal decay to $\tilde{X}(200)$, an 11% fraction to $\tilde{X}(300)$, and an 8% fraction to $\tilde{X}(100)$. Less than 2% of the population decays to $\tilde{X}(400)$, with lower probability decays below the measurement resolution. These VBF measurements were important for our later utilization of the state, since it confirmed new vibrational decay channels would not arise as long as the $\tilde{A}(200)$ was populated infrequently ($\lesssim 50$ times).

To find the rotational photon cycling line, we also conducted high-resolution narrow-band CW DLIF spectroscopy on the $\tilde{X}(000)$-$\tilde{A}(200)$ transition, similar to the above work on finding the $\tilde{B}(010)$, N' = 1 state. Since no rotational lines had been assigned at all in the excited state, however, the assignment was more difficult. After locating a few rotational features, the spectrum was fit using the PGopher program, with known constants as the inputs, using lowing vibrational manifolds' constants if necessary. The resulting fit accurately predicted the position of the laser cooling lines, which we confirmed spectroscopically by tracing rotational spacing and SR splitting across several rotational features. The energy of the $\tilde{A}(200), J' = 1/2^+$ excited state can be found in Table C.1.

$\tilde{X}(110)$

The decay from $\tilde{A}$ and $\tilde{B}$ vibrational states to $\tilde{X}(110)$ had been observed at low resolution in Ref. [46]. The observation made clear it was necessary to repump this state to sufficiently photon cycle for a MOT, but the data was not high enough resolution to locate the photon cycling ground state exactly. Additionally, given that it is the lowest vibrational combination mode, the presence and

size of possible anharmonic contributions to the energy were unknown.

To locate the position of the state more accurately, we started by driving the $\tilde{X}(000)$-$\tilde{B}(010)$ transition. Averaging of the dispersed fluorescence revealed a small decay from the excited state, consistent with $\Delta v_1 = 1$ (to $\tilde{X}(110)$). The axis of this spectral range was calibrated to ~ 1 cm^{-1} using several known laser frequencies. This calibration allowed extraction of the center of the presumed decay to $\tilde{X}(110)$ to similar uncertainty.

Similar to the $\tilde{A}(200)$ state, no rotational structure of the level had been previously identified. Scanning the laser over $\sim$ 1 cm^{-1} around the $\tilde{X}(110)$--$\tilde{B}(010)$ best-guess origin revealed several rotational features to the same vibrational state. Fitting of this decay spectrum was again assisted by PGopher to assign the lines. The resulting fit successfully predicted the energy of the $N'' = 1 \rightarrow J' = 1/2, +$ transition, identifiable from a $\sim$ 110 MHz SR splitting*. The $N'' = 2$ state was then identified by jumping a rotational frequency. The energy of the $\tilde{X}(110), N'' = 1, 2$ states can be found in Table C.1.

C.2 Depletion-Revival Spectroscopy

The DLIF spectroscopy above relied heavily on being able to drive a relatively strong transition out of a reasonably populated ground state. Combined with driving vibrationally off-diagonal transitions, this combination ensured a strong

*The CaOH experiment has pointed out that the SR splitting in an $\ell = 1$ mode should naively be $\sim 1/2$ the SR splitting in an $\ell = 0$ mode. However, the SR splitting in these modes was found to be similar in both cases, as measured in both $\tilde{X}(010)$ and $\tilde{X}(110)$, N" = 1 states. There is a parameter one can include in the effective Hamiltonian capable of explaining the discrepancy, but inclusion of the parameter is not well-motivated based on literature.

fluorescence signal whenever the excitation laser was resonant with a transition. The $\tilde{X}(300)$ ground state and $\tilde{A}(02^00)$ excited states do not meet both criteria: $\tilde{X}(300)$ is expected to barely be naturally populated after entrainment in the buffer gas beam, and $\tilde{A}(02^00)$ is not well-coupled to any highly-populated ground states.

The apparatus used in the following work was the MOT apparatus described in Chapter 4. Reiterating briefly, a CBGB beam of SrOH molecules traverses a 1.5 m beamline. Any or all of the optical cycling lasers can counterpropagate the molecular beam (with white light broadening), depending on the spectroscopic pathway. Molecules are detected in the MOT chamber at the end of the beam line with different detection schemes in each case, with fluorescence collimated by an in-vacuum lens and collected by a PMT outside of the vacuum chamber.

The spectroscopy of states in this apparatus was done via depletion-revival spectroscopy. In this class of schemes, a laser first pumps population through some transition that empties a specific ground state or set of ground states. The newly populated states can then be repumped through a known excited state, which can "revive" the population in a detection scheme. This method is especially effective when optical cycling, where including specific repumpers can be used to cycle effectively into a higher vibrational ground state, and/or make evident the return or disappearance of the population from the optical cycle. The layout of each state's specific spectroscopic layout is discussed in the respective subsections.

The $\tilde{A}\kappa(010)J" = 1/2, +$ repumping state was also identified via this method, despite nominally being compatible with DLIF searches as well.

$\tilde{X}(300)$

$\tilde{X}(300)$, $N'' = 1$ level, one of the least populated states in the optical cycle, had not been previously observed. However, unlike the $\tilde{X}(110)$ manifold, the dominant anharmonic contributions to the stretching vibrational mode rovibrational energies were measured in previous work on the $\tilde{X}(100)$ and $\tilde{X}(200)$ manifolds. This allowed prediction of the N" = 1 rotational line to within a few GHz using a standard rotational energy formula using previously measured constants.

To populate the state, the $\tilde{X}(000)$-$\tilde{A}(200)$ line was driven. From this transition, about 10% of the molecules decay into $\tilde{X}(300)$ in a single excitation. To increase the population further, the $\tilde{X}(000)$-$\tilde{A}(000)$, $\tilde{X}(100)$-$\tilde{B}(000)$, and $\tilde{X}(200)$-$\tilde{B}(100)$ transitions in the optical cycle were also driven by white-light broadened slowing light, which depleted the lower lying stretching modes and increased the $\tilde{X}(300)$ number.

A Ti:Sapph probe laser transversely intersected the molecular beam in a detection chamber downstream, and was scanned near the estimated $\tilde{X}(300)$-$\tilde{A}(100)$ transition. The depletion lasers were kept on continuously. When the scanning laser was resonant with the photon cycling line, the population from the $\tilde{X}(300)$ state was returned predominantly to the $\tilde{X}(100)$ state, which had been depleted of natural population. The $\tilde{X}(000)$-$\tilde{A}(000)$ and $\tilde{X}(100)$-$\tilde{B}(000)$ lasers could then cycle the revived population ~ 400 times before loss. A PMT

with optical filters collected fluorescence from $\tilde{B}(000)$ state, which was bluer than any lasers or other scattered light in the system, allowing nearly-background-free detection. In this way, the transition between these states was identified to high resolution. The energy of the $\tilde{X}(300)$, $N'' = 1$ level is recorded in Table C.1, which enabled driving of the actual repumping transition through $\tilde{A}(200)$.

$\tilde{A}(02^{0}0)$

The $\tilde{A}(02^{0}0)$ state is used to repump the $\tilde{X}(02^{2}0)$ state in the final cycling scheme. Second-order Renner-Teller interactions mix the excited state with some $\tilde{A}(02^{2}0)$ character making the transition relatively strong. The manifold had not been previously observed, the line positions were estimated from low-resolution pulsed DLIF taken with a pulsed dye laser taken in the manner described in the above section. The high-resolution spectroscopy was done using a depletion-revival method.

To populate the $\tilde{X}(02^{0}0)$, the earlier lasers in the cycle were pulsed for 40 ms counterpropagating to the molecular beam. A Ti:Sapph probe laser transversely intersected the molecular beam downstream, scanning over the best estimate for the $\tilde{X}(02^{0}0) \rightarrow \tilde{A}(02^{0}0)$ transition frequency. When the probe laser was resonant with the transition, the population that had accumulated in $\tilde{X}(02^{0}0)$ was emptied out. The nominal $\tilde{X}(02^{0}0)$ repumper was then used as a detection laser downstream, with fluorescence from the molecules collected by a PMT. When the probe light was off-resonant, the detection laser induced fluorescence from the population in the $\tilde{X}(02^{0}0)$ state. When the resonance condition was

met, the induced fluorescence was much smaller since the probe laser depleted the detected state. Using this method, several rotational features, including the photon-cycling line, were identified successfully through the patter of rotational and SR splittings. The energy of the $\tilde{A}(02^{0}0), J' = 1/2^{+}$ state is noted in Table C.1.

$\tilde{A}\kappa(010)$

The $\tilde{A}\kappa(010)$ state is used to repump $\tilde{X}(010), N'' = 2$. Originally, this ground state was repumped through $\tilde{B}(000)$, but the line was not strong enough to drive with the laser system we had planned. Driving through the $\tilde{A}\kappa(010)$ state would both necessarily be much stronger (since it is a vibrationally diagonal line) and also accessible via diode laser. The vibronic $\tilde{A}(010)$ levels had been observed previously in Ref. [163], but the low J' states had only been observed in wrong symmetry vibronic mainfolds (e.g. Σ^{-} and Δ) for optical cycling. Nevertheless, the constants and the matrix elements therein allowed calculation of the $N'' = 2, J'' = 3/2 \rightarrow J' = 3/2$ transitions from the $\tilde{X}(010)$ manifold to both the $\mu, \kappa\Sigma^{(+,-)}$ manifolds.

To find the states, a similar method to the $\tilde{X}(300)$ search was used. All lasers in the full optical cycling scheme were sent counterpropagating to the molecular beam to deplete as much of the population into $\tilde{X}(010)$, N" = 2 as possible. This ground state is populated from decays out of the $\tilde{B}(010)$ state, which is only populated late in the cycle, but also is low-lying enough to have non-negligible natural population. The cycling thus served both to increase pop-

ulation and empty the rest of the ground states for higher contrast. A probe laser then intersected the molecular beam as it scanned near the calculated resonances. First, a Ti:Sapph laser was used to probe the $\tilde{X}(010) \rightarrow \tilde{A}\mu\Sigma^{(-)}$ transition. While the laser frequency was scanned, the fluorescence from the decaying population was collected by a PMT. When the transition was reached, the fluorescence increase was mapped over the peak. The SR splitting was observed as expected by scaling the $\tilde{X}(010)$, N" = 1 value.

After this state was found, the process was repeated searching for the $\tilde{A}\kappa\Sigma^{(+)}$ vibronic manifold, the transition of which was easily accessible via ECDL. Given the confirmation of the low-N line in the other Σ vibronic manifold, this transition was predicted to within a few hundred MHz, and the transition was quickly observed. The energy of the $\tilde{A}\kappa\Sigma^{(+)}, J' = 1/2^+$ state can be found in Table C.1.

D

Symmetry Analysis

This appendix is reproduced from the appendix of the publication Frenett *et al.* [106]. It serves both as a useful stand-alone for the point groups discussed here but also as a template for extending the analysis to other molecular symmetries. We note, as a word of warning, that extending this analysis to C_{3v} seems quite difficult and was not successfully done by our group so far. The presence

	ΔK_a	ΔK_c	Exceptions
a-type	0	± 1	$\Delta N \neq 0$ for $K'_a \to K''_a = 0$
b-type	± 1	± 1	
c-type	± 1	0	$\Delta N \neq 0$ for $K'_c \to K''_c = 0$

Table D.1: Rotational transition rules for asymmetric tops, up to weak transitions allowed by perturbations (e.g., those that make N, K_a, or K_c imperfect state labels). In a structureless rigid rotor, $|\Delta N| \leq 1$.

of E electronic, vibrational, and rotational states makes the analysis very dense, though worthwhile if someone has the time and patience to do so.

D.1 Symmetry analysis for C_s and C_{2v} rovibronic branching

In this Appendix, we expand upon the ideas presented in Sec. 5.2 regarding the consequences of molecular symmetry point groups on the rotational closure in C_s and C_{2v} molecules. For each of these point groups, we present an overview of the relevant representation theory with connections to the special cases of $SrNH_2$ and SrSH. We also briefly treat the situation for C_1 molecules (for example, SrOCHDT) for comparison. We do not treat C_{3v} molecules here, as the essential concepts specific to that point group are already addressed in the literature [191]. We first discuss generic considerations of molecular structure, and then treat each point group individually. All representation theory results are derived from basic principles outlined in [75] but are developed here in detail for clarity and reference.

D.1.1 Transition selection rules and perturbations

For all asymmetric top molecules, the nominal transition selection rules are shown in Table D.1; see Ref. [83]. The a-type, b-type, and c-type selection rules apply for cases in which the transition dipole moment is along the a, b, and c axis, respectively. We denote a transition dipole moment component along the i axis (where $i = a, b, c$) by T_i. In realistic cases, a transition dipole moment may have nonzero components along multiple principal inertial axes. For example, the $\tilde{X}^2A'$–$\tilde{A}^2A'$ transition dipole moment in SrSH is predominantly along the b axis but also has a small component along the a axis. We also note that a given energy eigenstate might have contributions from multiple $(N_{K_aK_c})$ components. We warn the reader that in the literature, a single $(N_{K_aK_c})$ label may be employed to label an energy eigenstate based on the dominant rotational basis component, even if a small admixture of other rotational basis components is present. Up to hyperfine structure and the influence of external fields, J is a perfectly good quantum number, and for doublet molecules $N = J \pm 1/2$, constraining the identity of $(N_{K_aK_c})$ basis states that can mix. In C_s, C_{2v}, and C_{3v} molecules the parity of a state is also pure even in the presence of realistic perturbations. All dipole moment and rotational basis components will contribute to the transition strengths between two energy eigenstates according to Table D.1.

We now provide a general overview of vibronic decays. In the Born-Oppenheimer approximation (BOA), the vibronic transition dipole operator acts only on the electronic state, and the transition probability from an initial vibrational state

$|i\rangle$ to a final vibrational state $|j\rangle$ is proportional to $|\langle j|i\rangle|^2$ (i.e., governed by Franck-Condon factors). This inner product is non-zero only for a final vibrational state with the same representation as the initial vibrational state. Thus in the BOA, the representation of the vibrational state is unchanged during decay.

However, the vibronic representation is obtained from the product of electronic and vibrational representations. In certain cases, interactions can mix states of different electronic and vibrational symmetries but the same vibronic symmetry. This kind of vibronic coupling is a signature BOA breakdown. Typically, BOA-forbidden decays are weak (e.g., $\sim 10^{-3}$ branching fraction) but not necessarily negligible at the level of vibrational closure required for deep laser cooling. For this reason, here we will rely on the vibronic representation (rather than electronic and vibrational representations separately) to determine better-respected selection rules on transitions.

In the same manner that states of different electronic and vibrational representations (but the same vibronic representation) can mix via vibronic coupling, it is possible for states of different vibronic representations to mix. The first notable way in which mixing between states with different vibronic representations occurs is Coriolis interactions, which couple rigid body rotation with some other angular momentum (such as a vibrational or electronic angular momentum). These interactions can mix states only of the same total *rovibronic* representation. Such perturbations will typically be relatively small, and their effects (if any) on optical cycling have already been discussed in Ref. [83]. The second

notable way in which states with different vibronic representations mix is spin-orbit interactions, via a term in the Hamiltonian like $A^{\mathrm{SO}} L_i S_i$. This operator has the same representation as the angular momentum J_i, which is not generically the totally symmetric representation and therefore can produce mixed vibronic representations for an energy eigenstate. Such a term is possible because the full symmetry group of a spin-doublet molecule is an electron spin double group [75] rather than the molecular symmetry group that is more conventionally used in the literature (including here). We note that for molecules like SrSH and $SrNH_2$, because the ligand quenches orbital angular momentum (in low-J states), we can expect spin-orbit interactions to have a smaller influence on electronic state mixing than in species like SrOH or $SrOCH_3$ with $\sim\hbar$ of electronic orbital angular momentum around the molecular symmetry axis. Insofar as such effects do mix states of different overall vibronic symmetry, they play a role in laser cooling analogous to the Coriolis effects mentioned above.

All vibronic-symmetry-violating perturbations are expected to be weak and to affect rotational branching only at a low level, if at all (e.g., after scattering $\sim 10^3$–10^4 photons or more). As a result, any rotational leakage channels introduced by such effects will likely be important only for the vibrational states populated most frequently in an optical cycle, and can be addressed if needed by one or a few rotational repumps even in a deep optical cycle. Another perturbation that could conceivably be important in a sufficiently deep optical cycle is hyperfine interactions, which could mix states of different nuclear and rotational representations, but the same total molecular state representation.

Because hyperfine interactions are small ($\lesssim$ 1 MHz) in molecules like SrSH and $SrNH_2$, where the nuclear-spin-bearing hydrogen atoms are far from the metal-centered valence electron, here we treat them as having a negligible effect on rotational state purity.

To summarize, in the following treatment of symmetry-allowed and symmetry-forbidden transitions in C_s and C_{2v} molecules, we assume that there may be interactions that mix states of different electronic and vibrational symmetries, provided the *vibronic* symmetry remains pure. Specifically, we neglect any possible effect of Coriolis or spin-orbit interactions that could, in principle, mix states of different vibronic symmetry. We also neglect any possible effect of hyperfine interactions, which could mix states of different rotational symmetry. Otherwise, we allow for the possibility of mixing rotational state components ($N_{K_aK_c}$) in the excited manifold. We will not consider the effect of rotational state mixing in the ground electronic manifold. Such mixings have been considered in Ref. [83], and can result in rotational leakage on the order of $\sim 10^{-5}$. This is likely negligible for realistic experiments, and could easily be addressed by microwave or optical repumping schemes for any frequently-populated vibrational states in the ground electronic manifold. Vibrational states populated later in the optical cycle are even less likely to require repumpers to address these weak rotational leakage channels.

	E	E^*	A'	A''	Operators	State	K_c
A'	1	1	A'	A''	T_a, T_b, J_c	$\tilde{X}, \tilde{A}, \tilde{C}$	even
A''	1	-1	A''	A'	T_c, J_a, J_b	$\tilde{B}$	odd

Table D.2: Summary information for C_s, including the character table, product table, operator representations, electronic states in SrSH, and rotational state representations. Dipole operators T_i and angular momentum operators J_i assume the molecule is in the ab-plane. We also note the rotational symmetry for an $(N_{K_aK_c})$ state according to the even/odd identity of K_c.

$A'[(0_{00}) + \epsilon(1_{10})]^+ \rightarrow A'^-$	(1_{01})	(1_{11})	(2_{11})	(2_{21})
$A''[(0_{00}) + \epsilon(1_{10})]^- \rightarrow A''^+$	$a, \epsilon b$	$b, \epsilon a$	ϵa	ϵb

$A''[(0_{00}) + \epsilon(1_{10})]^- \rightarrow A'^+$	(0_{00})	(2_{02})	(1_{10})	(2_{12})	(2_{20})
$A'[(0_{00}) + \epsilon(1_{10})]^+ \rightarrow A''^-$	ϵc	—	c	—	ϵc

Table D.3: Possible decays from an excited state in its nominal ground rotational level, with a possible rotational state admixture, for each excited vibronic symmetry and to each ground vibronic symmetry. Superscript $\pm$ denotes parity. The second and further columns show ground rotational states and their possible population pathways. For SrSH only A' vibronic levels exist in the $\tilde{X}^2A'$ manifold but vibronic A'' ground levels are shown for the general case. Entries of $i = a, b, c$ denote fully allowed i-type transitions, while those with ϵ factors require an excited state admixture with (1_{10}) induced by perturbations. An entry of — shows states compatible with J and P selection rules for decays, but which cannot be populated via any mechanism considered here.

D.1.2 Analysis of C_s molecules

We now consider the symmetry properties of C_s molecules relevant to rotational and vibrational transitions. Summary information is presented in Tab. D.2. The operations in the C_s group are E (the identity) and E^* (inversion, or equivalently parity). The totally symmetric representation is A', and the odd-parity representation is A''.

In SrSH, the ground state is $\tilde{X}^2A'$ and the first three excited states are $\tilde{A}^2A'$, $\tilde{B}^2A''$, and $\tilde{C}^2A'$. All vibrational states and nuclear spin states are A'. Rotational states are A' if K_c is even, and A'' if K_c is odd. This implies, for example,

that states in the $\tilde{X}^2A'$ manifold are even (odd) parity when K_c is even (odd). By examining the character and product tables, we can see that $\tilde{X}^2A' \rightarrow \tilde{A}^2A'$ and $\tilde{X}^2A' \rightarrow \tilde{C}^2A'$ are $(a+b)$-type transitions, and $\tilde{X}^2A' \rightarrow \tilde{B}^2A''$ is a c-type transition. To a good approximation, in SrSH the $\tilde{X}^2A' \rightarrow \tilde{A}^2A'$ transition is b-type (with a small a-type amplitude) and the $\tilde{X}^2A' \rightarrow \tilde{C}^2A'$ transition is a-type (with a small b-type amplitude).

Because all vibrational states are A' in SrSH, no vibrational decays are forbidden in the BOA. Here we analyze rotational decays for all possible vibronic symmetry combinations involving an upper $(0_{00}; 1/2)$ state. Since we assume, for purposes of this treatment, that only states with the same J, parity, and vibronic symmetry can mix, a $(0_{00}; 1/2)$ excited state in either an A' or A'' vibronic state can mix only with a $(1_{10}; 1/2)$ state of the same vibronic symmetry. For example, the (1_{11}) rotational state (in a manifold with the same vibronic symmetry) would have opposite parity from (0_{00}), while a (2_{02}) rotational state cannot have $J = 1/2$. Furthermore, since (0_{00}) and (1_{10}) have the same rotational representation, namely A', there is no additional symmetry-based prohibition against these states mixing (as mentioned already in Sec. 5.2). In Table D.3 we show the possible rotational states populated in a ground vibronic manifold, from a combination of (0_{00}) and (1_{10}) in an excited vibronic manifold. All ground rotational states consistent with the appropriate parity selection rule and containing a $J = 1/2$ or $J = 3/2$ level are presented.

We see that for $A' \rightarrow A'$ or $A'' \rightarrow A''$ transitions, a nominal (0_{00}) state can decay to (1_{01}) via a-type transitions or to (1_{11}) via b-type transitions, as expected.

	E	(12)	E^*	$(12)^*$	A_1	A_2	B_1	B_2	Operators	State	K_aK_c
A_1	1	1	1	1	A_1	A_2	B_1	B_2	T_a	$\tilde{X}$, $\tilde{C}$	ee
A_2	1	1	−1	−1	A_2	A_1	B_2	B_1	J_a		eo
B_1	1	−1	−1	1	B_1	B_2	A_1	A_2	T_c, J_b	$\tilde{B}$	oo
B_2	1	−1	1	−1	B_2	B_1	A_2	A_1	T_b, J_c	$\tilde{A}$	oe

Table D.4: Summary information for C_{2v}, including the character table, product table, operator representations, electronic states in $SrNH_2$, and rotational state representations. Dipole operators T_i and angular momentum operators J_i assume the molecule is in the ab-plane and with the symmetry axis along a. We also note the rotational symmetry for an $(N_{K_aK_c})$ state according to the even/odd identity of K_a and K_c.

However, an admixture of an excited (1_{10}) component can also enable decays to (2_{11}) (a-type) and (2_{21}) (b-type) as well as additional decay pathways to (1_{01}) (b-type) and (1_{11}) (a-type). For example, in SrSH even if the $\tilde{A}^2A'$–$\tilde{X}^2A'$ transition dipole were exclusively b-type, an excited state admixture of (1_{01}) would result in the population of (1_{01}) and (2_{21}).

Additionally, J and parity selection rules alone would allow vibronic transitions $A'' \rightarrow A'$ or $A' \rightarrow A''$ originating from an excited $(0_{00}; 1/2)$ state to populate (0_{00}), (2_{02}), (1_{10}), (2_{12}), or (2_{20}). As seen in Table D.3, the nominal (0_{00}) excited state leads to population of (1_{10}) while the possible admixture of (1_{10}) can produce decays to (0_{00}) and (2_{20}). However, because both excited state components have $K_c = 0$, the (2_{02}) and (2_{12}) states with $K_c = 2$ should not be populated upon decay even though they possess $J = 3/2$ levels of the correct parity.

D.1.3 Analysis of C_{2v} molecules

We now consider C_{2v} molecules such as $SrNH_2$. The C_{2v} group possesses four symmetry operations: the identity, E; permutation of identical nuclei, (12); inversion, E^*; and permutation-inversion, $(12)^*$. Representations even under (12) are written A, while those odd under (12) are B. States even under $(12)^*$ obtain a subscript of 1, while those odd under $(12)^*$ obtain a subscript of 2. The four representations defined in this way are summarized in Tab. D.4.

A detailed treatment of the rovibronic structure is much more complicated in $SrNH_2$ compared to SrSH, for several reasons. In addition to the greater number of representations to consider, vibrational states and nuclear states may not be in the totally symmetric representation. We begin with an analysis of the nuclear state symmetry, followed by an analysis of allowed rotational decays from a nominal $(0_{00}; 1/2)$ state (with any combination of upper and lower vibronic representations).

Directly applying symmetry operations to nuclear states allows a given state's representation to be determined. For ordinary hydrogen with $I_H = 1/2$, the triplet $I = 1$ state has symmetry A_1 and the singlet $I = 0$ state has symmetry B_2. For deuterium with $I_H = 1$, the quintet with $I = 2$ and singlet with $I = 0$ both have representation A_1 and the triplet with $I = 1$ has representation B_2. With identical fermions, the total molecular wave function must be odd under hydrogen exchange and therefore transform as B_1 or B_2. On the other hand, with identical bosons, the total molecular wave function must be even under hydrogen (i.e., deuterium) exchange and therefore transform as A_1 or A_2. This

Γ_{ev}	I_H	$\Gamma_{\rm rot} = A_1$	$\Gamma_{\rm rot} = A_2$	$\Gamma_{\rm rot} = B_1$	$\Gamma_{\rm rot} = B_2$
A_1	1/2	$B_2, 0; B_2, +$	$B_2, 0; B_1, -$	$A_1, 1; B_1, -$	$A_1, 1; B_2, +$
A_2	1/2	$B_2, 0; B_1, -$	$B_2, 0; B_2, +$	$A_1, 1; B_2, +$	$A_1, 1; B_1, -$
B_1	1/2	$A_1, 1; B_1, -$	$A_1, 1; B_2, +$	$B_2, 0; B_2, +$	$B_2, 0; B_1, -$
B_2	1/2	$A_1, 1; B_2, +$	$A_1, 1; B_1, -$	$B_2, 0; B_1, -$	$B_2, 0; B_2, +$
A_1	1	$A_1, e; A_1, +$	$A_1, e; A_2, -$	$B_2, 1; A_2, -$	$B_2, 1; A_1, +$
A_2	1	$A_1, e; A_2, -$	$A_1, e; A_1, +$	$B_2, 1; A_1, +$	$B_2, 1; A_2, -$
B_1	1	$B_2, 1; A_2, -$	$B_2, 1; A_1, +$	$A_1, e; A_1, +$	$A_1, e; A_2, -$
B_2	1	$B_2, 1; A_1, +$	$B_2, 1; A_2, -$	$A_1, e; A_2, -$	$A_1, e; A_1, +$

Table D.5: Relationship between vibronic representation, nuclear spin, and rotational representation in C_{2v} molecules. Rows correspond to vibronic representations Γ_{ev} and hydrogen nuclear spins I_H, while columns correspond to rotational representations. Entries are of the form $\Gamma_{\rm nuc}, I; \Gamma_{\rm tot}, P$ specifying the required nuclear state representation, nuclear spin, total molecular state representation, and associated state parity. A nuclear spin of e indicates allowed values of $I = 0$ or $I = 2$.

implies that not all nuclear spin states are compatible with a given rovibronic state. The allowed nuclear state representation, nuclear spin states, total molecular representation, and total state parity for every combination of vibronic representation, rotational representation, and hydrogen spin magnitude is shown in Table D.5.

The rotational representation of an $(N_{K_aK_c})$ state depends on whether both K_a and K_c are even or odd. However, the parity of a state is, as for C_s, determined only by whether K_c is even or odd (see Table D.4). Thus the combination of parity and J selection rules alone would enable (0_{00}) in an excited vibronic manifold to mix with, at most, a (1_{10}) state with the same vibronic symmetry. However, unlike in the C_s case, the (0_{00}) and (1_{10}) states have different rotational symmetries and therefore do not ordinarily mix under the classes of perturbations we consider, described in Sec. D.1.1. Specifically, (0_{00}) has A_1 symmetry while (1_{10}) has B_2 symmetry. Viewed another way, as seen

in Table D.5, the (0_{00}) and (1_{10}) states exist for different nuclear isomers and can only mix via hyperfine interactions, provided the vibronic representation is pure.

We show the resulting rovibronic transitions in Table D.6. For completeness, we construct tables with the possibility of mixing excited state (0_{00}) and (1_{00}) components, but adopt a new rotational state label notation $(N^I_{K_aK_c})$ to emphasize the appropriate nuclear state I in each case. As already mentioned, in every case the admixture of (1_{10}) into (0_{00}) requires mixing states with different total nuclear spin values. If we assume that such a mixing is absolutely negligible, $\epsilon \to 0$, then for every combination of ground and excited vibronic representations there is exactly one rotational state that can be populated from the excited $(0_{00}; 1/2)$ level (except for cases where the vibronic manifolds differ by an A_2 representation, in which case the transition is vibronically forbidden regardless of the rotational levels involved). These results do not depend on the value of the hydrogen spin, I_H. The increased symmetry of C_{2v} compared to C_s therefore provides strong protection against rotational leakage channels.

D.1.4 Analysis of C_1 molecules

Totally asymmetric (chiral) molecules such as SrOCHDT have also been considered for laser cooling. In this case, the only operation in the molecular symmetry group is the identity, E, and the only representation is the totally symmetric representation, A. A molecule in C_1 cannot be in a parity eigenstate because parity maps an enantiomer to its opposite chirality, regardless of the ro-

$A_1[(0^e_{00})+\epsilon(1^1_{10})]^+ \to A_1^-$	(1^e_{01})	(2^e_{21})	(1^1_{11})	(2^1_{11})
$A_2[(0^e_{00})+\epsilon(1^1_{10})]^- \to A_2^+$	a	—	ϵa	ϵa
$B_1[(0^1_{00})+\epsilon(1^e_{10})]^- \to B_1^+$	(1^1_{01})	(2^1_{21})	(1^e_{11})	(2^e_{11})
$B_2[(0^1_{00})+\epsilon(1^e_{10})]^+ \to B_2^-$	a	—	ϵa	ϵa
$A_1[(0^e_{00})+\epsilon(1^1_{10})]^+ \to B_2^-$	(1^1_{01})	(2^1_{21})	(1^e_{11})	(2^e_{11})
$A_2[(0^e_{00})+\epsilon(1^1_{10})]^- \to B_1^+$	ϵb	ϵb	b	—
$B_1[(0^1_{00})+\epsilon(1^e_{10})]^- \to A_2^+$	(1^e_{01})	(2^e_{21})	(1^1_{11})	(2^1_{11})
$B_2[(0^1_{00})+\epsilon(1^e_{10})]^+ \to A_1^-$	ϵb	ϵb	b	—

$A_1[(0^e_{00})+\epsilon(1^1_{10})]^+ \to B_1^-$	(0^1_{00})	(2^1_{02})	(2^1_{20})	(1^e_{10})	(2^e_{12})
$A_2[(0^e_{00})+\epsilon(1^1_{10})]^- \to B_2^+$	ϵc	—	ϵc	c	—
$B_1[(0^1_{00})+\epsilon(1^e_{10})]^- \to A_1^+$	(0^e_{00})	(2^e_{02})	(2^e_{20})	(1^1_{10})	(2^1_{12})
$B_2[(0^1_{00})+\epsilon(1^e_{10})]^+ \to A_2^-$	ϵc	—	ϵc	c	—
$A_1[(0^e_{00})+\epsilon(1^1_{10})]^+ \to A_2^-$	(0^e_{00})	(2^e_{02})	(2^e_{20})	(1^1_{10})	(2^1_{12})
$A_2[(0^e_{00})+\epsilon(1^1_{10})]^- \to A_1^+$	—	—	—	—	—
$B_1[(0^1_{00})+\epsilon(1^e_{10})]^- \to B_2^+$	(0^1_{00})	(2^1_{02})	(2^1_{20})	(1^e_{10})	(2^e_{12})
$B_2[(0^1_{00})+\epsilon(1^e_{10})]^+ \to B_1^-$	—	—	—	—	—

Table D.6: Allowed decays from an excited state in its nominal ground rotational level, with possible rotational state admixture of (1_{10}), for each excited vibronic representation and to each ground vibronic representation. Superscript $\pm$ denotes parity, and superscripts within a rotational state label denotes nuclear spin I. For $I_H = 1/2$, e signifies $I = 0$ while for $I_H = 1$, e signifies $I = 0$ or 2. The second and further columns show ground rotational states and their possible population pathways. Entries of $i = a, b, c$ denote fully allowed i-type transitions, while those with ϵ factors require an excited state admixture with (1_{10}) induced by perturbations. Entries of — show states compatible with J and P selection rules on decays, but which cannot be populated via mechanisms considered here.

tational composition. In principle, one may obtain parity eigenstates of a chiral molecule by considering an extended set of states that includes both left-handed and right-handed configurations; the parity eigenstates are constructed from even and odd linear combinations of enantiomers. However, in most practical cases the tunneling time between enantiomers is extremely long and a chiral isomer may be considered in isolation, so that the C_1 molecular symmetry group is appropriate.

In this situation, rotational branching is constrained only by J selection rules. An excited (0_{00}) state can decay to the $J = 1/2$ or $J = 3/2$ sublevels of (1_{10}), (1_{01}), or (1_{11}). Furthermore, excited state rotational mixing of (0_{00}) with (1_{01}), (1_{10}), and (1_{11}) may enable additional decays to (0_{00}), (2_{02}), (2_{11}), (2_{12}), (2_{20}), and (2_{21}). Nevertheless, the magnitudes of any excited state mixing or transition strength must be assessed on a case-by-case basis, and these 9 ground rotational states will not typically be comparably populated.

References

[1] M. D. Schwartz, *Quantum Field Theory and the Standard Model*, 1 (Cambridge University Press, 2014).

[2] T. Aoyama, M. Hayakawa, T. Kinoshita, and M. Nio, Phys. Rev. D **91**, 033006 (2015).

[3] X. Fan, T. G. Myers, B. A. D. Sukra, and G. Gabrielse, Phys. Rev. Lett. **130**, 071801 (2023).

[4] M. Peskin and D. Schroeder, *An Introduction To Quantum Field Theory* (CRC Press, 2015).

[5] M. S. Safronova, D. Budker, D. DeMille, D. F. J. Kimball, A. Derevianko, and C. W. Clark, Rev. Mod. Phys. **90**, 025008 (2018).

[6] P. Zyla *et al.* (Particle Data Group), PTEP **2020**, 083C01 (2020), and 2021 update.

[7] I. Esteban, M. C. Gonzalez-Garcia, M. Maltoni, T. Schwetz, and A. Zhou, J. High Energ. Phys. **2020** (9).

[8] M. C. Gonzalez-Garcia, M. Maltoni, and T. Schwetz, Nufit: Three-flavour global analyses of neutrino oscillation experiments (2021).

[9] S. Weinberg, Phys. Rev. Lett. **37**, 657 (1976).

[10] C. A. Baker, D. D. Doyle, P. Geltenbort, K. Green, M. G. D. van der Grinten, P. G. Harris, P. Iaydjiev, S. N. Ivanov, D. J. R. May, J. M. Pendlebury, J. D. Richardson, D. Shiers, and K. F. Smith, Phys. Rev. Lett. **97**, 131801 (2006).

[11] J. M. Pendlebury, S. Afach, N. J. Ayres, C. A. Baker, G. Ban, G. Bison, K. Bodek, M. Burghoff, P. Geltenbort, K. Green, W. C. Griffith, M. van der Grinten, Z. D. Grujić, P. G. Harris, V. Hélaine, P. Iaydjiev, S. N. Ivanov, M. Kasprzak, Y. Kermaidic, K. Kirch, H.-C. Koch, S. Komposch, A. Kozela, J. Krempel, B. Lauss, T. Lefort, Y. Lemière, D. J. R. May, M. Musgrave, O. Naviliat-Cuncic, F. M. Piegsa, G. Pignol, P. N. Prashanth, G. Quéméner, M. Rawlik, D. Rebreyend, J. D. Richardson, D. Ries, S. Roccia, D. Rozpedzik, A. Schnabel, P. Schmidt-Wellenburg, N. Severijns, D. Shiers, J. A. Thorne, A. Weis, O. J. Winston, E. Wursten, J. Zejma, and G. Zsigmond, Phys. Rev. D **92**, 092003 (2015).

[12] A. D. Sakharov, Pis'ma Zh. Eksp. Teor. Fiz **5** (1967).

[13] M. B. Gavela, P. Hernández, J. Orloff, and O. Pène, Mod. Phys. Lett. A **09**, 10.1142/s0217732394000629 (1994).

[14] R. D. Peccei and H. R. Quinn, Phys. Rev. Lett. **38**, 1440 (1977).

[15] C. Cesarotti, Q. Lu, Y. Nakai, A. Parikh, and M. Reece, J. High Energ. Phys. **2019** (59).

[16] D. F. Jackson Kimball and K. van Bibber, *The Search for Ultralight Bosonic Dark Matter* (Springer Nature, 2022).

[17] V. C. Rubin, N. Thonnard, and J. Ford, W. K., Astrophys. J. **225**, 10.1086/182804 (1978).

[18] T. Lin, Tasi lectures on dark matter models and direct detection (2019), arXiv:1904.07915 [hep-ph] .

[19] E. G. Ferreira, Ultra-light dark matter (2021).

[20] Y. Ema, T. Gao, and M. Pospelov, Phys. Rev. Lett. **129**, 231801 (2022).

[21] T. S. Roussy, L. Caldwell, T. Wright, W. B. Cairncross, Y. Shagam, K. B. Ng, N. Schlossberger, S. Y. Park, A. Wang, J. Ye, and E. A. Cornell, Science **381**, 46 (2023).

[22] I. B. Khriplovich and S. K. Lamoreaux, *CP Violation Without Strangeness* (Springer Berliner, 1997).

[23] M. Denis, Y. Hao, E. Eliav, N. R. Hutzler, M. K. Nayak, R. G. Timmermans, and A. Borschesvky, J. Chem. Phys. **152**, 84303 (2020).

[24] R. H. Parker, M. R. Dietrich, M. R. Kalita, N. D. Lemke, K. G. Bailey, M. Bishof, J. P. Greene, R. J. Holt, W. Korsch, Z.-T. Lu, P. Mueller, T. P. O'Connor, and J. T. Singh, Phys. Rev. Lett. **114**, 233002 (2015).

[25] L. P. Gaffney, P. A. Butler, M. Scheck, A. B. Hayes, F. Wenander, M. Albers, B. Bastin, C. Bauer, A. Blazhev, S. Bönig, N. Bree, J. Cederkäll, T. Chupp, D. Cline, T. E. Cocolios, T. Davinson, H. De Witte, J. Diriken, T. Grahn, A. Herzan, M. Huyse, D. G. Jenkins, D. T. Joss, N. Kesteloot, J. Konki, M. Kowalczyk, T. Kröll, E. Kwan, R. Lutter, K. Moschner, P. Napiorkowski, J. Pakarinen, M. Pfeiffer, D. Radeck, P. Reiter, K. Reynders, S. V. Rigby, L. M. Robledo, M. Rudigier, S. Sambi, M. Seidlitz, B. Siebeck, T. Stora, P. Thoele, P. Van Duppen, M. J. Vermeulen, M. Von Schmid, D. Voulot, N. Warr, K. Wimmer, K. Wrzosek-Lipska, C. Y. Wu, and M. Zielinska, Nature **497**, 10.1038/nature12073 (2013).

[26] V. V. Flambaum and J. S. M. Ginges, Phys. Rev. A **65**, 032113 (2002).

[27] N. Auerbach, V. V. Flambaum, and V. Spevak, Phys. Rev. Lett. **76**, 4316 (1996).

[28] L. I. Schiff, Phys. Rev. **132**, 2194 (1963).

[29] E. D. Commins, J. D. Jackson, and D. P. DeMille, Am. J. Phys. **75**, 10.1119/1.2710486 (2007).

[30] P. G. H. Sandars and E. Lipworth, Phys. Rev. Lett. **13**, 718 (1964).

[31] P. G. Sandars, Phys. Lett. **22**, 290 (1966).

[32] A. N. Petrov, N. S. Mosyagin, T. A. Isaev, and A. V. Titov, Phys. Rev. A **76**, 030501 (2007).

[33] L. V. Skripnikov, A. N. Petrov, and A. V. Titov, J. Chem. Phys. **139**, 10.1063/1.4843955 (2013).

[34] R. Bala, V. S. Prasannaa, M. Abe, and B. P. Das, Eur. Phys. J. Plus **138**, 10.1140/epjp/s13360-023-04115-w (2023).

[35] ACME Collaboration, Science **343**, 269 (2014).

[36] ACME Collaboration, Nature **562**, 355 (2018).

[37] W. B. Cairncross, D. N. Gresh, M. Grau, K. C. Cossel, T. S. Roussy, Y. Ni, Y. Zhou, J. Ye, and E. A. Cornell, Phys. Rev. Lett. **119**, 10.1103/physrevlett.119.153001 (2017).

[38] Y. Takahashi, C. Zhang, A. Jadbabaie, and N. R. Hutzler, Phys. Rev. Lett. **131**, 183003 (2023).

[39] C. Zhang, P. Yu, A. Jadbabaie, and N. R. Hutzler, Phys. Rev. Lett. **131**, 193602 (2023).

[40] S. Bickman, P. Hamilton, Y. Jiang, and D. DeMille, Phys. Rev. A **80**, 023418 (2009).

[41] D. DeMille, Physics Today **68**, 34 (2015).

[42] S. G. Karshenboim, Can. J. Phys. **83**, 10.1139/p05-047 (2005).

[43] I. Kozyryev, Z. Lasner, and J. M. Doyle, Phys. Rev. A **103** (2021).

[44] K. Beloy, M. G. Kozlov, A. Borschevsky, A. W. Hauser, V. V. Flambaum, and P. Schwerdtfeger, Phys. Rev. A **83**, 062514 (2011).

[45] L. F. Pašteka, A. Borschevsky, V. V. Flambaum, and P. Schwerdtfeger, Phys. Rev. A **92**, 012103 (2015).

[46] Z. Lasner, A. Lunstad, C. Zhang, L. Cheng, and J. M. Doyle, Phys. Rev. A **106**, 20801 (2022).

[47] R. Grimm, M. Weidemüller, and Y. B. Ovchinnikov, Advances in Atomic, Molecular and Optical Physics **42**, 10.1016/S1049-250X(08)60186-X (2000).

[48] L. Anderegg, B. L. Augenbraun, Y. Bao, S. Burchesky, L. W. Cheuk, W. Ketterle, and J. M. Doyle, Nature Phys. **14**, 890 (2018).

[49] C. Hallas, N. B. Vilas, L. Anderegg, P. Robichaud, A. Winnicki, C. Zhang, L. Cheng, and J. M. Doyle, Phys. Rev. Lett. **130**, 153202 (2023).

[50] I. Kozyryev and N. R. Hutzler, Phys. Rev. Lett. **119**, 133002 (2017).

[51] J. Lim, J. R. Almond, M. A. Trigatzis, J. A. Devlin, N. J. Fitch, B. E. Sauer, M. R. Tarbutt, and E. A. Hinds, Phys. Rev. Lett. **120**, 123201 (2018).

[52] P. Jansen, H. L. Bethlem, and W. Ubachs, J. Chem. Phys. **140**, 010901 (2014).

[53] A. Shelkovnikov, R. J. Butcher, C. Chardonnet, and A. Amy-Klein, Phys. Rev. Lett. **100**, 150801 (2008).

[54] D. Hanneke, R. A. Carollo, and D. A. Lane, Phys. Rev. A **94**, 050101 (2016).

[55] D. Hanneke, B. Kuzhan, and A. Lunstad, Quant. Sci. Tech. **6**, 014005 (2020).

[56] J. Kobayashi, A. Ogino, and S. Inouye, Nature Comm. **10**, 10.1038/s41467-019-11761-1 (2019).

[57] N. B. Vilas, C. Hallas, L. Anderegg, P. Robichaud, A. Winnicki, D. Mitra, and J. M. Doyle, Nature **606**, 70 (2022).

[58] C. Hallas, G. K. Li, N. B. Vilas, P. Robichaud, L. Anderegg, and J. M. Doyle, High compression blue-detuned magneto-optical trap of polyatomic molecules (2024), arXiv:2404.03636 [physics.atom-ph] .

[59] I. Kozyryev, *Laser cooling and inelastic collisions of the polyatomic radical SrOH*, Ph.D. thesis, Harvard University (2017).

[60] I. Kozyryev, L. Baum, K. Matsuda, P. Olson, B. Hemmerling, and J. M. Doyle, New J. Phys. **17**, 045003 (2015).

[61] I. Kozyryev, L. Baum, K. Matsuda, B. Hemmerling, and J. M. Doyle, J. Phys. B **49**, 134002 (2016).

[62] I. Kozyryev, L. Baum, K. Matsuda, and J. M. Doyle, ChemPhysChem **17**, 3641 (2016).

[63] I. Kozyryev, L. Baum, K. Matsuda, B. L. Augenbraun, L. Anderegg, A. Sedlack, and J. M. Doyle, Phys. Rev. Lett. **118**, 173201 (2017).

[64] I. Kozyryev, L. Baum, L. Aldridge, P. Yu, E. E. Eyler, and J. M. Doyle, Phys. Rev. Lett. **120**, 063205 (2018).

[65] B. L. Augenbraun, *Methods for Direct Laser Cooling of Polyatomic Molecules*, Ph.D. thesis, Harvard University (2021).

[66] B. L. Augenbraun, Z. D. Lasner, A. Frenett, H. Sawaoka, C. Miller, T. C. Steimle, and J. M. Doyle, New J. Phys. **22**, 022003 (2020).

[67] B. L. Augenbraun, Z. D. Lasner, A. Frenett, H. Sawaoka, C. Miller, T. C. Steimle, and J. M. Doyle, New J. Phys. **22**, 022003 (2020).

[68] I. Kozyryev, Z. Lasner, and J. M. Doyle, Phys. Rev. A **103**, 043313 (2021).

[69] Y. Bao, *Ultracold molecules in an optical tweezer array: From dipolar interaction to ground state cooling*, Ph.D. thesis, Harvard University (2024).

[70] S. Burchesky, *Engineered Collisions, Molecular Qubits, and Laser Cooling of Asymmetric Top Molecules*, Ph.D. thesis, Harvard University (2023).

[71] L. Anderegg, *Ultracold molecules in optical arrays: from laser cooling to molecular collisions*, Ph.D. thesis, Harvard University (2019).

[72] J. M. Brown and A. Carrington, *Rotational spectroscopy of diatomic molecules* (Cambridge Univ. Press, 2003).

[73] G. Herzberg, *Spectra of Diatomic Molecules*, 2nd ed. (Van Nostrand, 1950).

[74] E. Hirota, *High-Resolution Spectroscopy of Transient Molecules* (Springer Berlin, Heidelberg, 1985).

[75] P. R. Bunker and P. Jensen, *Molecular Symmetry and Spectroscopy*, 2nd ed. (NRC Research Press, 2006).

[76] J. P. Grivet, J. Chem. Ed. **79**, 10.1021/ed079p127 (2002).

[77] J. J. Sakurai and J. Napolitano, *Modern Quantum Mechanics* (Cambridge University Press, 2017).

[78] S. McArdle, S. Endo, A. Aspuru-Guzik, S. C. Benjamin, and X. Yuan, Rev. Mod. Phys. **92**, 015003 (2020).

[79] M. Nielson and I. Chuang, *Quantum Computation and Quantum Information* (Cambridge University Press, Cambridge, 2010).

[80] A. R. Allouche, G. Wannous, and M. Aubert-Frécon, Chem. Phys. **170**, 10.1016/0301-0104(93)80087-P (1993).

[81] S. F. Rice, H. Martin, and R. W. Field, J. Chem. Phys. **82**, 10.1063/1.448676 (1985).

[82] J. Klos and S. Kotochigova, Phys. Rev. Research **2** (2020).

[83] B. L. Augenbraun, J. M. Doyle, T. Zelevinsky, and I. Kozyryev, Phys. Rev. X **10**, 031022 (2020).

[84] J. C. Phillips, Phys. Rev. **123**, 420 (1961).

[85] R. C. Morrison, J. Chem. Phys. **96**, 10.1063/1.461875 (1992).

[86] A. Kramida, Yu. Ralchenko, J. Reader, and and NIST ASD Team, NIST Atomic Spectra Database (ver. 5.11), [Online]. Available: `https://physics.nist.gov/asd` [2024, July 29]. National Institute of Standards and Technology, Gaithersburg, MD. (2023).

[87] K. E. Smith, *Groups and their representations*, Tech. Rep. (University of Michigan, 2010).

[88] R. Butcher, C. Chardonnet, and C. Borde, Phys. Rev. Lett. **70**, 2698 (1993).

[89] D. Forthomme, C. Linton, A. G. Read, D. W. Tokaryk, A. G. Adam, L. E. Downie, A. D. Granger, and W. S. Hopkins, J. Mol. Spect. **270**, 108 (2011).

[90] A. J. Merer and J. M. Allegretti, Can. J. Phys. **49**, 10.1139/p71-343 (1971).

[91] A. Jadbabaie, Y. Takahashi, N. H. Pilgram, C. J. Conn, Y. Zeng, C. Zhang, and N. R. Hutzler, New J. Phys. **25**, 10.1088/1367-2630/ace471 (2023).

[92] W. Quapp and B. P. Winnewisser, *J. Math. Chem.*, J. Math. Chem. **14**, 259 (1993).

[93] J. T. Hougen, J. Chem. Phys. **37**, 10.1063/1.1701334 (1962).

[94] L. Baum, N. B. Vilas, C. Hallas, B. L. Augenbraun, S. Raval, D. Mitra, and J. M. Doyle, Phys. Rev. A **103**, 043111 (2021).

[95] L. Baum, N. B. Vilas, C. Hallas, B. L. Augenbraun, S. Raval, D. Mitra, and J. M. Doyle, Phys. Rev. A **103**, 043111 (2021).

[96] Y. Hao, L. F. Pašteka, L. Visscher, P. Aggarwal, H. L. Bethlem, A. Boeschoten, A. Borschevsky, M. Denis, K. Esajas, S. Hoekstra, K. Jungmann, V. R. Marshall, T. B. Meijknecht, M. C. Mooij, R. G. Timmermans, A. Touwen, W. Ubachs, L. Willmann, Y. Yin, and A. Zapara, J. Chem. Phys. **151**, 10.1063/1.5098540 (2019).

[97] J. D. Tandy, J. G. Wang, J. Liévin, and P. F. Bernath, J. Mol. Spect. **270**, 10.1016/j.jms.2011.08.009 (2011).

[98] C. Zhang, C. Zhang, L. Cheng, T. C. Steimle, and M. R. Tarbutt, J. Mol. Spect. **386**, 10.1016/j.jms.2022.111625 (2022).

[99] E. T. Mengesha, A. T. Le, T. C. Steimle, L. Cheng, C. Zhang, B. L. Augenbraun, Z. Lasner, and J. Doyle, J. Phys. Chem. A **124**, 3135 (2020).

[100] J. J. McClelland and J. L. Hanssen, Phys. Rev. Lett. **96**, 143005 (2006).

[101] S. Popa, S. Schaller, A. Fielicke, J. Lim, B. G. Sartakov, M. R. Tarbutt, and G. Meijer, Phys. Rev. X **14**, 021035 (2024).

[102] Z. Zeng, S. Deng, S. Yang, and B. Yan, (2024), arXiv:2405.17883 .

[103] M. D. Di Rosa, Eur. Phys. J. D **31**, 395 (2004).

[104] G. Z. Zhu, D. Mitra, B. L. Augenbraun, C. E. Dickerson, M. J. Frim, G. Lao, Z. D. Lasner, A. N. Alexandrova, W. C. Campbell, J. R. Caram, J. M. Doyle, and E. R. Hudson, Nature Chem. **14**, 10.1038/s41557-022-00998-x (2022).

[105] C. Zhang, B. Augenbraun, Z. D. Lasner, N. B. Vilas, J. M. Doyle, and L. Cheng, J. Chem. Phys. **155**, 91101 (2021).

[106] A. Frenett, Z. Lasner, L. Cheng, and J. M. Doyle, Phys. Rev. A **110**, 022811 (2024).

[107] B. L. Augenbraun, Z. D. Lasner, A. Frenett, H. Sawaoka, A. T. Le, J. M. Doyle, and T. C. Steimle, Phys. Rev. A **103** (2021).

[108] I. Kozyryev, T. C. Steimle, P. Yu, D.-T. Nguyen, and J. M. Doyle, New J. Phys. **21** (2019).

[109] I. J. Smallman, F. Wang, T. C. Steimle, M. R. Tarbutt, and E. A. Hinds, J. Mol. Spec. **300**, 3 (2014).

[110] J. F. Barry, D. J. McCarron, E. B. Norrgard, M. H. Steinecker, and D. Demille, Nature **512**, 286 (2014).

[111] T. Chen, W. Bu, and B. Yan, Phys. Rev. A **94**, 063415 (2016).

[112] H. Metcalf, Rev. Mod. Phys 10.1103/RevModPhys.89.041001 (2017).

[113] V. Voitskhovich, M. Danileiko, A. Negriiko, V. I. Romanenko, and L. P. Yatsenko, Pisma Zh. Eksp. Teor. Fiz. **49** (1989).

[114] E. Ilinova, J. Weinstein, and A. Derevianko, New J. Phys. **17**, 055003 (2015).

[115] T. G. Freegarde, J. Walz, and T. W. Hänsch, Optics Comm. **117**, 262 (1995).

[116] V. I. Romanenko, Y. G. Udovitskaya, A. V. Romanenko, and L. P. Yatsenko, Phys. Rev. A **90**, 53421 (2014).

[117] V. I. Romanenko and L. P. Yatsenko, J. Phys. B **44**, 115305 (2011).

[118] B. Nölle, H. Nölle, J. Schmand, and H. Andrä, Europhys. Lett. **33** (1995).

[119] A. Goepfert, I. Bloch, D. Haubrich, F. Lison, R. Schütze, R. Wynands, and D. Meschede, Phys. Rev. A **56**, R3354 (1997).

[120] M. Chieda and E. Eyler, Phys. Rev. A **84**, 063401 (2011).

[121] L. Aldridge, S. Galica, and E. Eyler, Phys. Rev. A **93**, 013419 (2016).

[122] J. Dalibard and C. Cohen-Tannoudji, J. Opt. Soc. Am. B **6**, 2023 (1989).

[123] A. Prehn, M. Ibrügger, R. Glöckner, G. Rempe, and M. Zeppenfeld, Phys. Rev. Lett. **116**, 063005 (2016).

[124] D. Comparat, Phys. Rev. A **89**, 043410 (2014).

[125] N. J. Fitch and M. R. Tarbutt, ChemPhysChem **17**, 3609 (2016).

[126] B. L. Augenbraun, A. Frenett, H. Sawaoka, C. Hallas, N. B. Vilas, A. Nasir, Z. D. Lasner, and J. M. Doyle, Phys. Rev. Lett. **127**, 263002 (2021).

[127] E. Chae, *Laser slowing of CaF molecules and progress towards a dual-MOT for Li and CaF*, Ph.D. thesis, Harvard University, Cambridge, MA (2015).

[128] H. Sawaoka, A. Frenett, A. Nasir, T. Ono, B. L. Augenbraun, T. C. Steimle, and J. M. Doyle, Phys. Rev. A **107**, 022810 (2023).

[129] N. R. Hutzler, H.-I. Lu, and J. M. Doyle, Chem. Rev. **112**, 4803 (2012).

[130] J. F. Barry, E. S. Shuman, and D. DeMille, Phys. Chem. Chem. Phys. **13**, 18936 (2011).

[131] T. C. Steimle, C. Linton, E. T. Mengesha, X. Bai, and A. T. Le, Phys. Rev. A **100**, 052509 (2019).

[132] R. F. Curl, Molecular Physics **9**, 585 (1965).

[133] M. R. Tarbutt, Contemp. Phys. **59**, 356 (2018).

[134] N. J. Fitch, J. Lim, E. A. Hinds, B. E. Sauer, and M. R. Tarbutt, Quantum Science and Technology **6**, 014006 (2020).

[135] K. Dunfield, C. Linton, T. Clarke, J. McBride, A. Adam, and J. Peers, J. Mol. Spect. **174**, 433 (1995).

[136] P. Aggarwal, H. L. Bethlem, A. Borschevsky, M. Denis, K. Esajas, P. A. B. Haase, Y. Hao, S. Hoekstra, K. Jungmann, T. B. Meijknecht, M. C. Mooij, R. G. E. Timmermans, W. Ubachs, L. Willmann, and A. Zapara, The European Physical Journal D **72**, 10.1140/epjd/e2018-90192-9 (2018).

[137] T. C. Steimle, S. Frey, A. Le, D. DeMille, D. A. Rahmlow, and C. Linton, Phys. Rev. A **84**, 012508 (2011).

[138] M. Denis, P. A. B. Haase, R. G. E. Timmermans, E. Eliav, N. R. Hutzler, and A. Borschevsky, Phys. Rev. A **99**, 042512 (2019).

[139] J. Tandy, J.-G. Wang, J. Liévin, and P. Bernath, J. Mol. Spect. **270**, 44 (2011).

[140] A. Jadbabaie, N. H. Pilgram, J. Kłos, S. Kotochigova, and N. R. Hutzler, New J. Phys. **22**, 022002 (2020).

[141] J. Lee, E. Meyer, R. Paudel, J. Bohn, and A. Leanhardt, J. Mod. Opt. **56**, 2005 (2009), https://doi.org/10.1080/09500340903349930 .

[142] S. M. Sickafoose, A. W. Smith, and M. D. Morse, J. Chem. Phys. **116**, 993 (2002), https://doi.org/10.1063/1.1427068 .

[143] F. Wang and T. C. Steimle, J. Chem. Phys. **135**, 104313 (2011), https://doi.org/10.1063/1.3635441 .

[144] Y. Chamorro, A. Borschevsky, E. Eliav, N. R. Hutzler, S. Hoekstra, and L. c. v. F. Pašteka, Phys. Rev. A **106**, 052811 (2022).

[145] B. L. Augenbraun, J. M. Doyle, T. Zelevinsky, and I. Kozyryev, Phys. Rev. X **10**, 031022 (2020).

[146] T. A. Isaev, S. Hoekstra, and R. Berger, Phys. Rev. A **82**, 052521 (2010).

[147] T. Isaev, A. Zaitsevskii, and E. Eliav, J. Phys. B **50**, 225101 (2017).

[148] Z. Yang, J. Li, Q. Lin, L. Xu, H. Wang, T. Yang, and J. Yin, Phys. Rev. A **99**, 032502 (2019).

[149] R. Mitra, V. S. Prasannaa, B. K. Sahoo, N. R. Hutzler, M. Abe, and B. P. Das, Atoms **9**, 10.3390/atoms9010007 (2021).

[150] L. Xu, Y. Yin, B. Wei, Y. Xia, and J. Yin, Phys. Rev. A **93**, 013408 (2016).

[151] E. Chae, Phys. Chem. Chem. Phys. **23**, 1215 (2021).

[152] R. R. Wright and T. A. Miller, J. Mol. Spec. **194**, 219 (1999).

[153] E. B. Norrgard, D. S. Barker, S. Eckel, J. A. Fedchak, N. N. Klimov, and J. Scherschligt, Comm. Phys. **2**, 1 (2019).

[154] Y. Hao, P. Navrátil, E. B. Norrgard, M. Iliaš, E. Eliav, R. G. E. Timmermans, V. V. Flambaum, and A. Borschevsky, Phys. Rev. A **102**, 052828 (2020).

[155] P. Crozet, F. Martin, A. J. Ross, C. Linton, M. J. Dick, and A. G. Adam, J. Mol. Spect. **213**, 28 (2002).

[156] D. Mitra, N. B. Vilas, C. Hallas, L. Anderegg, B. L. Augenbraun, L. Baum, C. Miller, S. Raval, and J. M. Doyle, Science **369**, 1366 (2020).

[157] J. Nakagawa, R. F. Wormsbecher, and D. O. Harris, J. of Mol. Spect. **97**, 10.1016/0022-2852(83)90336-3 (1983).

[158] C. R. Brazier, P. F. Bernath, S. Kinsey-Nielsen, and L. C. Ellingboe, J. Chem. Phys. **82**, 1043 (1985).

[159] M. A. Anderson, W. L. Barclay, and L. M. Ziurys, Chem. Phys. Lett. **196**, 10.1016/0009-2614(92)85948-A (1992).

[160] T. C. Steimle, D. A. Fletcher, K. Y. Jung, and C. T. Scurlock, J. Chem. Phys. **96**, 2556 (1992).

[161] P. I. Presunka and J. A. Coxon, Can. J. Chem. **71**, 10.1139/v93-211 (1993).

[162] D. A. Fletcher, K. Y. Jung, C. T. Scurlock, and T. C. Steimle, J. Chem. Phys. **98**, 1837 (1993).

[163] P. I. Presunka and J. A. Coxon, J. Chem. Phys. **101**, 201 (1994).

[164] D. A. Fletcher, M. A. Anderson, W. L. Barclay, and L. M. Ziurys, J. Chem. Phys. **102**, 10.1063/1.469482 (1995).

[165] P. I. Presunka and J. A. Coxon, Chem. Phys. **190**, 10.1016/0301-0104(94)00330-D (1995).

[166] D.-T. Nguyen, T. C. Steimle, I. Kozyryev, M. Huang, and A. B. McCoy, J. Mol. Spec. **347**, 7 (2018).

[167] C. J. Foot, Oxford Master Series (2005).

[168] H. J. Metcalf and P. Van der Straten, *Laser cooling and trapping* (Springer Science & Business Media, 2012).

[169] C. Cohen-Tannoudji, J. Dupont-Roc, and G. Grynberg, *Atom—Photon Interactions* (Wiley Interscience, 1998).

[170] J. F. Barry, E. S. Shuman, E. B. Norrgard, and D. DeMille, Phys. Rev. Lett. **108**, 103002 (2012).

[171] B. Hemmerling, E. Chae, A. Ravi, L. Anderegg, G. K. Drayna, N. R. Hutzler, A. L. Collopy, J. Ye, W. Ketterle, and J. M. Doyle, J. Phys. B **49**, 174001 (2016).

[172] V. Zhelyazkova, A. Cournol, T. E. Wall, A. Matsushima, J. J. Hudson, E. A. Hinds, M. R. Tarbutt, and B. E. Sauer, Phys. Rev. A **89**, 053416 (2014).

[173] M. Yeo, M. T. Hummon, A. L. Collopy, B. Yan, B. Hemmerling, E. Chae, J. M. Doyle, and J. Ye, Phys. Rev. Lett. **114**, 10.1103/physrevlett.114.223003 (2015).

[174] S. Truppe, H. J. Williams, M. Hambach, L. Caldwell, N. J. Fitch, E. A. Hinds, B. E. Sauer, and M. R. Tarbutt, Nat. Phys. (2017).

[175] M. T. Hummon, M. Yeo, B. K. Stuhl, A. L. Collopy, Y. Xia, and J. Ye, Phys. Rev. Lett. **110**, 143001 (2013).

[176] L. Anderegg, B. L. Augenbraun, E. Chae, N. R. Hutzler, A. Ravi, A. L. Collopy, J. Ye, W. Ketterle, and J. M. Doyle, Phys. Rev. Lett. **119**, 103201 (2017).

[177] A. L. Collopy, S. Ding, Y. Wu, I. A. Finneran, L. Anderegg, B. L. Augenbraun, J. M. Doyle, and J. Ye, Phys. Rev. Lett. **121**, 213201 (2018).

[178] D. J. Berkeland and M. G. Boshier, Phys. Rev. A **65**, 10.1103/PhysRevA.65.033413 (2002).

[179] H. J. Williams, S. Truppe, M. Hambach, L. Caldwell, N. J. Fitch, E. A. Hinds, B. E. Sauer, and M. R. Tarbutt, New J. Phys. **19**, 113035 (2017).

[180] N. J. Fitch and M. R. Tarbutt, in *Advances In Atomic, Molecular, and Optical Physics*, Vol. 70 (Elsevier, 2021).

[181] J. A. Coxon, M. Li, and P. I. Presunka, J. Mol. Spect. **150**, 10.1016/0022-2852(91)90191-C (1991).

[182] M. Li and J. A. Coxon, J. Chem. Phys. **102**, 10.1063/1.468643 (1995).

[183] S. Truppe, H. J. Williams, N. J. Fitch, M. Hambach, T. E. Wall, E. A. Hinds, B. E. Sauer, and M. R. Tarbutt, New J. Phys. **19**, 022001 (2017).

[184] T. K. Langin and D. DeMille, New J. Phys. **25**, 10.1088/1367-2630/acc34d (2023).

[185] I. Kozyryev and N. R. Hutzler, Phys. Rev. Lett. **119**, 133002 (2017).

[186] T. A. Isaev, A. V. Zaitsevskii, and E. Eliav, J. Phys. B **50**, 225101 (2017).

[187] N. R. Hutzler, Quant. Sci. Tech. **5**, 044011 (2020).

[188] S. Eckel, P. Hamilton, E. Kirilov, H. W. Smith, and D. DeMille, Phys. Rev. A **87**, 052130 (2013).

[189] D. DeMille, Physics Today **68**, 34 (2015).

[190] I. Kozyryev, L. Baum, K. Matsuda, and J. M. Doyle, Chem. Phys. Chem. **17**, 3641 (2016).

[191] D. Mitra, N. B. Vilas, C. Hallas, L. Anderegg, B. L. Augenbraun, L. Baum, C. Miller, S. Raval, and J. M. Doyle, Science **369**, 1366 (2020).

[192] V. V. Flambaum and I. B. Khriplovich, Phys. Lett. A **110**, 121 (1985).

[193] V. A. Dzuba, V. V. Flambaum, and Y. V. Stadnik, Phys. Rev. Lett. **119**, 223201 (2017).

[194] I. Kozyryev, Z. Lasner, and J. M. Doyle, Phys. Rev. A **103**, 043313 (2021).

[195] Q. Wei, S. Kais, B. Friedrich, and D. Herschbach, J. Chem. Phys. **135**, 154102 (2011).

[196] M. L. Wall, K. Maeda, and L. D. Carr, Ann. Phys. (Leipzig) **525**, 845 (2013).

[197] M. L. Wall, K. Maeda, and L. D. Carr, New J. Phys. **17**, 025001 (2015).

[198] P. Yu, L. W. Cheuk, I. Kozyryev, and J. M. Doyle, New J. Phys. **21**, 093049 (2019).

[199] N. Balakrishnan, J. Chem. Phys. **145**, 150901 (2016).

[200] J. L. Bohn, A. M. Rey, and J. Ye, Science **357**, 1002 (2017).

[201] M. Li, J. Kłos, A. Petrov, and S. Kotochigova, Comm. Phys. **2**, 148 (2019).

[202] A. C. Paul, K. Sharma, M. A. Reza, H. Telfah, T. A. Miller, and J. Liu, J. Chem. Phys. **151**, 134303 (2019).

[203] J. Kłos and S. Kotochigova, Phys. Rev. Res. **2**, 13384 (2020).

[204] C. Zhang, N. R. Hutzler, and L. Cheng, J. Chem. Theory Comput. **19**, 4136 (2023).

[205] G.-Z. Zhu, G. Lao, C. E. Dickerson, J. R. Caram, W. C. Campbell, A. N. Alexandrova, and E. R. Hudson, J. Phys. Chem. Lett. **15**, 590 (2024).

[206] H. L. Bethlem and G. Meijer, Int. Rev. Phys. Chem. **22**, 73 (2003).

[207] B. K. Stuhl, B. C. Sawyer, D. Wang, and J. Ye, Phys. Rev. Lett. **101**, 243002 (2008).

[208] I. Kozyryev, T. C. Steimle, P. Yu, D.-T. Nguyen, and J. M. Doyle, New J. Phys **21**, 52002 (2019).

[209] R. F. Wormsbecher and R. D. Suenram, J. Mol. Spect. **95**, 391 (1982).

[210] L. C. O'Brien, C. R. Brazier, and P. F. Bernath, J. Mol. Spect. **130**, 13 (1988).

[211] C. R. Brazier and P. F. Bernath, J. Chem. Phys. **91**, 4548 (1989).

[212] A. J. Marr, F. Grieman, and T. C. Steimle, J. Chem. Phys. **105**, 3930 (1996).

[213] M. J. Dick, . P. M. Sheridan, J.-G. Wang, and . P. F. Bernath, J. Chem. Phys **124**, 174309 (2006).

[214] R. F. Wormsbecher, M. Trkula, C. Martner, R. E. Penn, and D. O. Harris, J. Mol. Spect. **97**, 29 (1983).

[215] A. M. Bopegedera, C. R. Brazier, and P. F. Bernath, J. Phys. Chem. **91**, 2779 (1987).

[216] C. R. Brazier and P. F. Bernath, J. Mol. Phys. **201**, 116 (2000).

[217] J. M. Thompsen, P. M. Sheridan, and L. M. Ziurys, Chem. Phys. Lett. **330**, 373 (2000).

[218] G. H. Fuller, J. Phys. Chem. Ref. Data **5**, 835 (1976).

[219] W. T. Fernando, R. S. Ram, L. C. O'Brien, and P. F. Bernath, J. Phys. Chem. **95**, 2665 (1991).

[220] D. T. Halfen, A. J. Apponi, J. M. Thompsen, and L. M. Ziurys, J. Chem. Phys. **115**, 11131 (2001).

[221] P. M. Sheridan, M. J. Dick, J. G. Wang, and P. F. Bernath, Mol. Phys. **105**, 569 (2007).

[222] T. Ichino, J. Gauss, and J. F. Stanton, J. Chem. Phys. **130**, 174105 (2009).

[223] L. Baum, N. B. Vilas, C. Hallas, B. L. Augenbraun, S. Raval, D. Mitra, and J. M. Doyle, Phys. Rev. Lett. **124**, 133201 (2020).

[224] B. L. Augenbraun, Z. D. Lasner, A. Frenett, H. Sawaoka, A. T. Le, J. M. Doyle, and T. C. Steimle, Phys. Rev. A **103**, 022814 (2021).

[225] H. L. Bethlem, G. Berden, F. M. Crompvoets, R. T. Jongma, A. J. Van Roij, and G. Meijer, Nature **406**, 491 (2000).

[226] R. Fulton, A. I. Bishop, and P. F. Barker, Phys. Rev. Lett. **93** (2004).

[227] G. Dong, W. Lu, and P. F. Barker, Phys. Rev. A **69**, 10.1103/PhysRevA.69.013409 (2004).

[228] L. Wang, P. F. Barker, S. Willitsch, R. Fulton, A. I. Bishop, and M. N. Shneider, J. Phys. B **39**, 1097 (2006).

[229] R. Fulton, A. I. Bishop, M. N. Shneider, and P. F. Barker, Nature Phys. **2**, 10.1038/nphys339 (2006).

[230] P. F. Barker, S. M. Purcell, P. Douglas, P. Barletta, N. Coppendale, C. Maher-Mcwilliams, and J. Tennyson, Faraday Discussions **142**, 175 (2009).

[231] Y. Xia, Y.-L. Yin, X. Ji, and J.-P. Yin, Chin. Phys. Lett. **29**, 10.1088/0256-307X/29/5/053701 (2012).

[232] S. Hou, Q. Wang, L. Deng, and Y. Yang, Chin. Phys. B **27**, 53701 (2018).

[233] A. Singh, L. Maisenbacher, Z. Lin, J. J. Axelrod, C. D. Panda, and H. Müller, Phys. Rev. Res. **5**, 033008 (2023).

[234] X. Wu, T. Gantner, M. Koller, M. Zeppenfeld, S. Chervenkov, and G. Rempe, Science **358**, 645 (2017)

This thesis was typeset using LaTeX, originally developed by Leslie Lamport and based on Donald Knuth's TeX. The body text is set in 11 point Egenolff-Berner Garamond, a revival of Claude Garamont's humanist typeface. The above illustration, "Science Experiment 02", was created by Ben Schlitter and released under CC BY-NC-ND 3.0. A template that can be used to format a PhD thesis with this look and feel has been released under the permissive MIT (X11) license, and can be found online at github.com/suchow/Dissertate or from its author, Jordan Suchow, at suchow@post.harvard.edu.